This work is protected by copyright and other intellectual property rights and duplication or sale of all or part is not permitted, except that material may be duplicated by you for research, private study, criticism/review or educational purposes. Electronic or print copies are for your own personal, non-commercial use and shall not be passed to any other individual. No quotation may be published without proper acknowledgement. For any other use, or to quote extensively from the work, permission must be obtained from the copyright holder/s.

ELECTRON STIMULATED ELECTRON EMISSION FROM SOLID SURFACES

A thesis presented for the degree of

Doctor of Philosophy at the

University of Keele

by

B. Wright Grad. Inst. P.

Physics Department,
University of Keele,
Staffordshire.

August, 1974

UNIVERSITY
OF KEELE

CONTENTS

RESULTS AND DISCUSSIONS - PART 1

Selected problems in Auger electron spectroscopy and associated techniques

ACKNOWLEDGEMENTS

The author wishes to thank and acknowledge:

Professor D.J.E. Ingram and Professor W. Fuller for the use of the laboratory facilities.

Dr. E.B. Pattinson for his splendid supervision and help throughout this work.

Dr. M. Suleman, Dr. P.R. Harris, Mr. S. Singh and Mr. W.R.C. Stewart and other colleagues in the Physics Department for useful suggestions and discussions.

The technical staff of the department and in particular, Mr. G. Dudley, Mr. W. Brearley and Mr. M.G. Davies for their helpful assistance throughout this work.

Mr. M. Daniels for his photographic work.

The Council for Valve Development and the Science Research Council for the provision of personal financial support during this work.

Mrs. A. Seaton for her efficient typing and duplication of this thesis.

My wife and parents for their generous help.

ABSTRACT

The topic of electron stimulated secondary electron emission is introduced in relation to studies in surface physics. In addition, some of the more recent literature in this subject is reviewed and critically appraised.

An apparatus for high resolution energy analysis of low energy (0-2keV) secondary electrons is described, along with its associated circuitry. Additional experimental features are discussed enabling both scanning electron microscopy and quantitative Auger electron spectroscopy to be used in the experimental apparatus. Ultra-high vacuum techniques (giving 10^{-10}torr pressure) enabled the observation of clean surfaces for many hours, before contamination ensued.

The results presented relate to several problems in Auger electron spectroscopy and affiliated techniques. The problems of quantifing Auger spectroscopy are discussed and the cesium on gold system is investigated for quantification purposes. Calibration curves for this system are given. Also, the strong surface reactivity of zirconium is investigated using Auger spectroscopy. Zirconium is now in wide use as a bulk gettering material although little is known about its pumping action. The presented results shed more light on this topic. The production and analysis of temperature-resistant low secondary yield metal blacks, indicate a strong preference for platinum black coated surfaces in many technological applications. Also, observations of the anomalous 'free-electron like' behaviour of antimony are made, using the technique of electron energy loss spectroscopy.

Perhaps the most important results, relate to characteristic slow secondary electrons originating from 'very clean' magnesium and aluminium surfaces. Much of the recent literature in this area is shown to be inaccurate by these new experimental data. Also, a new interpretation of these data indicates that high-energy band structure can

influence slow secondary electron energies. The interpretation enables critical point energies to be determined accurately. In addition, this slow peak spectroscopy is shown to be capable of greater sensitivity to surface contamination than Auger electron spectroscopy.

CHAPTER 1

INTRODUCTION

When a beam of charged particles strikes a solid surface, many interactions and excitations take place in the surface which may result in the emission of electrons. The complete analysis of such electrons (e.g. angular variations, energies, intensities etc.) can yield much information regarding surface and electronic structures, surface species, chemical environments and so on. One of the best means of exciting such electrons is electron stimulation using a primary electron beam. This is due to the fact that an electron is a strongly interacting particle in matter.

The main topics of this thesis will be concerned with electron stimulated secondary electron emission and its uses in studies of surfaces. This subject also has many technological applications in fields such as friction, corrosion, fracture, adhesion etc. In addition, the subject is related to devices such as electron multipliers, camera tubes and microwave power tubes requiring specific secondary yield values for surfaces.

Although some work was done between 1920 and 1940 on the energy distribution of secondary electrons, it was Lander [1] in 1953 who made the significant step of suggesting Auger electron analysis for surface compositional studies. It is the technique of Auger electron spectroscopy which has enabled the confident determination of the atomically 'clean' surface.

Some related techniques for surface analysis are beiefly introduced at the beginning of this chapter. The remainder of the chapter is concerned with electron stimulated secondary electron emission, which will be divided into four basic areas of work as follows:

(i) Secondary electron yield

(ii) Auger electron spectroscopy

(iii) Characteristic energy loss spectroscopy

(iv) Slow secondary electron spectroscopy

TABLE 1.1

Relationship between forms of energy input and output for various spectrographic methods.

Energy in / Energy out	Electromagnetic Radiation ($h\nu$)	Electrons (e)	Ions	Electrostatic Energy
$h\nu$	X-ray fluorescense	Electron Microprobe APS	IEX	
e	Auger electrons UPS & XPS	AES	Ion Neutral-ization	FIM Atom Probe
Ions			Ion mic-roprobe SIMS ISS Ruther-ford high energy ions	

KEY: AES -- Auger electron spectroscopy; APS -- Appearance potential spectroscopy; XPS and UPS -- X-ray photoelectron spectroscopy and Ultra-violet photoelectron spectroscopy; FIM -- Field ion microscopy; IEX -- Ion- X-ray spectroscopy; ISS -- Ion scattering spectroscopy; SIMS -- Secondary ion mass spectroscopy.

1.1 Some Techniques for Surface Analysis

Various forms of excitation energy may be used as probes for surface analysis; these are electromagnetic radiation, electrons, ions and electrostatic energy. Emitted energy can be detected using an appropriate spectroscopy for electromagnetic radiation, electrons and ions. Table 1.1 shows the many spectroscopies available for surface analysis together with their respective excitation and detection means. Several of these spectroscopies will be briefly discussed together with the technique of low energy electron diffraction(LEED). Auger electron spectroscopy(AES) will be discussed in greater detail in sub-section 1.2.3.

The electron microprobe (Reuter[2]) identifies the presence of chemical species by the emission of characteristic X-rays generated in the specimen by a focussed electron beam (up to 30keV). The spatial resolution can be better than one micron; with quantitative measurements of about 5% error. However, the electron microprobe is not a true 'surface' tool since the sampled depth is usually greater than one micron due to the depth of penetration of the electron beam.

The atom probe and field-ion microscopy (Müller[3]) are powerful surface characterization techniques. The atom probe field ion microprobe can identify single atoms. The specimens however, must be in the form of fine spherical tips (radius of a few hundred Angströms). In addition, the surfaces must be studied under very large applied electric fields, and the methods are only applicable to refractory metals.

In the ion microprobe, a focussed beam of rare-gas ions strike the surface and surface atoms are sputtered into a sensitive mass spectrometer (Socha[4]). The method can detect surface concentrations down to a few parts in 10^9, with quantitative interpretation. The technique is sensitive to the top surface layer, but is destructive and requires complex instrumentation.

X-ray photoelectron spectroscopy(XPS) was developed by Siegbahn and co-workers (Siegbahn et. al.[5]). A beam of X-rays is directed onto a specimen and the emitted electrons are collected and energy analysed. Direct photoelectrons ejected from the specimen have well-defined energies allowing the emitting species to be identified. Information on the chemical state of the emitting atom can be obtained by the measurement of the 'energy shift' from that of the free-atom energy. In ultra-violet photoelectron spectroscopy (UPS), excitation is by ultra-violet radiation and detailed information on the outer bonding electronic energies may be obtained. Both XPS and UPS are surface sensitive techniques since the sampling depth is determined by the escape depth of the ejected electrons, as in AES (see sub-section 1.2.3c). However, the cross-section for photoelectron emission is small and long counting times are needed in this method.

Ion scattering methods measure the change in energy of light ions, usually H^+ or He^+ scattered inelastically from a surface (Smith[6]). The energy loss may be related to the scattering particle and ion masses, hence the scattering particle can be identified. The method requires an accelerator and incident energies from keV to MeV have been used. The technique is destructive and is without quantitative interpretation.

Perhaps the most productive and widely used method to date is that of low energy electron diffraction(LEED), (Estrup and McRae[7], Prutton[8]). LEED is a true surface technique, sensitive only to the top few atomic layers, but it is applicable only to single-crystal surfaces. It gives only structural information concerning the two dimensional surface order and exact unambiguous interpretation is difficult, especially in the absence of surface chemical information. For this reason, the majority of LEED systems are now combined with AES (Weber and Peria[9]).

In the LEED technique, a low energy (10-1,000eV) electron beam is made to strike a crystal surface at normal incidence. Elastically scattered electrons are accelerated to a fluorescent screen and usually produce a geometrical pattern of bright spots on the screen. Diffraction occurs when the primary electron wavelength is a simple fraction of the surface atomic spacing. The complete analysis of LEED data is still open to question, but the technique has proved of great value in adsorption studies.

It is therefore apparent, that no single technique is capable of giving all the surface information potentially available. Hence many workers are now using a combination of such techniques, in order to maximise data. This is particularly important in clean surface work, where it may be difficult to observe a specific surface for more than a few hours or minutes, depending on contamination problems.

Secondary electron emission spectroscopy (including AES) is another powerful tool for obtaining chemical and solid-state electronic information for surfaces. The subject will now be discussed in detail in the remaining part of this chapter.

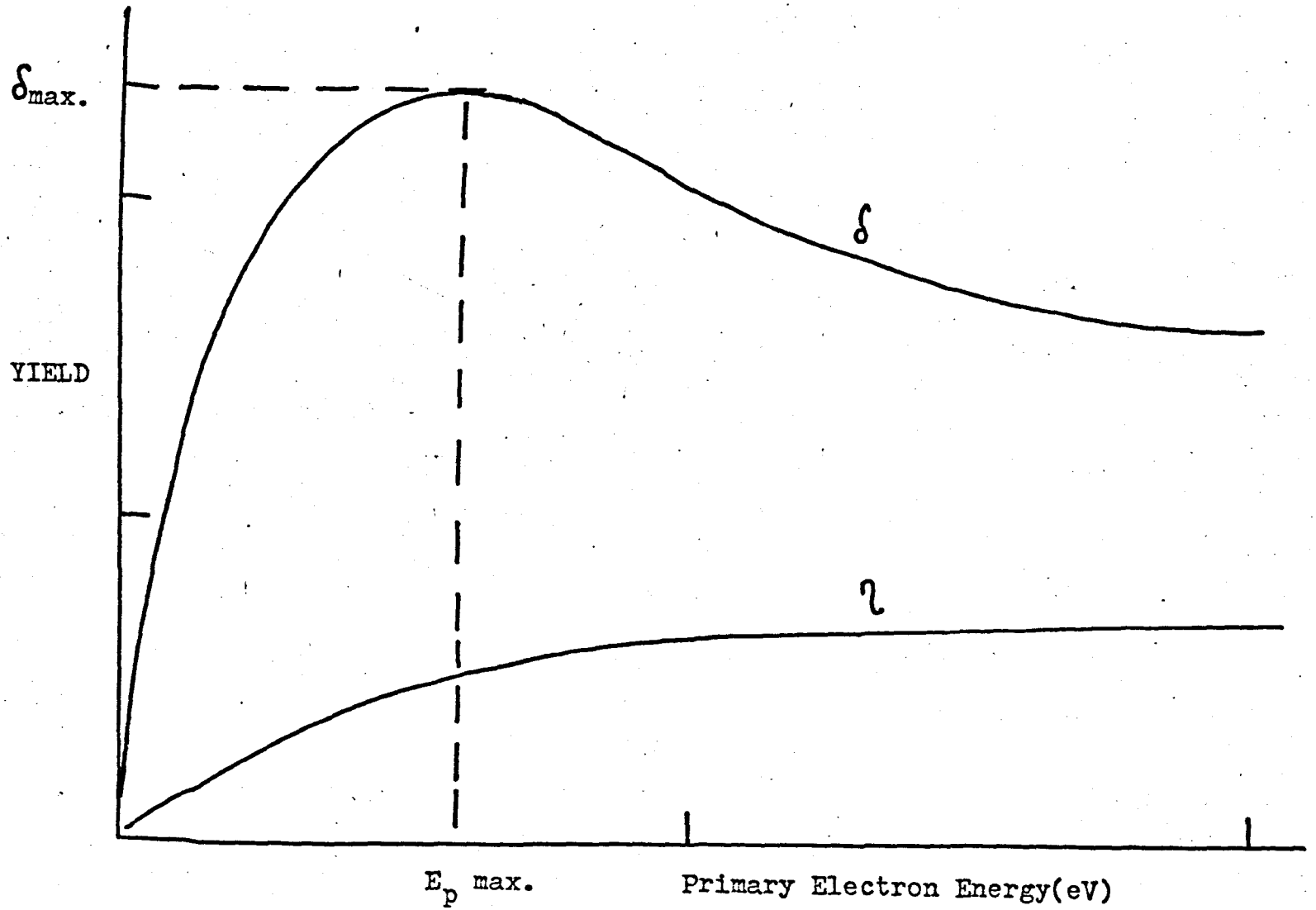

Figure 1.1 Schematic Yield Curve

1.2 Secondary Electron Emission

An electron may be emitted from a solid surface if it reaches the surface with sufficient energy to overcome the surface potential barrier. Secondary electrons may originate in a variety of ways; some will have energies that are characteristic of the surface atoms and others not so. Those electrons with characteristic energies, yield much information about the physical and chemical make-up of the surface, whilst the 'random' energy electrons have only nuisance value at present, by giving noise problems. This spectral variety of secondary electrons will be systematically discussed.

1.2.1 The secondary electron yield

When a surface is bombarded with electrons, it may be possible for the surface to emit more, or less electrons, than those in the primary beam. Hence, conventional current can either flow to or from the target. The secondary electron yield δ, is a ratio which quantifies this property. If i_s and i_p are the total secondary and primary currents respectively, then δ is defined as:

$$\delta = i_s/i_p$$

Also, a backscattering coefficient η may be defined as the ratio of the backscattered current to primary current, so:

$$\eta = i_{backscattered}/i_p$$

Secondary electrons with energies greater than 50eV are arbitrarily defined as backscattered, constituting the backscattered current.

The relationships of δ and η to primary electron energy E_p, are useful in many technological areas and are known as yield curves. Such curves are shown schematically in Fig. 1.1 The yield δ increases linearly at low primary beam energies, reaches a maximum $\delta_{max.}$ at $E_{p\ max.}$ and then decreases at higher energies. Insulators may have maximum yields much greater than unity ($\delta_{max.} > 1$), which make measurements difficult due to surface charging effects (Bruining[10]). Low yield surfaces such as metal blacks may have yield values as low as 0.5 (see Chapter 6).

The yield curves have the following qualitative interpretation. At low values of E_p, most of the primary beam energy is dissipated close to the surface, allowing secondaries to escape easily. As E_p increases, so the primary beam penetration increases, and many secondaries produced at deep levels ($\gtrsim 30\text{Å}$), suffer inelastic collisions before reaching the surface and fail to escape. Hence, when this penetration depth is reached by the primary beam, the yield curve turns over to form a maximum and then falls away. In contrast, the η curve rises and flattens as E_p increases, since backscattered electrons have approximately the same penetrating power as the primary beam. Hence, the backscattered electrons ($\gtrsim 50\text{eV}$) can easily penetrate to the surface and escape. From the above argument, it can be seen that a glancing incidence primary beam will give a larger value of δ than a normal incidence beam, since more secondary electrons will be created close to the surface so allowing more electron escapes. In addition, contamination can severely effect the yield curve, either by shielding the surface or by influencing the work function. This makes ultra-high vacuum (UHV) a prerequisite condition for accurate yield measurements.

Although no completely satisfactory quantitative theory of secondary electron emission has been developed to date (Bruining[10], Hachenberg and Brauer[11]), several attempts have been made to formulate a unified theory, which predicts a 'universal yield curve' for all materials, in view of the fact that, apart from quantitative differences, the secondary yield curves exhibit the same general shape. This has been observed to be the case for metals, semi-conductors and a variety of inorganic insulating materials [10,11]. Also, Willis and Skinner[12] have recently demonstrated the validity of the 'universal yield curve' in organic polymer films.

The information obtained from these yield studies is relatively limited and more valuable data may be obtained by the study of the energy distribution of secondary electrons. This topic is discussed in the following sub-sections.

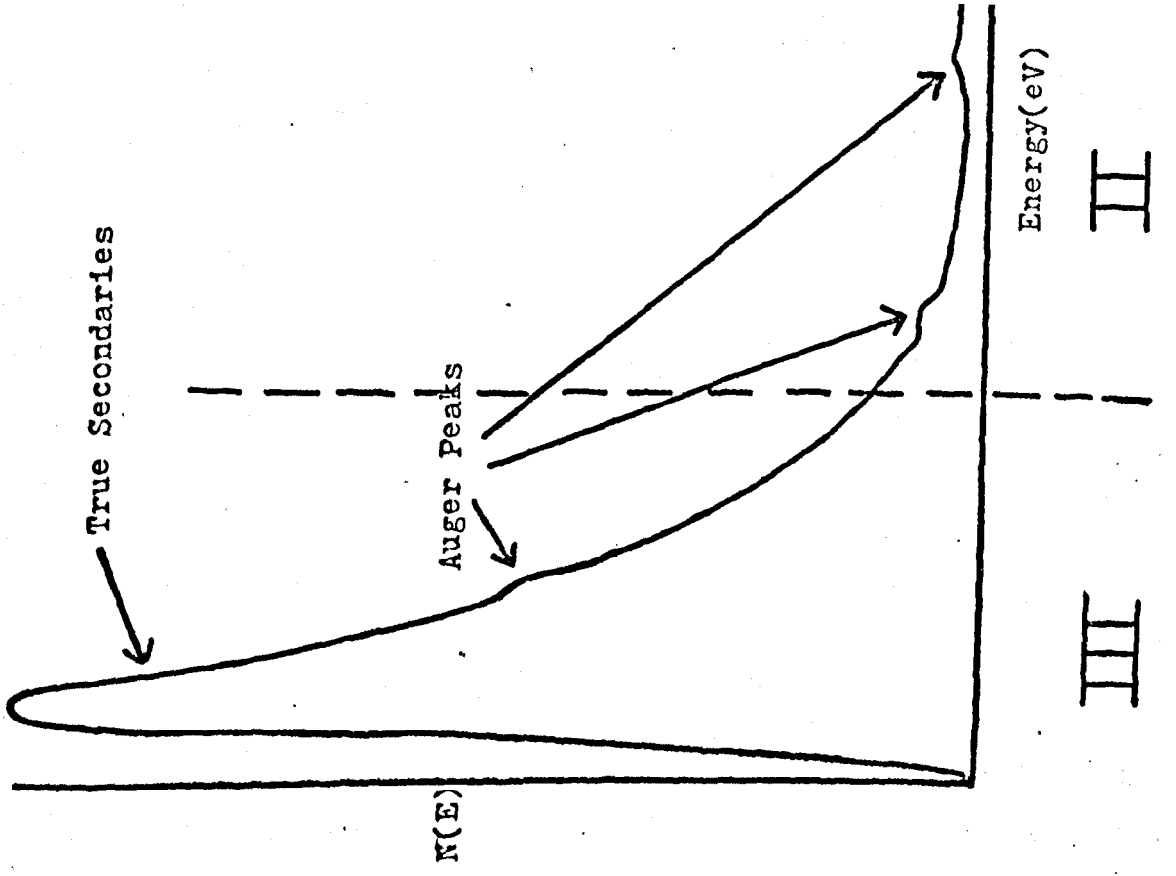

Figure 1.2 Schematic energy spectrum of secondary electrons.

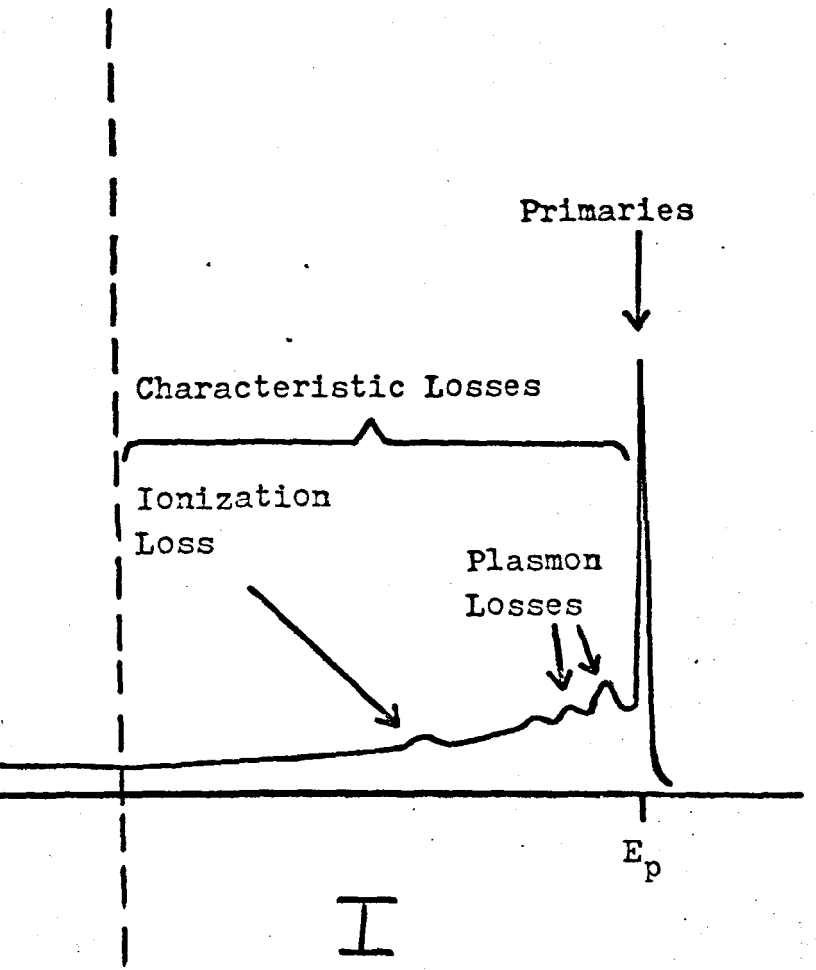
Primaries
Characteristic Losses
Ionization
Loss
Plasmon
Losses
E_p
I

1.2.2 The Secondary Electron Energy Distribution

A schematic diagram of the energy distribution of secondary electrons under primary electron excitation is shown in Fig. 1.2. This distribution curve is usually known as the N(E) curve, where E is the energy of electrons leaving the surface of the solid. E_p is the kinetic energy of the impinging electron. E and E_p are referenced to zero at the vacuum level of the target. For convenience, the distribution curve is usually divided into the three energy regions shown in Fig. 1.2.

Region I contains the elastic peak ($E=E_p$) and the characteristic energy loss region. These loss peaks appear at an energy $E=E_p-E'$ where E' is an energy characteristic of the mechanism producing the peak. Hence, these loss features move as E_p is varied. The loss peak is observed when an incident electron produces a characteristic excitation in the solid (e.g. ionisation/plasmon generation etc.) and is backscattered out of the surface with the loss of this characteristic energy. Hence, region I contains energy features which are essentially associated with the elastic peak.

The small peaks observed mainly in region II are of particular interest since they arise from Auger electrons emitted from the surface. In order to observe them more easily however, it is clear that a convenient means must be found for suppressing the large background current. Harris[13] first pointed out that this could readily be done by electronically differentiating the energy distribution thereby obtaining $dN(E)/dE$ and suppressing the background. The details of the method are discussed in Chapter 3.

The large peak at low energy (2-5eV) in region III, is due to the so-called "true secondaries". The energy position of both this low energy peak (slow peak) and Auger peaks is essentially independent of primary energy E_p. Such structure is truly the result of secondary

processes, i.e. the emitted electrons have no "knowledge" of the initial excitation energy. Hence, the Auger peak is easily detected by the fact that its energy does not change as E_p is varied. This is also true of the 'slow' peak. However, the magnitude of particular structure will invariably change with E_p variations, resulting from changes in the excitation strength.

Other features in the energy distribution include the broad high energy background of secondaries, which while featureless, is important with respect to measurement problems. Also there are two step processes involving for example both an Auger electron and a discrete energy loss. These will be discussed as necessary.

1.2.3 Auger Electron Spectroscopy (AES)

Auger electron spectroscopy has emerged as one of the most important experimental techniques for the characterization and study of solid surfaces. Up to the present, the technique has been used more for studying the 'chemistry' of solid surfaces than as a high energy spectroscopy applicable to solid-state physics. This results primarily from the relative complexity of the physics of the Auger process as compared to XPS or UPS (section 1.1). While these complexities make it somewhat difficult to determine energy levels using AES, they do not in general render the spectra so complex as to impede the qualitative analysis. Indeed, the high sensitivity achieved by the use of electron impact excitation and the high transmission of electron energy analyzers make the technique unrivaled in terms of surface sensitivity.

In 1925, Pierre Auger[14] discovered the Auger electron while studying particle tracks in a cloud chamber irradiated with white X-rays. He detected not only photoelectrons but also electrons of constant energy irrespective of the X-ray excitation energy. As stated earlier, it was Lander[1] in 1953, who first pointed out the applicability of AES for surface analysis and suggested that the technique

provided a complement to soft X-ray emission for the determination of energy band densities of states. However, it seems that Lander's work went virtually un-noticed (perhaps due to the lack of ultra-high vacuum technology) until 1968 when Harris[13,15] reported his extensive studies of the Auger spectra of metals, by detecting the differential of the energy distribution (dN(E)/dE). The work of Weber and Peria[9] and Palmberg, Bohn and Tracy[16] demonstrated the use of LEED analysers and cylindrical mirror analysers (see sub-section 2.5.2) for obtaining Auger spectra. The scene was then set for rapid growth in the AES field.

In view of the relatively brief introduction to the topic of AES, the reader is referred to the following introductory papers; Chang[17], Gallon and Matthew[18], Gjostein and Chavka[19] and Weber[20].

a) The Auger Process

Auger electrons are emitted when an atom, excited by a primary beam, relaxes to a lower lying energy state. Fig. 1.3 shows the energy level diagram for aluminium and aluminium oxide (binding energies in eV). A typical Auger process is depicted on the left of the figure. The primary beam produces a vacancy or 'hole' in an inner level (aluminium $L_{2,3}$ level) thus forming a highly excited ion. The coulomb replusion between two higher lying electrons (in the valence band in this case) may give rise to a radiationless deexcitation producing an ejected (Auger) electron and leaving a doubly ionised ion of lower energy. Of course, in the case given in Fig. 1.3, the final two hole state will be relaxed immediately by valence band electrons. Thus, the Auger process consists of a higher level electron moving down into the core hole and giving its energy to a second outer lying electron which is then emitted.

The Auger transitions are usually designated according to the three levels participating in the process. This is done with the aid of the X-ray level notation K - 1s; L_1 - 2s; $L_{2,3}$ - 2p; M_1 - 3s; $M_{2,3}$ - 3p; $M_{4,5}$ - 3d etc. Thus, in Fig. 1.3 (for aluminium), the

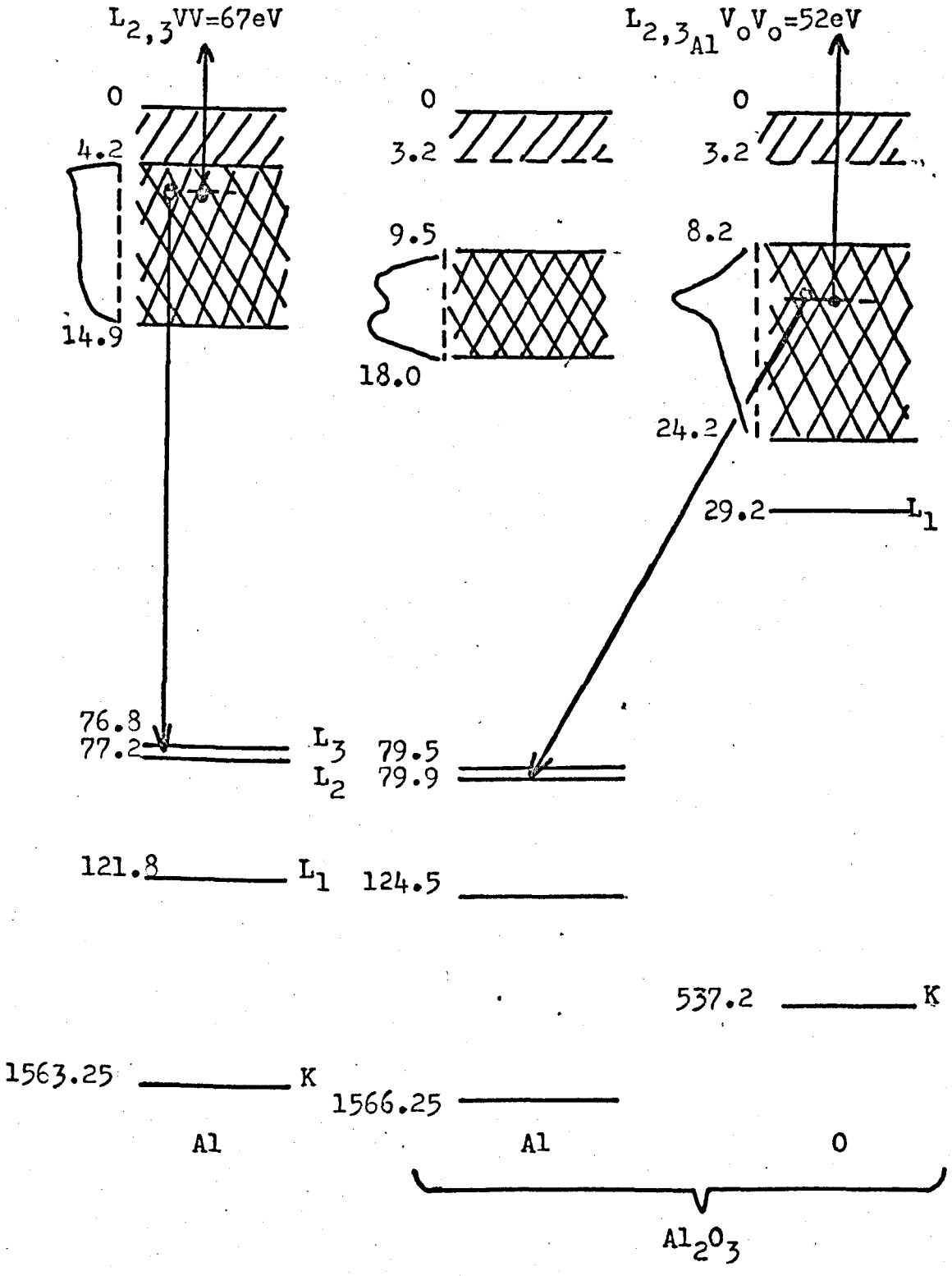

Figure 1.3 Energy level diagram for aluminium and aluminium oxide showing Auger transitions.

initial hole was in the $L_{2,3}$ level and the two participating electrons were in the valence band. Hence, the designation is $L_{2,3}VV$ for the 67eV Auger electron, where V represents the valence band electron. Also, the convention of order is to write the subshells in order of increasing index. Therefore, with a K-shell vacancy and L_1 and L_2 participating electrons, the Auger electron process would be KL_1L_2 <u>not</u> KL_2L_1. The Auger electron group originating from K-shell holes and L-shell electrons is termed the KLL Auger electron group and so on for other groupings.

Fig. 1.3 (right-hand side) shows a possible origin for the 'chemical shift' of Auger electron energies when chemical bonding of the element occurs. In the case of oxidised aluminium, it has been suggested (Quinto and Robertson[21]) that the valence band structures for aluminium and oxygen are different, and that the Auger spectrum of the oxidised surface results from a 'cross-transition' i.e. a vacancy in the $L_{2,3}$ level of aluminium is filled by electrons from the high density region of the oxygen valence band. Such a cross-transition is believed to be permissible as a result of the overlap of the wave functions that occurs due to band formation between aluminium and oxygen. Hence, the new Auger electron energy is 52eV. Such chemical shifts will be reviewed later in sub-section 2.2.4.

Inner shell ionisation for primary energies of 3keV occurs in times less than 10^{-16} sec. The lifetime of a core hole is usually greater than 10^{-15} sec., therefore it is easy to see why the Auger electron energy distribution is independent of the primary energy. Hence, Auger electrons are <u>characteristic</u> of the excited atoms from which they are emitted.

An excited ion may relax by Auger electron or X-ray emission. The probability for X-ray emission is called the fluorescence yield 'w', while that for Auger electron emission is 'a', the Auger yield. Clearly 'a+w' must equal unity. However, for binding energies $\lesssim$2keV, the fluorescence yield is less than 10% and hence the Auger mechanism dominates.

In order to maximise the number of inner shell vacancies, the primary electron beam energy is normally set to between three and six times the core level binding energy (Bishop and Rivière[22]). In other words, this primary energy gives an approximate maximum for the ionisation cross-section of the inner shell level. Complications to this argument can arise since many ionisations are produced by backscattered electrons (Neave, Foxon and Joyce[23]). However, in practice, this general rule is satisfactory.

Finally, when considering Auger processes involving L and M shell holes, one must take account of a special type of radiationless process called a Coster-Kronig transition. These are of the type L_kL_jX or M_iM_jX and involve transitions between subshells of a particular shell. These transitions are very strong when energetically allowed, and cause a rapid redistribution of core holes which strongly influences the relative intensities of the observed lines in the L and M groups.

b) Auger Electron Energies

An approximate equation for the calculation of Auger electron energies is given below,

$$E_{ABC} = E_A - E_B - E_C - \phi_A \qquad \text{- - - - - - - - (1)}$$

where E_A, E_B and E_C are the binding energies of the three electrons involved in the process, and ϕ_A is the work function of the analyser. This simple summation can be easily seen by reference to Fig. 1.3. For the Aluminium $L_{2,3}VV$ process, we have :

$$E_{L_{2,3}VV} = 77 - 4.2 - 4.2 - \phi_A = 68.6 - \phi_A \text{ (eV)}$$

where V is the approximate peak in the density of states (about 4.2eV), and ϕ_A is approximately 4eV. The agreement with experiment is fair.

However, upon ionisation of the inner shell electron (energy level A), all the electrons, especially those in shells outside of A, are subject to an effective higher nuclear charge. Consequently, their ionisation potentials should shift towards the corresponding levels of the

atom with the next higher atomic number (i.e. from Z to Z+1). Hence Burhop[24] suggested equation (2) to account for this effect.

$$E_{ABC}(Z) = E_A(Z) - E_B(Z) - E_C(Z+1) - \phi_A \quad \text{- - - - - - - (2)}$$

However, for processes involving outer shell electrons, the situation is even more complicated. If B and C are <u>different levels</u> then experimental agreement with equs. (1) and (2) is not so good. Chung and Jenkins[25] pointed out that the transitions E_{ABC} and E_{ACB} are quantum mechanically equivalent since the initial and final states of the transitions are identical in both cases. Hence, the kinetic energy of the Auger electron (taking the <u>average</u> process) becomes:

$$E_{ABC} = E_{ACB} = E_A(Z) - \tfrac{1}{2}(E_B(Z) + E_B(Z+1)) - \tfrac{1}{2}(E_C(Z) + E_C(Z+1)) - \phi_A \quad \text{- - - - - - (3)}$$

In the case when the two electrons involved in the Auger transition are equivalent in energy level, equs. (2) and (3) become identical. Chung and Jenkins[25] claim to obtain better agreement with the observed Auger electron energies using equ. (3) rather than equ. (2), but the difference is only marginal.

Hence we see that Auger electron energy spectra act as a 'fingerprint' of the emitting atom, enabling chemical indentification of that atom. Fig. 1.4 shows the principal Auger electron energies of the elements. Immediately one can see that each element has its own characteristic set of Auger electron energies. In addition, there are the obvious trends in each Auger 'family' (i.e. KLL,LMM etc.) to higher energies, as the atomic number increases in conjunction with the binding energies.

<u>c) Electron Transport and Surface Sensitivity</u>

The surface sensitivity of the features of the secondary electron energy distribution depends fundamentally on the short mean free path $\lambda_e(E)$ of electrons in solids in the energy range of interest. The electron-electron interactions giving rise to the short λ_e are the cause of the surface sensitivity and the 'slow' peak. Additionally,

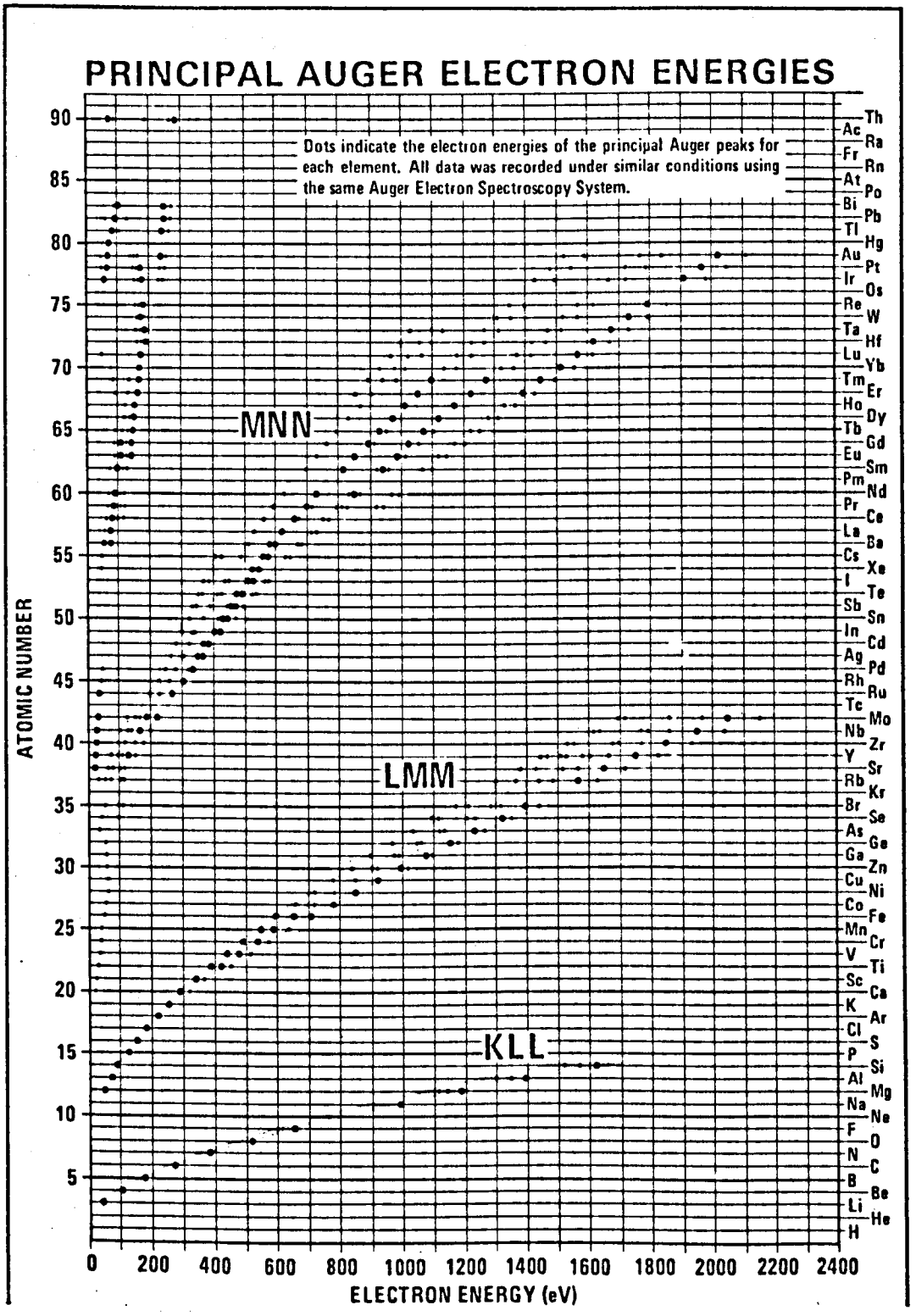

Figure 1.4 Principal Auger electron energies of the Elements

the interactions cause Auger electrons to lose energy before reaching the surface, hence diminishing the observed Auger signal. In the case of AES, where the depth of penetration of the primary beam is generally greater than the escape depth of Auger electrons, the sampled depth is approximately $\lambda_e(E)$. The relatively few measurements of the escape depth (approx. λ_e) of electrons in the energy range of interest are plotted in Fig. 1.5. The data in Fig. 1.5 clearly show that despite wide variation in Z, the mean free path for electrons in this energy region is extremely short (2-10Å). While this demonstrates the surface sensitivity of <u>any</u> spectroscopy which relies on electron transport in this energy range, the observation of submonolayer quantities of adsorbed atoms, which is discussed later (see sub-section 2.2.3 and Chapter 4), is perhaps even more convincing for the Auger case.

<u>d) Means of Excitation</u>

One of the easiest methods for exciting Auger spectra is electron beam stimulation. These beams are readily focussed electrostatically and positioned by simple deflection plates at various points on the target. The cross-section for ionisation is quite large, often exceeding 10^{-19} cm^2 and is reasonably independent of primary energy over a wide range from three to six times the binding energy of the initial core hole. This combination leads to high sensitivity and therefore high speed measurement.

However electron excitation does give rise to a large secondary background and it is the energy dependence of this background which provides the sensitivity limit of electron excited AES in determining surface impurities. Another complication arises in quantitative AES when the large number of high energy "rediffused" primaries constitute a backscattered current producing secondary ionisation.

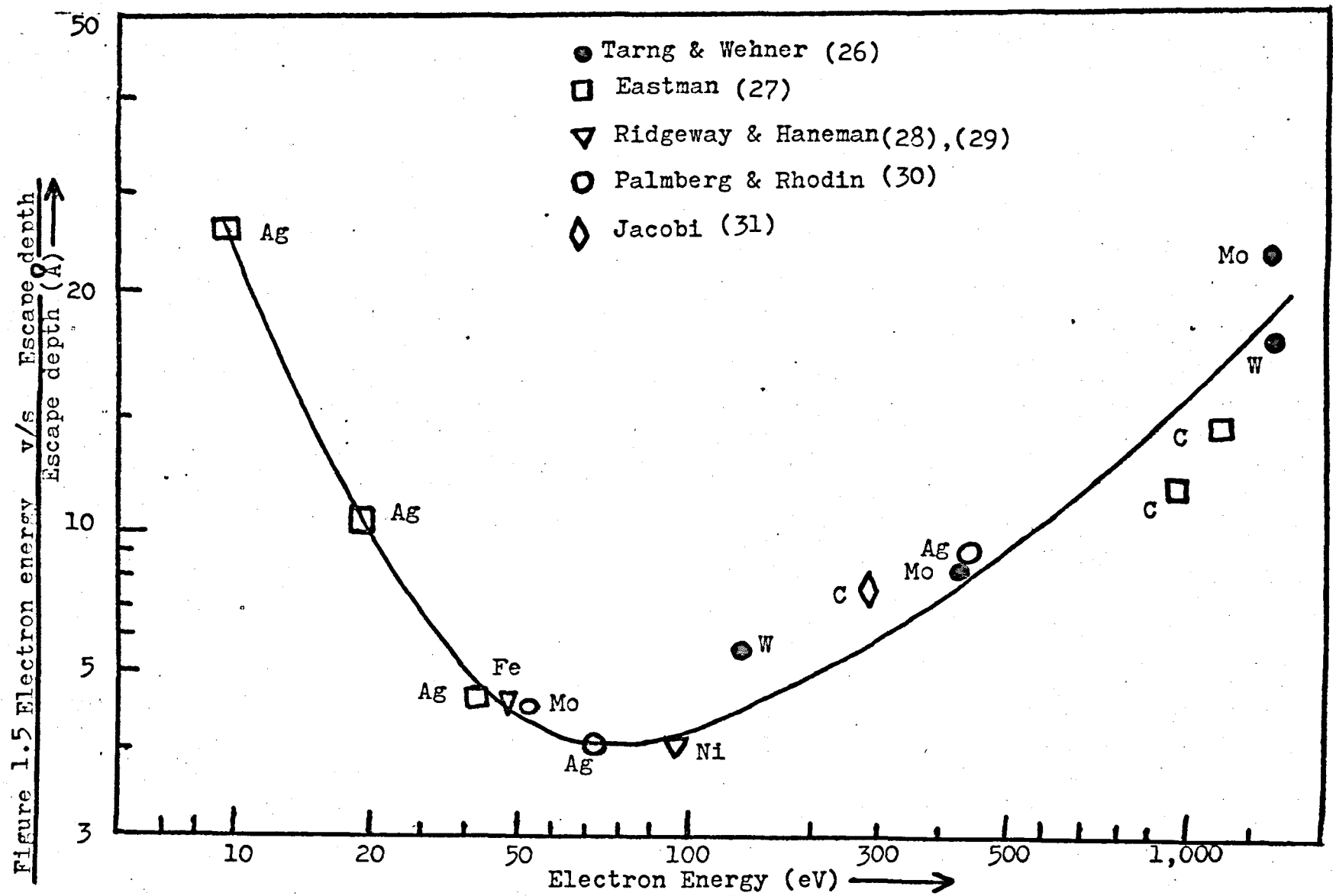

Figure 1.5 Electron energy v/s Escape depth

X-ray induced ionisation also has both advantages and disadvantages. Firstly, the scan time is usually in the order of tens of minutes whilst electron beam stimulation gives scan times of only a few seconds. Also, X-ray induced measurement is usually of N(E) since the strong "rediffused" primary electron background is absent. Where highly sensitive surfaces are under study such as photocathodes, X-ray stimulation is valuable since the X-ray interactions with the surface are much weaker than electron interactions.

Musket and Bauer[32] have recently demonstrated that high energy (350 keV) protons can be used to produce core holes in the surface region within the escape depth of low energy Auger electrons. The Auger yield was comparable to electron excitation. They suggest that the straight line trajectories of the protons eliminate any backscattering correction as used in the electron excitation case. However, a high energy accelerator is needed and beam currents are low ($1\mu A$).

e) Vacuum Requirements

While the characteristic surface sensitivity of AES is extremely useful for a wide class of problems, it at the same time places extremely stiff requirements on the vacuum environment in which the experiments must be carried out. If a clean metal surface is exposed to an ambient pressure of 10^{-6}torr (mm. of Hg) of an active gas (CO, H_2O, O_2etc.), it will be covered in adsorbed molecules within several seconds; hardly enough time to carry out a useful experiment. Hence, for typical work on clean surfaces, background pressures of 10^{-10}torr are required, so that a 'defined' surface is observeable for a few hours.

However, a variety of surfaces including most semiconductors, oxides and some clean metals, have a low sticking probability (<0.001) for the ambient gases. In these cases, the vacuum requirements are less crucial. Even here, artifacts can occur such as electron beam stimulated adsorption which frequently occurs when the ambient atmosphere is rich in water vapour.

In the increasingly popular technique of 'depth profiling', Auger analysis is performed on a surface while that surface is being sputter-etched by a separate ion gun. The vacuum requirements here are determined by the sputter-etch rate. If the residual gas which sticks on the surface is removed as rapidly as it adsorbs, then no artificial contamination will be observed.

f) Surface Physics Studies.

The most widespread application of AES has been in the area of fundamental surface studies. Workers involved in single crystal surface research using LEED during the 1960's, were acutely aware of the shortcomings of LEED in determining surface cleanliness and monitoring the chemical condition of the surface during the course of a given experiment. AES has confirmed those fears in many cases. Hence, particular care must be taken in drawing conclusions from the pre-Auger literature in this field.

AES has made very clear the difficulty of obtaining clean surfaces by pointing out the importance of surface segregation, impurities introduced by improper sputtering techniques, and the pitfalls in thin film evaporation studies. Also, AES has demonstrated that heating alone, to any temperature below the melting point, is rarely sufficient to clean a surface. Additionally, the AES user has a means of determining the quantitative influence of a surface impurity.

Other AES contributions have been made in the fields of gas adsorption, catalysis studies and surface characterisation in epitaxial growth. Also, the technique of "depth profiling" (see sub-section 2.2.2) has been extensively applied to semiconductor problems and analysis.

1.2.4 Characteristic Energy Loss Spectroscopy (CELS)

CELS is highly relevant and complimentary to many AES studies. This region of the secondary electron energy distribution has been briefly introduced, in relation to Fig. 1.2. The varicus features observed in the characteristic energy loss region will now be discussed.

a) The Elastic Peak

The elastic peak occurs at the highest energy ($E=E_p$) in the secondary electron energy distribution (Fig. 1.2). The peak is made up of those electrons which have been backscattered by ion cores without significant energy loss (within the resolution of the energy analyser). The peak will also contain electrons backscattered off phonons ($\Delta E=0.5eV$).

The elastically scattered electrons are of course studied extensively in LEED. In Auger electron studies, the elastic peak is of considerable experimental value as it provides an ideal calibration of the energy scale as well as a monitor of analyser performance with respect to alignment, resolution and transmission.

b) Plasma Losses

As a primary electron moves through a solid it will perturb the potential which normally influences the valence band electrons. One of the most important responses to this change in potential is the collective oscillation of the valence electrons at the so-called plasma frequency w_p. This frequency corresponds to the point at which the dielectric function is a minimum and the system responds with a polarisation equal but opposite to the applied field. The primary electron can be thought of as producing a time varying field on the valence electrons and thus in effect subjects them to the full spectrum of excitation frequencies. The valence electrons respond most strongly at the plasma frequency w_p and the resulting collective mode is moderately long lived relative to the primary electron transit time.

Hence the volume plasmon is the quantum of electron (or hole) density oscillation. According to the pioneering work of Pines and Bohm[33], the quantum energy of the volume plasmon in a free electron gas with equilibrium electron density n_o is:

$$\hbar w_p = \hbar (n_o e^2 / m)^{\frac{1}{2}} \quad ------ (4)$$

where w_p is the plasma frequency (Langmuir resonant frequency) and e and m are the charge and rest mass of the electron respectively.

However, in a real solid the electrons are not truly free, and the energy of these oscillations may be written approximately as:

$$E_{vp} = \hbar(\quad n_v e^2 / m^*)^{\frac{1}{2}}$$

where n_v is the valence band density of electrons and m* is the 'plasma' effective electron mass. This equation holds well for free-electron-like metals such as the alkalis, Al, Mg, Be etc. In the case of semi-conductors or doped semimetals, the plasmon energy quantum is given by:

$$E_{vp} = \hbar(\quad n_f e^2 / m^* \epsilon_o)^{\frac{1}{2}}$$

where n_f is the carrier density and ϵ_o is the high frequency dielectric constant of the lattice.

An incident electron may be able to excite multiple plasmons, corresponding to the excitation of more than one plasmon during the time the electron interacts with the solid. Hence, metals such as Mg and Al may show multiple loss behaviour with loss peaks occurring at E_{vp}, $2E_{vp}$, $3E_{vp}$, $4E_{vp}$ etc. (the energies are relative to E_p), each with decreased amplitude (see Fig. 1.2).

If the plasma oscillation occurs close to a surface, then the energy of the plasma quantum is modified. The new plasma quantum is termed the surface plasmon. Ritchie[34] predicted the surface plasmon with an angular frequency $w_p/\sqrt{2}$ and an energy of $\hbar w_p/\sqrt{2}$. This result is applicable to clean surfaces and a solid/vacuum interface.

The more general case of a semi-infinite electron gas bounded by a semi-infinite dielectric medium was derived by Stern and Ferrell[35]. The frequency of surface oscillations is given by the relation:

$$w_s = w_p/ (1+\epsilon)^{\frac{1}{2}} \text{ - - - - - - - - - (5)}$$

$$= w_p/\sqrt{2} \quad \text{for the solid/vacuum interface,}$$

where ϵ is the dielectric constant of the overlayer. Equ. (5) is only strictly accurate when the dielectric overlayer is infinitely thick. Stern and Ferrell also derived the plasma frequency for overlayers of varying thicknesses (see subsections 2.4 and 8.4). Hence, in the case

of a contaminated surface ($\epsilon \neq 1$), the surface plasmon loss is severely attenuated and shifted in energy.

Plasmon loss peaks are clearly very strong in certain materials and as might be anticipated, they often appear as low energy and high energy satellites on Auger peaks (sub-section 2.2.5). In addition, plasmon effects are thought to occur in the 'slow' peak but the interpretation is still tentative and worthy of further examination.

c) Inter/Intra-band transitions and Ionisation losses.

These energy losses are classified as single particle excitations, where an electron at some lower level may be excited into an upper empty energy level. This may result in the ionisation of a particular atom if a core electron is removed, or in the case of the valence bands, inter-band and/or intra-band transitions are possible.

The ionisation loss peak (Fig. 1.2) arises when the primary electron causes ionisation of a core level (as might precede an Auger deexcitation) and leaves the solid without further inelastic interaction. These features in the energy distribution appear at $E = E_p - E_b$ where E_b is the binding energy of the level which has been ionised. For $E_p \gg E_b$ the final state of the system following ionisation will contain an excited ion of energy E_b and two electrons the sum of whose kinetic energy is $E_p - E_b$. This energy may be partitioned in any way (neglecting energy band effects) between the two electrons. At the extreme, one electron will be at the Fermi level (energy equals zero) and the second electron may leave the crystal with kinetic energy $E_p - E_b$. No electrons of energy greater than $E_p - E_b$ could result from this ionisation. In other words, this process takes electrons from the elastic peak and puts them in the energy interval between 0 and $E_p - E_b$. This will have the effect of producing an 'edge' in the N(E) curve at the energy loss value of E_b. The identification of such a peak as a loss peak, is ascertained by observing its energy shift when E_p is varied. The energy shift of the loss peak and that of E_p should be identical.

The observation of such ionisation loss events has recently become known as ionisation spectroscopy (Gerlach[36]). However, more recently doubts have been cast on the technique and the matter will be discussed in section 2.4.

d) Summary

This region of the secondary electron energy distribution adjacent to the elastic peak, is therefore capable of giving much information in its own right and is also of great relevance to AES. In some cases, the measurement of ionisation losses will give energy levels of use in the calculation of Auger electron energies. Also, contamination effects on the energy losses (especially the surface plasmon loss) can be identified with the use of AES. Shifts in the surface plasmon energy can be used to obtain overlayer thicknesses (section 8.4).

With the use of the plasma theory of Bohm and Pines, band transitions and ionisation events, it has been possible to explain the energy loss spectra of many materials, although in the case of transition and noble metals, argument still remains.

1.2.5 Slow Secondary Electron Spectroscopy

The electrons found at the low energy end (region III in Fig. 1.2) of the secondary electron distribution curve constitute the majority of the total current leaving the sample during electron bombardment. They are usually considered as those electrons with an energy less than 50eV. These slow electrons result from a pair-production cascade in which the primary beam excites electrons from the valence band which in turn may have enough energy to excite other valence band electrons and so forth. These are so-called electron-electron interactions. The net effect is to build up an internal (to the solid) energy distribution of slow electrons which has its peak below the vacuum level. Some of these excited electrons will have sufficient energy and momenta to escape into the vacuum and be measured. Thus the observed 'slow' peak will be the product of an

internal energy distribution and an escape function. The electron-electron scattering is so strong at these low energies that a given electron will have experienced numerous interactions before escaping and will therefore lose any memory of the primary excitation.

Apart from this continuous distribution of slow electrons, there are also electrons of fixed energy superimposed on the large 'slow' peak. Such electrons may result from plasmon and high-energy band structure effects. The retarding potential spectrometer (sub-section 2.5.1) is an ideal instrument for the 'slow' peak spectroscopy due to its high sensitivity in this region. However, the spectrometer must be carefully shielded from stray electric and magnetic fields in order to maintain good energy resolution for these slow electrons.

a) Production of Slow Secondary Electrons

Generally, theories of secondary electron emission consider the action of a fast moving primary electron on a slow moving lattice electron and attempt to evaluate the transition rate for the transfer of different amounts of energy from the primary electron to the lattice electron. The inelastic scattering events of the primary electrons will produce slow secondary electrons which then undergo some sort of diffusion process through the solid, multiplying and losing energy, until they reach the surface with sufficient energy to escape or till they fall back into the 'sea' of conduction electrons.

Most theories simply describe the diffusion process by an exponential absorption term and a mean depth of creation for the secondary electrons. The theory of Wolff[37] assumes that secondaries lose energy only by scattering from conduction electrons and on average, an electron loses half its energy per collision. The results of Wolff's analysis are that in a cascade produced by an incident electron of energy E_p, the number of secondary electrons with energy E_s per unit energy interval is:

$$n(E_s) = A\,(E_p / (E_s + E_1))^x \qquad \text{- - - - - - - - (6)}$$

'A' is a constant, E_s is the secondary electron energy in vacuum and E_1 is the inner potential of the metal. 'x' is a function that is just greater that 2 for electrons with sufficient energy to escape from the surface.

The theory of Streitwolf[38] predicts a spectrum of the form:

$$n(E_s) \propto \frac{1}{(E_s + \phi)^2} \qquad \text{- - - - - - - - - - - (7)}$$

where ϕ is the work function. This theory assumes that secondary electrons are produced directly as a result of the interaction of the primary electron with the lattice electrons. Of course, both equs. (6) and (7) must be multiplied by a surface escape probability function to convert the internal secondary electron energy spectrum into the externally measured spectrum.

Both theories give a reasonable agreement with experiment (Seah[39]), but under some experimental conditions (e.g. non-normal primary electron incidence) the models are not adequate. It may well be that band structure and plasmon effects must be taken into account in such theories.

b) Plasmon Effects and Band Structure Considerations

When plasmons decay, they may emit photons or they may transfer their energy to conduction electrons. It may then be possible to observe electrons which have been emitted from the solid with their initial energy plus the discrete energy of a plasmon. Experimental evidence for this effect in both photoelectric and secondary electron emission, was first pointed out by Gornyi[40]. Very recently, Henrich[41] has put forward another explanation involving the rôle of both surface and bulk plasmons, which explains experimental data. He suggests that slow electron energy structure is due to hot electrons losing energy by the creation of plasmons rather than by the excitation of single electrons by decaying plasmons. However this latter interpretation will be dealt with in greater detail in Chapter 2.

We will now consider the case of a plasmon decay, giving its energy to a conduction electron. We can see that such a 'plasmon gain' electron may originate from any energy level (via a direct transition since the wave vector of the decaying plasmon is usually small) in the density of conduction states. We could therefore expect the plasmon gain electron energies to closely follow the density of states curve. However these emitted electrons are superimposed on the large slow peak and so can only be detected easily in the differential mode dN(E)/dE, in which the only marked feature will be the cut-off at the Fermi energy. Thus, the observed peaks may in fact only be edges in the true N(E) curve. Therefore the observed features on the slow peak should correspond exactly to electrons emitted from the Fermi level.

It has also been suggested (Jenkins and Chung[42]) that plasmon gain effects can occur with electrons from the slow peak. Apart from the difficulties in defining the 'true' slow peak positions which presumably should be below the vacuum level (the observed peak being due to a cut-off at the vacuum level), the very short lifetime of plasmons would be expected to make this process far too weak to be observed. Thus, plasmon gain peaks are very difficult to observe on elastic peaks (section 2.2.5). On the other hand both conduction and Auger electrons should be untroubled by a lifetime problem as the coupling of these electrons to plasmons should be strong. In the case of Auger electrons (sub-section 2.2.5), this coupling is thought to result from the disturbance by the ionised (Auger electron emitting) atom of the conduction electrons associated with the plasmon.

The plasmon effects just described will justify perhaps two peaks associated with the slow peak i.e. surface and bulk plasmon gains. However, when the slow peak is viewed under high resolution, much fine structure is obtained (Chapters 4, 6, 8 and 9) and a further interpretation must be sought in terms of band structure effects.

An incident electron beam of energy greater than 50eV, will cause the population of most final states in the conduction band due to interband transition mechanisms. In view of this, Willis et. al.[43] have suggested that energy structure in the slow peak may be interpreted as being due to high densities of final states at critical points in the conduction band. The relative intensities of the energy structure will not necessarily reflect the true densities of states however, since it is possible that electrons excited to higher states in a conduction band may populate lower band minima in the same band by relaxation processes (e.g. electron-electron and electron-phonon scattering) and be emitted from there. Such mechanisms can be seen in relation to Fig. 1.6, showing the energy band structure of graphite. Electrons can be excited into the σ_1 band at the Q^+_{1u} saddle point via direct or indirect interband transitions. They may then be emitted at this energy and analysed or they may relax in the σ_1 conduction band into the energetically lower minimum at Γ^+_{3u}. Therefore the relative population of these final states (Q^+_{1u} and Γ^+_{3u}) is observed to remain constant with increasing excitation energy.

The conduction states of interest in secondary electron emission will lie above the vacuum level (i.e. above E_v in Fig. 1.6). One point of interest with regard to these high energy states, is that in the case of the higher excited states in the third Brillouin zone (30-50eV above E_F), large discrepancies can occur due to the multilayer interaction (note the dashed curve in Fig. 1.6 relates to a single graphite layer and the full curve, the multilayer crystal). It appears likely that surface contamination layers may therefore cause a strong perturbation in high-energy band structures; hence the slow peak energy structure may be expected to be highly sensitive to the presence of small quantities of surface contamination. This is indeed observed to be the case (Chapter 8).

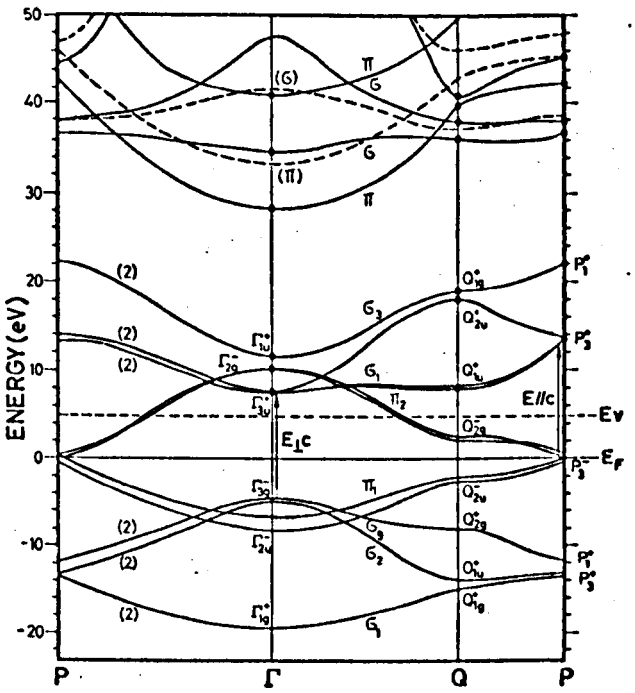

Figure 1.6 Energy band structure of graphite calculated by Painter and Ellis(Ref. 44) showing the location of high densities of final states at critical points in the conduction band.

Another interesting observation made by Willis et. al.[43] relates to the presence of interband transition thresholds. This indicates that excitation occurs via direct transitions obeying optical selection rules (i.e. the wave vector k is conserved in the transition). The reason for this observation is not understood.

As well as direct emission from critical points above the vacuum level, it may be possible for Auger processes to occur between critical point energies (using k conservation). The possibility of this process, makes the unambiguous interpretation of experimental data extremely complex at present.

1.3 Conclusion

The topic of secondary electron emission has been introduced along with some other techniques for surface analysis. Four main areas in secondary electron emission were discussed namely; the secondary electron yield, Auger electron emission, characteristic electron energy losses and slow secondary electron emission. Some interelationships between these four areas of work were also considered. The usefulness of slow secondary electron analysis for the determination of high-energy band structure was discussed in some detail.

Some of the more recent literature in the field of secondary electron emission will now be reviewed, with a special emphasis on work of relevance to the experimental results of this thesis.

CHAPTER 2

REVIEW OF PREVIOUS WORK

2.1 Introduction

A review is now made of electron stimulated secondary electron emission; the topic being sub-divided into the categories of Chapter 1. AES is reviewed in relation to four areas of work of current interest and debate. In the following sections, slow secondary electron spectroscopy is reviewed; the literature being divided into plasma and band-structure interpretations. Then CELS is discussed in relation to the previous sections. Finally, a comparative study is made between various types of electron energy analysers in section 2.5.

2.2. Auger Electron Spectroscopy

2.2.1. Introduction

Auger electron spectroscopy (AES) has rapidly developed in the past six years into a powerful technique for surface analysis. Minute quantities of surface contaminants in concentrations as low as 10^{12} atoms cm^{-2} can be detected in a surface layer no more than three or four atomic layers deep. Although AES was first applied to fundamental problems in surface physics and chemistry, it is now used as a tool in the solution of both long and short range technological problems.

The purpose of this review section is to discuss the current uses of AES along with other literature associated with the field. The topics chosen for review, taken from the large volume of current literature, are related to the experimental results of this thesis, and in addition, are at present in a state of debate.

2.2.2. Applied Auger Electron Spectroscopy

It was Lander[1] in 1953 who first suggested that Auger electron emission could be used as a method for surface analysis. Later, Harrower[45] reported the Auger spectra of tungsten and molybdenum and Zinke[46], that of magnesium. The sensitivity of their methods was poor, but the little-known work of Zinke produced relatively good Auger spectra, characteristic of clean magnesium. These latter spectra were achieved by the continuous evaporation of magnesium onto a target (under simultaneous analysis) at only 10^{-6} torr pressure. Harris[13,15] finally overcame the lack of sensitivity by obtaining the differential of the energy distribution ($dN(E)/dE$).

Between 1968 and 1970, the literature was mainly concerned with the cataloging of Auger spectra. To this end, work was published by Haas, Grant and Dooley[47], Palmberg and Rhodin[30] and Aksela, Pessa and Karras[48]. Haas et. al.[47] studied the Auger spectra of transition metals in the periods 4-6 and found a similarity between the spectra of elements in the same period (apart from energy differences). Palmberg and

Rhodin[30] obtained the Auger spectra of the fcc metals Au, Ag, Cu, Pd and Ni, and in addition, obtained values for the escape depth of Auger electrons (Fig. 1.5). High resolution LMM Auger spectra were published by Aksela et. al.[48] for ten elements, using an electrostatic cylindrical spectrometer. A complete catalogue of Auger spectra from Be to Th has now been published by Palmberg et. al.[49]

An important new technique has recently been described by Palmberg[50] using AES and inert gas sputtering for obtaining chemical profiles. The apparatus he used is shown in Fig. 2.1a. The target on the carrousel holder, is sputtered using the sputter-ion gun and simultaneously it undergoes AES analysis with the electron analyser on the right (cylindrical mirror analyser, sub-section 2.5.2). To obtain the chemical profile, the pass energy of the analyser is scanned repetitively through the energy range of interest while the target is simultaneously sputtered with 1000eV Argon ions. A typical result is shown in Fig. 2.1b. When the sputtering etch rate is found, one may substitute depth for sputtering time to obtain the chemical profile. One can see from Fig. 2.1b that phosphorus segregates in an exponential fashion on the surface of the 304 stainless steel (note that the peak-to-peak signal height is approximately proportional to the surface concentration).

A natural outgrowth of basic Auger studies on pure materials has been the detection and identification of various contaminants found to segregate on surfaces and at the grain boundaries of metals. Dooley[51] has made a study of segregation effects on the mechanical properties of Zircaloy alloys which have uses in the field of nuclear engineering. It was found that carbon segregation produced a surface metal carbide whose formation could be related to ductility properties. Ellis[52] has published work on the bulk to surface equilibra of impurities on thorium metal. Using AES, Ellis found that the interstitial contaminants of S, C and P segregated rapidly to the surface at elevated temperatures, even though the bulk concentrations of these contaminants were only in the parts per million range.

a)

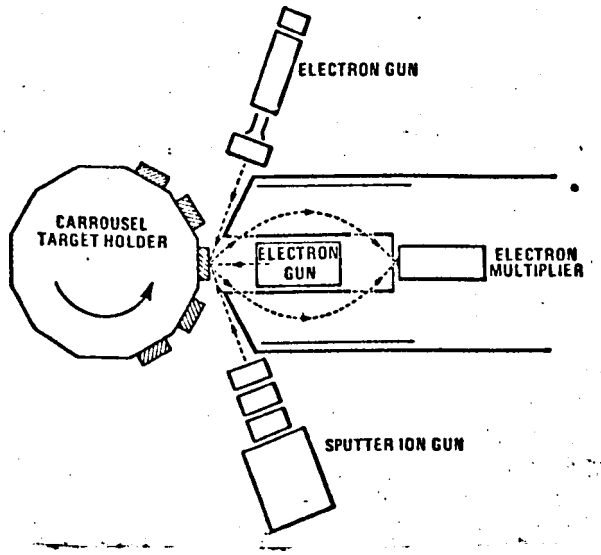

b)

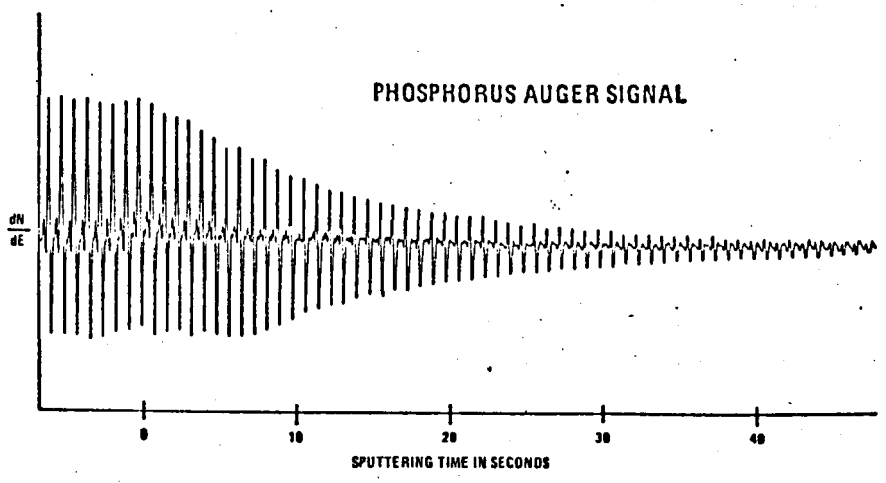

Figure 2.1a)Experimental arrangement for simultaneous sputter etching and Auger electron analysis.

b)Repetitive Phosphorus Auger signal from heated 304 stainless steel while sputtering.

The use of AES in a scanning electron microscope (SEM) was first reported by Macdonald[53]. More recently, Waldrop and Marcus[54] have reviewed the 'state of the art' with particular attention given to a computerised AES-SEM system and its uses. They found that with such a system it was possible to non-destructively determine surface chemistry with sub-micron area resolution and approximately 10Å (1nm) depth resolution, accompanied by an accurate correlation to surface topography. They obtained Auger electron 'images' of a number of surfaces including fracture faces and solid-state semiconductor devices. In addition, Arthur[55] has used the technique of scanning Auger microscopy to identify contamination effects in molecular beam epitaxy of GaAs and GaP. The spatial resolution in this case was only 0.1mm.

AES has many useful applications in metallurgical studies, including corrosion, alloy formation, nucleation, diffusion, catalysis, epitaxy, thin-film growth and fractography. Dooley and Haas[56] have reviewed some of these metallurgical applications. In particular, they have proposed a new technique for the production of high purity zirconium and hafnium in small quantities. They showed that zirconium atoms, normally present to some extent even in high purity hafnium, will segregate on the surface of hafnium which has been heated in ultra-high vacuum. These zirconium atoms can then be removed from the hafnium surface by means of argon ion bombardment. Hence the bulk purity of the hafnium will increase.

In the field of catalysis studies, Bonzel[57] has recently reported some work concerned with the oxidation of sulphur on a Cu(110) surface to produce SO_2 in the gas phase. Using a combination of LEED, mass spectroscopy and AES he was able to make detailed measurements of the adsorption of S(from H_2S) and its subsequent removal by oxygen at low pressures and elevated sample temperatures. Using his data, Bonzel was able to construct a catalysis model for the process. However in the

analysis of such data, consideration must be given to the possibility of electron beam artifacts, such as stimulated adsorption or desorption.

2.2.3 Quantitative Auger Electron Spectroscopy

The peak height of an Auger signal from a surface contains quantitative information on the number of atoms of a certain type in the surface region. Relatively few papers have been concerned with the quantitative aspects of AES. Generally one has to compare the Auger data with some independent method to calibrate the peak heights and to establish the relationship between the peak height and the corresponding number of atoms. A method for the calculation of Auger electron currents is discussed firstly and then some independent calibration techniques will be reviewed.

The production of Auger electrons depends on the ionisation cross-section of the inner level which is involved in the Auger process, and the number and the energy of the ionising electrons (both the primary and the backscattered electrons). The contribution from the backscattered electrons is usually given relative to the contribution from the primary electrons.

Vrakking and Meyer[58] developed the following relation for the measured Auger electron current:

$$I_A = \sigma(E_p)(1-w)\ I_p \csc \phi_p\, \Omega\, T \sum_i (N_i p_i q_i (1+s_i)) \qquad (8)$$

where I_A is the Auger electron current, $\sigma(E_p)$ is the ionisation cross-section of the inner level at a primary energy E_p, $(1-w)$ is the probability that an Auger process follows the ionisation of the inner level, ϕ_p is the angle between the incident electron beam and the crystal surface, Ω is the solid angle in which the Auger electrons are detected and T is the transparency of the grid system for electrons. The summation is introduced for the different sites in the crystal which the atoms can occupy. N_i is the number of atoms per cm^2 on site i. There is a screening factor p_i for the primary electrons and q_i for the Auger electrons.

The relative contribution from the backscattered electrons is s_1. Unfortunately, many of these parameters are difficult to obtain and so a semi-empirical approach is usually adopted.

Vrakking and Meyer[58] have calibrated the elements of C, N, O, P, S and Cl on the substrates of Si and Ge using the quantitative technique of ellipsometry (King[59]). Their results were in agreement with equ. (8) and the backscattering contributions were 20% for the silicon substrate and 30% for the germanium substrate.

Weber and Johnson[60] calibrated the potassium Auger peak by monitoring the deposition of potassium ions from an alumino-silicate alkali-ion source. Also, Thomas and Haas[61,62] have recently used the same method for other alkali atoms. This method will not be discussed here since it forms the basis of Chapter 4, concerned with quantitative AES. Florio and Robertson[63] correlated LEED intensity data with surface coverage to calibrate the Auger peak height of chlorine on silicon. Perdereau[64] determined the coverage of sulphur on nickel by a radioactive tracer method and related the results to the sulphur Auger peak heights. Pollard[65] derived the surface coverage of thorium on tungsten from work function measurements. Ridgeway and Haneman[28,29] achieved a calibration of the Auger peaks of iron and nickel on silicon by determining the surface coverage with a piezo-electric mass detector. The same method was used by Levenson et. al.[66] to calibrate phosphorus on silicon. Musket and Ferrante[67] took Auger data for oxygen on tungsten as a function of exposure and assumed monolayer coverage at saturation. The main point reached by all of these workers is that there appears to be a linear relationship between the surface coverage and the number of emitted Auger electrons for the first monolayer or so.

Other workers have considered the use of a ratio of two Auger peak heights from a binary surface system. Bouwman et. al.[68] considered an internal calibration method for binary alloys of known bulk composition.

It comprises the in situ breaking of prenotched, homogenised, alloy rods in UHV and the immediate analysis of the fracture face. They found that the observed signal intensity ratio of the two constituent elements was proportional to the corresponding atomic ratio of the elements, suggesting that matrix effects do not play an important role. Seah[69] has made use of the Auger signal ratio of an overlayer film of tin on a substrate of iron, to obtain a fractional coverage figure. Shell and Rivière[70] made use of a similar ratio in quantifing phosphorus on iron. The number of phosphorus atoms segregating to the surface of iron at specific temperatures was determined with the help of the Crank diffusion equation. This 'empirical' determination was found to agree closely with a theoretical approach based on the relative ionisation cross-sections of the two elements, with the inclusion of Coster-Kronig contributions to the ionisations.

A final point must be mentioned here concerned with the 'quantity' to be measured in the Auger electron signal. Houston[71] has shown that when the Auger yield is defined as the peak signal in the energy spectrum (N(E)) for a particular Auger feature (i.e. the area under a peak in the derivative spectrum, dN(E)/dE), and when the applied modulation amplitude is small (sub-section 3.2.2), the relationship between measured and true Auger yield is a simple proportionality involving only the modulation amplitude. As the amplitude approached the width of the Auger peak, the relationship becomes sensitive to the detailed shape of the feature. However when the yield is defined as the area under an Auger peak in the N(E) spectrum (i.e. the double integral of the feature in the dN(E)/dE spectrum), it is found that the relationship remains independent of peak shape regardless of the magnitude of the oscillation amplitude.

This conclusion by Houston[71] has been checked by Grant, Haas and Houston[72,73] in the case of the titanium LMM Auger spectra. They showed that the double integration technique recovered the signal strength

lost by taking data in the derivative modes (sub-section 3.2.2) and, in addition, made the Auger yield almost independent of 'chemical effects' (in the case of titanium, oxidation produces striking changes in the LMM Auger spectrum).

2.2.4 Chemical Effects

It is well known in the AES field that the chemical environment of an atom can strongly influence the Auger peak energies of that atom and can also affect the 'line-shape' of its spectrum. The majority of published work has been concerned with metallic oxidation. Firstly however, the origin of 'chemical shifts' will be discussed; the cross-transition mechanism which was explained in sub-section 1.2.3a will not be elucidated further.

X-ray measurements have shown that small shifts in atomic energy levels occur when an atom undergoes chemical bonding. Hence we may expect the Auger electron energy to shift upon atomic bonding by an amount ΔE_{ABC} given by:

$$\Delta E_{ABC} = \Delta E_A - \Delta E_B - \Delta E_C \quad \text{- - - - - - - - - (9)}$$

where ΔE_A, ΔE_B and ΔE_C are the shifts in the individual levels involved in the transition. However equ. (9) is inadequate because the final state of the Auger transition consists of two interacting vacancies in the core levels of the atom (or bands of the solid). Hence the energy of this 'divacancy' is unique for each configuration and cannot necessarily be expressed as the sum of the corresponding single vacancy energies. Thus equ. (9) should be re-written:

$$\Delta E_{ABC} = \Delta E_A - \Delta E_{BC} \quad \text{- - - - - - - - - - - - (10)}$$

In addition to changes in the energy levels, we would expect changes in the transition probabilities between states and in the distribution of states within each level, as illustrated in Fig. 1.3. This also will cause changes in Auger electron intensities and line shape. Hence techniques involving single electron states, such as UPS or XPS

should prove more useful than AES for determining the distribution of electronic energy levels at surfaces.

However such complexities have not prevented the publication of much work concerned with this topic. Baker and McNatt[74] studied the adsorption of monolayer amounts of oxygen on yttrium films and molybdenum foil. Chemical shifts were observed in the yttrium Auger peaks involving the 4p, 4d and valence levels, but not in the corresponding molybdenum Auger spectra. The initial stages of oxidation of chromium surfaces were observed by Ekeland and Leygraf[75] using LEED and AES. Chemical shifts in uranium Auger electron energies due to oxidation were studied by Allen and Wild[76]. The lanthanides Sm, Gd and Tb have been studied by Färber and Braun[77]; they found that Auger transitions involving the valence bands were affected by oxidation. Szalkowski and Somorjai[78] used AES to determine chemical shifts and Auger peak intensities in vanadium, the vanadium oxides and oxidised vanadium. They found that the relative intensities of the oxygen and vanadium Auger peaks could be used to determine the surface composition of the different oxides. Also, by use of chemical shifts and the vanadium to oxygen Auger peak ratios for the different oxides, they followed the oxidation of vanadium metal to V_3O_5 with increasing temperature.

Finally, both sulphur and carbon have been shown to produce Auger spectra dependent on their chemical environment. Farrell[79] has shown that the Auger spectrum of sulphur from Na_2SO_4 has two low energy satellite peaks below the main $L_{2,3}VV$ peak, whereas in $Na_2S_2O_5$, the satellites were not present. . A molecular orbital approach was used to interpret the presence of the satellite peaks. Grant and Haas[80] have been able to distinguish between three types of carbon, namely carbon which segregated onto a Mo surface during heating, carbon from CO on clean Mo and carbon in graphite. Again in this case one distinguishing feature was the presence of low energy Auger satellite peaks.

Most of the reported work on chemical effects is of an empirical nature since the Auger processes involved are not well understood. However even in this limited capacity, chemical effects are extremely useful for surface compositional studies.

2.2.5 Plasmon Gain/Multiple Ionisation Concepts

The presence of a low energy Auger satellite peak below the main KVV or $L_{2,3}VV$ Auger peaks of many free-electron metals has been interpreted as a 'plasmon loss' peak[42,84,85]. Here, an escaping Auger electron generates a volume plasma quantum before leaving the surface and so its energy becomes $E_{KVV} - \hbar\omega_p$. Also there may be a high energy satellite peak with an energy separation from the main Auger peak of about $\hbar\omega_p$. This leads to the idea that an escaping Auger electron could gain the energy of a decaying plasmon. In opposition to this, is the interpretation involving an initial multiple ionisation event prior to the Auger process.

Two basic mechanisms concern the plasmon gain concept. Firstly, the ionisation and the relaxation can be treated as a single entity, the satellite being due to an incomplete relaxation of the primary vacancy when the Auger electron is emitted (i.e. the plasmon is physically associated with a primary vacancy). According to this theory (Watts[81]), the structure of the satellite peak and its separation in energy from the main peak are determined by the volume plasmon excitation. Another explanation, given by Jenkins and Chung[82], assumes that there is a complete relaxation and suggests that the high energy satellite is due to absorption of a plasmon created by the bombarding electrons.

The observation of high energy satellites in soft X-ray emission (Hansson and Arakawa[83]) has led to an opposing interpretation for high energy Auger satellites in terms of a multiple ionisation event. It is proposed that an incident electron can create a double vacancy in the K or L shells, with a subsequent Auger process ($(K)_2VV$ perhaps) leaving the atom in a triply ionised state. The controversy is not yet fully resolved

but opinion seems to be hardening against the plasmon gain interpretation.

Jenkins and Chung have reported results for Cu[82], Si[84], Al[42] and Mg[85], and in each case they have attributed the high energy satellite to a plasmon gain mechanism. However in the cases of Si, Al and Mg, the multiple ionisation mechanism predicts very similar satellite energies to those predicted by the plasmon gain, and other workers (Rowe and Christman[86], Löfgren and Wallden[87], Salmeron et. al.[88]) have concluded that the satellites are due to the multiple ionisation mechanism. These conclusions were based on the satellite energy separation as well as a determination of the primary electron energy thresholds necessary for producing these satellites. Indeed Rowe and Christman[86] found that the satellite occurred at the same energy in Si and SiC, while the plasmon energy increases from 17eV in Si to 22eV in SiC.

Other workers supporting the plasmon gain include Suleman and Pattinson[89], Dufour et. al.[90] and Powell and Woodruff[91]. Recently, Schilling and Raether[92] have observed a surface plasmon gain directly on the elastic peak with 10keV primary electrons. The primaries were reflected at grazing incidence from a very smooth surface of liquid indium.

Fortunately, lithium and beryllium are materials in which the energy of the satellite events (produced by the opposing mechanisms) should have values which would be easily resolvable. Although lithium was recently examined by Löfgren and Wallden[87], these authors found no evidence for the occurrence of either event. Zehner et. al.[93] however, did find a peak relating to the double core ionisation event, but they found no evidence for a plasmon gain peak. The lithium surface used by Zehner et. al.[95] did contain both Na and K, but there is no reason to believe that this should substantially affect their results.

Again in the case of beryllium there is conflicting evidence in the literature. Jenkins et. al.[94] claim to have observed both mechanisms giving two distinct satellites, whereas Thomas[95] claims that only one

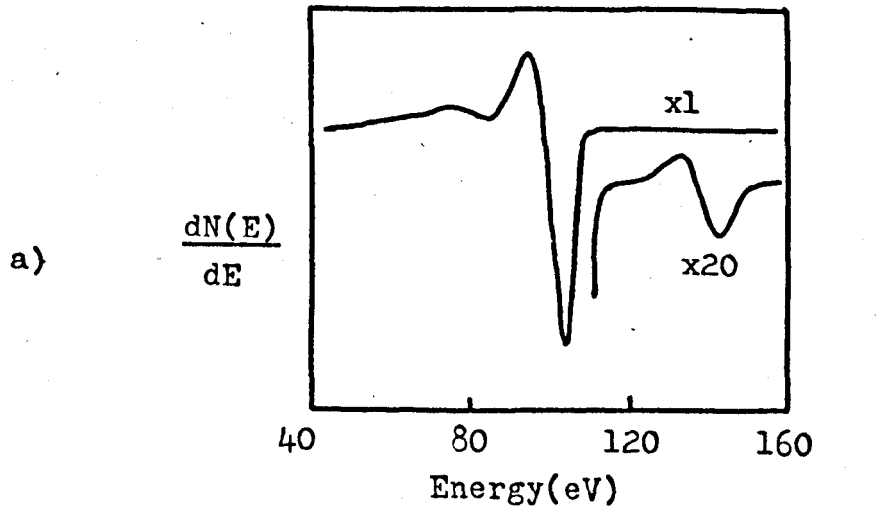

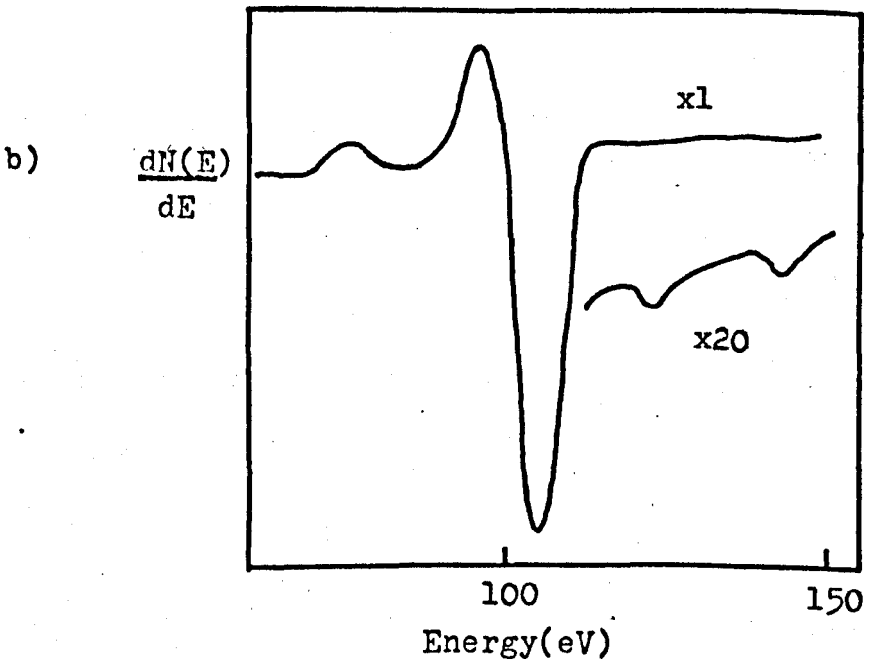

Figure 2.2 Auger and higher energy satellite spectra from Be surfaces.

a) Thomas[95]

b) Jenkins et. al.[94]

high energy satellite exists corresponding to the $(K)_2VV$ Auger transition in beryllium. Fig. 2.2 portrays the conflicting spectra. The KVV Auger peak in both cases is at 104eV, and the low energy satellite peaks at 85 and 67eV are the first and second order volume plasmon loss peaks. The high sensitivity given by the cylindrical mirror analyser (section 2.5) is utilised in curve a, but a signal averager was used in curve b as the analysis made use of LEED optics (section 2.5). Also, since Jenkins et. al.[94] admitted that there was some carbon contamination present, it appears that the results of Thomas[95] are the more worthy of belief (i.e. a plasmon gain peak is not detectable in the Auger spectrum of Be). From the weight of the foregoing evidence presented in this section, it appears that high energy satellite peaks, above Auger peaks, are likely to have their origin in multiple ionisation events.

2.3 Slow Secondary Electron Spectroscopy

2.3.1 Plasmon Effects

In 1966, Gornyi[40] pointed out that the effects of collective electron oscillation could be observed in both secondary electron and photoelectron emission. This work appears to have gone un-noticed until 1970, when von Koch[96] observed a peak at an arbitrary energy of 15.2eV, superimposed on the slow peak of aluminium. His interpretation involved a plasmon decay releasing its energy to a Fermi electron.

Since 1970, many more workers have published results and interpretations related to secondary electron energy structure in the slow peak region. The most prolific authors to date are Jenkins and Chung, who have investigated such properties in Al[42], Be[94], Mg[85], Si[84] and Cu[82]. In general, they have observed structure under poor resolution and they have usually interpreted their spectra in terms of the plasmon gain mechanism. The cases of Mg and Al will be taken up in Chapters 8 and 9, and the presented results will be used to criticize those of Jenkins and Chung. Powell and Woodruff[91] have endorsed the experimental

results of Jenkins and Chung in the case of Al, and also use the plasmon gain mechanism as their interpretation. More recently, Henrich[41] (again under low resolution) has investigated the slow peak of Al. His experimental results are of poor quality but are in general agreement with other workers. However, his interpretation is somewhat more subtle. He postulates that the shape of N(E) curve is determined by the various loss channels available to hot electrons. If plasmon creation is available as a loss mechanism for hot electrons, this mechanism will cause peaks in N(E) at energies corresponding to the energies of the loss channel (i.e. peaks at surface and volume plasmon energies relative to the Fermi level). The observed peaks in Al (relative to E_f) are at 10 and 14eV, which is in reasonable agreement with the surface and bulk plasmon energies; 11 and 16eV respectively.

Wright and Pattinson have pointed out that the slow peaks of both Mg[97,98] and Al[99] have considerably more complex structures than have been previously observed. Also, Harris and Pattinson[100] reached this conclusion in the cases of Cu, Ag and Al. It is these new results which now lead us into the next sub-section, concerned with the effects of high energy band structure on slow secondary electron emission.

2.3.2 Band Structure Interpretations

The complex energy structures sometimes observed in slow secondary electron emission have usually been interpreted in terms of high energy electronic band effects. In 1956, Gornyi[101] observed peaks in the slow secondary electron peak from crystalline copper oxide; he was able to correlate the energy loss structure with the 'energy gain' structure in the slow peak. His argument involved the postulation of inter-band transitions, with the higher band having an energy above the vacuum level. Hence, electrons in these high energy bands could escape from the surface and be analysed. In 1967, Scheibner and Tharp[102] observed structure in the slow peaks from single crystal copper, tungsten and graphite. Again the inter-band mechanism was used as the interpretation.

However, with the advent of the increased sensitivity using the differential mode[13,15] in 1968, some workers began to study this region of the secondary electron energy distribution with more vigour. Willis et. al.[43,103,104] have done a thorough investigation of the band structure of graphite, using both photon and electron stimulation. The main conclusions of this work were in verifying the band structure calculation of Painter and Ellis[44], and showing the usefulness of slow peak spectra in determining the critical point energies in a band structure above vacuum level. The basic arguments they used have already been discussed in Chapter 1. Willis et. al.[105] have also studied slow secondary electron spectra from amorphous germanium films. Their results show that slow peak spectra are sensitive to disorder effects, determined by substrate deposition and annealing temperatures.

Koshikiwa and Shimizu[106] have observed weak structure in the slow peak from a Cu-Be alloy, but they made no serious attempt at an interpretation, apart from referring to the work of Willis et. al.[105] A somewhat different explanation has been given by Seah[39], concerning single peaks observed in copper, silver and gold. He postulates that the peaks originate from the decay of surface states, since the emitted electrons are highly directional (normal to the surface) and the peaks have a narrow width.

Other authors who have used band structure interpretations include Ellis[107], Wright and Pattinson[97,98,99] and Harris and Pattinson[100]. Ellis[107] studied a single crystal of arsenic using Auger, energy loss and X-ray photoelectron spectroscopy, whilst the latter authors studied Mg and Al, and Cu, Ag and Al respectively.

2.4 Electron Energy Loss Spectroscopy

This spectroscopy is much older than the other electron spectroscopies, so that in order to keep this review to a reasonable size, only relatively recent literature will be discussed. However, the earlier work has been reviewed by Raether[108]. The review will start with some

theoretical work in the subject and will then move on to experimental studies.

The earlier work on surface and volume plasma quanta was reviewed in Chapter 1. Ritchie[109] has indicated that surface plasmon energies are perturbed in spherical systems (as in small spherical particles). This latter effect was first theoretically described by Fujimoto and Komaki[110] and proved experimentally by Fujimoto et.al.[111].

It may be possible for an electron to generate a double-plasmon excitation (i.e. a single excitation of energy $2\hbar\omega_p$). Ashley and Ritchie[112] performed a calculation for the mean free path of such an event, and found that the second order quanta could have an important influence in the interpretation of certain experimental results. The inverse mean free path for the double quanta generation is given by:

$$(\lambda_{2p})^{-1} = 0.0103\, r_s^2 \quad (\lambda_p)^{-1}$$

where λ_{2p} and λ_p are the mean free paths for double and single quanta generation respectively, and r_s is the average interelectron separation in the electron gas. In the case of aluminium, $\lambda_{2p}^{-1} = 0.04\,\lambda_p^{-1}$.

Powell and Swan have investigated the characteristic energy losses of Mg[113], Al[114] and the oxidation effects on the two metals.[115] They observed strong plasma losses in the metals and a shift in the surface plasmon loss energy upon oxidation of the metal films. However, Stern and Ferrell[35] predicted a progressive shift in the surface plasmon energy as oxidation proceeded. Murata and Ohtani[116] have recently observed this progressive energy shift and have suggested that the energy loss value may be used to determine the dielectric overlayer thickness (sub-section 8.4). In addition, they claim that since Powell and Swan[115] used a poor vacuum (10^{-6}torr), their oxide layers grew as thick islands, whereas in UHV the growth is uniform allowing the observation of the progressive surface plasmon energy shift.

Bishop and Rivière[117] and Gerlach[36] have suggested that ionisation losses can be used to determine the core level energies of atoms, which of course ispotentially useful in AES. However, Fiermans and Vennik[118] have pointed out that the use of ionisation losses to determine exact energy level positions is at present limited to a few cases where transitions into well defined energy levels occur. This is so since many metals show important density of states maxima above the Fermi level. This point is of special importance in the measurement of 'chemical shifts' occurring in the core levels after the atom has chemically combined with another atomic species.

Finally, Salmeron et. al.[119] have observed that plasmon creation by an incident electron beam in enhanced by ionisation processes. They found that the plasmon losses associated with the $L_{2,3}$ ionisation loss have intensities comparable to those of the elastic peak. This observation means that the Fermi electron gas must be coupled with the inner electron core levels and so adds weight to the idea that a plasmon gain peak (observed as a high energy satellite above an Auger peak) originates from a single step process[81].

2.5 Electron Spectrometers and Instrumentation

The review at this point will be restricted mainly to two analysing schemes; namely the retarding potential and cylindrical mirror analysers, which have been widely employed in a number of laboratories. These analysers have several features in common; they are electrostatic, compact, constructed so as to withstand the rigours of the UHV environment, and provide easy sample access. Also these two analysers are compatible with instrumentation for other measurements, including LEED, work function measurement, photoemission etc.

2.5.1 Retarding Potential Spectrometers

As noted in the introduction, the popularity of LEED for studying single crystal surfaces grew rapidly through the 1960's. The basic apparatus for this technique is a spherical retarding potential analyser such as that shown in Fig. 2.3. An electron beam impinges normal to the target surface and secondaries move radially outwards in the field free region between the target and the first grid. A negative voltage (E_R) is applied to the second grid which retards those impinging electrons with a kinetic energy less than eE_R, to the first grid or target. The third grid minimises field penetration of the collector (in this case the fluorescent screen) potential into the retarding region. If we measure the number of electrons reaching the collector ($N_c(E_R)$) as a function of the retarding voltage E_R, it will be related to the energy distribution of secondaries by:

$$N_c(E_R) = \int_{E_R}^{E_p} N(E) \, .dE$$

where E_p is the primary electron energy. A further analysis of the detection technique is given in sub-section 3.2.2.

Palmberg[120] and Scheibner and Tharp[102] independently recognized that the energy distribution N(E) could be obtained from the collector current by electronic differentiation, i.e. a small modulating voltage ($k \sin \omega t$) is applied to the second grid, as well as the retarding voltage, and the component of the collector current at the modulation frequency (ω), is proportional to N(E). After Harris'[13] success in extracting Auger peaks using the dN(E)/dE mode, Weber and Peria[9] recognized that by detecting the second harmonic 2ω of the collector current, dN(E)/dE could be obtained from a retarding potential spectrometer.

A double retarding grid system was first used by Palmberg[121] to improve the energy resolution from 2.5% to 0.5%. Taylor[122] has considered the performance of modulated LEED retarding potential analysers

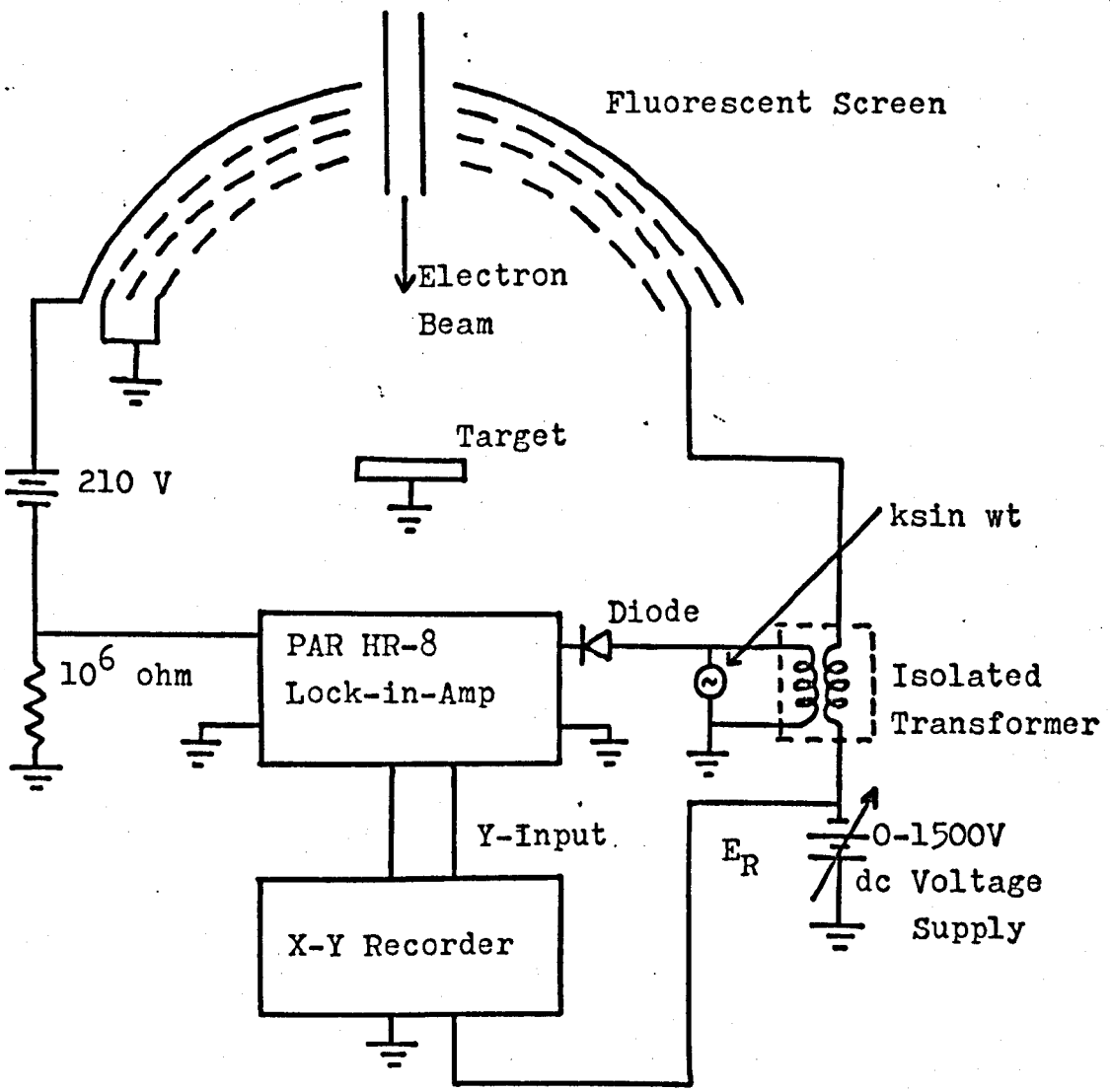

Figure 2.3 Retarding potential analyser used by Palmberg and Rhodin.[30]

in considerable detail; however such details of performance will be found in sub-section 3.2.2.

2.5.2 Other Electron Spectrometers

The cylindrical mirror analyser (CMA), first described by Blauth[123], appears to be the best analyser for AES analysis of surfaces, from a constructional and performance standpoint. It received limited attention in several gas phase studies until its rapid growth as the standard for AES studies.

Palmberg, Bohn and Tracy[16] were the first to use a CMA for Auger electron studies. Their arrangement is shown in Fig. 2.4. The analyser consists of two coaxial cylinders, the inner of which is grounded and has two cylindrical gridded apertures properly positioned along its length. A negative voltage is applied to the outer cylinder such that electrons from that part of the target sufficiently close to the axis of the analyser which enter into the region between the cylinders, tend to be deflected towards the second aperture. For a given applied voltage on the outer cylinder, electrons of energy eV_{pass} will be focussed onto the exit aperture located along the axis of the analyser.

There are several noteworthy features of this analyser. The acceptance half angle $\Delta\alpha$ for the design resolution of 0.3% is 6°. Furthermore, the analyser accepts electrons around the full 360° of the cone of half angle α whose apex is at the target. This results in the collection and analysis of as many as 10% of all the electrons leaving the surface if we assume an isotropic angular distribution. Thus the transmission of the CMA is extremely high for a dispersive analyser. Other dispersive analysers such as the 127° analyser used by Harris[13] in his pioneering work, have several orders of magnitude lower transmission. While the transmission of the CMA is comparable with that of the retarding potential analyser, it has the advantage that it only measures those electrons at the pass energy i.e. the CMA is a band pass filter, whereas

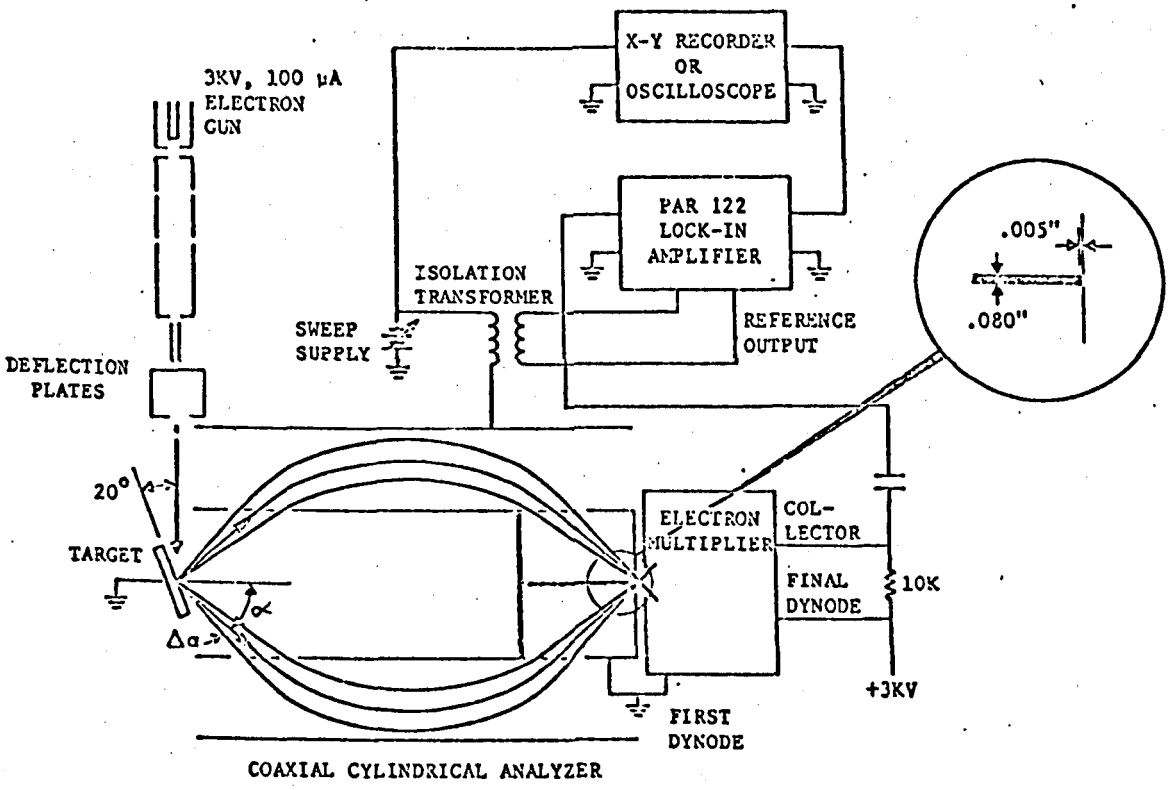

Figure 2.4 The cylindrical mirror analyser[16].

the retarding analyser is a high pass filter. The consequent reduction in shot noise gives the CMA a much improved signal to noise ratio, as much as a factor of 100. The detailed analysis of the CMA is complicated but has been treated by several authors, the most recent of whom is Roy and Carette[124].

There are several important differences in the electronic details between Figs. 2.4 and 2.3. An electron multiplier is used as the pre-amplifier for the CMA because it is the lowest noise, widest bandwidth low current amplifier available. Since the multiplier collector is at a high positive potential, it is capacitively coupled to the synchronous detector input. This arrangement permits modulation frequencies up to 50kHz to be used, thereby allowing .high speed scans (> 10,000 eV/sec) and oscilloscope displays. The CMA produces a remarkably flat spectrum down to as low as 25eV but the analyser is relatively insensitive in the slow peak region since the gain of the first dynode is determined by the energy of the impinging electron. Hence, the retarding potential analyser is a desirable electron spectrometer in this low energy region since it maintains its inherent sensitivity. However, while the gain for the retarding grid system must be changed over as much as a factor of 300 over the whole energy range, the CMA will record a complete energy spectrum using only a single gain.

Gerlach[125] has proposed a two-stage spherical retarding potential CMA which has the advantages of both types of analysers. In addition, Zashkvara et. al.[126] have suggested the use of a tandem CMA (i.e. double focussing) in which target alignment problems are less crucial. Bas and Bänninger[127] have developed a CMA and a special target stage in which it is possible to observe surfaces at a temperature of 3000K. Their preliminary work was concerned with oxygen-tungsten adsorption studies in the temperature range 1800 - 2600K.

Earlier in this review, it was stated that an Auger spectrometer has been used in conjunction with a scanning electron microscope (SEM). Recently, it has been suggested that the reverse situation may also be of use; that is to use a SEM attachment to an Auger electron spectrometer. Ashwell et. al.[128] have described a procedure for the conversion of a UHV Auger electron spectrometer (LEED system) to allow 'in situ' scanning electron microscopy. The conversion process requires only the addition of external driving and detection electronics. The combined instrument allows the recognition of surface heterogeneities and the location of the exciting electron beam for Auger analysis at points of interest, to an accuracy governed only by the beam diameter. Function generators provide appropriate sawtooth waveforms for the X and Y deflection plates of the exciting electron gun. Also, the waveforms are sampled and are applied to the X and Y inputs of an oscilloscope. The SEM image is obtained by modulation of the oscilloscope intensity (Z input) by means of the amplified target drain current (absorptive mode). The details of the electronics and some preliminary scanning electron micrographs will be discussed in sub-section 3.3.1.

Morabito[129] has described a similar combined instrument, though in this case a CMA was used as the electron analyser. His electronic scheme is different, in that the SEM image is obtained with electronic superposition of the target and secondary electron currents. Morabito has presented results, which illustrate the capabilities of the combined AES/SEM system in the qualitative and quantitative analysis of thin film electronic materials used in the fabrication of precision thin film resistors, capacitors and conductors.

2.6 Conclusions

The expanding field of secondary electron spectroscopy has been reviewed with a special emphasis on the literature of relevance to the topics of this thesis. Many theoretical aspects of AES are not well understood but some progress along these lines is now evident. The spectroscopy of the slow secondary electron peak has been neglected in recent years, but is now yielding considerable information of use in the determination of solid-state electronic structure. The combination of AES with electron energy loss spectroscopy was shown to be a powerful tool for determining the plasma behaviour of materials and electronic energy levels. Finally, the trends in electron spectrometers and instrumentation is towards both a high speed electron energy analysis, and a combination of surface analytical techniques.

The chapter which follows, contains a discussion of the experimental apparatus and techniques used to obtain the experimental results of this thesis.

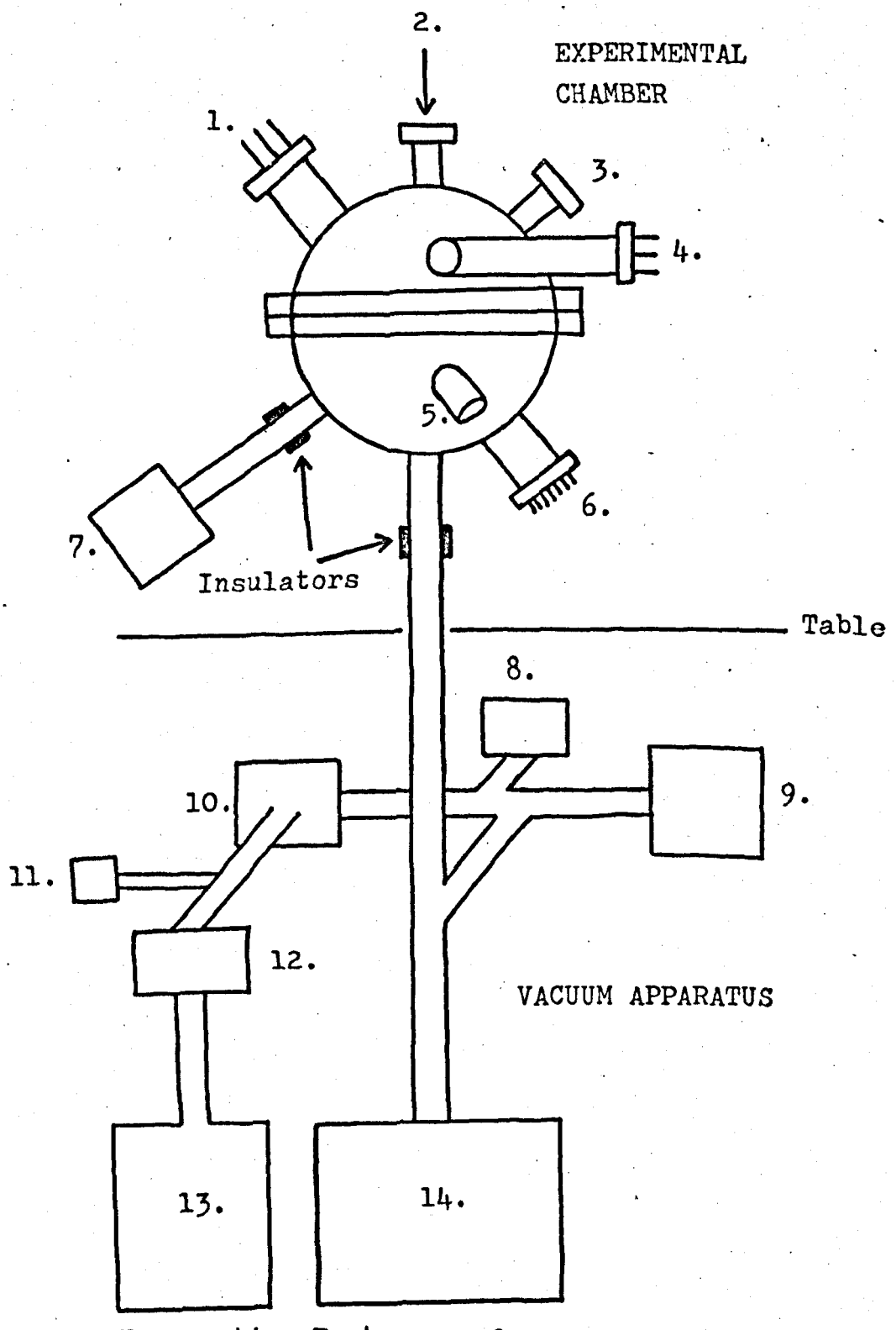

1. Evaporation Port
2. Gas Leak
3. Viewing Port
4. Q.R.G.A.
5. 10-pin feedthrough
6. Electron Gun
7. U.M. feedthrough
8. Trigger Gauge
9. Ion Pump (8l/s)
10. Bakeable Valve
11. Pirani Gauge
12. Viton Valve
13. Sorption Pump
14. Ion Pump(50l/s)

Figure 3.1 General Schematic of Apparatus

CHAPTER 3

EXPERIMENTAL APPARATUS AND TECHNIQUES

3.1 Introduction

This chapter describes the principles and operation of a retarding potential analyser suitable for secondary electron spectroscopy. In addition, complimentary experimental features will be discussed which considerably extend the usefulness of the electron spectrometer..

The basic apparatus including the vacuum chamber, pumps and much of the electronics, was already in existence at the beginning of the period of research. However, the apparatus was in need of a number of improvements to give it a more satisfactory performance. Studies in secondary electron emission have become considerably more complex in recent years, so that pertinent experiments usually involve much additional experimental apparatus. Some complimentary experimental features are described in this chapter; namely a low power SEM attachment, an alkali-ion gun, a universal-motion feedthrough and a gas handling system. Since many of the results of this thesis relate to slow peak spectroscopy, the effect of tertiary electrons on slow peak spectra was investigated to ascertain the extent of this problem. Finally, the techniques used for surface cleaning are discussed and two novel methods are investigated.

3.2 Experimental Apparatus

3.2.1 General Features

The general scheme of the apparatus is shown in Fig. 3.1. The experimental chamber is capable of measuring both the secondary electron energy distribution and the total secondary yield, since a 360° analysis is performed in the spherical chamber. The chamber acts as an electron collector and is isolated from earth via the two insulators marked.. Both the chamber and tube appendages were constructed from 304 stainless steel, and vacuum seals were made using copper gaskets and knife-edge flanges. Magnetic shielding materials (Netic* and Conetic*) were used both to reduce the stray fields from the ion pumps and also to minimise magnetic fields

* Perfection Mica Co. Chicago

in the vicinity of the experimental chamber. The shields were simply boxes placed over the ion pump magnets and over the experimental chamber, so that the chamber was entirely 'enclosed'.

The target was welded to a stainless steel rod attached to the universal motion (U.M.) feedthrough. The electron gun was at right angles to the target support rod, and a target rotation allowed the target to present any angle to the incident electron beam. Of course, even at glancing incidence, all secondary electrons would still be analysed due to the 4π collection angle. Partial pressure analysis down to 10^{-8}torr could be performed using the Varian quadrupole residual gas analyser (Q.R.G.A.), which was attached directly to the chamber. A three filament atomic beam source was also available, allowing evaporations of materials in UHV conditions. Also, pure gas leaks were possible allowing the observation of surface/gas interactions.

UHV technique demands the use of stable, low vapour pressure materials in order to reach pressures in the 10^{-10}torr range. Hence the experimental chamber and all ancillary vacuum equipment were capable of being baked up to 350°C without any degradation. This necessitated the use of alumina insulators, refractory metal structures, pyrex windows etc; and an argon arc all-welded construction. The chamber was initially "roughed" out to 10^{-2}torr using a sorption pump, consisting of a liquid nitrogen-cooled molecular sieve material enclosed in a stainless steel envelope. At this pressure, the titanium diode sputter-ion pumps (Ferranti FPD 50 and FPD 8) became effective and the viton valve and bakeable valve (Vacuum Generators) were closed. Without baking, the chamber pressure would then fall to 10^{-7}torr within a few hours. Generally, the system was baked at about 250°C for 48 hours and afterwards the pressure fell to the 10^{-10}torr region. This pressure could be monitored on the trigger gauge or the Q.R.G.A. The baking operation could be performed either with an external oven or using an internal 1kW projection lamp filament plus heating tapes and "bako-foil" heat shields.

Plate 3.1

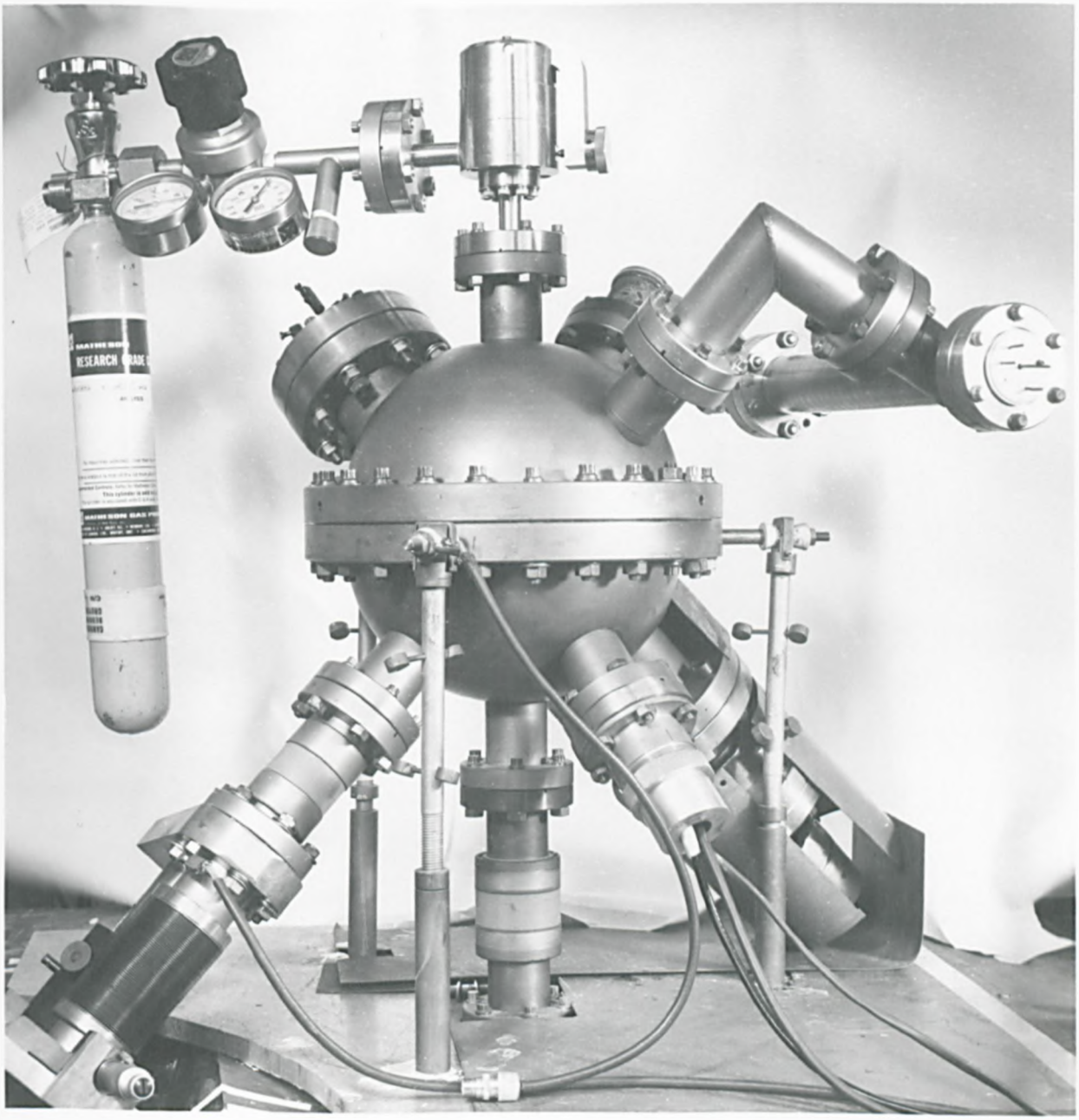

Plate 3.2

In situ leak testing could be performed using the Q.R.G.A., but a 20th Century mass spectrometer leak detector was found to be satisfactory for day-to-day leak testing.

Plate 3.1 shows a general view of the spectrometer and instrumentation. The Lektrokit box in the foreground contains the collector and input circuitry, whilst the shielded ion pumps can be seen beneath the table. The magnetic shielding has been removed to allow the spherical collector to be viewed.

Plate 3.2 shows a close-up of the experimental chamber. The two hemispherical collector shells are joined by a 10" flange to form the complete spherical collector. Multiple tube appendages are welded on radii of the sphere, so that the electron and atomic beams converge on the target at the centre of the sphere. The details of the detection and input circuitry will be discussed in sub-section 3.2.3.

3.2.2 Detection Techniques

As pointed out in sub-section 2.5.1, it is possible to obtain both the energy distribution of secondary electrons $N(E)$ and the differential $dN(E)/dE$, by means of electronic manipulation of the retarding potential analyser. Firstly however, a few words must be said concerning the method of retardation.

If reference is made to Fig. 2.3, it may be seen that retardation of electrons is produced by a negative voltage $-E_R$, applied to a spherical grid. This grid is usually made from very fine tungsten mesh in an attempt to produce an equipotential surface, so that electrons travelling radially outwards with an energy eE_R, will just be stopped by the grid. Of course, in practice a potential variation will occur between the grid wires causing a severe loss of resolution (Taylor[122]). Hence, a double retarding grid system (two linked grids separated by a small distance) is now used by most workers (Palmberg[121]). Taylor[122] has also calculated the optimum grid dimensions by accounting for electron divergence effects in the cells of the mesh of the inner grid. The

divergence is minimised by using an inner grid radius half that of the retarding grids and by the use of fine mesh. These design criteria have been adopted in the construction of the grid meshes and have enabled an energy resolution of 0.2% to be achieved.

If we now measure the current Ic to the collector as a function of the retarding voltage E_R, it will be related to the energy distribution N(E) by:

$$I_c(E_R) = I_p \int_{E_R}^{E_p} N(E).dE \quad \text{- - - - - - - - - - (11)}$$

where the energy distribution is normalised so that:

$$\int_0^{E_p} N(E).dE = \delta$$

where δ is the secondary yield. Thus for E_R more negative than Ep, all secondaries will be cut off and Ic=0, while for E_R positive with respect to the target Ic= δ Ip. Now consider the current $Ic(E_R)$ at the retarding voltage E_R. The change in Ic on moving to a slightly different energy is given by expanding Ic (E) in a Taylor series about E_R. Thus:

$$I_c(E)=I_c(E_R) + \left.\frac{dI_c(E)}{dE}\right|_{E=E_R} (E-E_R) + \left.\frac{d^2I_c(E)}{dE^2}\right|_{E=E_R} (E-E_R)^2 . \frac{1}{2!} + \ldots .$$

Substituting from equ. (11) (and reversing the integration limits since E_R is normally positive with respect to Ep),

$$I_c(E) = I_c(E_R) - I_p N(E_R)(E-E_R) - \left.I_p \frac{dN(E)}{dE}\right|_{E=E_R} \frac{(E-E_R)^2}{2!} + \ldots \text{ - - - (12)}$$

As stated in sub-section 2.5.1, the energy distribution $N(E_R)$ can be obtained by modulating E such that $(E - E_R) = k \sin wt$ and measuring the component of Ic(E) at the frequency w. From equ. (12):

$$Ic(w) = -k\ Ip\ N(E_R)\ \sin wt$$

(neglecting higher order terms). This component is therefore $-kIpN(E_R)$ for small modulation voltages. In this way, Palmberg[120] and Scheiber and Tharp[102] were able to obtain N(E) using the LEED system. Weber and Peria[9] recognised that the third term in equ. (12) provided a simple means

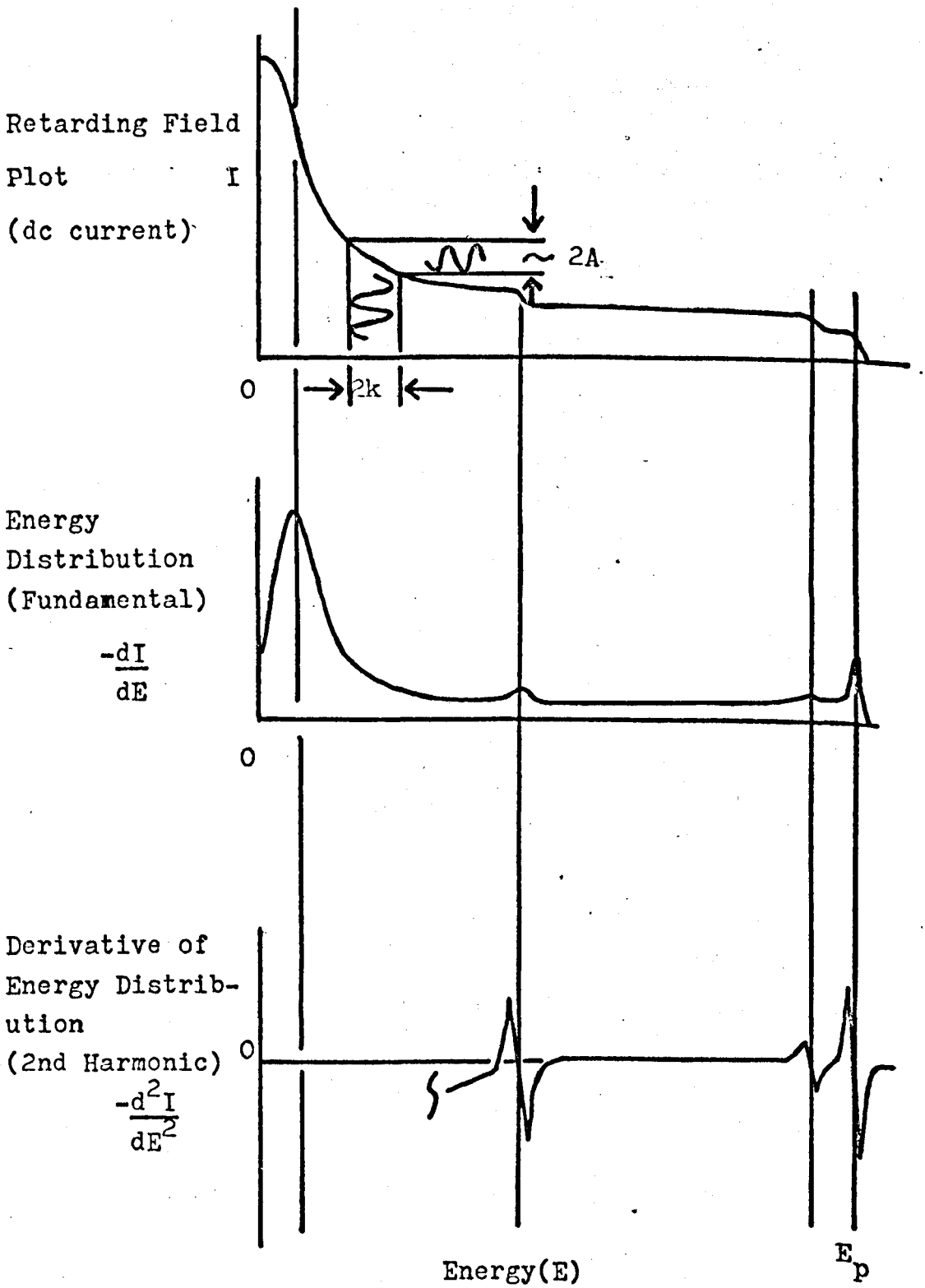

Figure 3.2 Characteristics of Retarding Field Analysers.

for obtaining dN(E)/dE spectra, hence for small k:

$$I_c(2w) = \tfrac{1}{4} k^2 I_p \left.\frac{dN(E)}{dE}\right|_{E=E_R} (\cos 2wt) \text{ - - - - - - - - - (13)}$$

Hence, by measuring the component of Ic(E) at the second harmonic, the dN(E)/dE spectrum is easily obtained.

These detection characteristics are shown in Fig. 3.2. A peak - to - peak modulation amplitude of 2k is applied to the d.c current characteristic and the output 2A at the frequency w, produces the energy distribution curve (middle plot). When the $2w$ component is plotted, the lower curve is obtained. It is important to see that the Auger and loss features are enhanced in the dN(E)/dE mode, and use is made of this by utilising the energy value of the minimum excursion, as a datum point for the Auger electron energy. In this mode, Ic($2w$) is proportional to the square of the modulation amplitude which must be considered when viewing actual Auger spectra. However, Bishop and Rivière[22] found that the square relation was only accurate up to a modulation amplitude approaching the r.m.s width of the energy feature; after this Ic($2w$) flattened off to a constant value. At the larger modulation voltages, the even higher harmonics in the expansion series become significant and cause the pertubation.

3.2.3 Detection Circuitry

From the previous sub-section it is apparent that the measurement of dN(E)/dE requires the detection of the second harmonic of the collector current. However, a large signal at the fundamental frequency will be present due to capacitive coupling between the retarding grids and collector, which must be suppressed; e.g. by the use of a $2w$ tuned load. In addition, phase sensitive detection is used so that a satisfactory signal to noise ratio is obtained; suitable for use as the Y - channel input to an X - Y recorder.

UNIVERSITY OF KEELE

Fig. 3.3 shows the circuitry used for the second differential detection. Firstly, we will consider the experimental chamber which contains three-grids of diameters 100, 167 and 187mm , and a collector (chamber walls) of 200mm diameter. Plate 3.3 shows the internal arrangement of the grids, gun and target as viewed after the removal of a hemispherical collector and grid assembly. The whole grid structure is held by four stainless steel rods welded to the chamber with the necessary sintox insulators sheathing the rods. The complete spherical grid meshes are formed when the top hemispheres are placed on the lower ones and attached to the sintox insulators via wire hooks. Both the inner grid and target are earthed externally through a picoammeter (Keithley 409). The electron gun collimator can be seen protruding through the grids, in Plate 3.3. The electron gun (Superior 5UP) was converted to an oxide cathode type, since its original directly heated cathode gave a relatively poor emission current. As mentioned earlier, an internal projection lamp filament was used as a heater and this may be seen close to the centre of the hemisphere.

The voltage supplies needed to drive the electron gun were obtained from a resistor chain connected to a stabilized high voltage supply (Fluke 413 C). With this arrangement, primary electron energies up to 2.5keV could be used with target currents of up to 120μA; typical spot analysis diameters were between one and three millimeters, as viewed on a phosphor screen target. Electrostatic deflection plates provided X and Y deflection of the electron beam over the target.

The modulation voltage was derived from a Farnell LFM 2 oscillator, and was applied to a tuned transformer having a second harmonic rejection ratio of 250:1 and a step -up ratio of 2:1. A synchronous output of the oscillator was fed to a frequency doubler, consisting of a step - down transformer and a rectifying bridge. The 2ω rectified signal was applied to a tuned filter and phase shifter which produced a good square wave reference signal for the phase sensitive

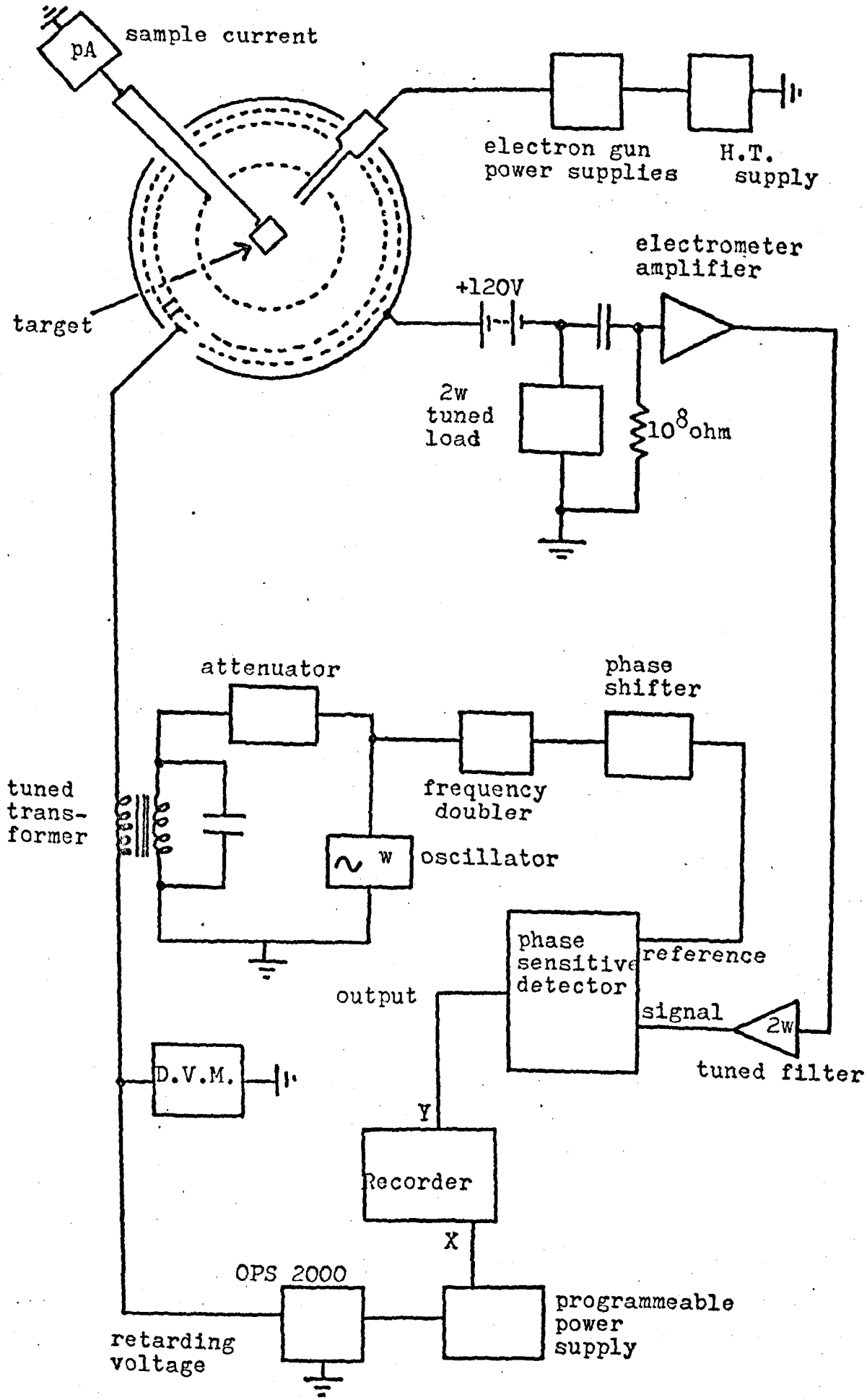

Figure 3.3 Schematic of the second differential detection circuit.

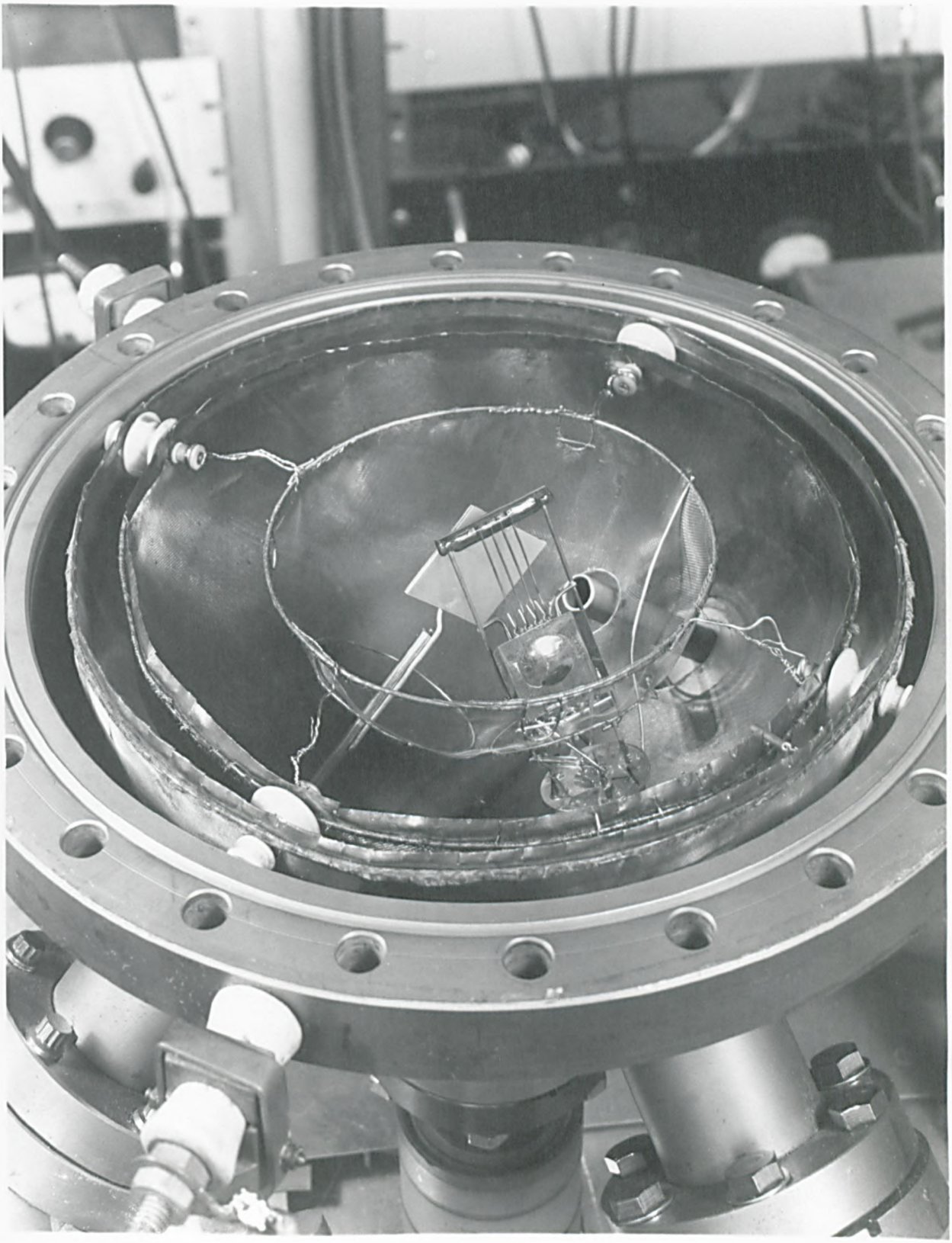

Plate 3.3

detector (P.S.D). An AIM* system 5 contained the tuned filters, phase shifter and P.S.D.

The circuitry required for obtaining a strong $2w$ output signal will now be discussed. Firstly, to be sure of collecting all incident electrons, the collector was biased to +120V, to prevent the escape of tertiary electrons from the walls of the chamber. One of the unfortunate problems encountered when using such an "external" collector is its high capacitance to earth. C_{CE}. C_{CE} must be incorporated in any tuned load circuit where high collector to earth impedance is required. A parallel LCR tuned circuit was used as the tuned load, with a resonant impedance at $2w$ of 24 M ohm and an w rejection ratio 250:1. A blocking capacitor between the +120 V batteries and the head amplifier of the electrometer prevented charging - up of the electrometer input. If a $2w$ signal developed across the tuned load, the impedance to earth would be comparable to the 10^8 ohm load resistor and the signal would be amplified. At any other frequency the tuned load would partially short - circuit the signal to earth, and this signal would not be amplified. Prior to the signal entering the P.S.D., it was passed through an AIM system 5 tuned filter to remove any w signal still present. The resonant frequency of the tuned load was 6,200 Hz and it was tunable over a few hundred Hertz. Some slight tuning was sometimes necessary when C_{CE} varied due to the addition of experimental apparatus to the collector. However, the oscillator was nominally set at 3,100 Hz and the tuned filters at 6,200 Hz. Finally, the output from the P.S.D. was fed to the Y input of an X - Y recorder. This output of the synchronous detector is proportional to dN(E)/dE since the detector performs the integral of the input signal times $\sin w_{ref}.t$. For $w_{ref} = 2w$

$$E_{\text{out}}^{\text{P.S.D.}} = C \frac{1}{T} \int_0^T I_c(t) \sin (2w t + \phi)\, dt \quad \text{- - - - - - - (14)}$$

where C is a constant, ϕ is an adjustable phase angle and T is the time

*Trade name

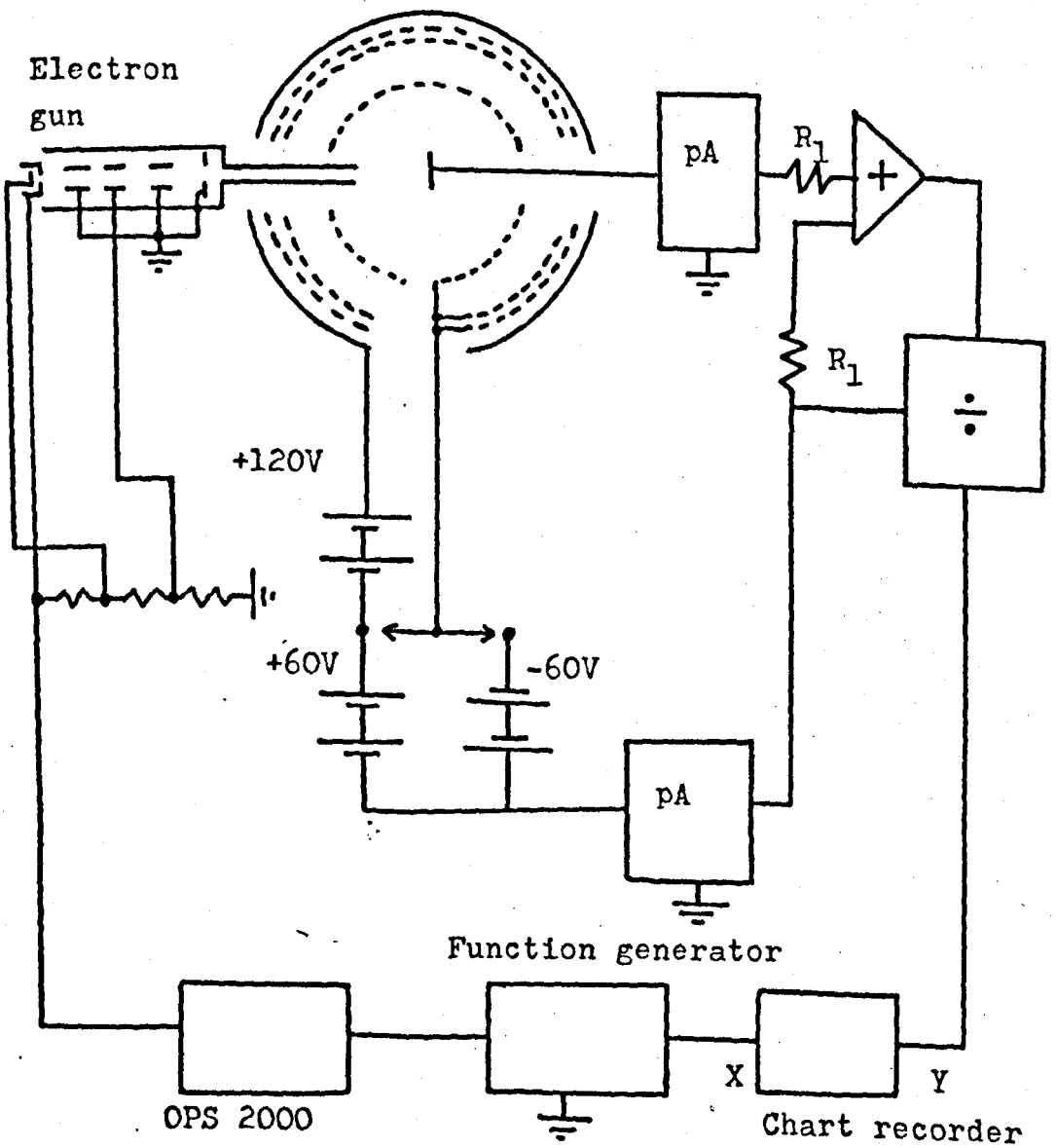

Figure 3.4 Circuit for secondary yield measurement

constant. For T long compared with $1/2w$, this integral will be zero for all frequency components present in $I_c(t)$ except $I_c(2w)$. Since this $2w$ component is cos 2wt(equ. 13), ϕ must be $\pi/2$. Therefore substituting for $I_c(t)$ from equ. (13) into equ.(14) we have:

$$E_{out} = \frac{C}{4} k^2 I_p \left.\frac{dN(E)}{dE}\right|_{E=E_R} \quad \text{- - - - - - - - - - - - (15)}$$

which is the desired result. Thus by measuring E_{out} as a function of E_R we obtain the spectrum of dN(E)/dE.

The retarding voltage E_R is obtained from a Kepco operational power supply (OPS 2000) driven by a Kepco function generator (FG 10C); the generator also provides a ramping voltage output for the X input of the chart recorder. The generated voltage function was a linear ramp from 0 - 2000V (negative voltage) with a wide ramping time capability. In addition, the OPS 2000 had an internal voltage bias supply which was used to provide "base line" voltages. This was particularly useful when observing the loss region of the secondary electron distribution, since the baseline voltage could be set somewhat below the elastic peak energy, enabling the observation of the loss region under high X sensitivity.

3.2.4 Secondary Electron Yield Measurements

In these measurements, the output of the OPS 2000 was connected directly to the cathode of the electron gun, so that the primary beam energy could be ramped from 0 - 2,000 eV. Yield measurements were obtained using the circuit shown in Fig. 3.4. The battery voltages of +60V and +120V on all three grids and collector respectively, ensured the complete collection of secondaries leaving the target. The automatic yield measuring circuit has been described by Thomas and Pattinson[130], and will only be discussed briefly here.

Since the sum of the secondary current i_s and the target current i_t must equal the primary current i_p, when we sum the outputs of the two picoammeters using the adder, we obtain a voltage function proportional to i_p which is then fed to the divider. The second divider

input is proportional to i_s, so that the divider output is proportional to i_s/i_p which is the secondary yield δ. This output is fed to the X - Y recorder along with that of the function generator, to produce an automatic X - Y plot of δ, Ep (i.e. a yield curve). When the target current is nulled, the output is calibrated at $\delta = 1$ ($i_s = i_p$). If the grid bias polarity is reversed to -60V, the backscattering coefficient η is obtained and plotted in a similar way.

Some of the yield results presented in this thesis were taken in a smaller single-grid chamber, specially designed for such measurements. However, the above discussion remains equally valid.

3.2.5 Tertiary Electron Problems

Since a good deal of the experimental results of this thesis are concerned with slow electron spectroscopy, it was felt necessary to consider the spurious characteristics of the retarding potential analyser in this energy region. Both Cross[132] and Koshikawa and Shimizu[133] have recently pointed out that spurious peaks can occur in slow peak spectroscopy. These workers found that if a positive voltage was applied to the inner grid (normally earthed) of a retarding potential analyser, then a spurious peak could be extracted. In addition, by applying a few volts negative to the target, a second smaller spurious peak was observed by Cross[132].

It was concluded that these spurious peaks were due to "tertiary" electrons originating from the gun collimator and the grid mesh of the energy analyser. If one considers the secondary electron flux leaving the target, then it is apparent that this flux must pass through the inner grid before being analysed. This passage through the grid mesh must generate tertiary electrons which will add to the true slow peak already present. Furthermore, it is possible that secondary electrons will be generated in the gun collimator if the primary electrons are not contained in a well-focussed beam. Hence, the measured slow peak may well be a summation of three slow peaks, and so it is of importance to check the effects of these spurious peaks in any particular retarding potential spectrometer.

Fig. 3.5 shows a differential spectrum of the slow peak of partially oxidised aluminium, taken with -4.5V on the target and a series of positive voltages on the inner grid. The retarding grids were scanned positively to the left of zero and negatively to the right. The small differentiated peak on the left is due to the effect of tertiaries from the inner grid, whilst the large peak at about 4V is the true slow peak. The spurious peak is seen to move "in step" with the applied inner grid voltages and also to increase slightly in height as the inner grid voltage increases. When the inner grid voltage increases, more tertiaries will be created at the grid and the peak height increases. Also larger positive voltages will be required on the retarding grids in order to remove the tertiaries from the positive inner grid; hence the "in - step" energy shifts. The size of the spurious peak is very small compared to the results of Cross[132] who found that the spurious peak was comparable in size to the true slow peak, when +14V was applied to the inner grid. Another very small spurious peak can be seen at about 1.5V which was thought to be related to secondaries originating from the gun collimator. Since the target has a -4.5V potential, the true slow peak is shifted to a higher energy, but secondaries from the gun collimator will be analysed at their actual energies of about 1-3eV. Hence, this spurious peak may also be removed from the true slow peak.

It can be seen therefore from Fig. 3.5, that spurious peaks are not large in this experimental apparatus and should not substantially affect the measured slow peak spectra. Further evidence for this conclusion is apparent when one observes the considerable differences between slow peak spectra taken from different surfaces. Persistent spurious peaks have not been observed so far in our spectrometer.

A final check was made on the effects of spurious peaks by evaporating a clean aluminium film on to the target, and then taking slow peak spectra with and without the presence of spurious peaks.

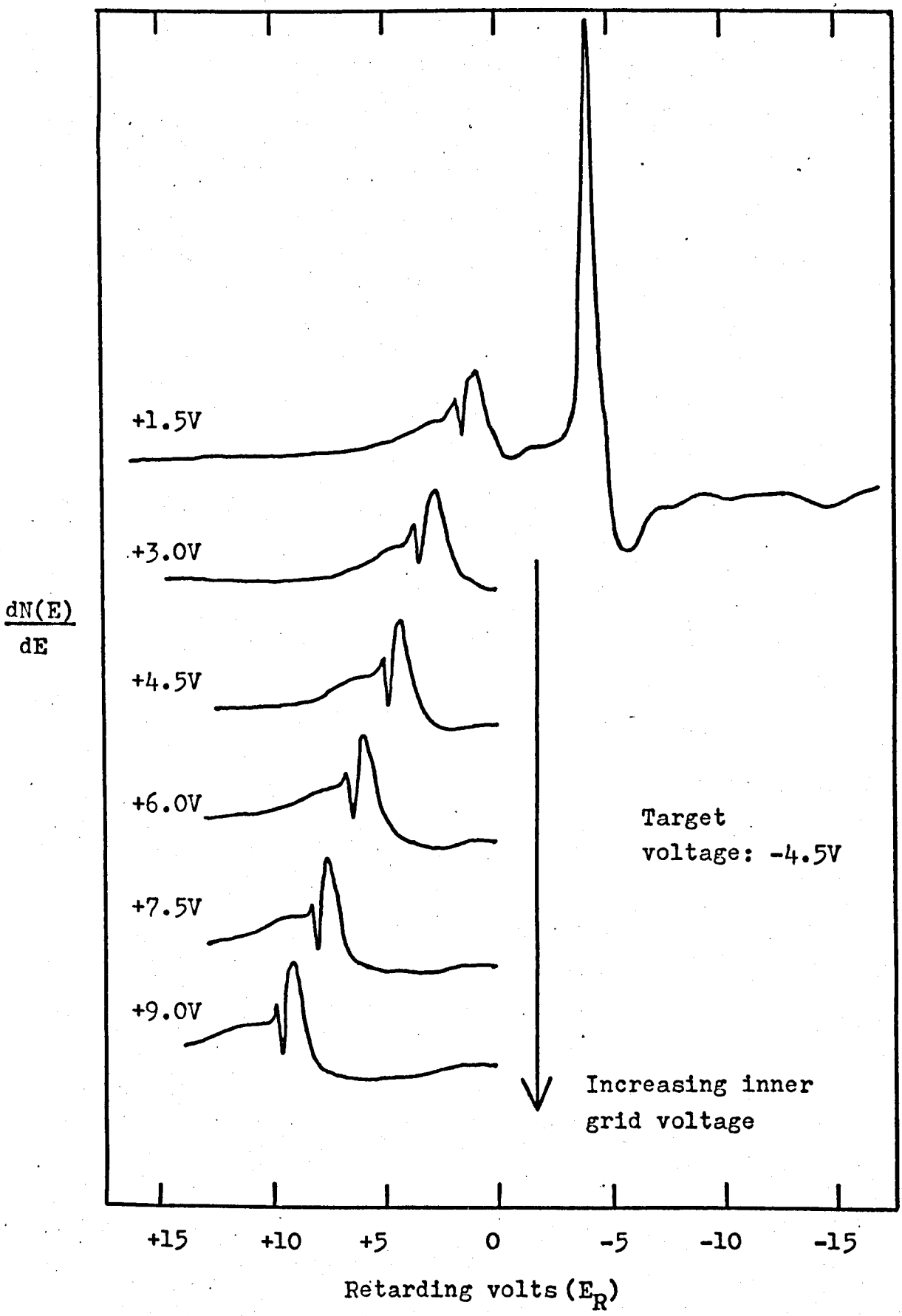

Figure 3.5 The extraction of spurious peaks in the slow peak

The result can be seen in Fig. 3.6. A small spurious peak is again seen on the left. The energy scales have been normalised to allow an easier structure comparison. One unfortunate effect of the voltage biassing is that it causes an energy broadening of peaks (i.e. loss of resolution). However, apart from this, the main energy structure is present in both plots and one may therefore conclude that at least in this case, the spurious peaks have no significant effect. The loss of resolution is however a serious problem and much fine structure would easily be lost by operating the spectrometer under these biassing conditions. Therefore, the majority of slow peak spectra were taken without voltage biassing.

3.2.6 Improvements to Existing Experimental Apparatus

Care must always be taken when using high impedance input techniques to avoid earth loop currents which can cause severe frequency modulation of the desired signal. To this end, the main's "earth" was disconnected from all power supply boards and a substitute earth was connected which was derived from a grounded bus bar. Subsequently, all the instrumentation was earthed directly to this earth line, thereby minimising 50 Hz pick - up.

Some trouble was occasionally experienced with a loss of collector signal strength and electrical breakdown between the retarding grids and collector. The problem was traced to electrical leakage paths built up across high voltage feedthroughs after metallic evaporations had been performed in the chamber. A leakage resistance of a few Megohm between collector and earth represented a significant signal loss. The leaking insulators were abraided with glass beads to remove the conducting films, and shielding insulators were added in order to mask the feedthroughs from such contamination.

The power supply to the electron gun filament was changed from a re-chargeable lead/acid battery to a Farnell constant voltage/current source (Farnell L 30F). This power supply was floated at

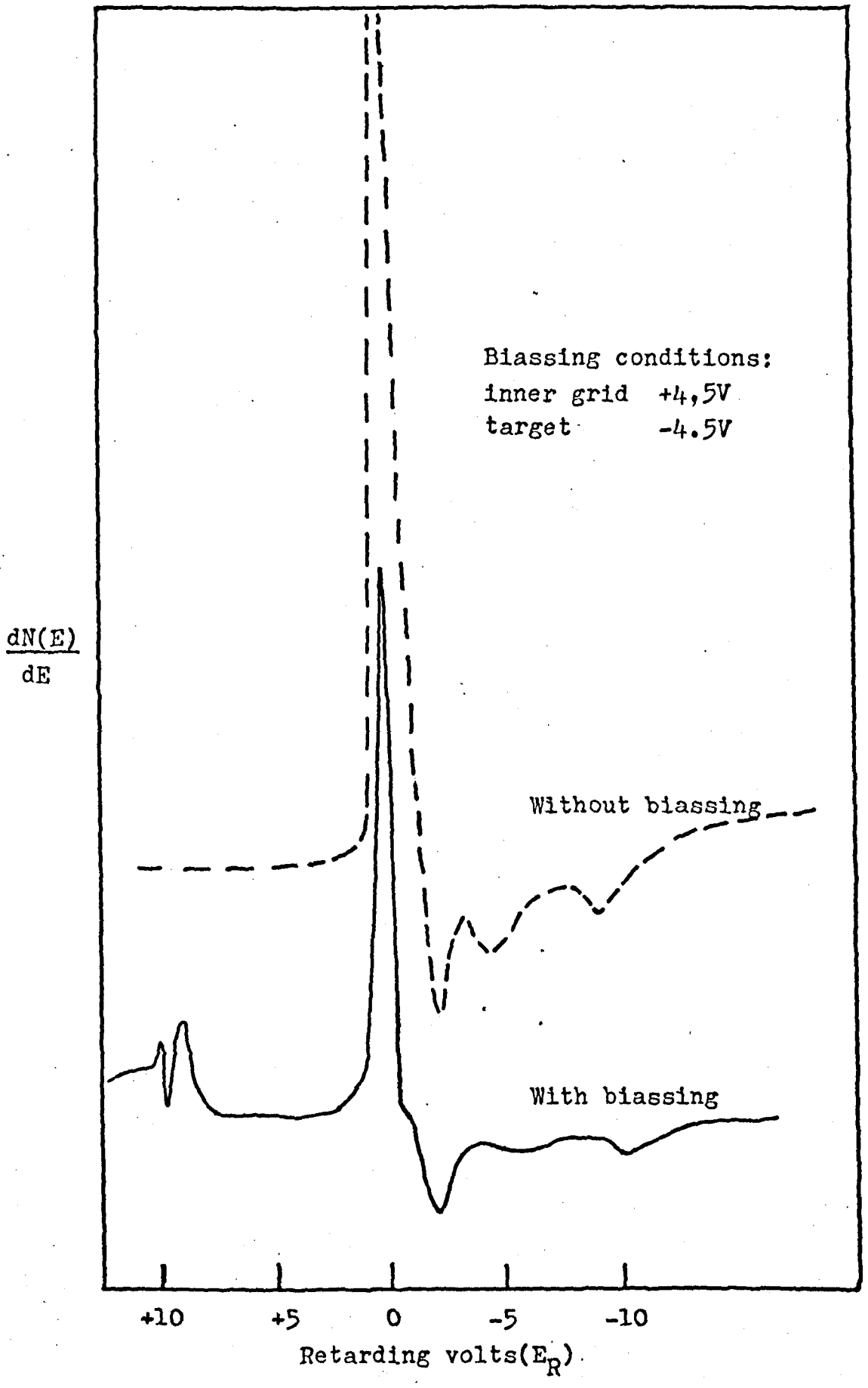

Figure 3.6 Effect of biassing conditions on slow peak spectra

cathode voltage (up to -2.5 kV) by means of a 1 : 1 isolating transformer. However, it was found necessary to place this transformer in an earthed metal box, to eliminate 50 Hz pick - up in the filament supply circuit.

A gas leak system was constructed to enable the observation of gaseous reactions at surfaces. In order to accurately monitor the constituent chamber gases, the Q.R.G.A. was moved from the ion - pump neighbourhood and attached directly to the experimental chamber as shown in Fig. 3.1. This necessitated the re-tuning of the tuned load due to the increase in C_{CE} (sub-section 3.2.3).

Although the energy resolution of the energy analyser was usually about 0.2% (i.e. $\Delta E/E$ X 100%), occasionally the resolution might fall to 0.4% after the grid system had been re-assembled. The reason for this was the fact that the grid hemispheres were not perfect around their "equators", and hence an exact matching to form a perfect sphere was difficult. In addition, some of the grids had a slight spherical distortion, especially near holes which had been cut to allow the target, gun etc., to pass through the grids.

Towards the end of the period of research, this problem was particularly acute and it was decided to construct a completely new set of retarding grids and a new grid former in which the "equators" of the hemispherical grids would be constrained in perfectly circular slots. The method of grid construction was similar to that described by Palmberg et.al.[131] The outer retarding grids were made from 102 x 102/0.03mm tungsten mesh whilst the inner grid required a smaller density mesh of 64 x 64/0.03mm. Glass spheres were made of 187, 167 and 100mm diameters with an accuracy of 0.5%. Each mesh was stretched over a hemisphere of the glass sphere and an equatorial ring of Advance metal strip was spot-welded to the mesh. Unfortunately, when the mesh was removed from the glass sphere, it was not self-supporting and it required chromium plating in the manner described by Palmberg et.al.[131], in order to strengthen it.

Fig. 3.7 shows the method for supporting and constraining the grid hemispheres. Each grid is retained in the slots by screws. The aluminium rings which hold the upper and lower hemispherical grids, lock together by means of locating pins and holes. This method of construction is more robust and should give an energy resolution perhaps less than 0.2%. Unfortunately, no results are available at present with regard to either the resolution or transmission of the new grid system.

3.3 Additional Experimental Features

3.3.1 Scanning Electron Microscope (SEM) attachment

It is obviously advantageous to be able to directly view a surface on which AES is to be performed. A displayed SEM image allows the recognition of surface heterogeneities which may then be selected and examined in detail by AES. In addition, an AES - SEM system greatly aids the location of small targets in a multi-target holder. The most important design criterion for such a system is the ease with which a specific point of interest in the SEM image can be analysed by AES. Further design considerations are that additional structures within the AES vacuum system are undesirable and that display of the SEM image on a standard oscilloscope is more convenient than the long persistence phosphor displays used in more conventional SEM work. The design considered here will allow the conversion of a standard AES system into a combined AES - SEM facility simply by addition of external electronics.

The basic layout of the combined AES - SEM system is shown in Fig. 3.8. The function generator provides appropriate sawtooth waveforms for the X and Y channels. They are fed via the attenuator, driver and shift controls to the deflector plates of the electron gun (Voltages V_r in scanning voltage diagram of Fig. 3.8). The attenuator and driving amplifiers allow the sawtooth amplitude to range from zero to 80V, per mitting magnification control in principle from "infinity" to approximately x 2. It is essential for AES analysis that the feature under examination lies at the centre of the retarding grid optics.

Dimensions in mm

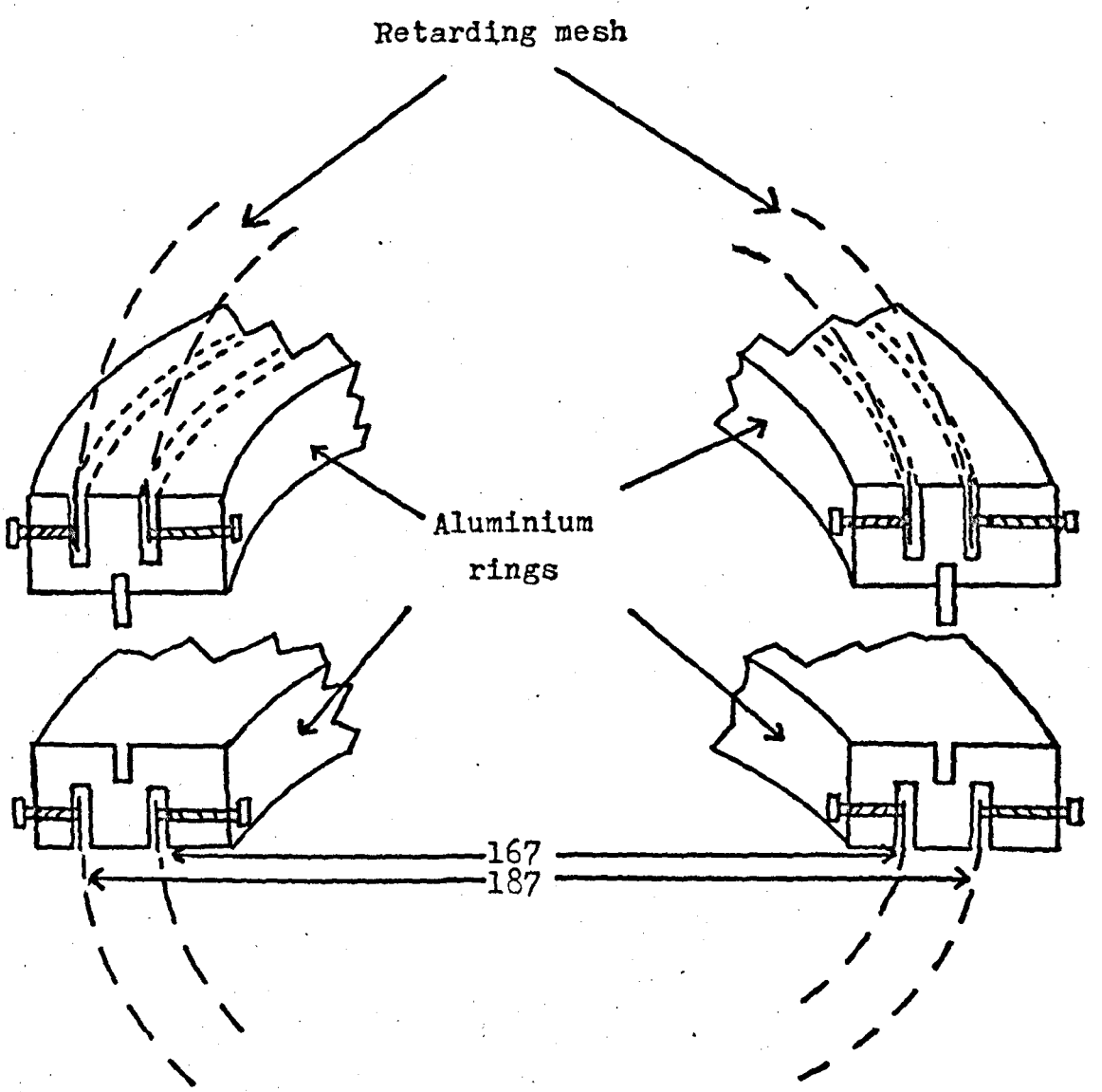

Figure 3.7 Schematic section through new grid assembly

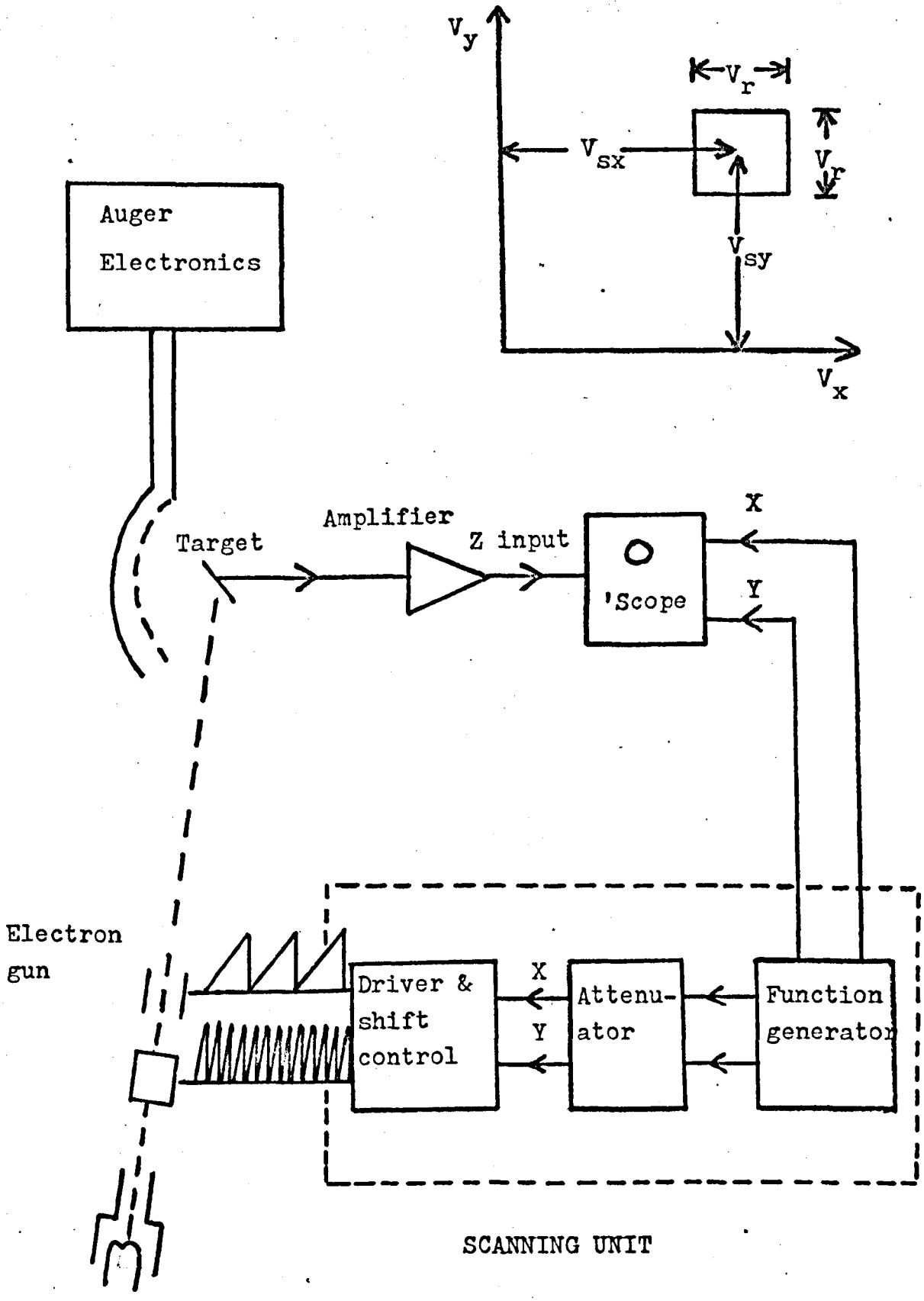

Figure 3.8 Layout of the combined AES-SEM system.

To help in this respect, the shift controls are used for DC offset of the X and Y raster mean voltages (Vsx and Vsy in scanning voltage diagram).

The output of the function generator is also fed into the X and Y deflection channels of the display oscilloscope (Hewlett Packard 130 C). The SEM image is obtained by modulation of the oscilloscope beam intensity (Z input) by means of the amplified target drain current (absorptive mode). To avoid the need for a long persistence display a frame rate of 13 Hz was found convenient. The sawtooth frequencies were 3kHz and 13 Hz for the Y and X channels respectively. The limiting resolution is the spot size on the oscilloscope which lowers the required number of picture points, and limits the necessary band-width of the target current amplifier to 2.5 MHz. The chosen sawtooth frequencies were eventually considered to be lower than necessary in practice, and with careful oscilloscope focussing and spot intensity adjustment, it is felt that the frequencies could be increased thereby giving more picture points and better picture quality.

The scanning unit consists of two independent, but basically similar circuits to drive the X and Y channels. The common design is shown in Fig. 3.9. A linear rise in voltage across C_1 is produced as it is charged through a constant current diode CL. When a value of about 12V is reached, TR_1 conducts and discharges C_1. Repetition of this process generates the required sawtooth waveform. The 10KΩ potentiometer (attenuator) is buffered from C_1 by TR_2. The oscilloscope input is derived from C_2. Transistor TR_3 acts as a phase splitter; each output has the same amplitude of about 9V, but the output at the collector is inverted. An amplification stage follows, in which the TR_4 and TR_5 stages have a voltage gain of 10. The outputs are fed to the deflector plates via C_5 and C_6. The required shift voltages are provided by the double-ganged 50KΩ potentiometer. The transistor types which are common to both X and Y scanning units are as follows: TR_1 -2N2646, TR_2 -BFX85, $TR_{3,4,5}$ -BF 259. Capacitors values (in μ F) for the X channel were:

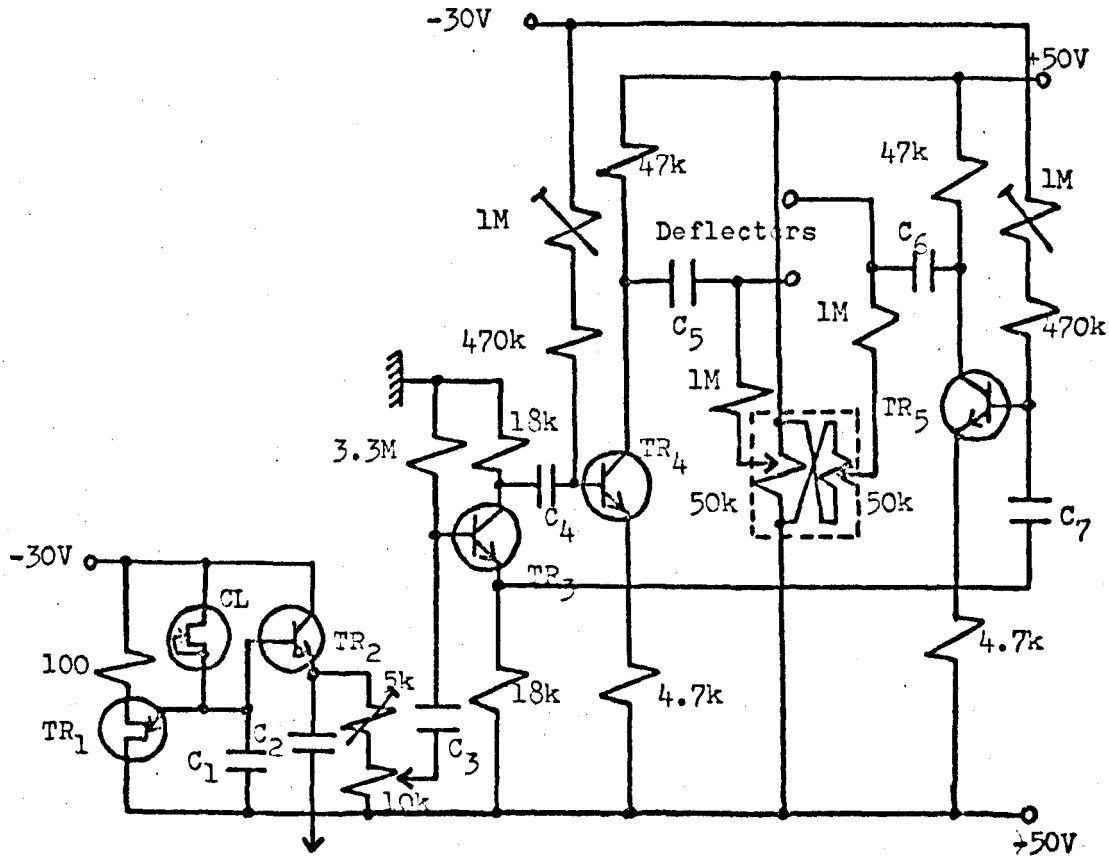

Figure 3.9 Scanning unit circuitry.

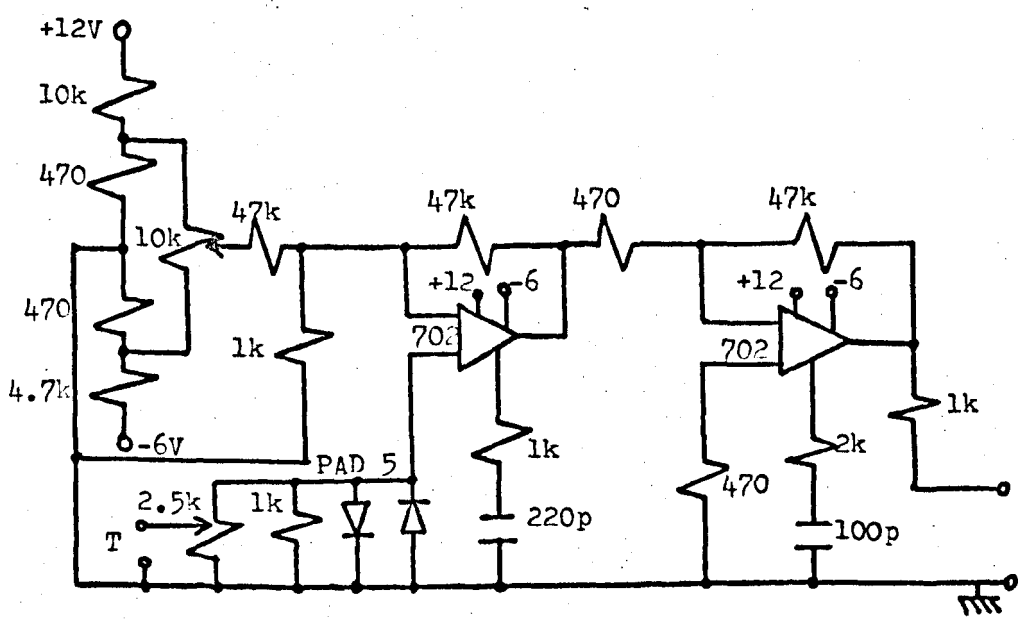

Figure 3.10 The signal amplifier circuit.

A

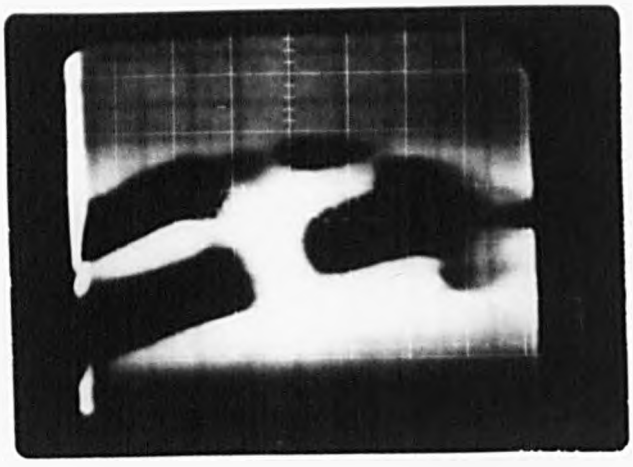

Micrograph of square Gold target - reverse side showing stainless steel claw holder

B

Micrograph of contaminated Cs film on Gold target

Plate 3.4 Preliminary scanning electron micrographs

C_1 -0.64, $C_{2,3}$ - 2.2, $C_{4,5}$ -4.7, $C_{6,7}$ -1.0 and for the Y channel: C_1 -0.0047, C_2 -0.033, C_{3-7} -0.01. Current limiting diodes (CL) were: X, CL 4710 and Y, CL 1020. Both scanning units were powered from an ITT power-card (PC 250A15/15) plus a Zener diode chain, but problems of cross-frequency coupling in the common power supply were encountered. It was found however, that a large value capacitor, placed across the Zener chain, effectively shunted AC to earth and prevented this coupling.

The two stage signal amplifier, shown in Fig. 3.10, has a gain of 5×10^3 and a 0 - 2.5 MHz bandwidth. The target connects to the 2.5KΩ potentiometer at T, which controls the input impedance and hence the image contrast. Diodes (PAD5) protect against a target being electron beam charged prior to connection. The 10kΩ potentiometer provides offset control and is preset to give zero output signal with zero input. The circuits just described are similar to those discussed by Ashwell et.al.[128], apart from slight component differences and the omission of a diode output network, which enables the signal amplifier of Fig. 3.10, to deliver up to 6V peak-to-peak without distortion.

With the shift controls fixed, a feature of interest may be mechanically moved to the centre of the display, and the magnification increased until the beam is stationary at this point. One can then do an immediate Auger analysis of the feature.

Plate 3.4 shows some preliminary low magnification (about x5) SEM images. A glancing incidence electron beam is used in image A and B, with a primary current of 8μ A. The cross-claw of the target holder can be seen in micrograph A, with a hook (on the right) turning under to hold the substrate. The claw was made from 2mm diameter wire, and the target is a 25x25mm square. The grid spacing of the oscilloscope screen is 10mm. Micrograph B shows a contaminated Cs film and reveals that contamination was not uniform over the film. Unfortunately, these heterogeneities were not rigorously correlated with Auger spectra at this time because of serious problems with the Auger electronics.

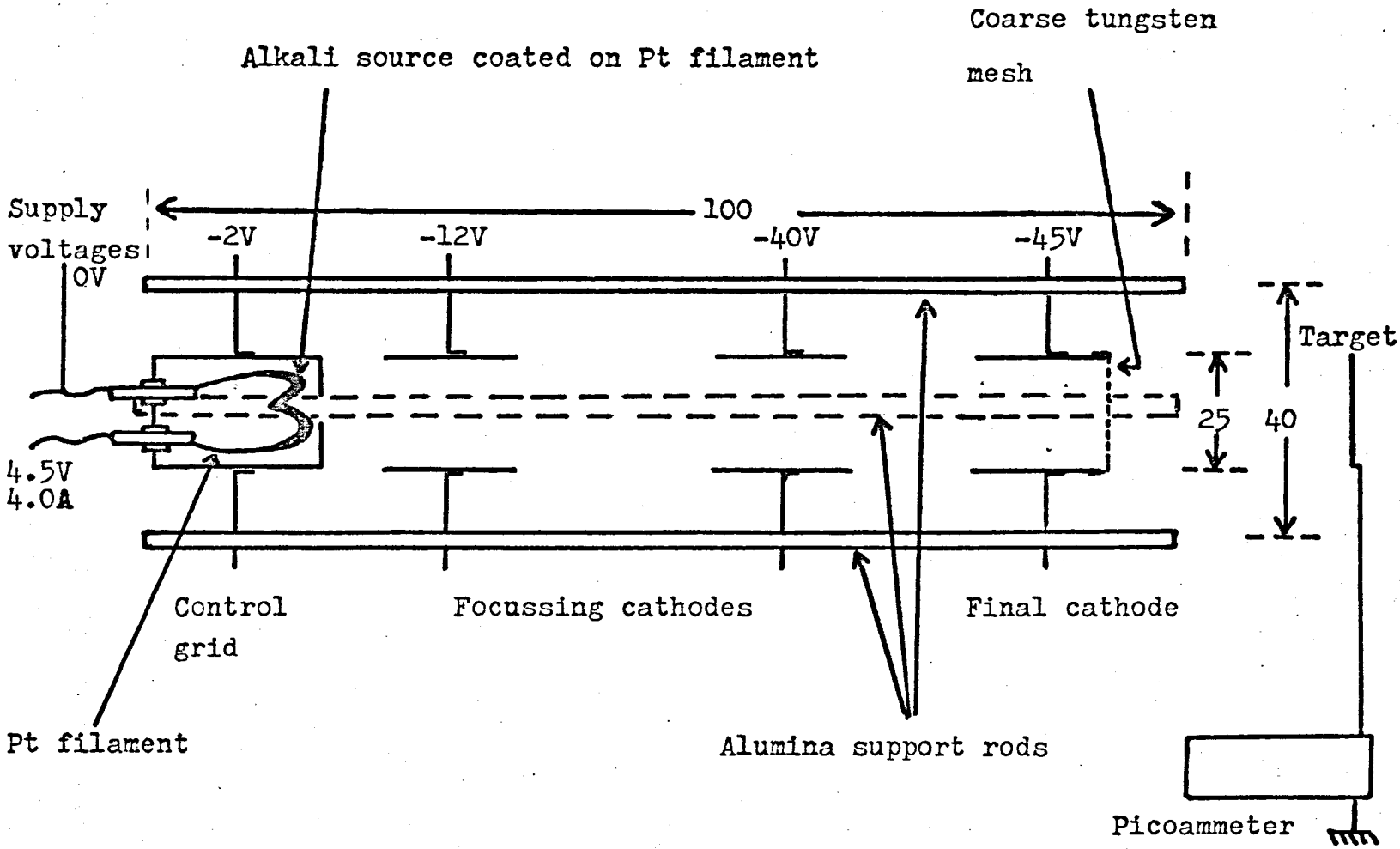

Figure dimensions in mm.

Figure 3.11 Cross-section through the Cs alkali ion gun.

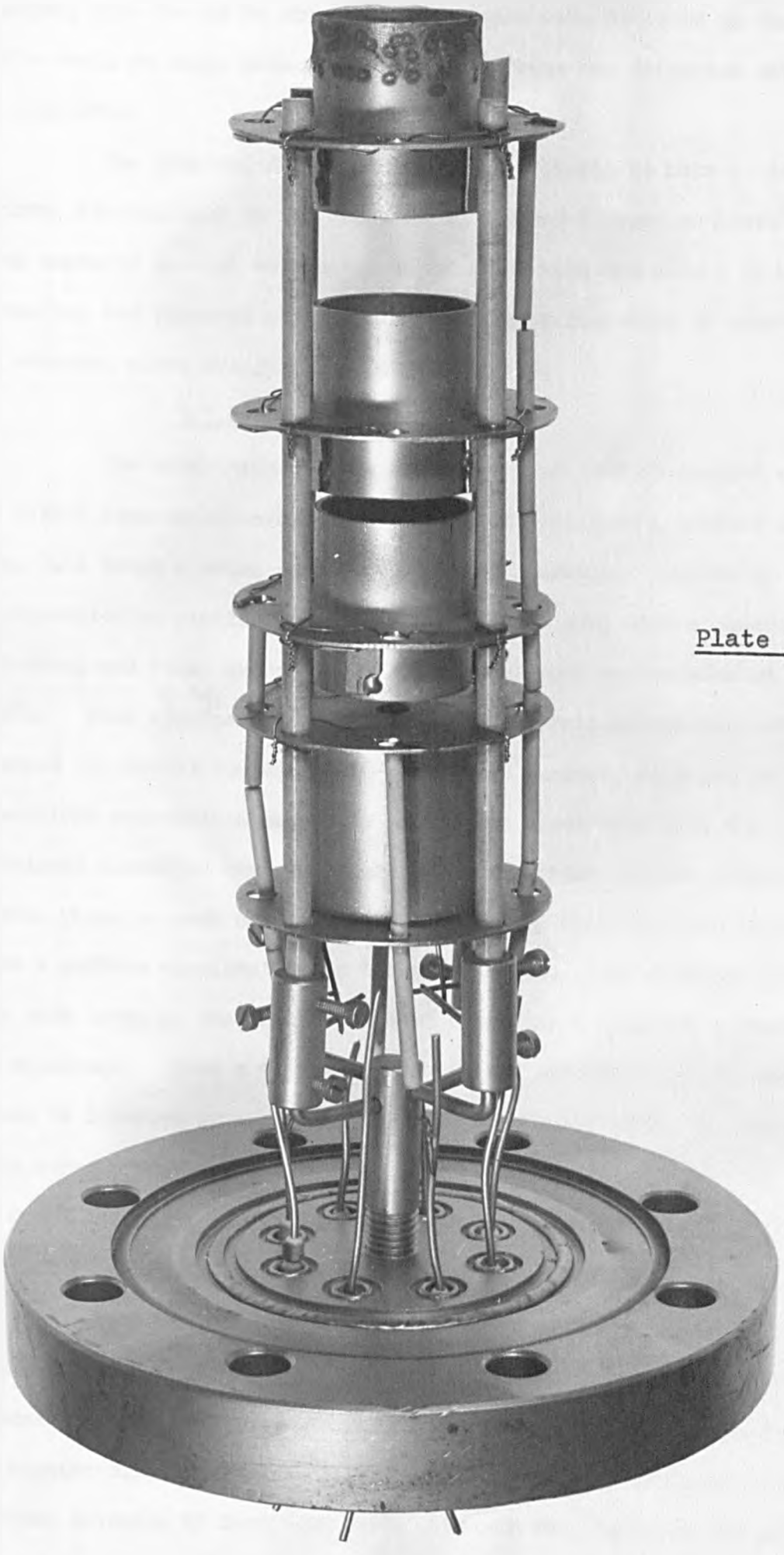

Plate 3.5

However, weak Fe and Ni Auger electron peaks were detected on the claw and a small Au Auger peak developed as the beam was deflected onto the Au substrate.

The combined AES-SEM instrument is likely to have a useful future, particularly in the field of integrated circuit analysis[129]. Much improved spatial resolution is expected with the advent of better circuitry and improved electron guns with beam diameters of less than 25 microns, which are just becoming available.

3.3.2 The Alkali-Ion Gun

The alkali-ion gun was constructed so that controlled amounts of alkali ions could be deposited on a substrate over a uniform area. Fig. 3.11 shows a cross-section of the gun assembly. Basically the construction is similar to that of an electron gun, with a control grid, focussing and final cathodes. The gun assembly was bakable up to about 400°C. Four alumina rods support the cylindrical electrodes and are clamped via barrel connectors to the flange support, as shown in Plate 3.5. Electrical connections were made to the gun electrodes with the use of insulated wires fed through holes in the electrode support rings. A coarse tungsten mesh was spot-welded on to the final cathode aperture to give a uniform acceleration to the alkali-ions. The filament housing was made large so that neutral alkali re-emission from hot surfaces will be minimised. When a target interrupts the ion beam, an ion current flows which is detected by a Keithley picoammeter (Model 409). By integrating this current with respect to time, the total number of deposited ions can be found and hence the surface coverage is estimated (the assumptions made in this statement will be considered in section 4.2).

Perhaps the most important feature of the gun, is the ion source. This was constructed in a similar manner to that described by Weber and Cordes[134] who found that when alkali atoms are thermally emitted from an alumino-silicate source, singly ionised ions were produced with a neutral emission of less than 1-2%. Cesium was chosen as the alkali

since it has a reasonably strong Auger transition at 45eV, and it also is in common use as a means for lowering work functions.

The cesium zeolite source was prepared by ion exchange with a sodium zeolite. Scdium zeolite (Na_2AlSiO_4) was obtained as a fine powder which was completely insoluble in water, making an ion exchange process into a lengthy affair. The following procedure was adopted to prepare the new zeolite. 3.7gm of sodium zeolite were added to 100ml of 1N cesium chloride solution; this composition gave the Cs ions a four fold excess over Na ions. This suspension was then sealed in a Pyrex tube, which was subsequently vibrated in a steam bath (95°C) for two days. The tube was then broken and the zeolite was filtered in a ground glass filter, followed by a washing in de-mineralised water. Fresh cesium chloride solution was added to the zeolite and the steam bath treatment was continued for a further two days. Afterwards the zeolite was filtered, washed, and dried in an oven at 100°C and finally ground into a fine powder. A heated fine platinum wire spiral was then dipped into the powder and removed; after about 20 or 30 such dippings, the zeolite coating on the platinum filament was about 2mm thick. At about 700°C, the coating slowly fused to the platinum wire to form a robust filament. This filament was then placed in the alkali-ion gun and was powered by a 4-5A dc supply.

The values of supply voltages were similar to those used in commercial alkali-ion guns (PHI model 04-141-Cs,K,Na). Proper ageing of the filament was necessary by drawing ion current for tens of hours, in order to remove carbon contamination from the ion beam. Typical ion current to the target was 3×10^{-8}A (about 2×10^{10} ions cm^{-2} s^{-1}). No alkali impurities were detected from the ion source which is in agreement with the findings of Thomas and Haas[61,62].

3.3.3 The Universal Motion Feedthrough

This mechanical device when attached to the target, enabled target movement in three directions, plus a rotation. Movement in three directions is particularly important when optimising the target position for best resolution, since the analysis area must be at the centre of the analysing grids. Also, this facility enabled features in the SEM image to be brought into the centre of view, ready for Auger analysis, with no loss of resolution. Target rotation is important since the exciting electron beam may then be used at glancing incidence so increasing the Auger yield and indeed the intensity of any 'surface' phenomena, such as surface plasmon energy losses.

Plate 3.6 shows the device attached to the experimental chamber. X and Y movement is obtained by rotation of the two micrometer screws which press against two sliding tables. The X and Y tables slide over a fixed common base-plate attached to the support column. This support column is fixed to the main base seen near the top of Plate 3.6. An inner threaded rod drive passes through the main support column and can be turned with a tommy bar as shown on the left of the picture. A nut is pinned to the common base-plate so that when the tommy bar is turned, the nut moves in the Z direction carrying the common base-plate with it. A linear bellows accomodates the Z movement of up to 10cm. An independent commercial (Vacuum Generators) rotary drive is seen near the bottom of Plate 3.6 and this rotating shaft connects directly to the target rod. The whole assembly, apart from the brass base-plates, was bakable up to 250°C. The elegant construction of the device in our workshop enabled the saving of a considerable sum of money.

3.3.4 Gas Inlet System

A pure gas leak is a useful facility in most studies of surface properties. Gases may be physi- or chemisorbed on a surface causing substantial changes in LEED, AES, work function etc. The main purpose of the construction of the present gas leak facility was to enable new

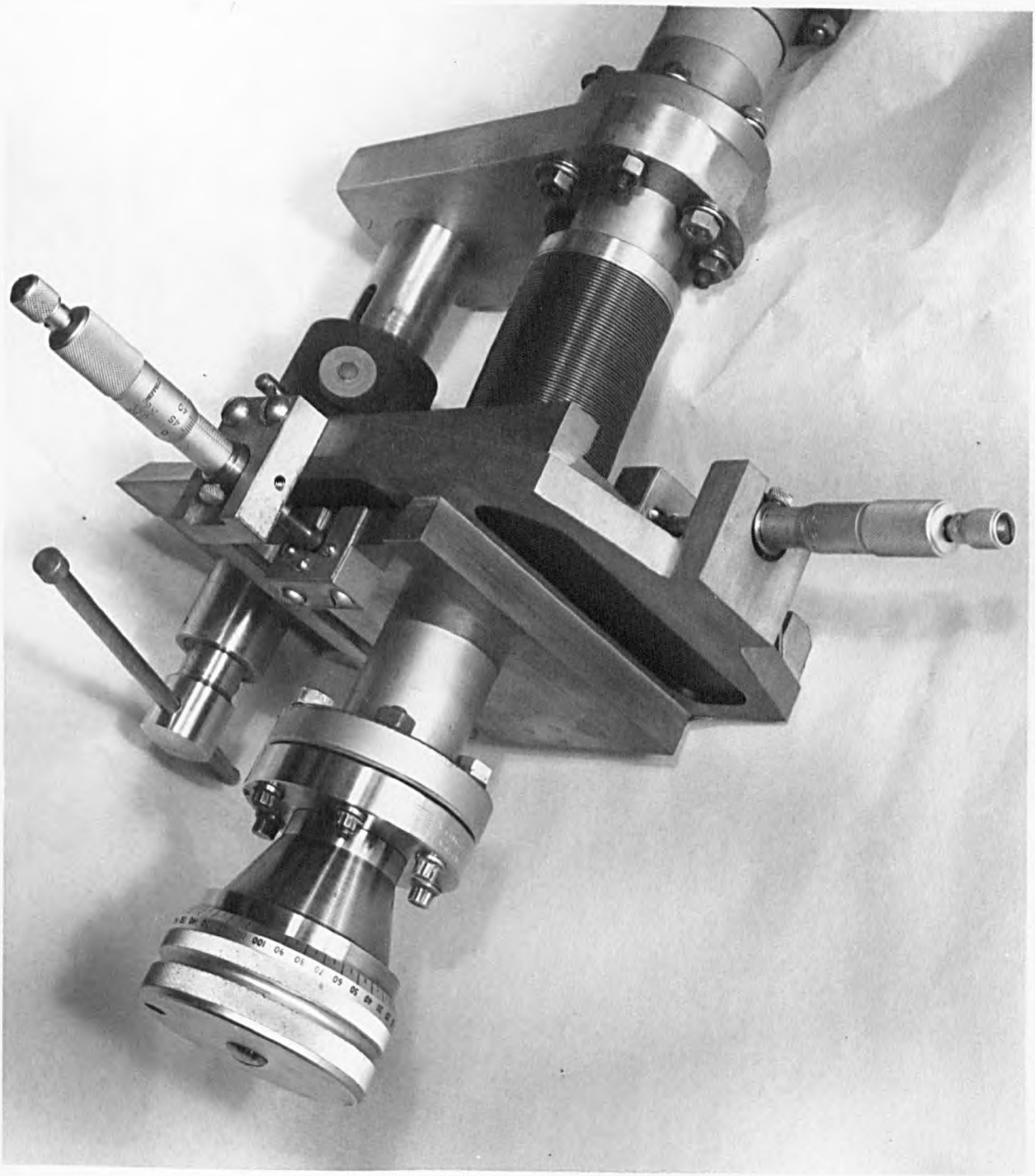

Plate 3.6

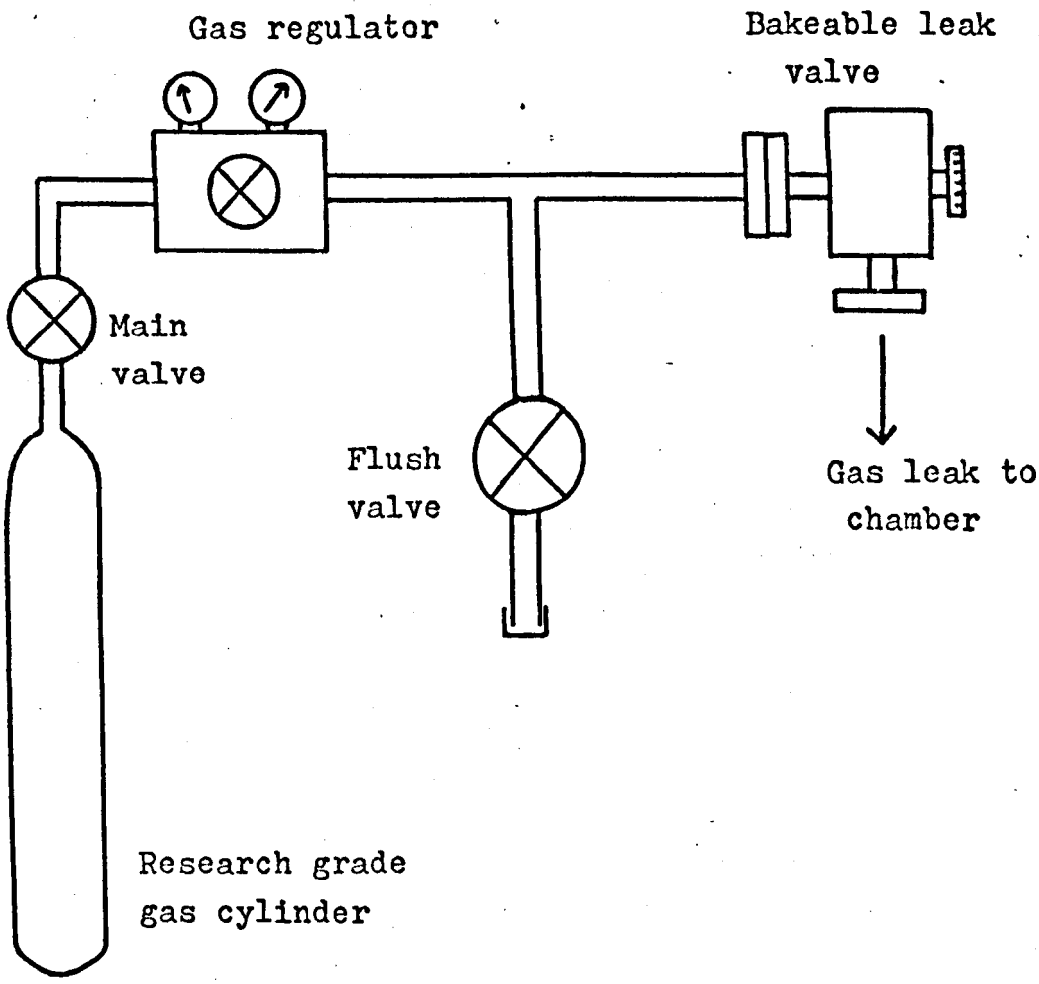

Figure 3.12 Schematic of gas leak system

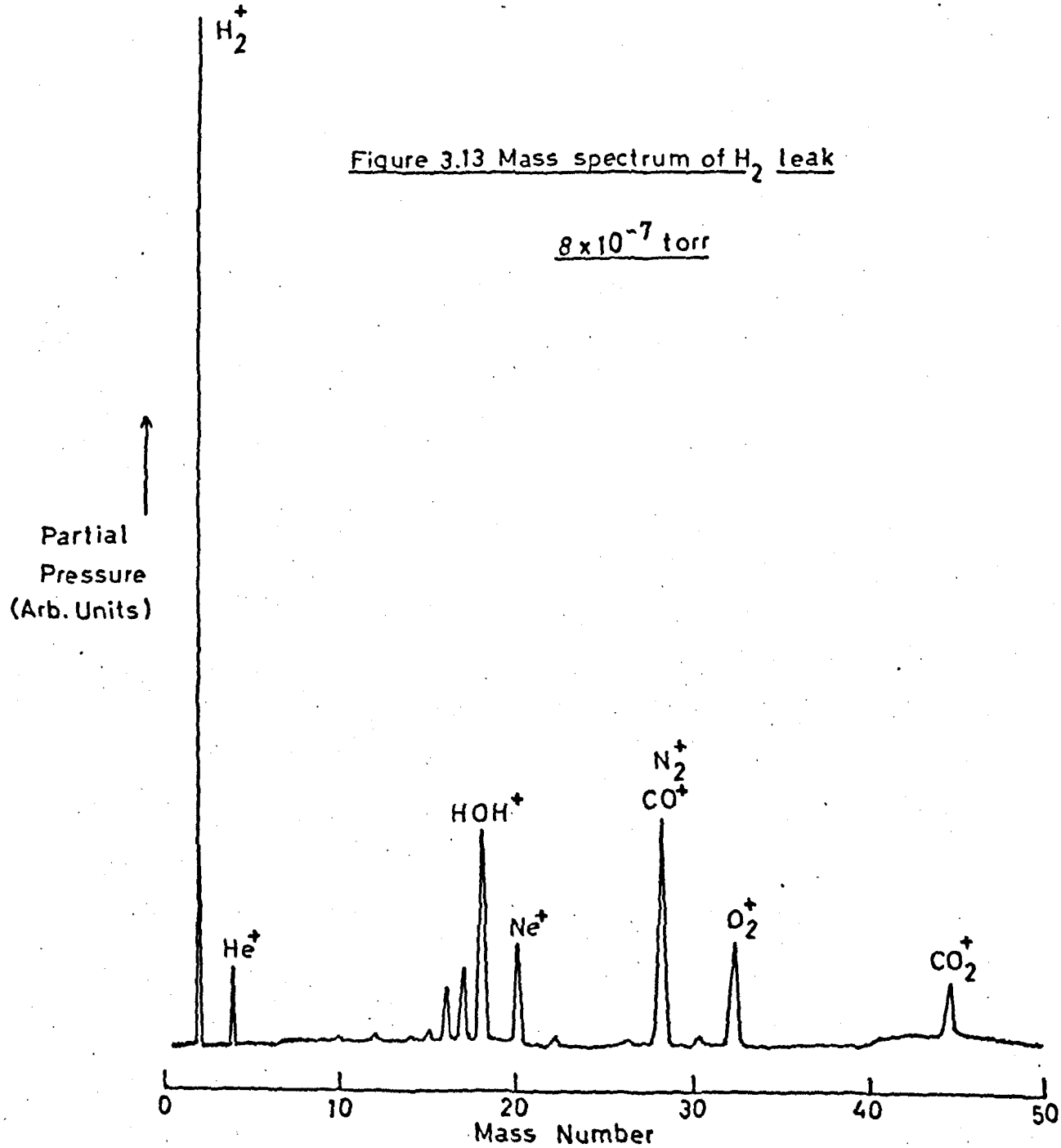

Figure 3.13 Mass spectrum of H_2 leak

8×10^{-7} torr

surface cleaning methods to be used i.e. cold-cathode sputtering and substrate heating in active gases. Such cleaning methods will be discussed in the next section.

A schematic diagram of the gas leak system is shown in Fig.3.12. Research grade gases (Matheson) were used in small 7 litre cylinders. The pipe-work from the gas regulator to the bakable valve was made from ½" stainless steel tube and could be baked up to 100°C. Gas leaks were continuously variable down to 10^{-10}torr with fine control allowed by the bakable leak valve (Vacuum Generators MD 6). A flushing procedure was used to remove impurity gases from the gas feed line, in the manner described below. The main valve on the gas cylinder was opened and gas was then allowed into the gas feed line via the regulator. When several atmospheres pressure had built-up, the regulator was closed and the flush valve opened for a few seconds, so that the pressure in the feed line dropped to slightly above atmosheric pressure. This procedure was then repeated several times. Although the method is relatively simple, it was found quite satisfactory for the required applications. A typical gas analysis for a hydrogen leak at 8×10^{-7}torr is seen in Fig. 3.13. The spectrum was taken with the Varian quadrupole residual gas analyser attached directly to the chamber. Unfortunately the filament in the gas analyser caused some of the observed contaminants in the mass spectrum, even though the degassing procedure was followed. Hence this filament was switched off during surface preparations. The large hydrogen partial pressure peak seen in Fig. 3.13, was found to be adequate for the removal of both chlorine and sulphur from a zirconium surface (sub-section 5.2.2).

3.4 Methods for Producing Clean Surfaces

Four methods have been studied in the present work and they are listed below:

a) Evaporation of materials onto a substrate,

b) Heating a surface in UHV or in active gases,

c) Cold-cathode sputtering in inert gases and

d) Alkali-ion bombardment.

Methods a) and b) are fairly common and will be considered first.

When a material is evaporated from say a tungsten wire basket, many of the impurities in the material will have a lower vapour pressure than that of the material, so that an atomic beam of the material should be rich in that particular species. In the case of aluminium, both carbon and aluminium oxide will be left behind in the basket due to their lower vapour pressures at the evaporation temperature of aluminium (800-900°C). When the atomic beam condenses on a substrate, a pure polycrystalline film should grow, if we assume no gaseous reactions in the passage from source to substrate. This method is particularly useful for stable materials with high vapours in the useful evaporation temperature range (600-2,000°C). The uses and pitfalls of the evaporation technique will be discussed as necessary throughout the remaining chapters.

Surface heating is perhaps the oldest method for surface cleaning. The basic idea is that heating will remove adsorbed gases and volatile surface impurities. However, in many instances the reverse is found to be true and impurities from the bulk may segregate to the surface on heating (sub-section 2.2.2). Hence this technique must usually be accompanied by heating in active gases or inert gas sputtering.

Cold-cathode inert gas sputtering is an offshoot of the more conventional inert gas sputtering. In the latter case, high energy (1,000eV) inert gas ions impinge on a surface and physically remove both contamination and true surface atoms from the surface. Surface damage is removed afterwards by an annealing process. Typical background

pressures during sputtering are between 10^{-5} and 10^{-4} torr. Argon ions are commonly used but the gas is inefficiently pumped by getter-ion pumps and special pumping facilities are usually required. To overcome this problem, it was found possible to produce a cold-cathode discharge of high power dissipation between an earthed target and a positive electrode, at a pressure of about one torr of nitrogen. The method was found suitable for inert substrate materials such as gold and silver[135]. The discharge was maintained at 300V, 5mA for about 20 minutes and then the chamber was pumped down to UHV and Auger spectra were taken. Some results for a gold substrate are seen in Fig. 3.14. The Auger peaks on the right correspond to the KVV Auger transition in carbon, at 268eV, whilst that on the left is the gold $N_{6,7}VV$ Auger peak at 69eV. Without sputtering, the Auger spectrum contains a strong carbon peak and no gold Auger peaks. The carbon layers are so thick that any Auger electrons emitted from the gold substrate are inelastically scattered before reaching the surface and are not observed. However when the cold-cathode discharge procedure is applied, the Auger peak from carbon reduces to about one third of its original size and a large Auger peak from the gold substrate is seen, indicating the removal of much carbon contamination. Further sputtering did not entirely irradicate the carbon Auger peak, and it is thought that the relatively high pressures used for sputtering caused a contamination equilibrium to be set-up, so that carbon was being removed as quickly as it was deposited from the 'rough' vacuum.

Tracy[136] has recently pointed out the possibility of surface sputtering using energetic alkali-ions. The main advantage is that the surface need never 'see' a vacuum worse than 10^{-9} torr. An alkali-ion source is used, such as the one described in sub-section 3.3.2, and the ions are accelerated to a negatively biassed target (about 300V) to produce the sputtering action. The surface is then annealed by mild heating, which also removes any adsorbed alkali atoms. Hence useful

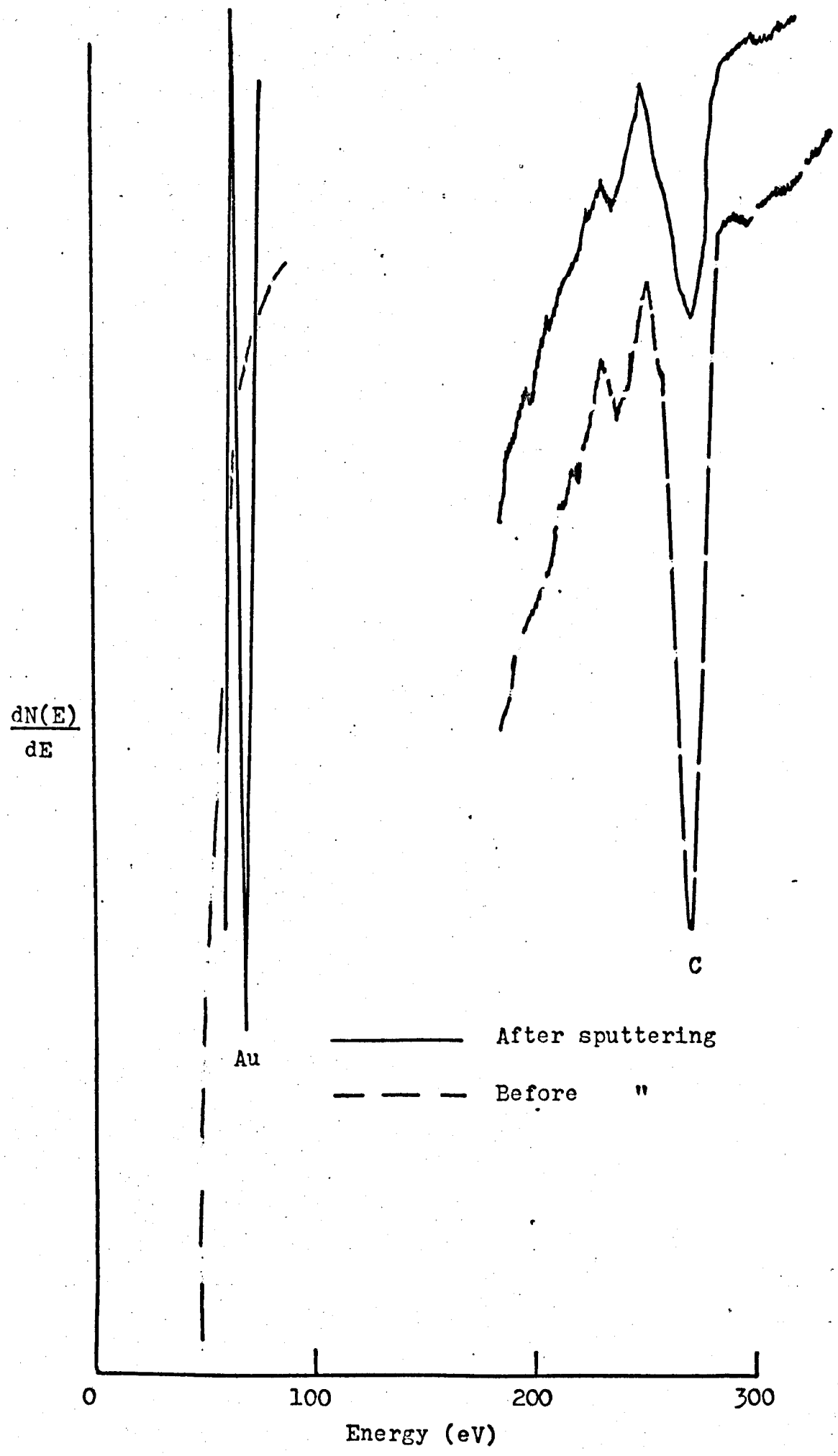

Figure 3.14 Effect of cold cathode discharge on Auger spectra of gold.

sputtering can be accomplished in a vacuum below 10^{-9}torr which is not possible using conventional sputtering techniques.

Fig. 3.15 indicates the feasibility of the technique, but unfortunately a premature failure of the alkali gun filament precluded further observations. Again these results are taken from a carbon-contaminated gold surface. Only a shoulder can be seen at 69eV in the case of the heavily contaminated gold surface, with a large carbon Auger peak predominating the spectrum. This target was then biassed at -300V and an ion current of only 10^{-8}A was passed for one hour at 10^{-9}torr (this corresponds to a total of 10^{14} Cs ions or about 10% of a monolayer). Even after this brief exposure, the carbon peak was significantly attenuated and a small gold Auger peak appeared at 69eV. Cs was not detected in this spectrum. This brief observation concurs with the work of Tracy[136] and has stimulated further work in our laboratory along these lines.

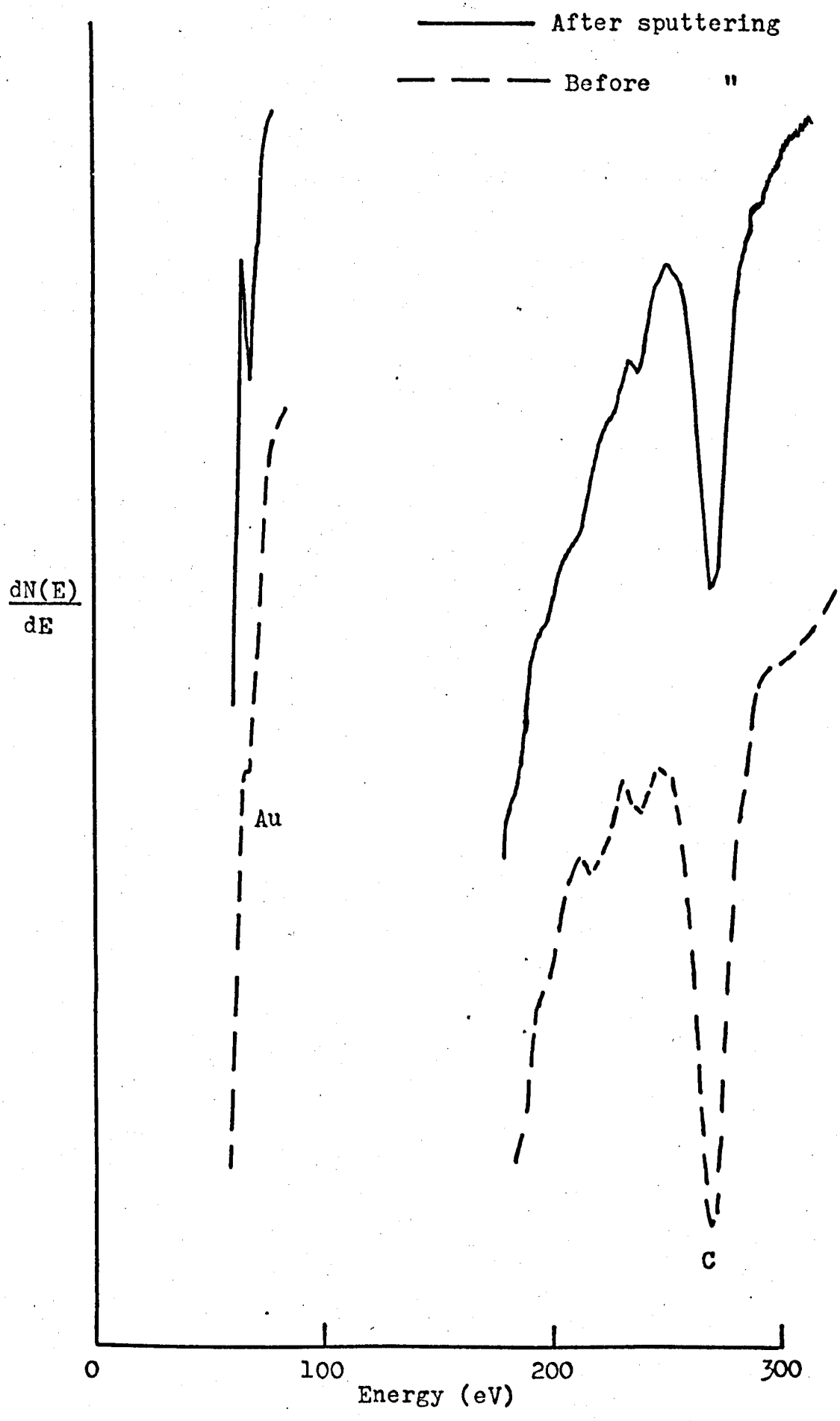

Figure 3.15 Effect of Cs-ion sputtering on Auger spectra of gold.

3.5 Conclusions

The essential features of the experimental apparatus have been discussed along with detection techniques and circuitry. It has been shown experimentally that tertiary electrons are present in the experimental chamber but do not represent a serious problem in slow peak spectroscopy. Some additional experimental apparatus has been discussed and its use will now be amplified in the remaining chapters. Also, the four basic methods used for surface cleaning were explained, with some indication as to their applications.

Several pieces of work were done using the apparatus and techniques just described, and are now related in the next six chapters. The first four chapters contain work on some selected problems in the AES field including quantitative AES, AES of zirconium, secondary emission from metal blacks and electron energy loss spectroscopy of antimony. These chapters contain results both of theoretical interest and of technological importance. The final two chapters of results illustrate the usefulness of slow peak analysis and some results will be used to criticize the work of recent authors.

RESULTS AND DISCUSSION - PART ONE

Selected Problems in Auger Electron Spectroscopy and Associated Techniques

CHAPTER 4

QUANTITATIVE AUGER ELECTRON SPECTROSCOPY USING THE ION-BEAM METHOD OF CESIUM ON GOLD

4.1 Introduction

One object of this piece of work was to deposit controlled amounts of Cs on a gold substrate using the alkali-ion gun described in sub-section 3.3.2. Much information can be gained from this controlled deposition, including the Auger electron calibration curve for Cs on Au, and an estimation of the absolute sensitivity of the apparatus to surface species (in this case Cs).

Also, the slow peak of Au was monitored as Cs was deposited, in order to check if submonolayer quantities of Cs had an appreciable effect on high energy band structure. If such small quantities of Cs were affecting band structure, then this situation would have serious implications in photoelectron spectroscopy where small amounts of Cs are routinely used to purely reduce work function. Christensen and Seraphin[137] have already pointed out that Cs may diffuse into the sample metal to form concentrations large enough to produce band structure changes, in the part of the sample reached by the photons. These doubts will be partially substantiated in this chapter.

In addition, the secondary electron emission properties of Cs can be found when the surface is saturated with Cs, which is useful since few results are available in this area, and indeed, those available are in conflict. Finally, an estimate may be made of the escape depth of the Auger electrons from Au, by monitoring the Au Auger signal as Cs is deposited.

4.2 Calibration Technique

The surface coverage of Cs can be measured by integrating the ion current flowing to the target:

$$n(t) = (1/eA) \times \int_0^t I(t).dt$$

where n(t) is the coverage at the exposure time t, e is the charge per ion, A is the exposed surface area of the substrate and I is the ion current collected by the target. For this relation to be valid, certain assumptions must be made. The sticking coefficient of the Cs ions is assumed to be unity and the effects of migration and re-evaporation are not considered to be large. Weber and Cordes[134] have shown that virtually all emitted alkali species will be in the form of singly ionised ions; this conclusion has been partially tested by both myself and Thomas and Haas[61,62], by suitably biassing the target with a positive voltage and showing that no Cs ions then arrive at the surface.

Contamination was found to be a serious problem when the ion gun was first used, with large amounts of carbon being deposited on the gold substrate. Much of this contamination was subsequently removed by cold cathode sputtering in nitrogen. Unfortunately, it was not found possible to remove all traces of carbon from the substrate so that the calibration results strictly apply to a partially contaminated Au surface, such as is shown in Fig. 3.14 (continuous line).

The Auger peaks chosen for calibration were the respective strongest peaks in the Auger spectra of Cs and Au; namely the $N_{6,7}VV$ transition at 69eV in Au and the $N_{4,5}O_{2,3}O_{2,3}$ transition at 45eV in Cs. Both of these peaks lie in the region of steep slope, so that it was necessary to use low values of modulation voltage (1.5-4.0V peak to peak amplitude), to reduce the slope error incurred when measuring the peak to peak value of the Auger signal (i.e. maximum to minimum of the excursion). In addition, such modulation voltages should not cause significant line broadening since the natural Auger line widths were

about 3-4eV wide. The errors incurred by such effects were discussed in sub-section 2.2.3. However, in the case of Au, the splitting of the $N_{6,7}$ level causes a splitting of 3eV in the Auger spectrum, at 66 and 69eV, as seen in Fig. 4.1 (taken under high resolution). Hence, a modulation voltage of 4Vpk-pk is required in quantitative measurements, so that the splitting does not interfere with the peak height measurements; in effect the larger modulation will 'smear out' the splitting, to produce a single peak. The Auger peaks in Fig. 4.1 are in basic agreement with the recent work of Joyner and Roberts[138], but their interpretation is somewhat complex and a discussion is not appropriate here.

About 10% of a Cs monolayer was deposited at a time and then Auger, and slow peak spectra were taken. In the initial calibration run, when 51% of a monolayer was reached, a mains electricity failure caused the ion pumps to stop for 45 minutes. When the pumps re-started, sulphur was found to have contaminated the Cs/Au surface so that this run was discontinued. However, the second run was more successful and a total theoretical deposit of 3.61 monolayers of Cs was made. All measurements ceased after this point, due to a premature filament failure in the alkali-ion gun.

Cs surface deposits were removed by mild substrate heating (200°C), enabling easy surface regeneration. However, the presence of Cs in the chamber had a detrimental effect on the oxide cathode of the electron gun, and eventually the gun current became noisy and the entire gun was replaced.

4.3 Calibration Results

Two calibration runs were made, with two different angles of incidence for the exciting electron beam, in order to show the effect of 'surface sensitivity' at high angles of incidence. Fig. 4.2 shows the growth of the $N_{4,5}O_{2,3}O_{2,3}$ Auger peak from Cs as the surface concentration of Cs increases. The peak energy occurs at 45eV and the figure contains

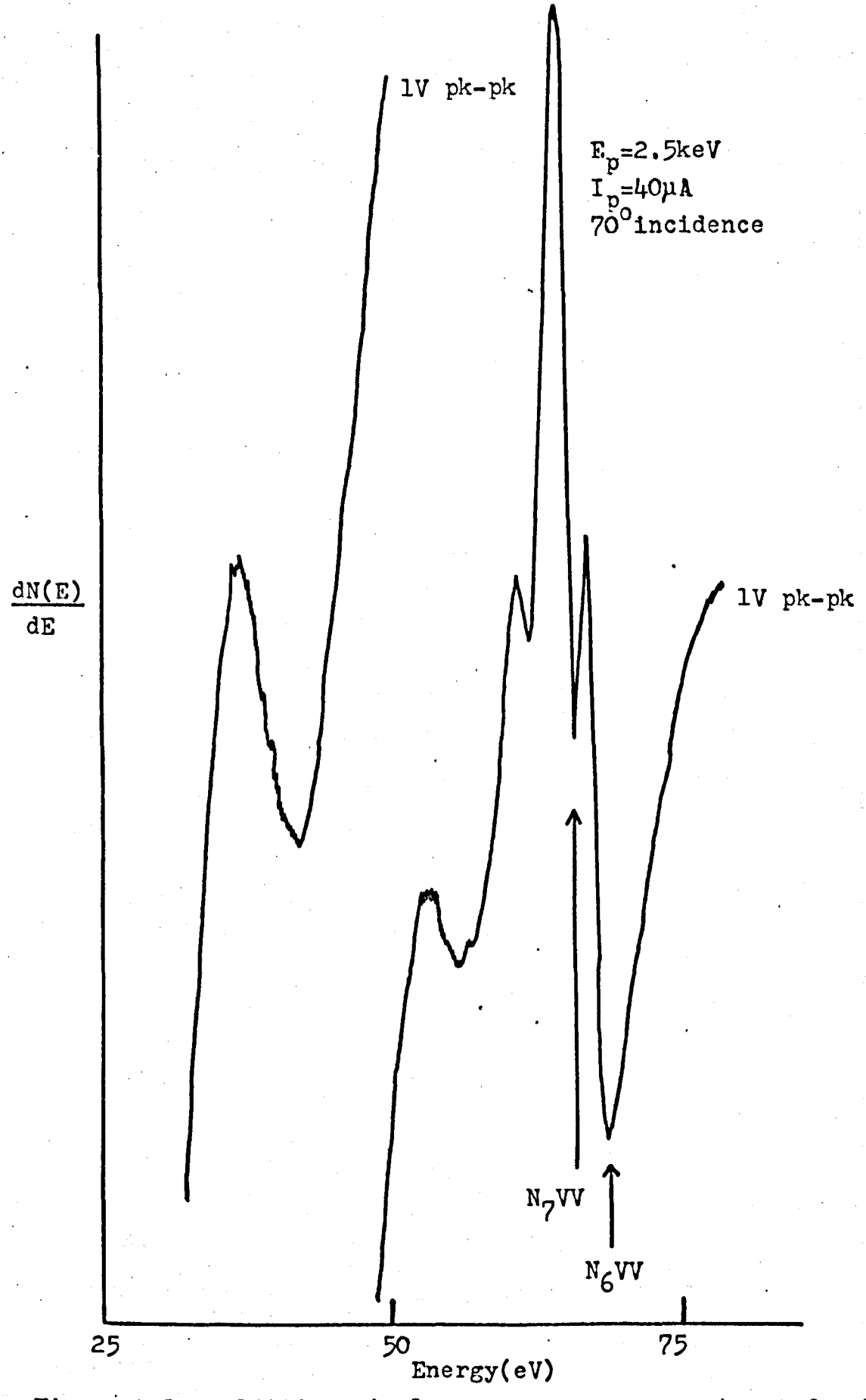

Figure 4.1 Splittings in low energy Auger spectrum of gold

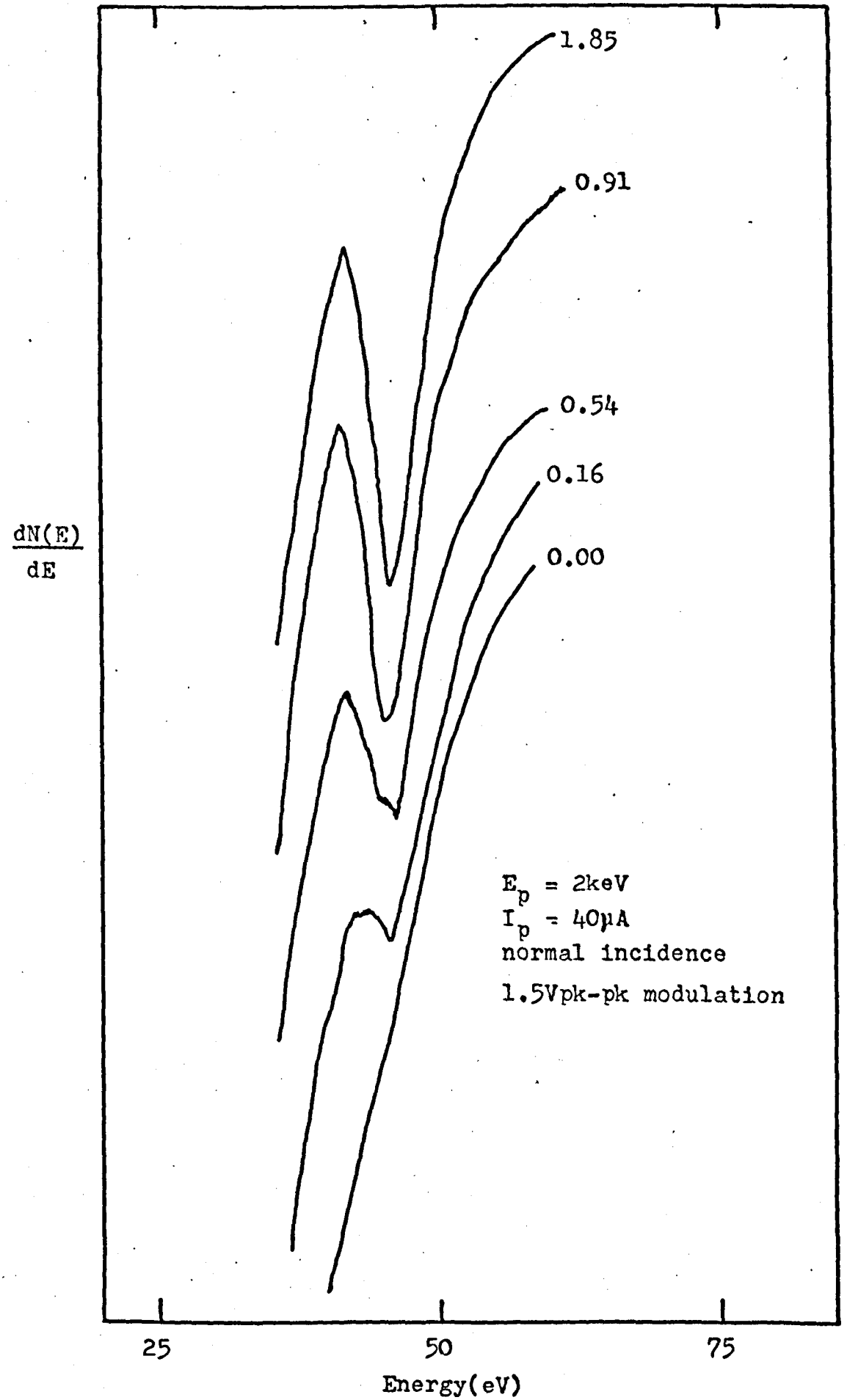

Figure 4.2 Growth of $N_{4,5}O_{2,3}O_{2,3}$ Auger peak of Cs with fractional monolayer coverage

only a representative number of spectra. The figure shows that the peak grows steadily as the Cs coverage increases, up to about one monolayer thickness when the growth slows, and finally ceases.

The coverage unit of Cs monolayers was chosen for the sake of clarity. A more fundamental unit would have been Cs atoms cm^{-2}, but this unit was transposed to the monolayer unit by assuming that a surface concentration of 9×10^{14} Cs atoms cm^{-2} was equivalent to one monolayer. This surface density equivalent was calculated on the assumption that the submonolayer structure was ionic[139,62] and that each Cs atom occupied a diameter squared, on the surface (atomic diameter of Cs equals 3.35 Å [62]). Thomas and Haas[61,62] used a somewhat different criterion for monolayer density, by assuming that a monolayer of Cs was complete when the Cs surface density equalled the substrate surface density. However, their reasoning for this assumption was not elucidated.

Fig. 4.2 also indicates that 0.16 monolayer of Cs forms a well resolved peak and in fact 0.06 monolayer was detected as a strong discontinuity at 45eV. It is therefore estimated that about 0.01-0.02 monolayer of Cs represents the limit of detection under the particular instrumental settings.

Fig. 4.3 illustrates the corresponding reduction in the $N_{6,7}VV$ Auger peak of Au, as the Cs coverage increases. Again, the coverage unit is fractional monolayer and one can see the 'drastic' attenuation of the peak size with submonolayer quantities of Cs. This indicates the strong surface sensitivity of AES to the presence of surface contaminants. The width of the peak (measured from maximum to minimum excursion) appears to remain fairly constant at about 5eV, irrespective of Cs surface coverage. The figure contains only a representative number of curves; the full data being left to Fig. 4.4. After two Cs monolayers were reached, the gold Auger peak was not fully resolved (i.e. a true max. and min. were not formed) but merely became a discontinuity in the curve at 69eV. It is perhaps worth noting that the 69eV gold Auger peak was reduced to about one half, when 50% of a monolayer of Cs was present.

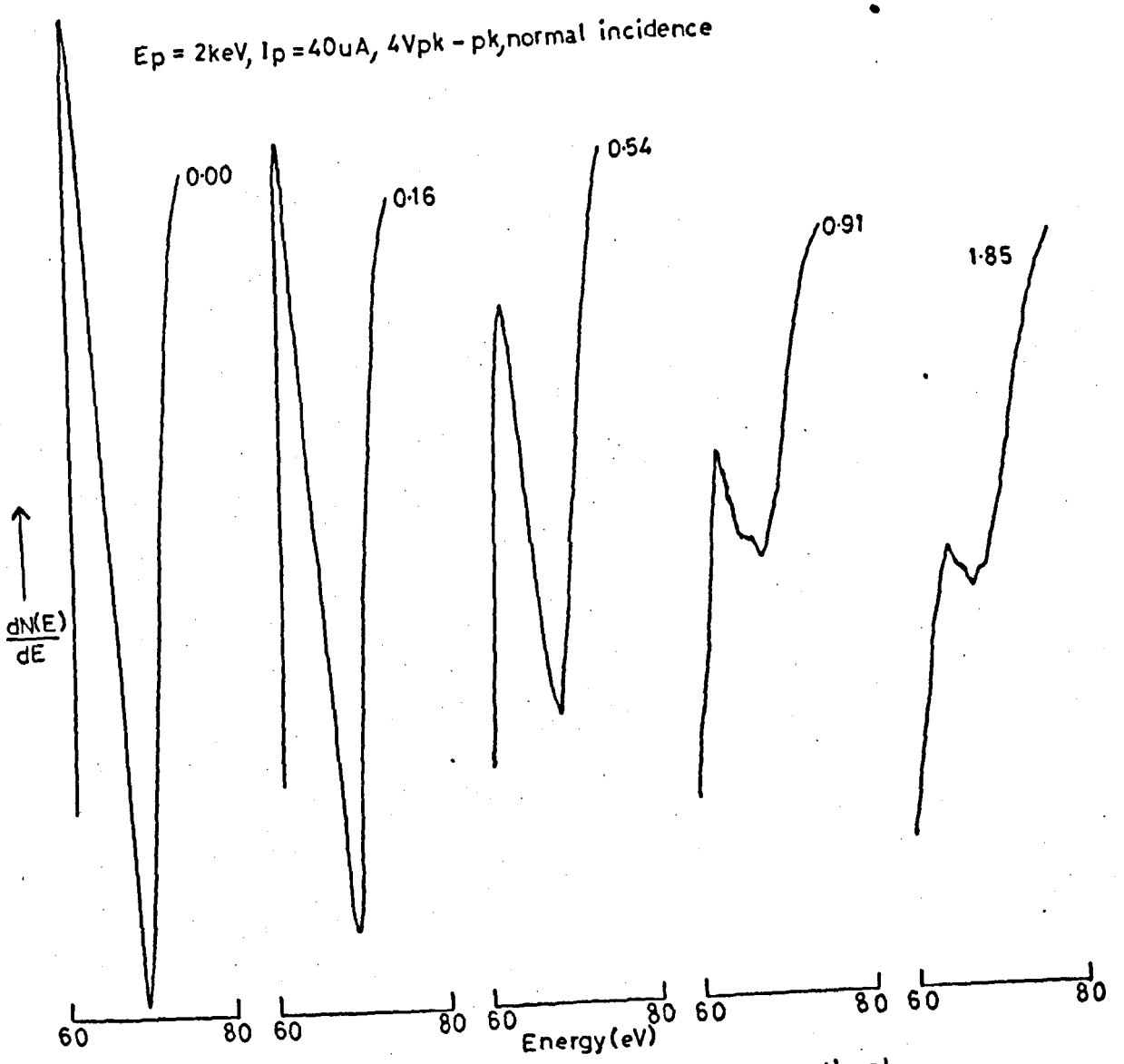

Figure 4.3 Attenuation of $N_{6,7}VV$ Auger peak of Au with Cs fractional monolayer coverage.

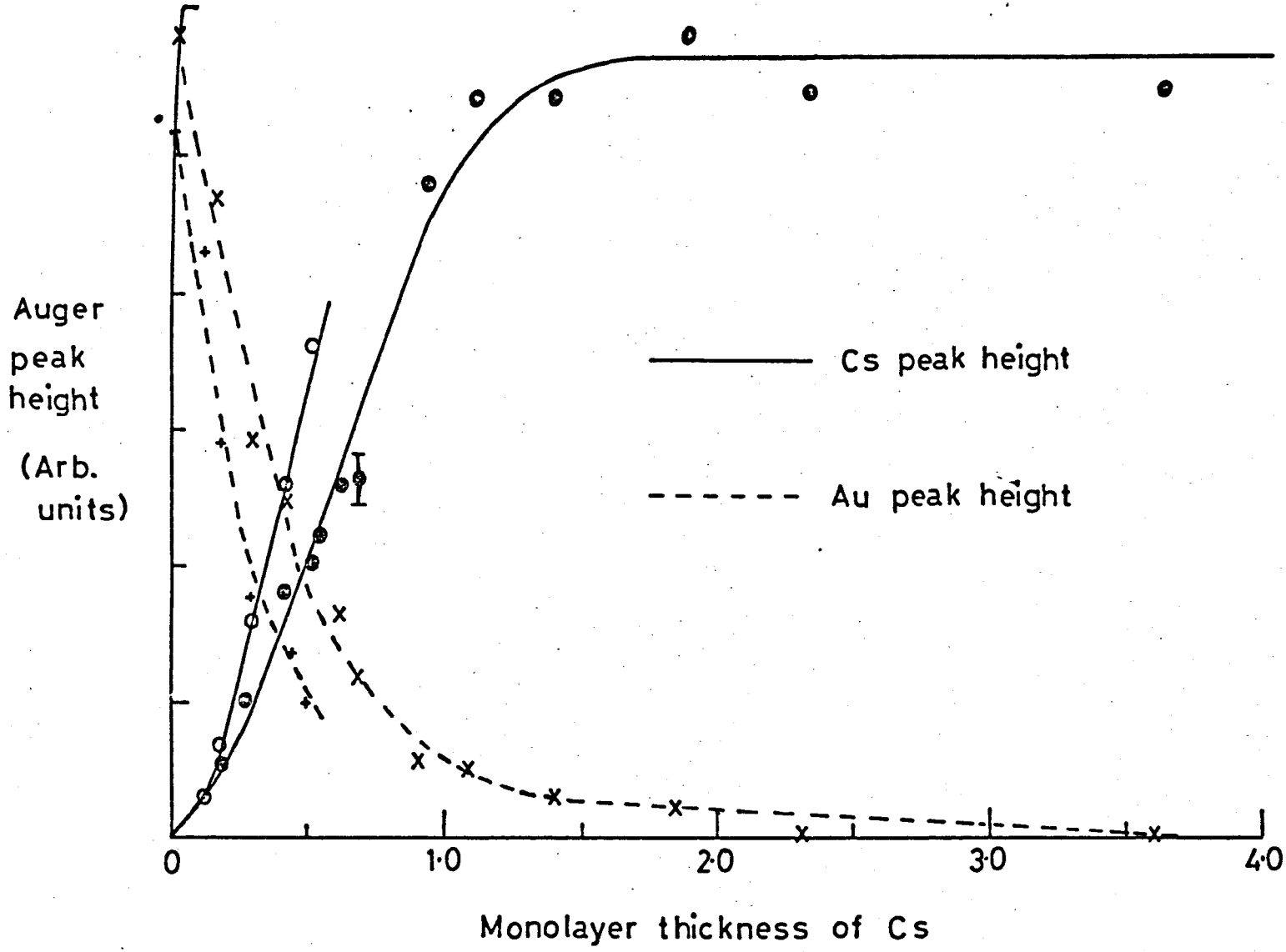

Figure 4.4 Calibration curves for Cs on Au

The complete results of the two calibration runs have been plotted in Fig. 4.4. Auger peak heights were determined by measurement of the maximum to minimum excursion of the signal in the differential mode, with no correction being made for the background slope. Both the growth and decay of the Cs and Au Auger signals respectively, are shown in the figure. The first calibration run is shown by the two curves which end abruptly at about 0.5 monolayer. The second run carried on to reach over 3.5 monolayers of Cs, although whether Cs will condense above two monolayers without substrate cooling, is questionable[62,139].

Cs signals on both runs show a fairly good linear rise with Cs submonolayer coverages. However, on the second run, there was evidence that the relation became 'distorted' near 0.6 monolayers when the Cs Auger signal stopped growing. The error bar given at the 0.70 monolayer point indicates the peak to peak noise error and it is seen that this point lies well outside the linear relation line. A possible explanation of this effect is given later. The steeper rise of the Cs signal in the first run is due to the higher angle of primary electron incidence (65°) as compared to normal incidence in the second run. This higher sensitivity at non-normal incidence is again seen in the corresponding Au Auger peak signals. These slopes are also fairly linear in the submonolayer region, and in the second run, the curve flattens and approaches a zero value.

Fig. 4.4 therefore represents a calibration curve for the Cs on Au Auger system, under the particular instrumental conditions stated. Besides this quantitative aspect, the work had much valuable 'spin-off' in terms of the Auger electron, electron energy loss and slow peak spectroscopy of cesium, which is useful because of the brevity of the literature in this area.

4.4 Auger Electron Spectroscopy of Cesium

The Auger spectrum of cesium was taken after about 3.5 monolayers of Cs had been deposited on the target. Since the background slope was no longer a problem, the modulating voltage was increased to 3Vpk-pk in order to view the finer structure of the Auger spectrum. Fig. 4.5 shows the low energy Auger spectrum so obtained. The large peak at 45eV was the one used for calibration purposes and a further small peak is seen at 58eV. In addition, two shoulders have appeared at 61 and 69eV.

A complete Auger electron scan from 100 to 1000eV is seen in Fig. 4.6, which relates to the same surface as Fig. 4.5. Small amounts of S, C and O contaminants are present on the surface (150, 270 and 510eV respectively), with a further peak at 475eV whose origin is uncertain. The weak Auger electron doublet corresponding to the $M_{4,5}$ ionised level of Cs, is seen unresolved at 560eV.

The Auger spectrum of clean Cs is still under debate in the literature, but my results appear to support the work of Thomas and Haas[61,62], rather than that of Desplat[140]. However, a fuller discussion of these results will be left to section 4.6.

4.5 Electron Energy Loss and Slow Peak Spectroscopy of Cesium

After 3.61 monolayers of Cs had been deposited, electron energy loss spectra were taken on the surface and are shown in Fig. 4.7. The differentiated elastic peak can be seen on the right of the figure with the associated losses being quite small. However with higher modulating voltage and more gain, we are able to resolve four energy losses at 8.0, 18, 20.5 and 38eV. The surface and bulk plasmon losses which are thought to be at 2.11 and 2.96eV (Hartley[141]) were not resolved. Table 4.1 gives the observed energy loss values with their possible assignments.

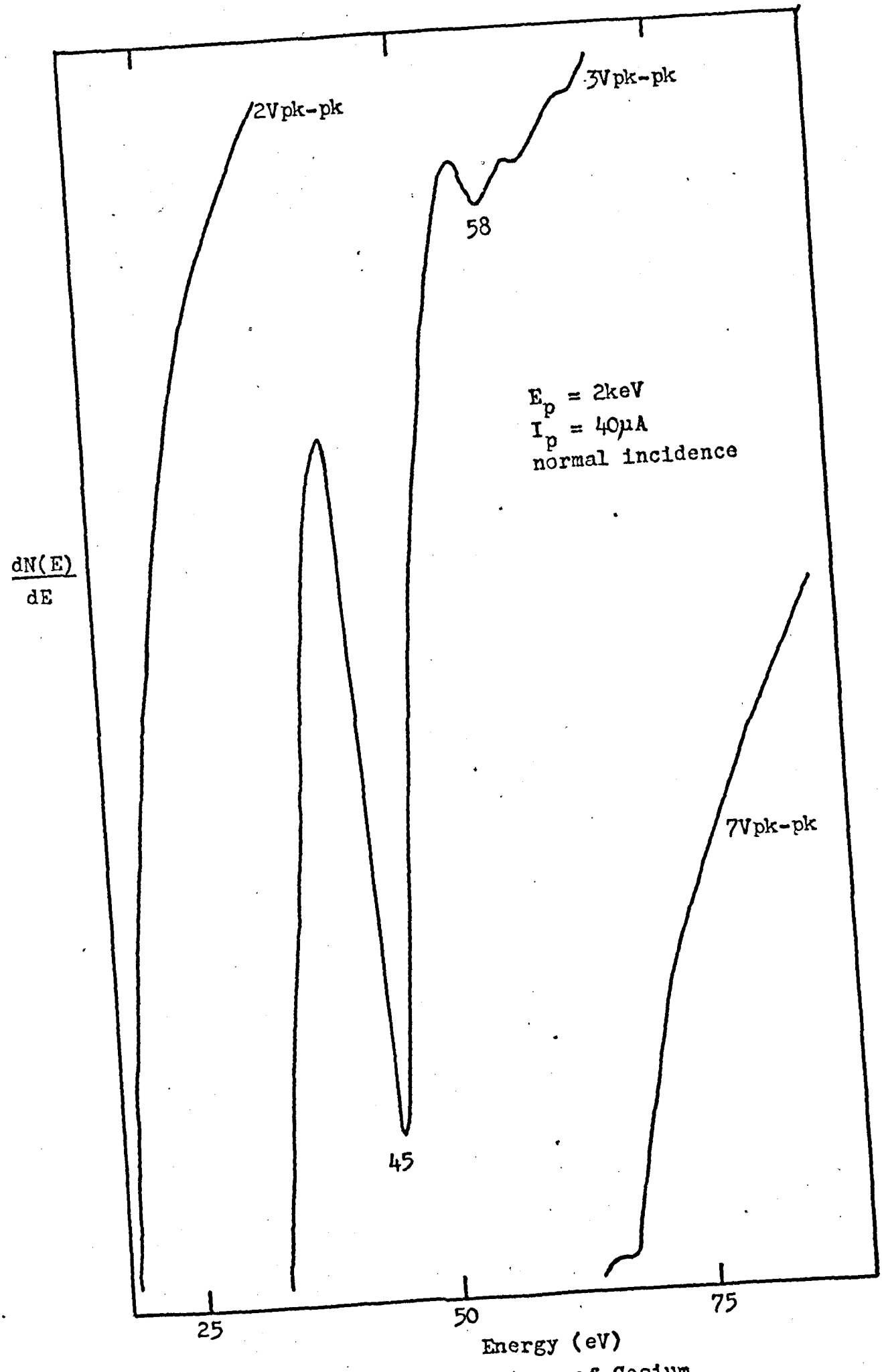

Figure 4.5 Low energy Auger spectrum of Cesium

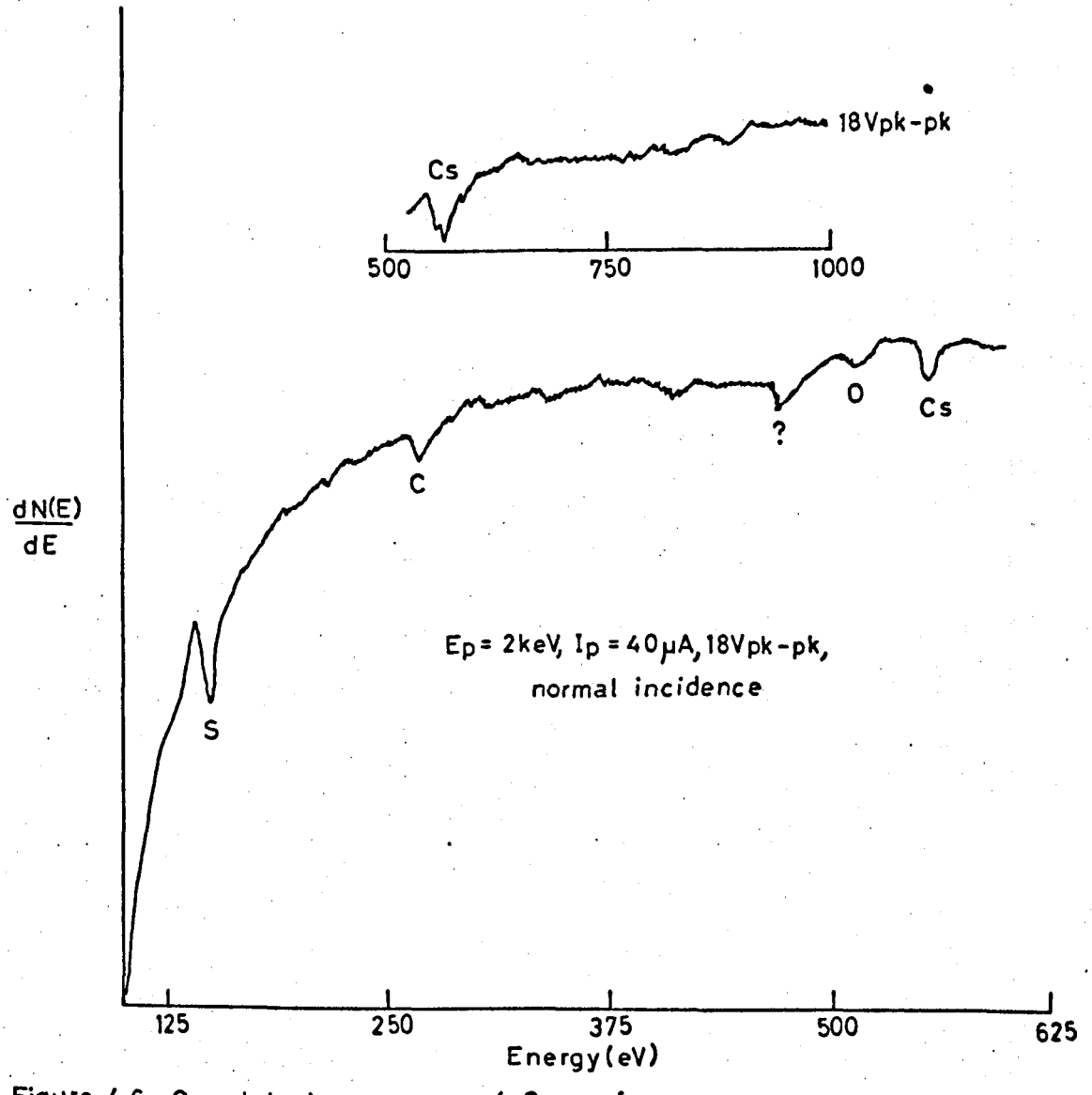

Figure 4.6 Complete Auger scan of Cs surface

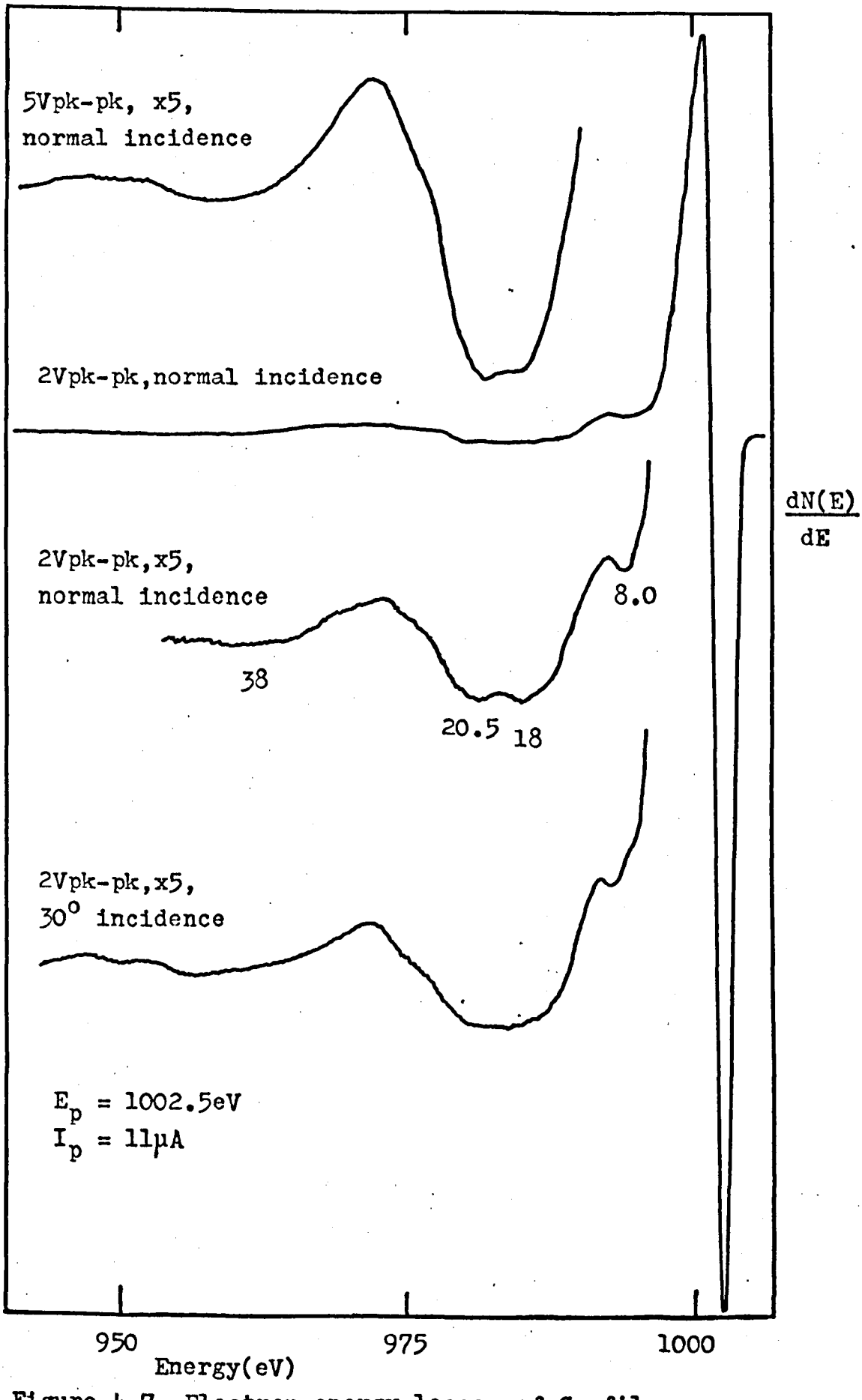

Figure 4.7 Electron energy losses of Cs film

Table 4.1

Energy Losses of Cesium (in eV)

Present Results			8.0	18.0	20.5	38
Hartley[141]	2.11	2.96		20.1		42.8
Assignments	S.P.	B.P.	I.B.	I.B. + I.L.		I.B.

S.P.: surface plasmon, B P.: bulk plasmon; I.B.: inter/intra-band transition, I.L.: ionisation loss.

It appears that the losses at 8. 18, 20.5 and 38eV are not connected to plasma behaviour since they show no strong variation with angle of incidence, as typified by the lower curve of Fig. 4.7. Hartley[141] makes the assumption that these higher lying losses must be interband transitions. However an energy level scheme for Cs (see next section) shows that an ionisation loss is possible, i.e. the O_1 level at 22.7eV, which could make a contribution to the broad split loss at about 20eV.

If these broad losses are indeed inter/intra-band transitions, then this points to the mechanism for the population of high energy, (above vacuum level) final states, since the upper band of the transition must be well above vacuum level. This conclusion is justified since the only available lower band levels are the O_1 and $O_{2,3}$ levels, which occur at 22.7 and about 12eV, hence a 38eV transition must take the transit electron well above vacuum level. It is now appropriate to move on to see the effects of the population of high energy states, on slow peak spectra.

The experimental effects of Cs deposition on the slow peak spectra from a gold surface will be considered next. Table 4.2 displays the observed slow peak characteristic energies for both the initial gold surface and the cesiated surface after the deposition of 3.61 monolayers of Cs. Since the slow peak spectra from the two elements

are different, it is interesting to observe the effects of submonolayer quantitites of Cs on the gold surface.

Table 4.2

Observed Slow Peak Characteristic Energy Values (in eV)

Cesium	1.2	1.8	2.3	3.0	3.5		4.8	5.5					
Gold	1.1		2.5	3.2		4.0	4.9	5.4	6.2	6.8	7.5	8.5	12.2

(These energy values are taken from minima in the dN(E)/dE mode)

A sequence of slow peak spectra were therefore taken periodically during the controlled deposition of Cs on Au, and these are shown in Figs. 4.8a-c. The first stages of deposition are seen in Fig. 4.8a and it is apparent that even 0.06 monolayer has a significant effect on the spectra. The sequence of Fig. 4.8a, sees a strengthening of the splittings at 1.4 and 2.4eV and the emergence of a strong peak at 3eV. Also, the weaker peaks between 6 and 10eV fade in strength. In Fig. 4.8b, the structure becomes less intense with a general movement to lower energies (although this may well be due to a change in contact potential difference between target and analyser grids). After the monolayer thickness is reached (Fig. 4.8c), the spectrum stabilises somewhat apart from a further general shift in energy. Although the unambiguous interpretation of these figures is not possible at this time, it is apparent that complex 'distortions' of high energy band structure are occurring with submonolayer amounts of Cs on Au.

Fig. 4.9 shows a set of slow peak spectra taken from the Au surface after 3.61 monolayers of Cs had been deposited. Since no gold Auger peaks were observed on this surface, the spectra were considered to have originated from a Cs surface (as described in section 4.4). The series of spectra show the effect of E_p variations. The strongest structure is seen at lower primary energies since this is when most of the primary energy is dissipated close to the surface. However, the majority of

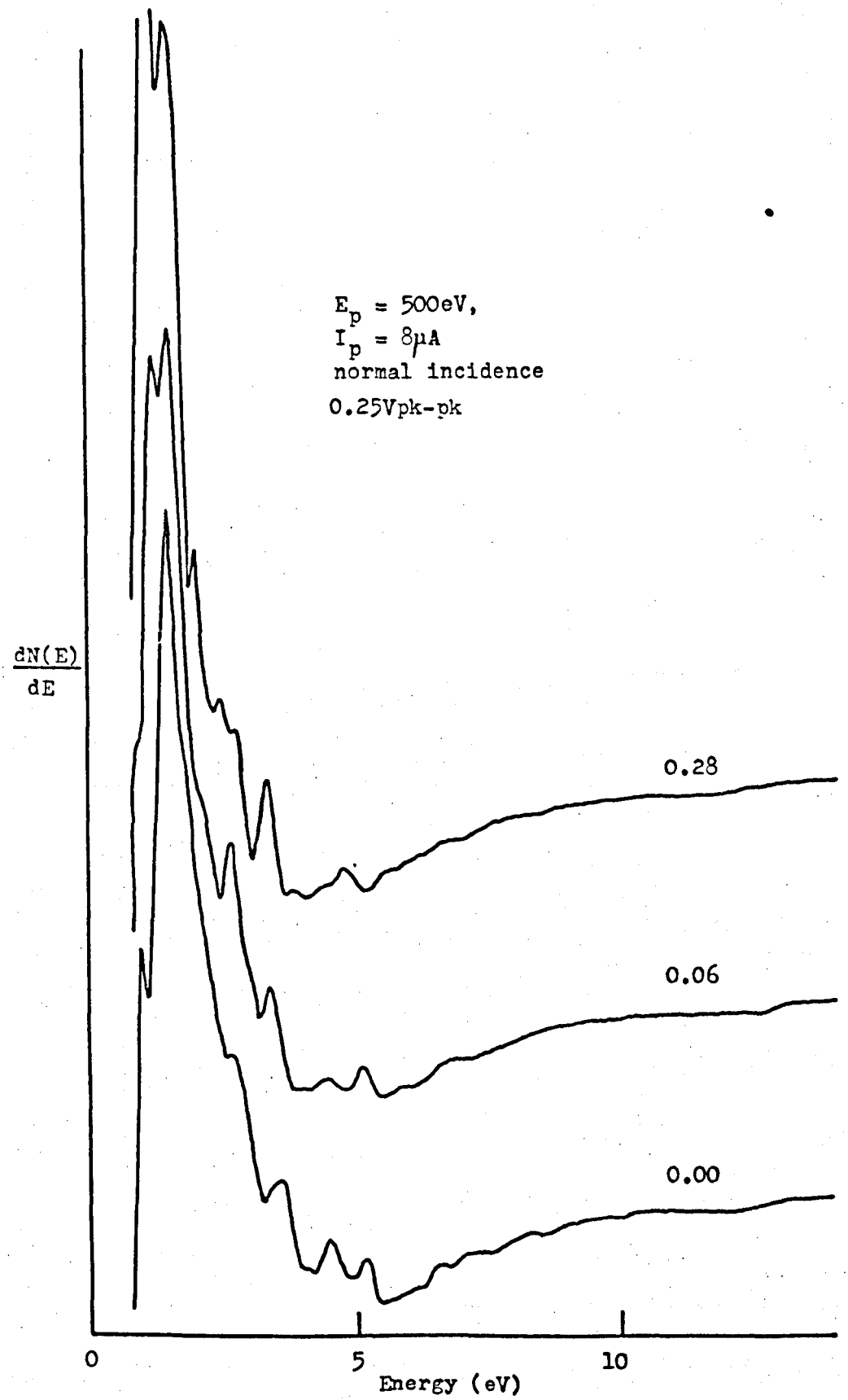

Figure 4.8a Slow peak of Au surface with Cs fractional monolayer coverage

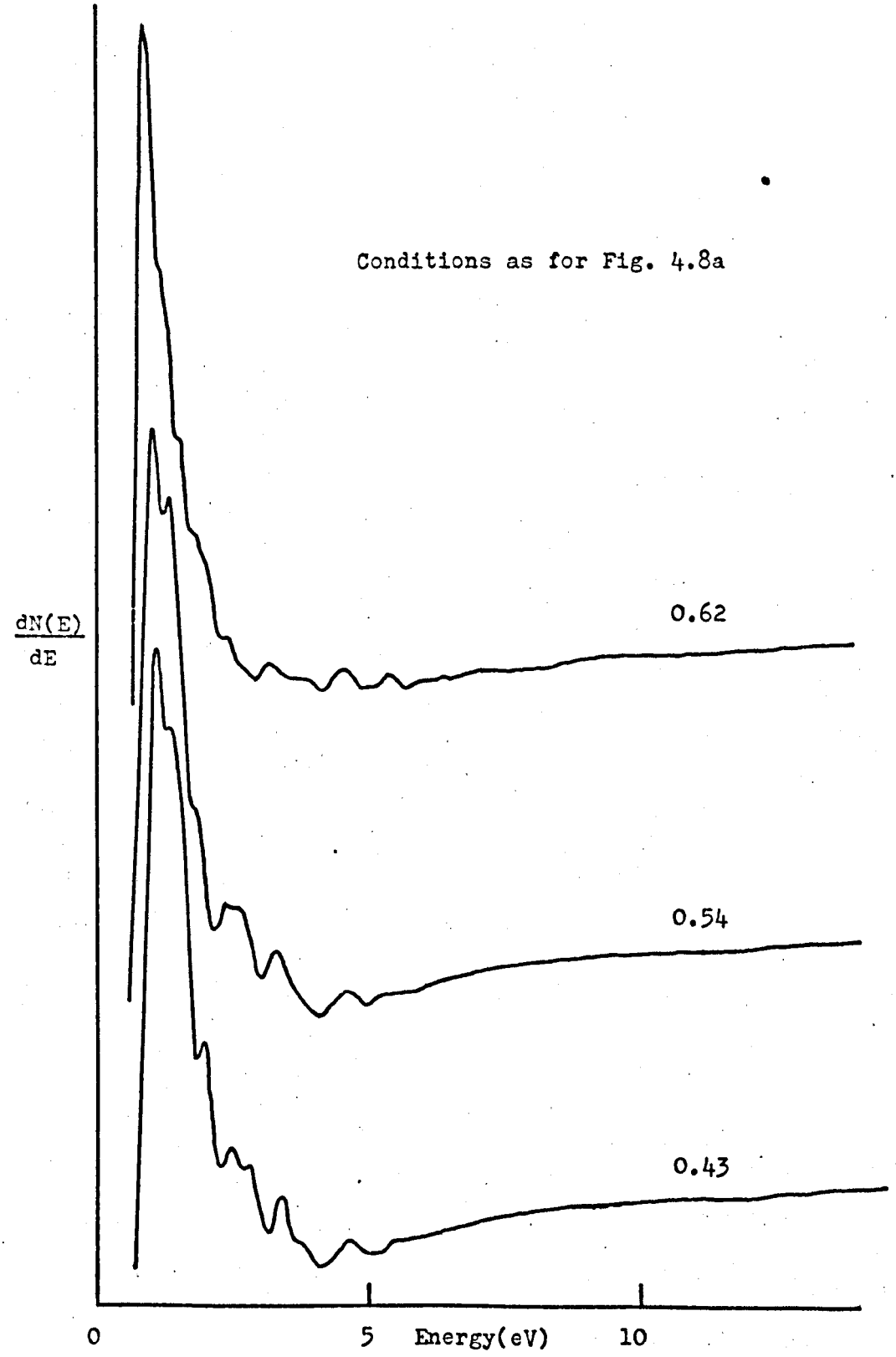

Figure 4.8b Slow peak of Au surface with Cs fractional monolayer coverage

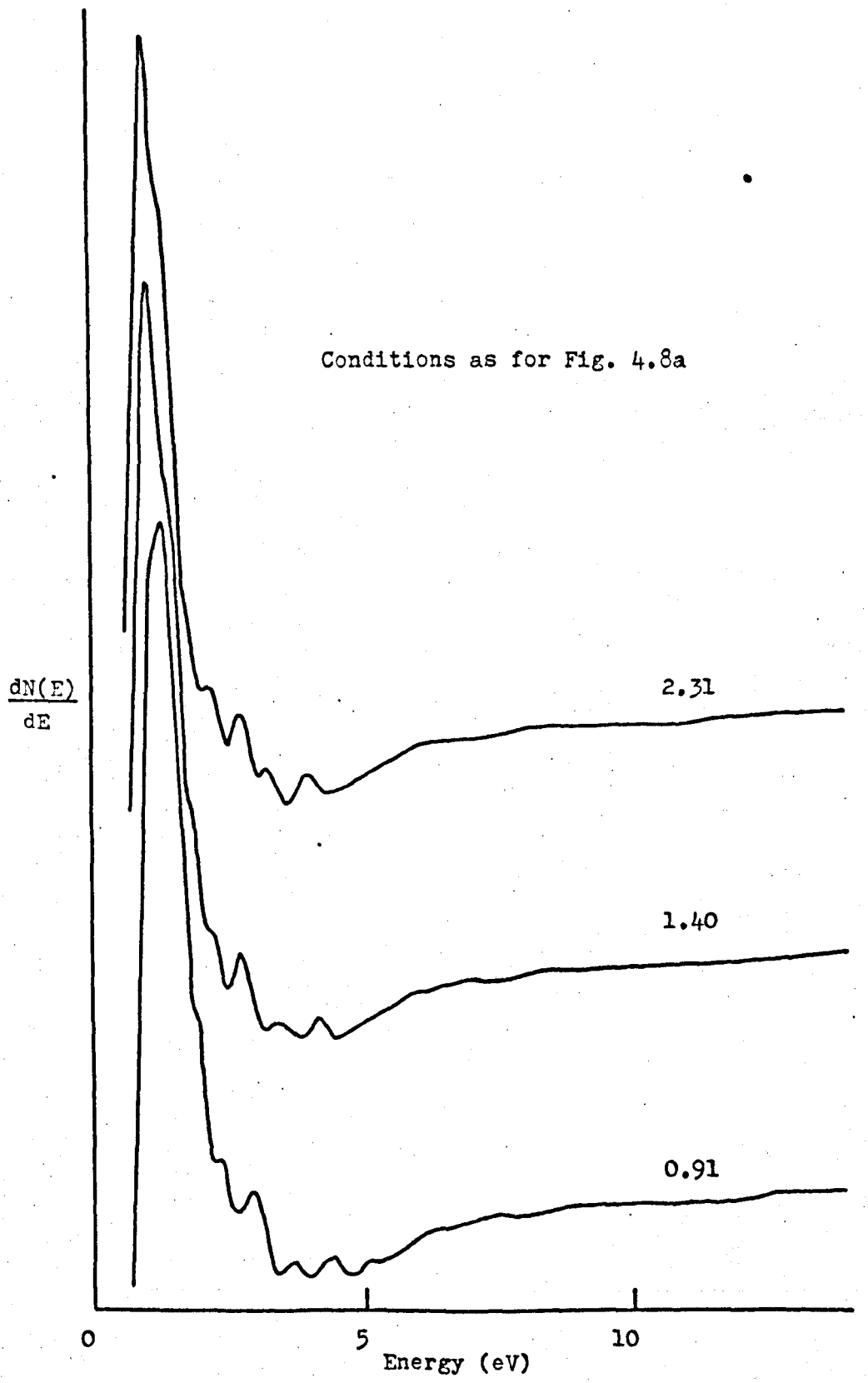

Figure 4.8c Slow peak of Au surface with Cs monolayer coverage

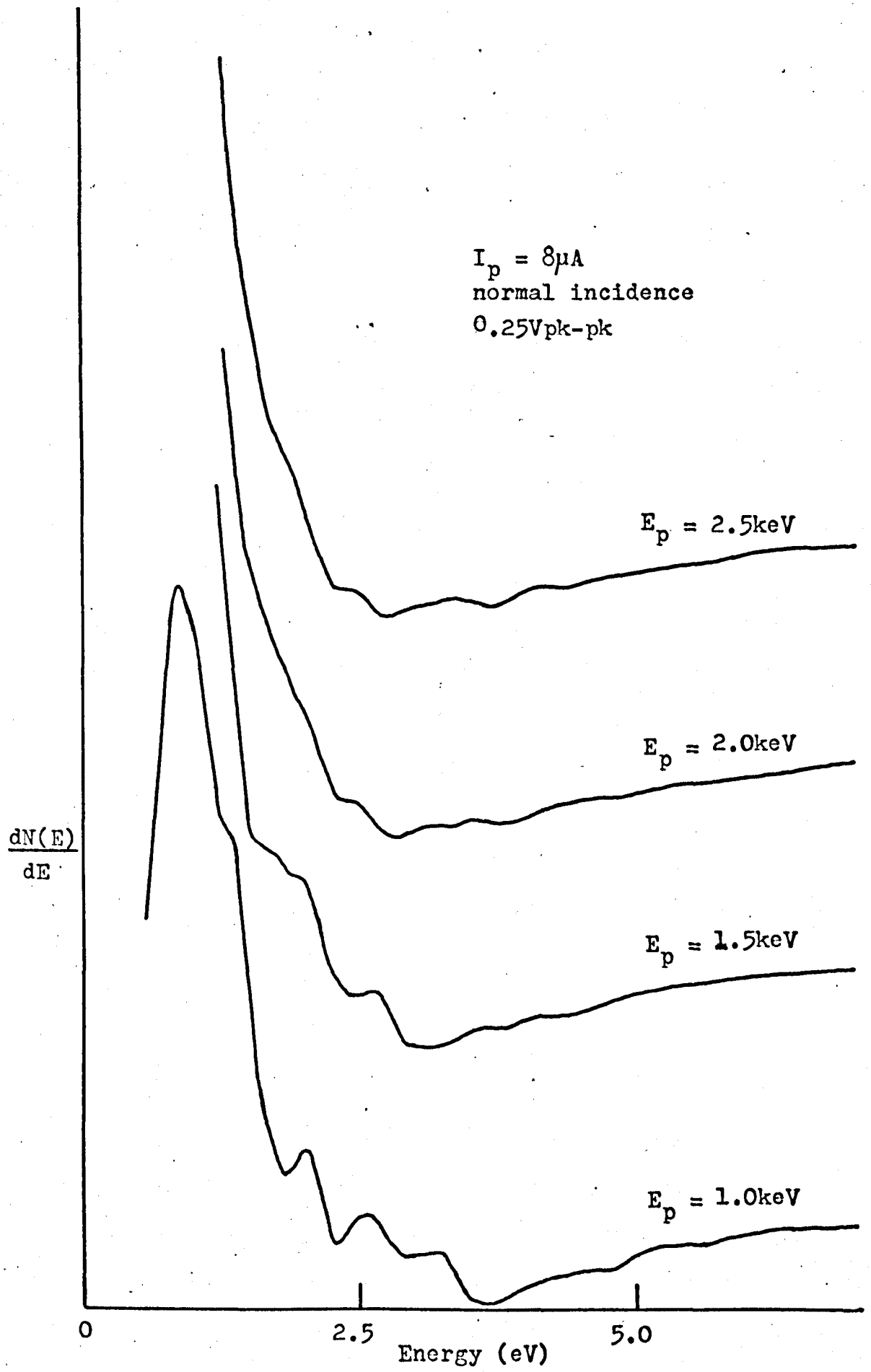

Figure 4.9 Slow peak of Cs film with E_p variation

the salient features are reproduced throughout the plots, although slight energy shifts do occur due to the changing background slope. The energy values in Table 4.2 were taken from these plots.

4.6 Discussion and Conclusions

The discussion of the foregoing results will be divided into three areas; firstly, quantitative AES and escape depths; secondly, AES of cesium and thirdly, slow peak spectroscopy of the Cs on Au system.

The steady growth of the Cs Auger signal, as submonolayer quantities of Cs are deposited, indicate the extreme surface sensitivity of AES. An approximate linear relationship has been found between the measured Auger peak-to-peak signal height and submonolayer coverage. Thomas and Haas[61,62] and Macrae[139] also found that the relationship was only approximate in the case of Cs deposition. Reasons for these deviations may be threefold. In the case of Thomas and Haas, there was interference from a tungsten Auger peak close to the Cs peak. Also there is the possibility that the sticking probability approaches zero as the coverage increases, since it is known[139] that substrate cooling is necessary in order to condense many layers of Cs. Thirdly there is a possibility that the Auger transition rate for the $N_{4,5}O_{2,3}O_{2,3}$ process in Cs, may be affected as coverage increases. Both Todd[142] and myself have independently considered this latter explanation, in the following manner.

Macrae et.al.[139] and Thomas and Haas[62] have observed the existence of two types of Cs structure on a tungsten surface. An ionic structure was observed up to about 0.5 monolayer and thereafter, a hcp structure was seen as specified by LEED patterns. The occurrence of this 'duo-layer' has been contested by Fehrs et. al.[143] who concluded that Macrae et. al.s' surfaces were probably contaminated. However, it must be pointed out that Macrae et. al. did use AES whilst Fehrs et. al. did not; a point apparently neglected by Fehrs et. al. If we can therefore make the assumption that such a 'duo-layer' does exist, it seems likely

that this structural change could well influence the Auger electron transition rate for the $N_{4,5}O_{2,3}O_{2,3}$ Auger electron in Cs. The $O_{2,3}$ level of Cs should be strongly affected by a structure change, since the level is only about 12eV below the Fermi level and in effect forms part of the valence band. A change in the valence band density of states could well alter the Auger transition rate for the $N_{4,5}O_{2,3}O_{2,3}$ Auger electron.

If we now refer to the calibration curve of Fig. 4.4, we see an apparent discontinuity at about 0.7 monolayer coverage, which could correspond to the hcp structure transition. Obviously further work is needed in this area, in order to establish whether Auger spectra are indeed sensitive to surface structure.

The detection limit for Cs on Au under the stated conditions, was found to be about 1-2% of a monolayer. This figure is in reasonable agreement with detection limits given by other workers[58,62] using retarding potential analysers. If a cylindrical mirror analyser were used, this figure could easily be lowered by an order of magnitude.

A study of the decrease in the substrate's Auger peak with adsorbate coverage can yield information on the mean free path and the maximum escape depth of Auger electrons in the adsorbed overlayers. The maximum escape depth is an important parameter since it is this thickness of the overlayer that one analyses in AES. The coverage corresponding to the complete extinction of the substrate's Auger peak gives the maximum escape depth of these electrons. Such a peak extinction is seen in Fig. 4.4 at about 2.2 monolayers of Cs ($\sim 7\text{Å}$, assuming the thickness of one layer equals the diameter of the Cs ion). In relation to Fig. 1.5, this depth appears large but it is in agreement with Thomas and Haas's[62] findings. The re-evaporation problem at larger thicknesses may well explain this exaggerated value for escape depth.

TABLE 4.4

Energy Level Diagram for Cesium (in eV)

	'B&B'* Z	'B&B'* Z+1	Siegbahn[145] Z
M_4	739.5	796.1	
M_5	725.5	780.7	
N_1	230.8	253.0	
N_2	172.3	191.8	
N_3	161.6	179.7	164
N_4	78.8	92.5	81
N_5	76.5	89.9	79
O_1	22.7	39.1	25
O_2	13.1	16.6	15
O_3	11.4	14.6	14
V			4

* 'B&B' - Bearden and Burr[144]

We will now move on to discuss the AES of cesium. The experimentally observed Auger electron peaks together with their assignments are given in Table 4.3. The table indicates that agreement between

TABLE 4.3

Observed Auger Electron Peaks of Cesium (energy in eV)

Present work	Desplat[140]	Thomas and Haas[62]	Palmberg[49]	Assignment	Calculated energy
45.3	43 45.8 48.4	47	47	$N_{4,5}O_{2,3}O_{2,3}$	48.5
58		57		$N_{4,5}O_{2,3}V$	57
61	62	62	(+small peaks from 400-700eV)	$N_{4,5}VV$	65.2
67	-	69		$N_{4,5}VV$	
560	-	555 566	563 575	$M_5N_{4,5}N_{4,5}$ $M_4N_{4,5}N_{4,5}$	552.5 566.5

different workers is not good which is no doubt partly due to the difficulty of obtaining a clean surface of Cs. However some agreement is apparent between the results of myself and Thomas and Haas.

The assignments were derived from the energy level diagram seen in Table 4.4. Equ. (2) (Chapter 1) was used to obtain the calculated Auger electron energies, using a ϕ_A correction of 4.5eV. One can expect most of the low energy Auger transitions to be initiated by $N_{4,5}$ holes due to Coster-Kronig processes, and in fact this assumption leads to quite good agreement with observed energy values. Hence the 58eV peak is not thought to originate from the N_3 vacancy, as suggested by Thomas and Haas[61]. The triplet of peaks near 47eV observed by Desplat[140], were not observed by any other workers and the triplet may well be due to tungsten contamination from his substrate (tungsten has Auger peaks at

39 and 49eV). Also, Desplat[140] has critised the work of Thomas and Haas[61], arguing that the 58eV peak is due to partially oxidised Cs. In Fig. 4.6 the oxygen peak is seen to be very weak though the 58eV peak in Fig. 4.5 is quite strong. These particular findings tend to support Thomas and Haas[61], and we must therefore conclude that Desplat[140] could well have had other contamination problems apart from possible tungsten contamination.

To sum up, we have found that submonolayer quantities of Cs on Au have a significant effect on high energy band structure, in the vicinity of the surface. The results portrayed in Figs. 4. 8a-c, tend to confirm the doubts of Christensen and Seraphin[137], concerning the generally accepted belief that monolayers of alkalis, simply reduce the work function value of the surface without altering band structure. Such techniques are frequently used in UPS when investigating band structures, but the consequences of alkali coverage effects are rarely considered. In particular, Fig. 4.8a shows that a Cs concentration as low as 0.06 monolayer, has an observable effect on slow peak structure. Therefore one cannot assume that such coverages will simply amplify existing structure, without serious distortions.

The slow peak spectra of Cs, as illustrated in Fig. 4.9, could not be compared with the results of other workers, due to the lack of data in the literature. However, the observed multiple peaks indicate that plasmon effects if present, must be accompanied by band structure effects, with a possible contribution from the underlying gold substrate. Unfortunately, a search through the literature for a high energy band structure for Cs was fruitless, and it was not possible therefore to correlate observed peaks with the calculated critical point energies.

CHAPTER 5

AUGER ELECTRON SPECTROSCOPY OF ZIRCONIUM

5.1 Introduction

Zirconium is known to have a strong chemical affinity for many elements and one might expect to observe many interesting surface properties of the metal using AES. Also, so far as is known, only Dooley and Haas[56] have published what they claim to be a 'clean surface' Auger electron spectrum of zirconium.

In addition, zirconium is known to have a gettering action in UHV, and commercially available bulk getter pumps (S.A.E.S. getters, Milan, Italy) utilise an alloy of aluminium and zirconium to obtain a pumping action. A typical bulk getter material is ST 101 (from S.A.E.S.), composed of 84% zirconium and 16% of aluminium. Harris and Pattinson[146] made a study of the surface composition of such an alloy but did not obtain a clean surface or discuss the segregation and gettering action of the material. Hence, some work was required to try to understand how such a bulk getter system might work.

Nuclear engineering has found many uses for zirconium especially when alloyed with small quantities of other metals (e.g. Sn, Ni, Fe in the cases of Zircaloy 2 and 4). Dooley[51] was able to correlate the ductility properties of Zircaloys with zirconium carbide formation at high temperatures, using AES. Such observations of surface chemical properties appear to be extremely useful in the diagnosis of alloying problems.

Two basic methods were tried in order to obtain clean surfaces of zirconium. Firstly, a bulk sample of zirconium (from Metals Research Ltd., purity 2N5) was analysed after heating in UHV and in active gases. Secondly, zirconium was evaporated from tungsten wire baskets onto the zirconium substrate in UHV, and the thin film was analysed using AES.

5.2 Bulk Zirconium

5.2.1 Heating in Ultra-high Vacuum

The bulk zirconium target was in the form of a thick foil of size 2.5 x 2.5 cm. This foil was spot-welded onto the stainless steel target rod and was then inserted into the UHV chamber. Prior to insertion, the target was passed through a de-greasing cycle in an ultra-sonic bath using carbon tetrachloride, acetone and de-mineralised water respectively. Three tungsten wire baskets were also filled with zirconium foil pieces and were out-gassed and vacuum-melted in a separate coating unit, prior to insertion in the UHV chamber. A chromel/alumel thermocouple was spot-welded to the back of the zirconium foil in order to measure its temperature. The thermocouple leads were fed to a radial feedthrough situated on the target tube of the chamber.

After baking, the pressure in the chamber fell to the 10^{-10} torr region and an Auger spectrum was taken from the foil's surface. Only two major peaks were seen at this stage; at 268 at 508eV, corresponding to carbon (KVV Auger peak) and oxygen (KVV Auger peak) contamination respectively. With radiant heating from the 1kW projection lamp filament, the zirconium foil reached 600°C and was held there for several minutes. The heater was then switched off and a complete Auger scan was taken which is shown in Fig. 5.1. This relatively mild heating reduced the carbon and oxygen Auger peaks so that some low energy Auger peaks were then visible under high gain. The peaks at 89, 113 and 148eV were thought to originate from zirconium whilst those at 181, 269 and 510eV were due to chlorine ($L_{2,3}VV$ Auger peak), carbon and oxygen respectively. Also sulphur probably represented a component of the 148eV peak since the $L_{2,3}VV$ Auger peak of sulphur lies at about 149eV. The carbon peak at this stage showed no evidence of low energy Auger satellite peaks as seen when carbide formation occurs[80]. Presumably, the carbon was therefore of graphitic nature.

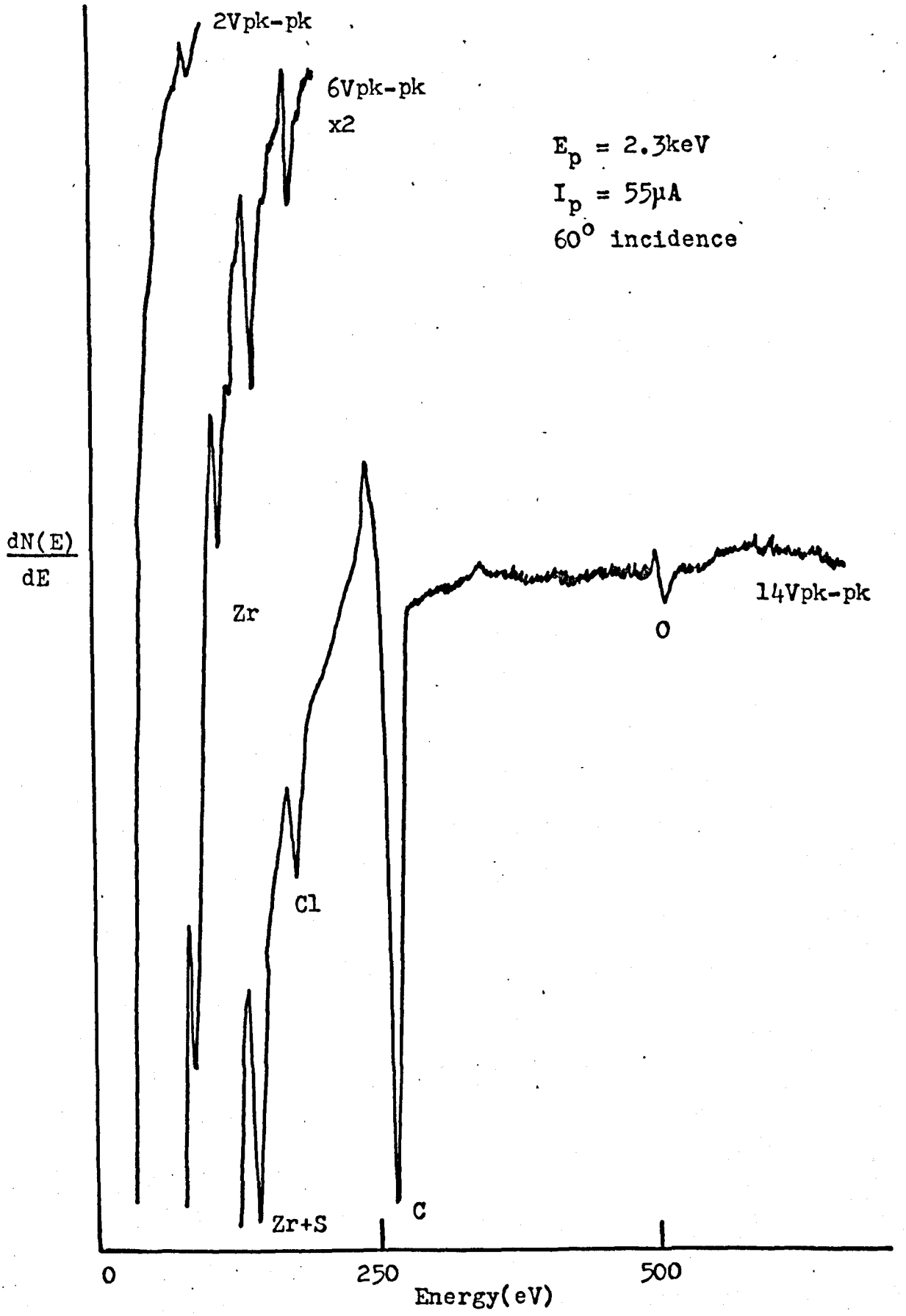

Figure 5.1 Auger spectrum of heavily contaminated Zr

Heating the target to above 600°C, required the use of electron bombardment heating in addition to radiant heating. The 1kW projection lamp filament was powered through a 'Variac'-driven isolating transformer which had its centre-tap output earthed. This arrangement effectively kept the filament close to earth potential. A variable high positive voltage (0-3kV) was placed on the target by adjusting the voltage input to an ion-pump power supply (Ferranti FPD-8) connected to the target. This high positive voltage on the target attracted electrons from the filament and electron bombardment ensued. Typical operating conditions necessary to reach a target temperature of 1100°C were: Target voltage, +2kV and emission current, 50mA. However with this arrangement, it was not possible to simultaneously heat the target whilst doing AES analysis, hence all the following spectra were taken as quickly as possible (5-10 minutes) after flashing the target.

Fig. 5.2 shows an Auger spectrum of zirconium after the surface (described by Fig. 5.1) had been flashed for one minute at 850°C, using the procedure just out-lined. The energy scale has been expanded in order to view the spectrum more easily. It may be seen that the small peaks of Fig. 5.1 are much more pronounced and further small peaks have appeared at 72, 124 and 172eV. All of these peaks were thought to originate from zirconium. The oxygen Auger signal has not changed substantially although that of carbon has considerable reduced in size and a small low energy satellite peak has appeared at 250eV. This latter event may well be due to a carbide formation. The peak at 181eV, due to chlorine, is still present however. Sulphur has become the main contaminant after flashing, with its large Auger peak at 148eV. It is worth noting at this stage that some low energy discontinuities are present at about 22, 33 and 45eV. Complete Auger scans from 0-1,000eV did not reveal any further energy structure. Several flashings for periods of minutes at 850°C, did not give spectra with any substantial differences to Fig. 5.2.

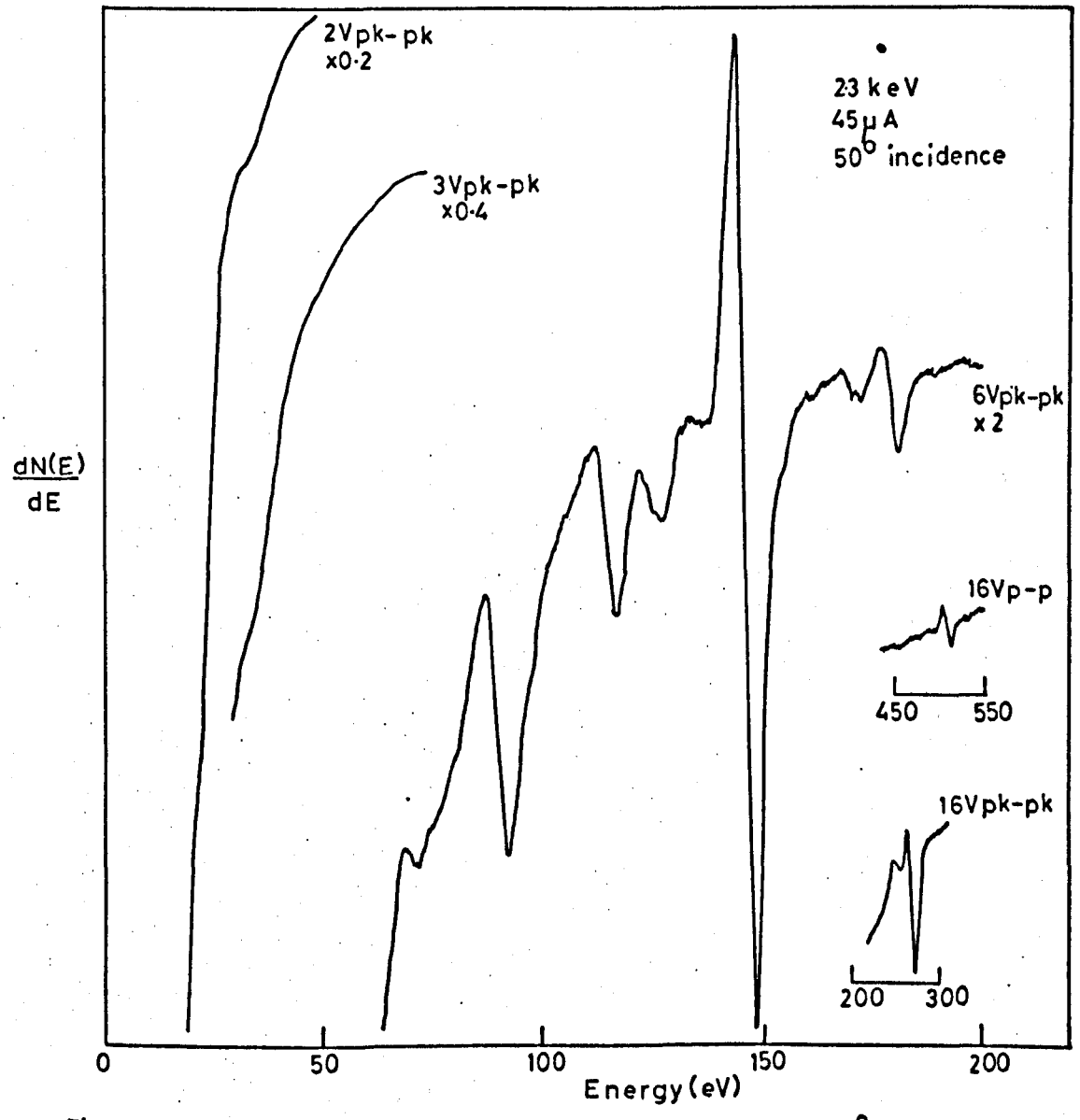

Figure 5.2 Auger spectrum of Zr after flashing to 850°C

Upon raising the flashing temperature to 950°C, several important changes did occur, as seen in Fig. 5.3. Firstly, a small resolved peak appeared at 22eV and there was a general increase in the strength of all peaks apart from those of carbon and oxygen. The higher temperature had apparently caused more carbon and oxygen to diffuse into the bulk giving an increase in strength of the remaining Auger peaks. Chlorine (180eV) has become a major contaminant with its peak size increasing by almost an order of magnitude. Since chlorine is expected to desorb well below this temperature[56], it seems likely that it has chemically combined with the zirconium surface. Further flashings at 950°C did not significantly reduce this chlorine Auger peak, so it was considered worthwhile at this point to try to remove chlorine by flashing in hydrogen.

5.2.2 Heating in Active Gas Ambients

Hydrogen was chosen as the active gas since it was thought that it might chemically combine with sulphur and chlorine on the zirconium surface, to produce the gases of H_2S and HCl which could then be pumped away. A hydrogen leak was therefore set up as described in sub-section 3.3.4, at a background pressure of 8×10^{-7} torr. Fig. 3.13 shows a typical mass spectrum of the residual gases in the chamber just before the zirconium was flashed. No mass spectra were taken during the flashing due to time limitations and background pressure changes whilst the flashing occurred.

At this stage of the experiment, the low energy Auger peak at about 22eV gradually disappeared after about an hour of exposure in UHV. Hence, after the flash at 950°C in the hydrogen ambient, Auger spectra were taken as quickly as possible (in the order of a few minutes), starting at low energy and working upwards towards the contaminant energy range. By this procedure it was hoped to minimise spectral distortions due to contamination build-up, which has a stronger effect at the lower Auger

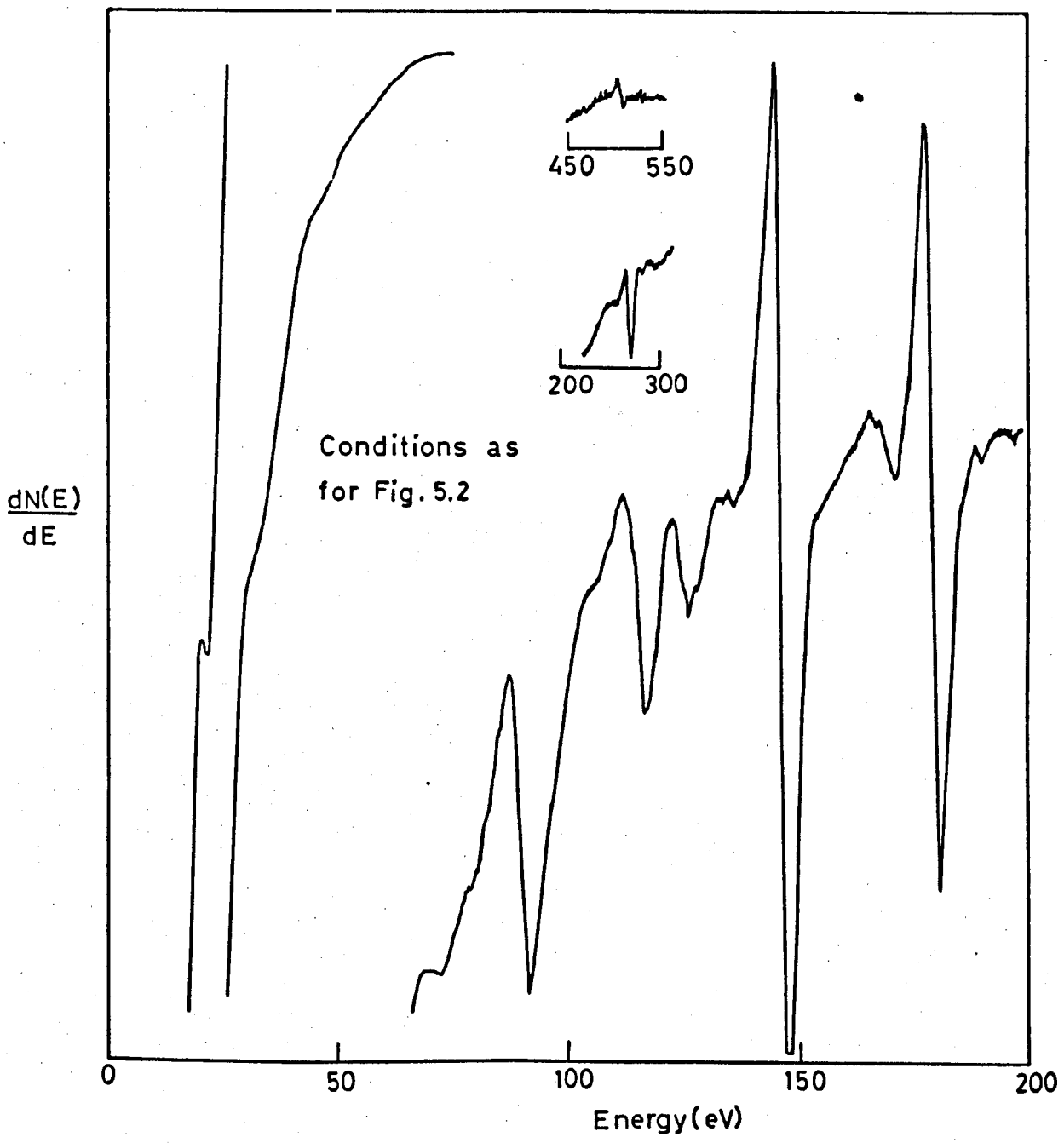

Figure 5.3 Auger spectrum of Zr after flashing to 950°C

electron energies. In fact the strength of the 22eV peak gave a good indication as to the level of contamination present on the surface, and it will be seen later that few authors mention, or observe this peak strongly, indicating possible contamination problems on their surfaces.

The results of the flashing in hydrogen can be seen in Fig. 5.4. The peak at 22eV is starting to increase in size due to the reduction of the carbon and oxygen Auger signals to near noise level. No new peaks are seen in the spectrum, but the sulphur peak has slightly increased in size. Further flashings in hydrogen up to 1050°C, did not reduce the chlorine peak height. At this point it was concluded that a dynamic equilibrium had been set-up in which the sulphur and chlorine were diffusing as quickly to the surface, as they were being removed from the surface by reaction with hydrogen. In order to lower the diffusion rate, the surface characterised by Fig. 5.4, was flashed at 700°C (i.e. a somewhat lower temperature) in the usual hydrogen ambient.

Fig. 5.5 appears to justify the previous conclusion, since both the sulphur and chlorine peaks have now disappeared. The original peak at 148eV has attenuated and shifted to 146eV and it is concluded that this peak is now a true undistorted zirconium Auger peak. Also the strongest peak in the spectrum is now at 92eV, instead of 148eV, which indicates the lack of sulphur contamination. Unfortunately, both carbon and oxygen have returned to the surface, causing the 22eV peak to all but disappear. The Auger peak of carbon is again seen to have low energy satellite peaks at 250 and 255eV, possibly indicating carbide formation.

After these treatments it was hoped that the bulk concentrations of both sulphur and chlorine would be lower, so that the surface segregation problems of these elements would be reduced. The target was therefore flashed again in UHV at 950°C and the Auger spectrum of this surface is shown in Fig. 5.6. Both sulphur and chlorine have returned but not so

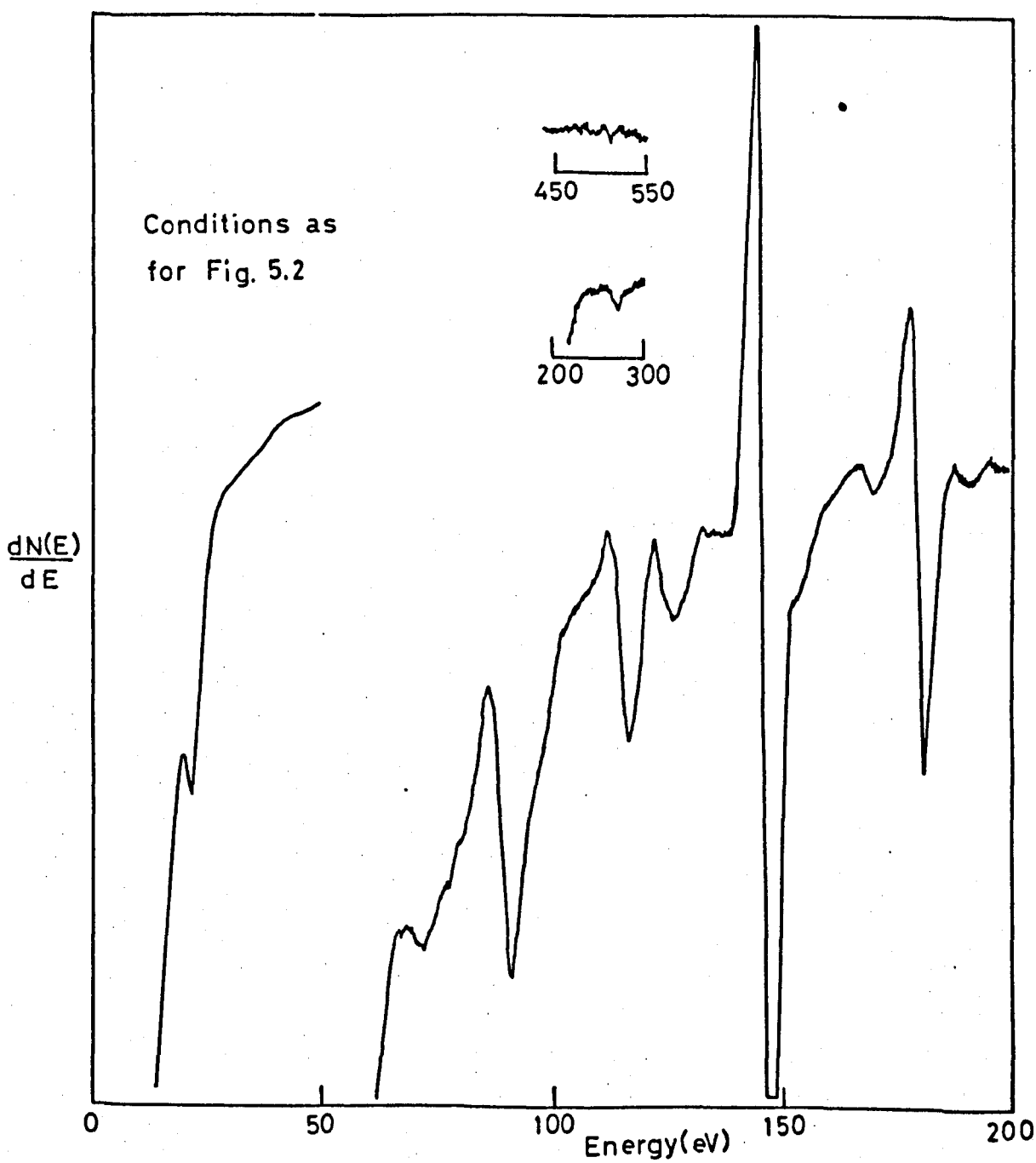

Figure 5.4 Auger spectrum of Zr after flashing to 950°C in H_2

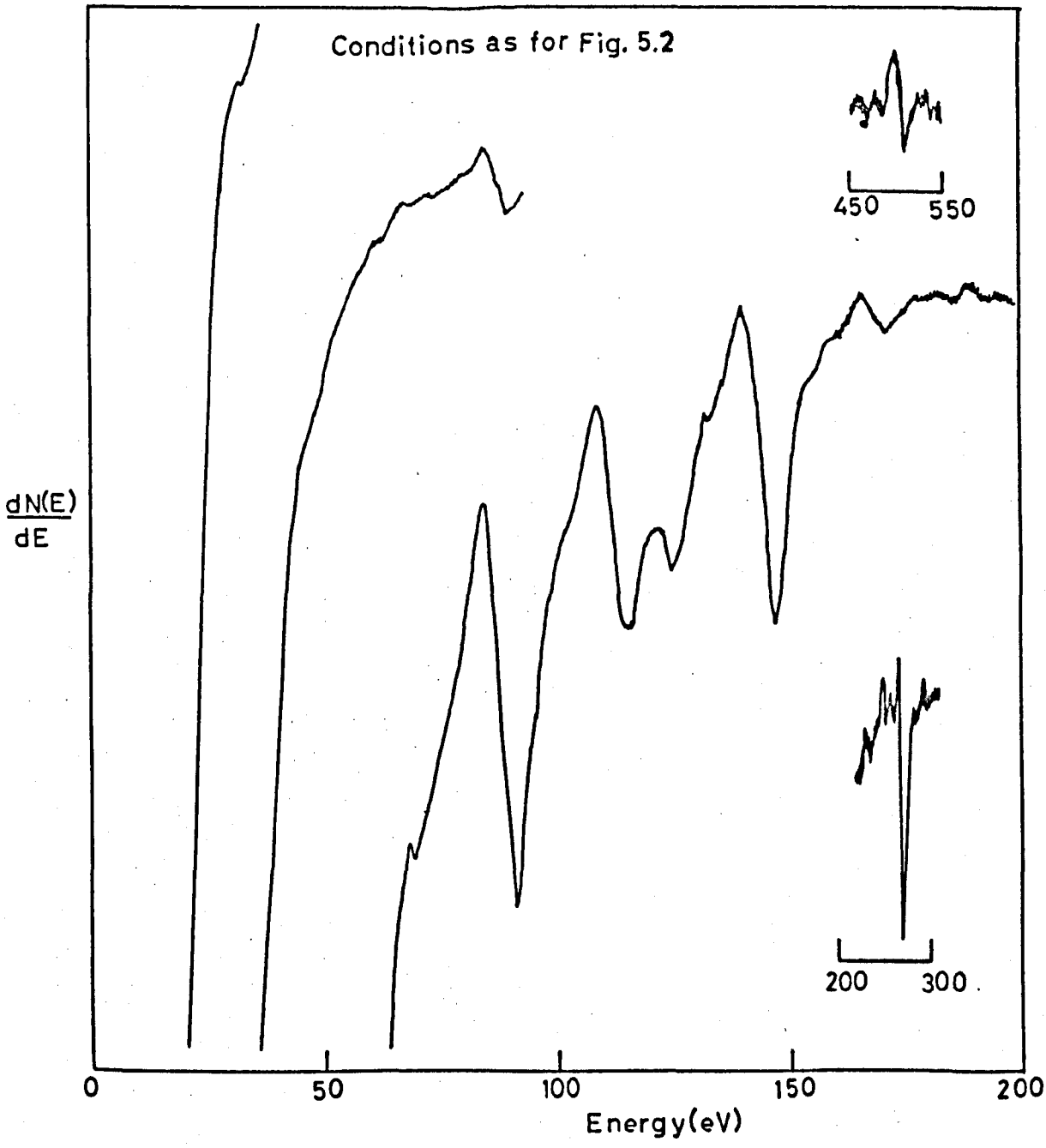

Figure 5.5 Auger spectrum of Zr after flashing to 700°C in H_2

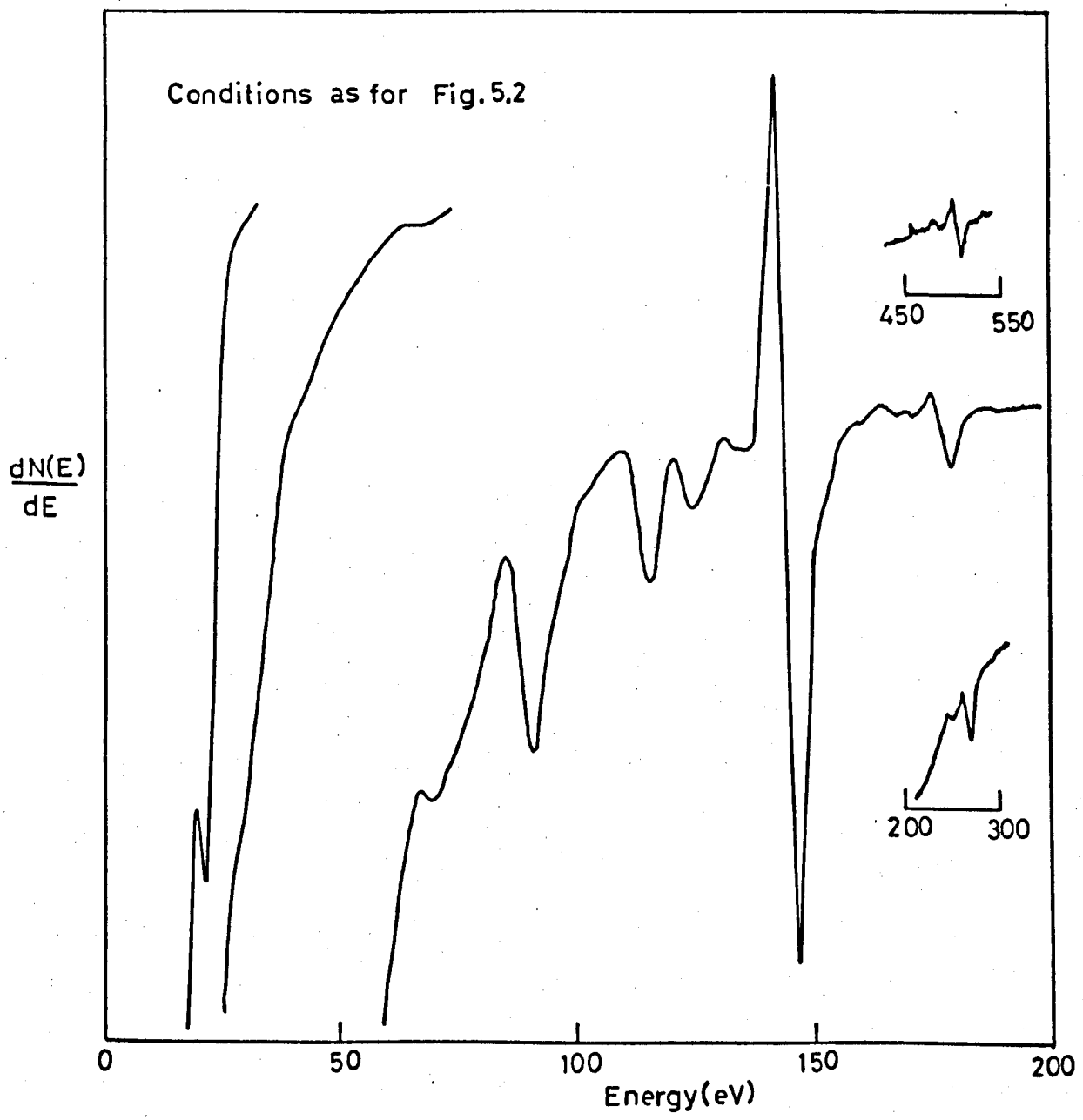

Figure 5.6 Auger spectrum of Zr after a further flashing to 950°C

strongly, especially in the case of chlorine. In keeping with the previous results, carbon and oxygen have reduced in size allowing the observation of the strongest 22eV peak so far seen.

A further flashing of this surface at 950°C in hydrogen, completely eliminated the carbon and oxygen Auger peaks to below the noise level, as seen in Fig. 5.7. This caused a further increase in the size of the 22eV peak. Chlorine was more successfully removed on this occasion, leaving a small peak at 180eV to the right of the 172eV zirconium Auger peak. The remaining zirconium Auger peaks occurred at 72, 92, 116, 126 and 147eV.

Fig. 5.7 represents the cleanest surface that was observed for a bulk zirconium sample; the only contaminants being sulphur and chlorine. It was this surface that was allowed to oxidise from the residual oxygen (or CO) present in the UHV chamber. Unfortunately, zirconium surfaces were found to suffer from severe electron beam stimulated adsorption effects which meant that the act of surface analysis was substantially affecting the Auger spectra. When the primary electron beam was deflected on to a fresh part of the target, after a period of a few hours on another area of the target, it was found that the two sets of Auger spectra showed significant differences. This process could be repeated many times over the target and a typical result is shown in Fig. 5.8. The upper dotted curve represents an area where the electron beam has been landing for a few hours, and the lower continuous curve, an area which has only been exposed to the beam during the spectral measurements (about 10 minutes). The upper spectrum shows considerable contamination from oxygen and carbon and an attenuation of the 148eV Auger peak. Also, a new peak has developed at 139eV. Some contamination from carbon and oxygen is also present on the fresh surface, but it is smaller especially in the case of oxygen.

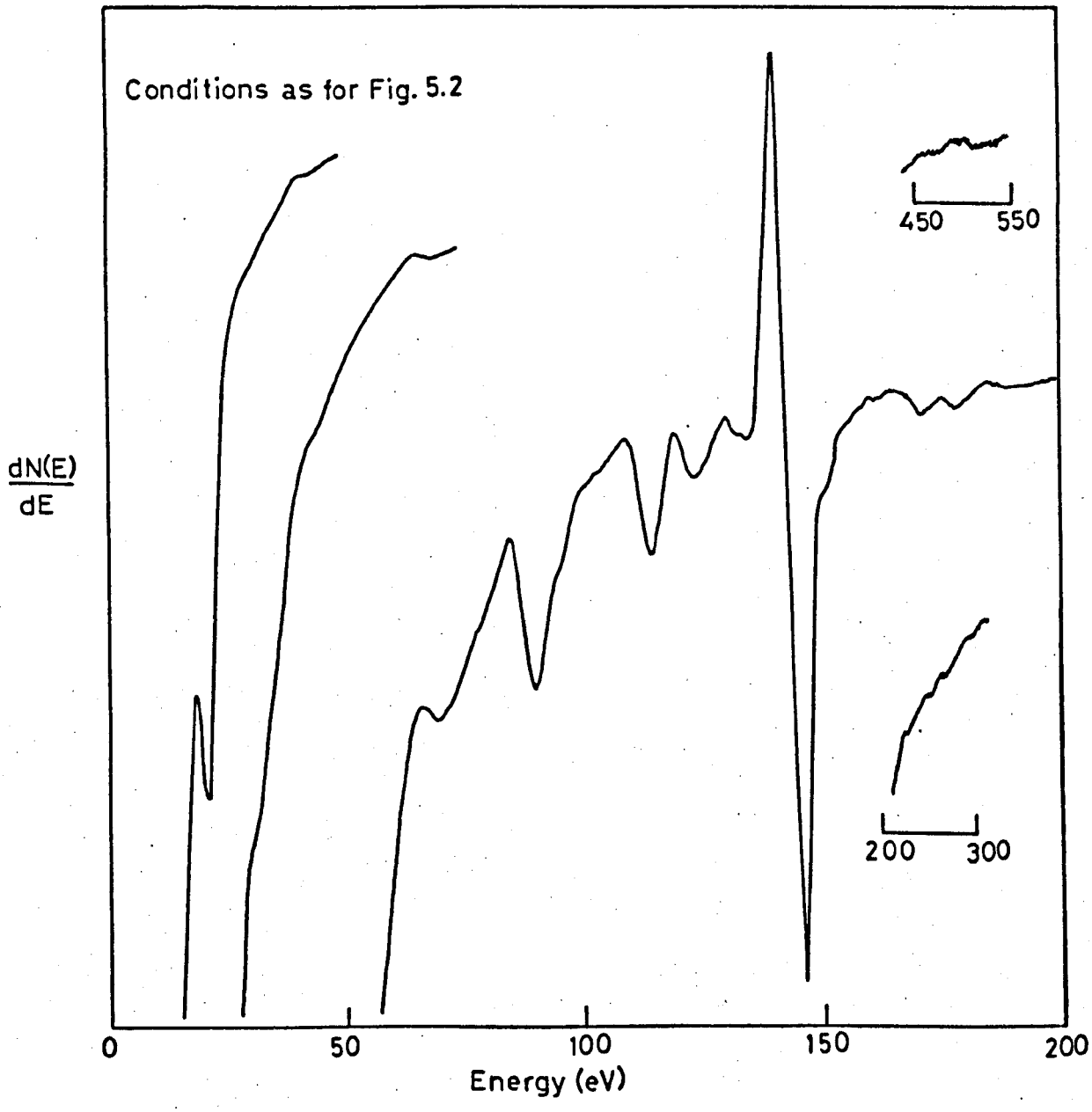

Figure 5.7 Auger spectrum of Zr after a further flashing to 950°C in H_2

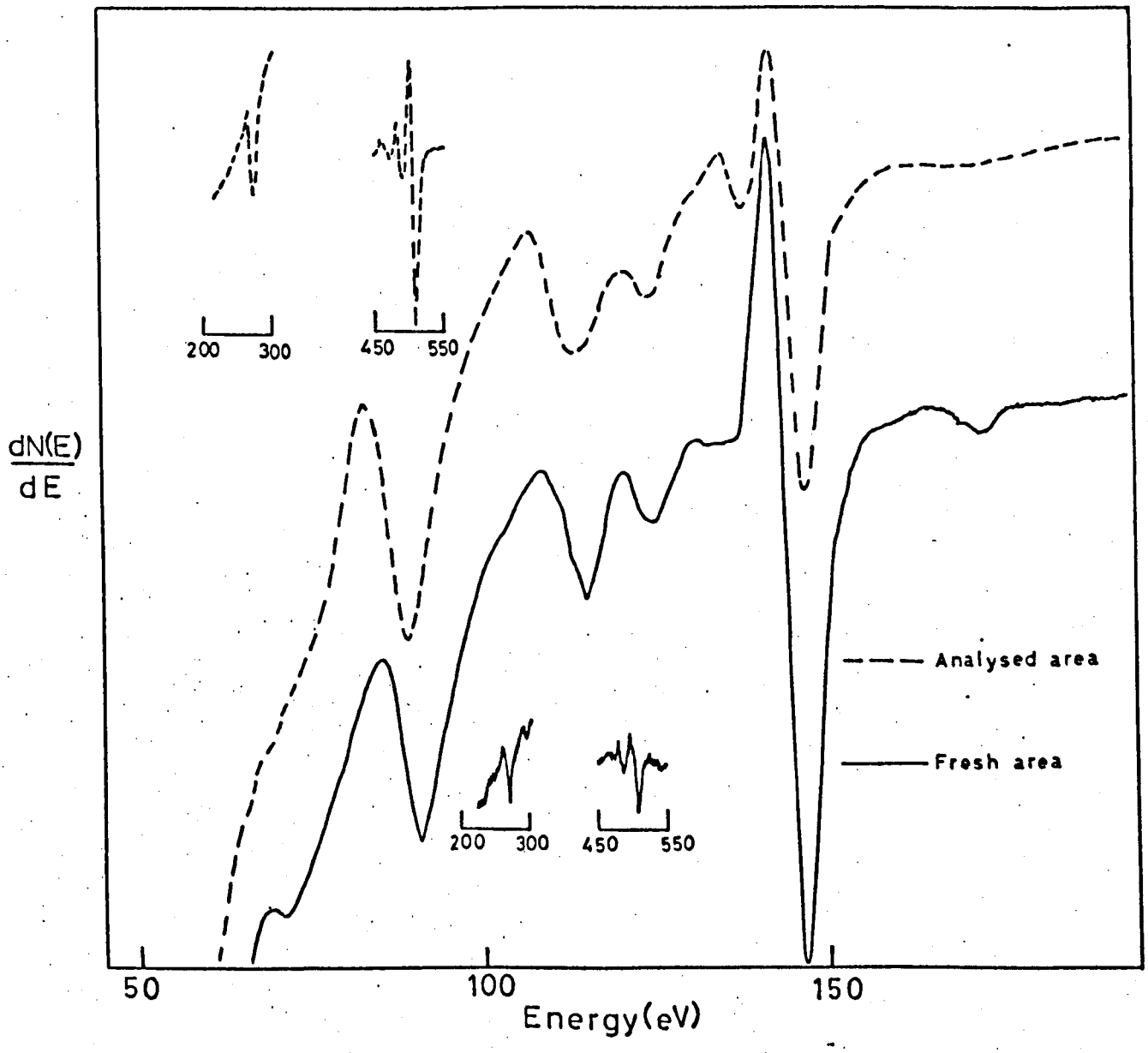

Figure 5.8 Electron beam effects on Zr surface

If one looks carefully at the two sets of spectra, one can see slight energy shifts between them. The dotted curve has peaks at 89, 113.5 and 124eV which are 1-2eV lower than in the corresponding peaks of the continuous curve. However the peak at 148eV has not shifted in energy, indicating that this peak may indeed be of a different origin to the other three peaks mentioned. These 'chemical shifts' were found to be somewhat more exaggerated when the surface was fully oxidised i.e. at the point when the oxygen Auger peak ceased to continue to grow. An Auger spectrum of such a surface is shown in Fig. 5.9. The main peak energies are at 88, 113, 139 and 147eV with the smaller peaks at 124 and 172eV being barely resolved due to contamination. Hence, the original peaks at 92, 116 and 126eV have shifted downwards between 2-4eV, upon oxidation. Also the carbon Auger peak of Fig. 5.9, now shows no evidence of low energy satellite structure.

5.3 Thin Film Zirconium

Three tungsten wire baskets were out-gassed at about 2,500°C in a commercial coating unit. Pieces of zirconium foil (purity 2N5) were then added to the baskets, and the zirconium was vacuum-melted, in a vacuum of 10^{-5}torr. The three baskets were then placed in the UHV chamber where they acted as three collimated sources for zirconium. Evaporations were performed at a filament temperature of about 2,000°C, onto the zirconium target.

Carbon and oxygen were found to be the main contaminants in the first few films deposited. Eventually after about six evaporations over a period of days, the carbon and oxygen Auger signals were reduced to low levels and the zirconium Auger spectrum came up strongly, as shown in Fig.5.10 These zirconium Auger peaks have been tabulated, along with those from the bulk zirconium (Fig. 5.7) and oxidised zirconium (Fig. 5.9), and are shown in Table 5.1.

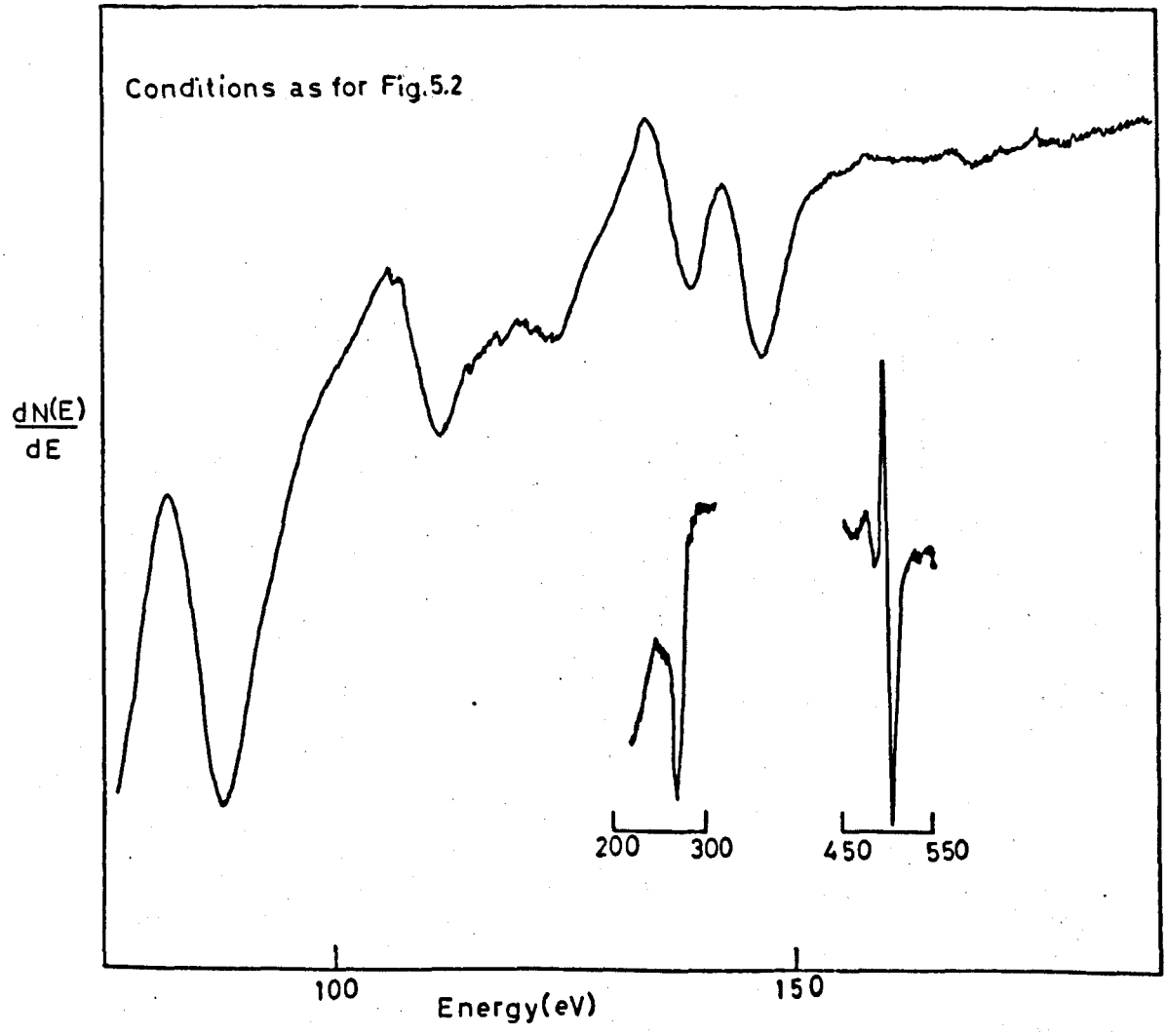

Figure 5.9 Low energy Auger spectrum of fully oxidised Zr

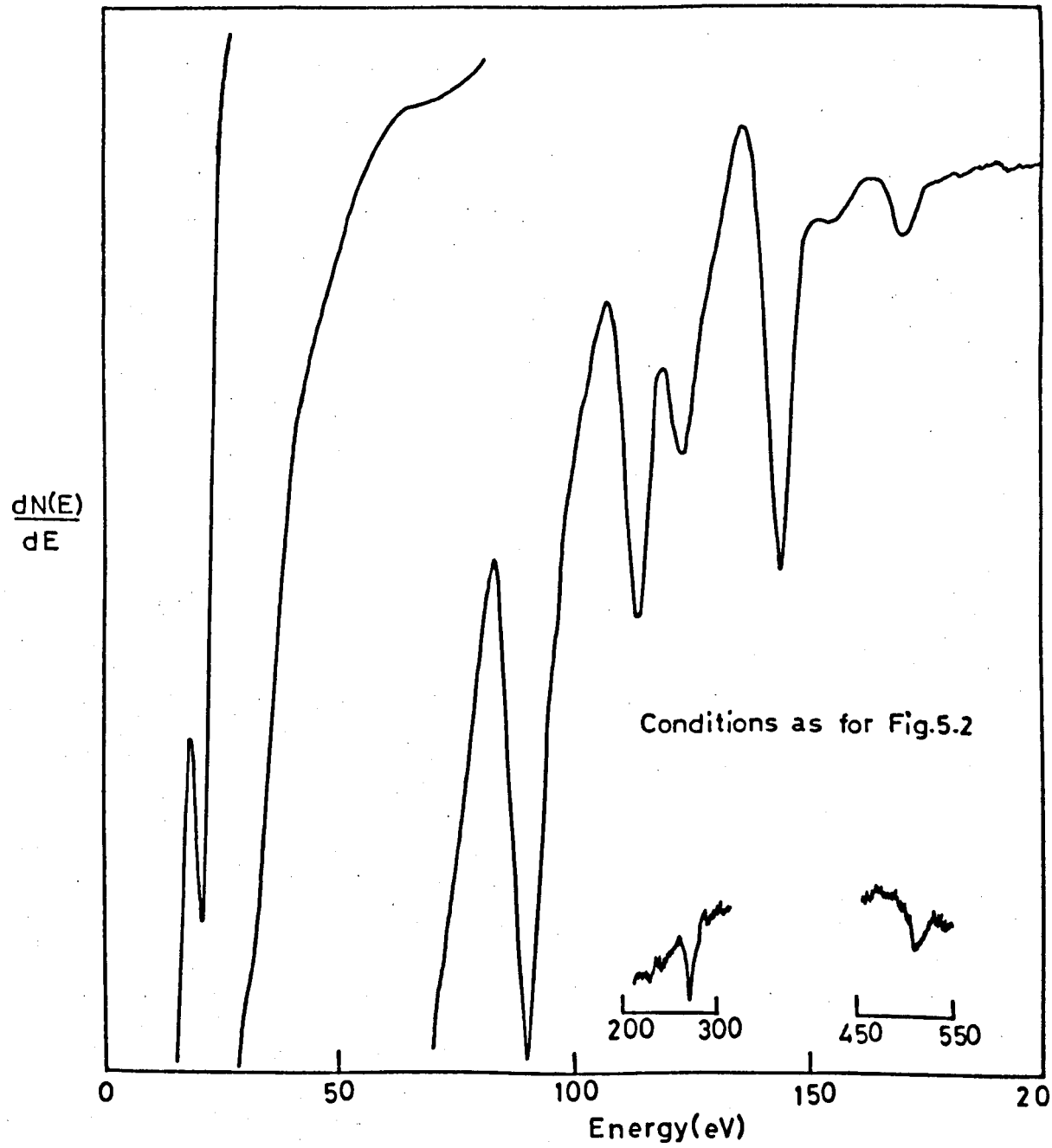

Figure 5.10 Auger spectrum of Zr thin film

TABLE 5.1

Low Energy Zirconium Auger Peak Energies Observed on Various Zirconium Surfaces (in eV)

Bulk Zr	22	33*	45*	72	92	116	126	148	173
Thin Film Zr	22	33*	45*	72	92	115	125	145	172
Oxidised Zr	-	-	-	-	88	113	124	140	147 -

*not fully resolved

Agreement between the peak values in bulk and thin film zirconium is evident apart from the peak at 148eV. It seems likely that the thin zirconium film will have a smaller contribution from sulphur and so the true zirconium Auger peak is probably represented by the 145eV peak in Fig. 5.10. The Auger spectrum seen in Fig. 5.10 represents the cleanest zirconium surface produced in this work and as shown later, this surface was less contaminated than published spectra to date. Evidence for this conclusion comes from the facts that the 22eV peak is stronger than observed previously, and also the peak at 92eV is now the strongest peak in the low energy zirconium Auger spectrum. All published spectra available to date show that the 148eV peak is strongest, indicating sulphur contamination. If we go back to Fig. 5.5, showing a surface contaminated with oxygen and carbon but not sulphur, we again see that the 92eV Auger peak is the largest peak in the spectrum.

5.4 Discussion and Conclusions

The discussion will be split-up into firstly; a discussion of the Auger spectrum of zirconium with comparisons with other workers' results and secondly, a discussion of the surface properties and segregation effects which have been observed in the previous figures.

The observation of Auger electron spectra from a clean zirconium surface is extremely difficult due to its surface reactivity with its own bulk and its gaseous environment. A comparison is made in Table 5.2 of the low energy Auger peak energies observed by a number of workers. Not all workers were able to detect the low energy Auger peaks of zirconium, presumably due to contamination problems. In fact, only Palmberg et.al.[49]

TABLE 5.2

Comparison of the Auger Peak Energies of Zr (energies in eV)

Present Work	Dooley and Haas (ref.56)	Palmberg et.al.(ref.49)	Harris and Pattinson (ref.146)	Haas et.al. (ref.47)
22	-	21	-	23
33	-	33	-	34
45	-	-	46	47
72	-	-	-	-
92	93	92	90	93
115	117	97 116	114	117
125	127	124 128	124 139	127
145	149	147	148	149
172	175	174	-	175

and myself have observed a strong 22eV peak. However most workers seem to agree that the 149-7eV peak is the strongest in their spectra, but as we have already stated, this is not the case for a sulphur-free surface; the 92eV peak then being the strongest. All workers, apart from Dooley and Haas[56], admit to having carbon and oxygen contamination. Dooley and Haas claim a clean surface of zirconium but since their 149eV peak is large and at the sulphur Auger peak value, it must be concluded that this claim is not true. Harris and Pattinson[146] claim a peak at 139eV and explain its occurrence as an Auger electron at 148eV suffering a characteristic energy loss before leaving the surface. A peak at 140eV was observed in Figs. 5.8 and 5.9, as the zirconium surface became oxidised and it is

TABLE 5.3

Auger Peak Assignments for Zirconium

Auger Transition	Calculated Energy (eV) from Equ. (2)	Observed Energy (eV)
$M_{4,5}N_{4,5}N_{4,5}$	172.6	172
$M_{4,5}N_{2,3}N_{4,5}$	144.6	145
$M_{4,5}N_1N_{4,5}$	122.0	125
$M_{4,5}N_{2,3}N_{2,3}$	114.0	115
$M_{4,5}N_1N_{2,3}$	91.3	92
$M_{4,5}N_1N_1$	66.1	72
$N_1N_{4,5}N_{4,5}$	44.8	45
		33
$N_{2,3}N_{4,5}N_{4,5}$	21.5	22

TABLE 5.4

Energy Level Scheme for Zirconium (in eV)

(from Bearden and Burr[144])

	Z	Z + 1
M_1	430.3	
M_2	344.2	
M_3	330.5	
M_4	182.4	
M_5	180.0	
N_1	51.3	58.1
$N_{2,3}$	28.7	33.9
$N_{4,5}$	0.7*	3.2

*Data from Holliday[147]

possible that this is the corresponding Auger peak to that of Harris and Pattinson, since an oxygen Auger signal was seen on their surface.

The Auger electron transitions in zirconium are tabulated in Table 5.3. Equ. (2) (Chapter 1) was used with the aid of the energy level scheme of Table 5.4, to calculate the theoretical Auger electron energies. We must expect a high population of initial holes in the $M_{4,5}$ level due to Coster-Kronig transitions, which will then dominate the following Auger processes. From Table 5.3 we can see that all low energy Auger peaks above 72eV will be initiated by $M_{4,5}$ holes, and the peak initiated by the N_1 hole (45eV) should be weak as observed. It is interesting to see that the calculated energy value of the $M_{4,5}N_{2,3}N_{4,5}$ Auger electron is much closer to the value from Fig.5.10 (145eV), than to the values obtained by other workers (147-149eV). All the observed Auger electron peaks are accounted for, apart from the weak inflection point at 33eV whose origin is as yet uncertain.

It is therefore claimed that Fig. 5.10 represents an undistorted low energy Auger spectrum of zirconium, as compared to published spectra. However this surface still suffered from slight carbon and oxygen contamination, but it is thought that this would merely cause a slight attenuation of the whole spectrum.

Also we have seen that 'chemical shifts' in Auger peaks occur when a zirconium surface oxidises. The shifts were not thought to be due to surface charging effects since the surface oxide layer should be very thin and in addition, the shifts were consistently reproducible. Energy shift values were between 2 and 4eV (depending on the peak chosen), and in a downward direction. Such shifts are explained by equs. (9) and (10) of Chapter 2, but a further analysis will not be attempted here.

Before continuing our discussion on the segregation of impurities onto a zirconium surface, perhaps it will be useful to make a few comments about segregation in general. A simple means of understanding segregation effects is in terms of the solid solubility of an impurity in a host matrix.

The solubility of an impurity may increase or decrease with temperature changes, causing the impurity to dissolve more easily, or to separate out at grain boundaries and surfaces. The reasons for segregation are related to atomic size and/or valency effects. A large atom impurity may cause stress in the host matrix, so that at high temperatures the atom will move to external or internal surfaces and remain there, so lowering the stress field. Also, the electronic structure of the solid is altered in the surface region, so that a high valence atom may be attracted to this region of increased electron density by Coulomb forces.

We can now look at the effects of this type of behaviour on a real surface. In Fig. 5.1, we see the four major impurities of S, Cl, C and O already present on the zirconium surface before any serious cleaning attempts were made. Such impurities may be found on any surface newly placed in UHV, so that no particular emphasis should be placed on these results, apart from saying that the carbon peak is graphitic in nature possibly pointing to an origin external to the zirconium target. After flashing at 850°C (Fig. 5.2), the small atoms of carbon and oxygen dissolve into the bulk, thereby lowering the surface concentrations of these two impurities and allowing the zirconium Auger spectrum to strengthen. Also, carbon has changed its form from graphitic to carbide. The larger and higher valency atoms of sulphur and chlorine have segregated to the surface. Further heating to 950°C (Fig. 5.3), causes more carbon and oxygen to dissolve into the bulk, but encourages even more sulphur and chlorine to segregate. Flashing in hydrogen at 950°C is not entirely efficient in removing sulphur and chlorine (Fig. 5.4), but by lowering the temperature, the process seems to 'work' (Fig. 5.5). It appears that at the lower temperature of 700°C, more sulphur and chlorine are being removed from the surface than are being supplied by thermal segregation. Unfortunately the deficiency of carbon and oxygen at the surface sets up a reverse concentration gradient and in Fig. 5.5, we can see that carbon and oxygen atoms diffuse back to the surface. This 'see-saw' action will not aid

our surface cleaning methods until we can remove either, all carbon and oxygen or, all sulphur and chlorine from the bulk. Both sulphur and chlorine were reduced on subsequent re-flashing (Figs. 5.6 and 5.7), but sulphur was extremely persistent on the zirconium surface, in agreement with the findings of Dooley and Haas[56].

Carbon and oxygen Auger signals were seen to build-up as a function of electron beam exposure time (Figs. 5.8 and 5.9). Since these two peaks grew together, it seems likely that CO (from the UHV residual atmosphere) is interacting with the zirconium surface under the influence of the electron beam. CO was found to be a major constituent of the UHV ambient and would be in plentiful supply to undergo stimulated adsorption on the zirconium surface. If the carbon were diffusing from the bulk, we might expect to see a carbide structure (as in Fig. 5.5), rather than the graphitic one observed in Figs. 5.8 and 5.9. Hence, the CO explanation of the phenomenon appears to be the better.

The carbide structure of the carbon KVV Auger peak, was seen on a zirconium surface after heat treatments at 850°C, but not at 600°C. Dooley[51] claims to have seen this structure in zirconium alloys with heat treatments at 300°C, but the alloys were complex and their previous histories may well have caused carbide formation prior to Auger analysis.

These studies of the thermal behaviour of zirconium surfaces indicate that the UHV pumping capability of such surfaces may be dynamic in nature[146]. In fact, the S.A.E.S. getter pumps operate between room temperature and 400°C and are 'activated' at 700°C, thereby allowing significant diffusion to occur. At these temperatures, zirconium atoms will chemically combine with many gases and then diffuse into the bulk, giving a pumping action. The high pumping speed of zirconium for hydrogen could not be investigated in this work, since the hydrogen atom will not undergo an Auger process.

CHAPTER 6

SECONDARY ELECTRON EMISSION FROM METAL BLACKS

6.1 Thermal Degradation of the Secondary Yield Values of Metal Blacks

The preparation and study of surfaces with low secondary electron yield values is of considerable technological importance in fields where secondary electron emission is undesirable. Many electron devices utilise low yield surfaces including external cavity klystrons, electron collectors, microwave windows, cylindrical mirror analysers etc.

Thomas and Pattinson[148] have made a study of metal black coated surfaces, indicating their suitability in UHV as a low yield coating. Metal black coatings may be produced by evaporating the parent metal, in a background pressure of 0.5torr of inert gas, onto a nearby substrate. Under these conditions, the metal deposits as a 'smoke', in a finely divided form, to produce a dense black coating over the substrate. Scanning electron micrographs[148] have shown that the surfaces of such coatings are extremely rough, and it is thought that this roughness acts to produce myraids of tiny 'Faraday cups', thereby giving high electron collection efficiency.

Whilst doing some routine yield measurements on a copper black coated surface, it was noticed that after a temperature excursion up to 700°C, the yield value of the surface greatly increased to a value close to that of a 'normal' copper surface. Also the coating had changed colour from its original black, to copper brown. This observation has serious implications in some electron device fabrication processes, in that a process such as vacuum brazing at 800°C, would cause such a copper black coating to loose its low yield value. Hence it was of importance to find a coating material which was capable of withstanding elevated temperatures whilst maintaining a low secondary yield value. Platinum will be shown to be such a material.

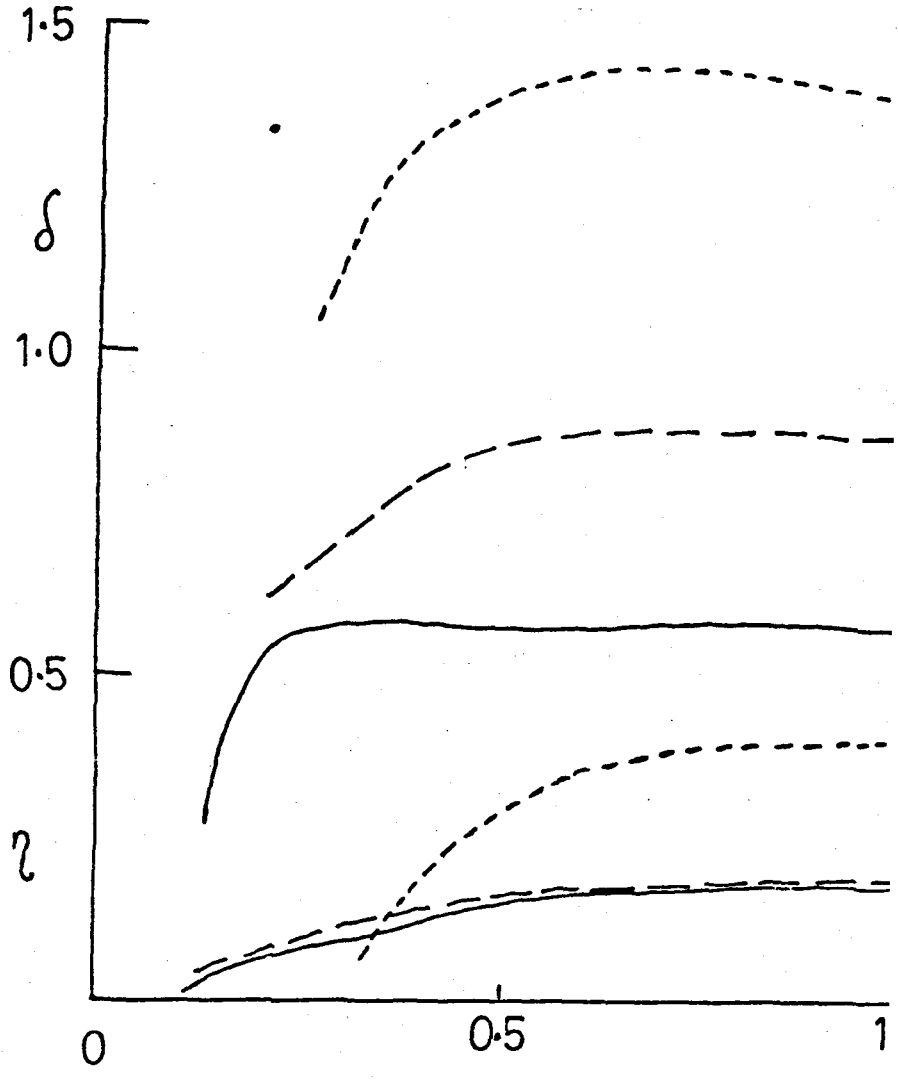
1·5
δ
1·0
0·5
η
0
0·5
1

Figure 6.1 δ, Ep and η, Ep curves for copper black on a nickel substrate

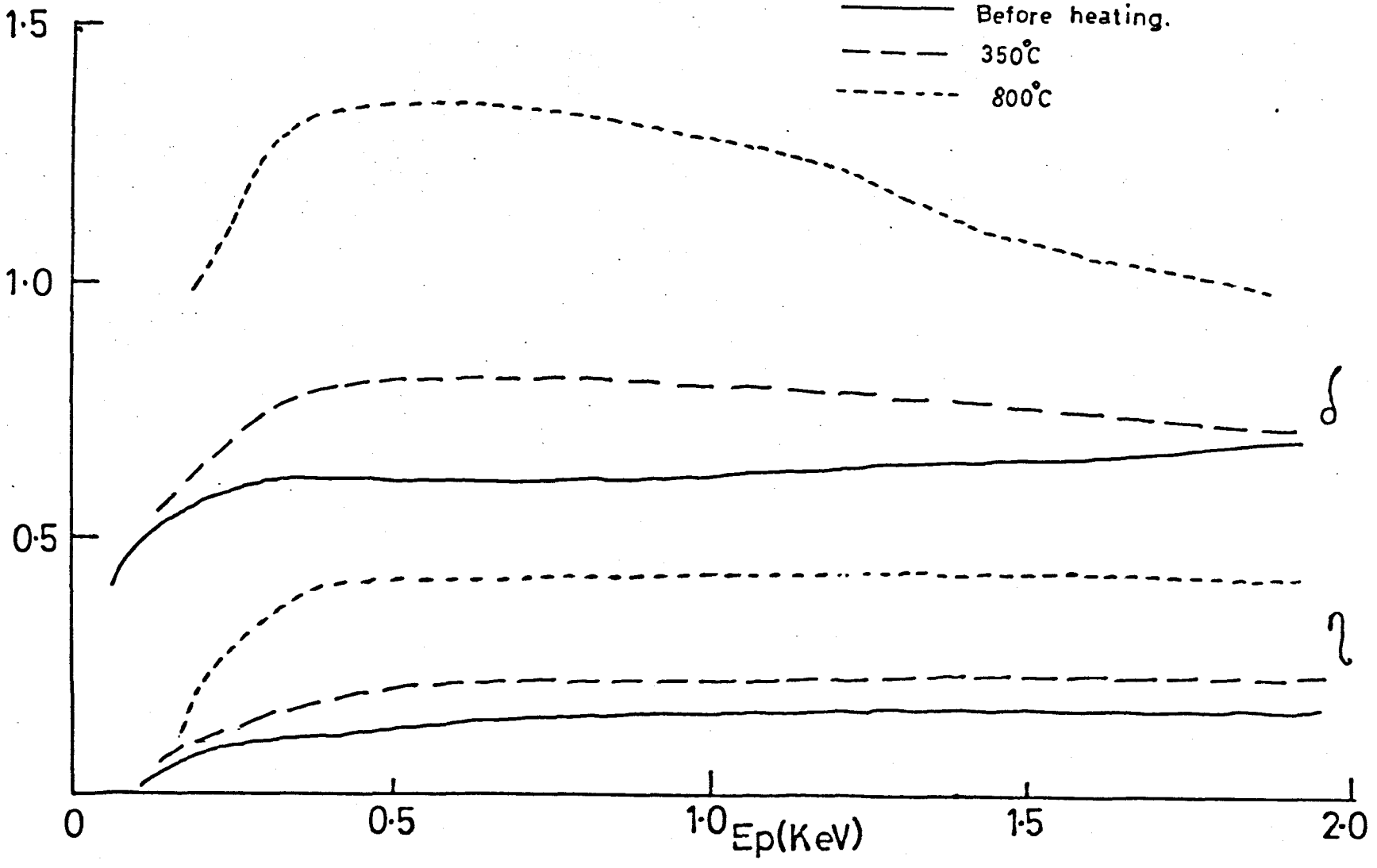

Figure 6.2 Yield curves for copper black on a copper substrate

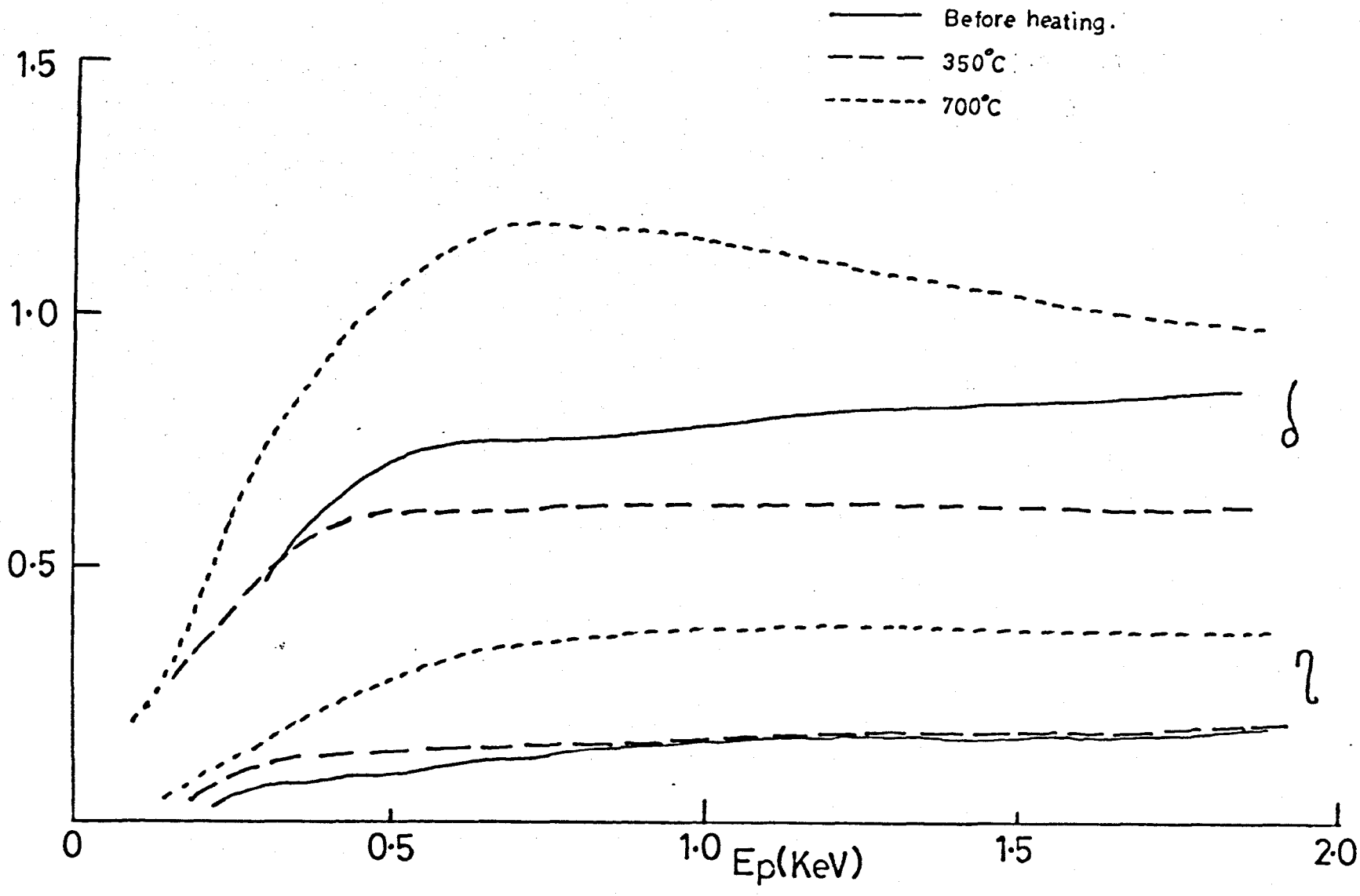

Figure 6.3 Yield curves for copper black on a sintox substrate

After the initial observation of the thermal degradation of copper black coatings, it was decided to conduct a more systematic series of measurements on such coatings. Copper (purity 5N) was evaporated from a tungsten basket on to three different substrates, at a background pressure of 0.5torr of argon. The chosen substrates were thought to be typical of many technological applications and were copper, nickel and alumina (Sintox). The coatings were produced in a commercial Edwards coating unit and were transferred to the single-grid UHV chamber (sub-section 3.2.4) after production. A chromel/alumel thermocouple was attached to the underside of the Sintox substrate and the three substrates were mounted in close proximity on a stainless rod. Each substrate was about 1 cm^2 in area and all the substrates could be heated with a 1kW projection lamp filament up to 500°C by radiation, and up to 950°C with additional electron bombardment.

Yield measurements were made using a normal incidence primary beam and in practice this position was found by finding the lowest yield value. Each target was presented in turn to the electron beam, by means of a linear bellows and a rotary feedthrough. The automatic measurement of δ and η was described in sub-section 3.2.4. Yield measurements were taken (all at room temperature) before heating and after heating to various temperatures for two hour periods. The temperature steps were multiples of 50°C or 100°C. Any colour changes in the metal black surfaces were observed through a window in the UHV chamber.

A selection of the yield curves from all three substrates are shown in Figs. 6.1, 6.2 and 6.3. It may be seen that with no heating, all the coatings gave a yield less than unity with no apparent maximum in the curves. After progressively raising the temperature, in steps up to 350°C, the yield value (measured when cold) for the copper and nickel substrates rises to about 0.8-0.9 whilst that of the Sintox substrate falls to 0.55. In all cases, a colour change occurred near this

temperature, from matt black to matt brown. Also, it is worth noting that in Figs. 6.1 and 6.2, the yield curve starts to form a maximum at about 750eV. $\delta_{max.}$ then stays in the range 0.8-1.0 until about 700°C is reached, when a $\delta_{max.}$ increase occurs in all three substrate coatings, to a value well above unity. The three yield curves of Figs. 6.1-6.3 now form a true maximum at about 500eV, and the values of $\delta_{max.}$ closely approach the value of a clean 'normal' copper surface ($\sim$ 1.33). A further colour change occurred at this temperature from matt brown to a red-brown, with a copper texture. All the above yield and colouration changes were found to be irreversible.

The most comprehensive data were taken on the copper and nickel substrate coatings, and this data has been plotted in Fig. 6.4 to produce a yield maximum/temperature profile. The profile indicates that at certain 'transition temperatures' (about 300°C and 700°C), δ_m changes abruptly, firstly to values close to unity and then to values close to δ_m for clean copper.

Obviously, a coating such as copper black will only have a limited usefulness due to its temperature limitations. A platinum black coating material will now be described, which is resistant to temperature up to at least 950°C, and indeed appears to slightly improve its low yield value by such heat treatments.

6.2 Thin Film Platinum and Platinum Black

Platinum was thought to be a suitable candidate for a temperature-resistant metal black due to its chemical stability and its high melting point (1770°C). However, this high melting point did pose a problem when evaporating platinum from a tungsten wire basket, in that the basket tended to fuse rapidly even with a small quantity of platinum in the basket. Tungsten was therefore expected to be found as an impurity in the coating, as was verified by the use of AES. The fusion problem was helped to some extent with the use of consecutive evaporations from three tungsten

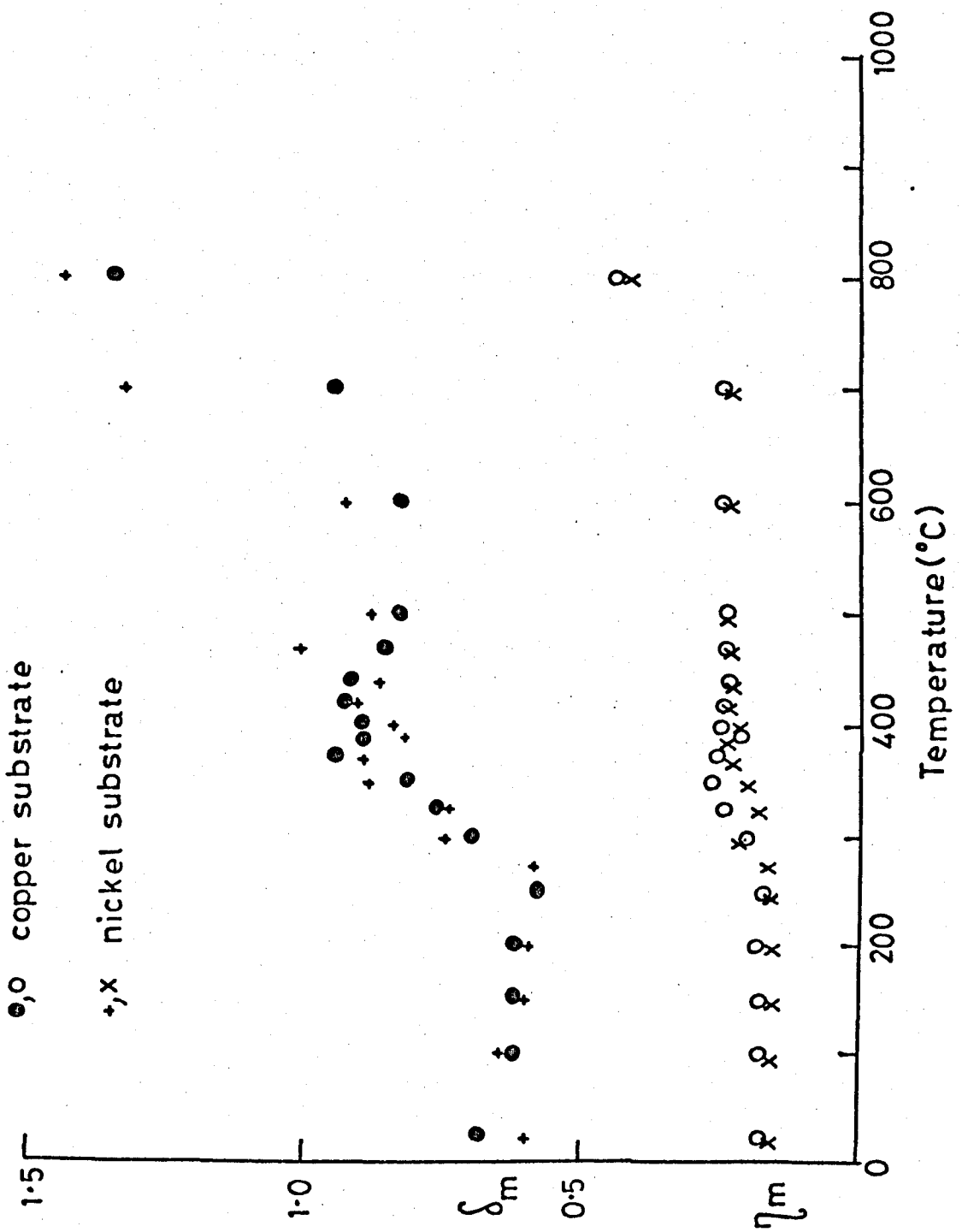

Figure 6.4 Max. yield / temperature profile for copper black on two substrates

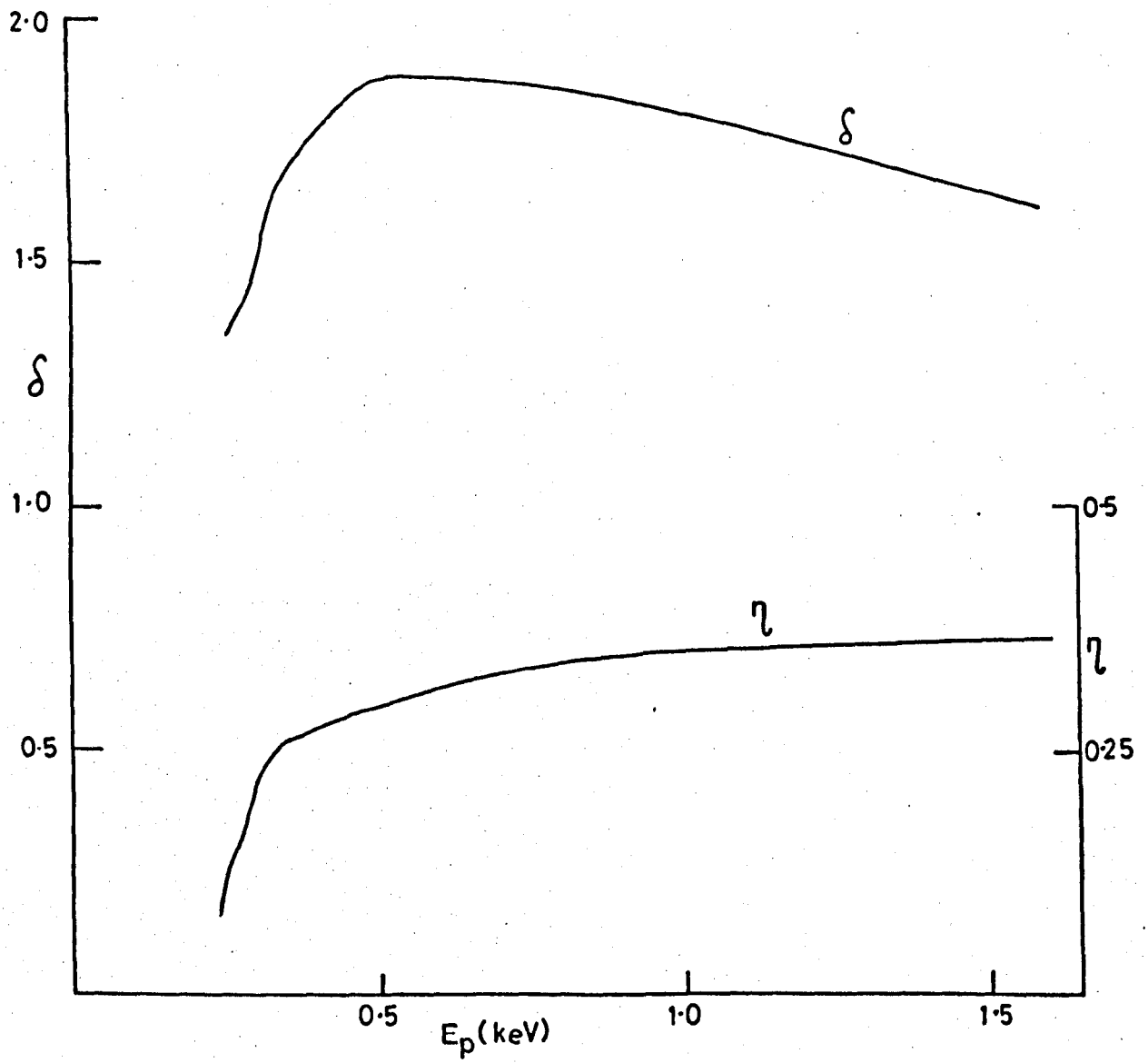

Figure 6.5 Yield curve for Pt thin film

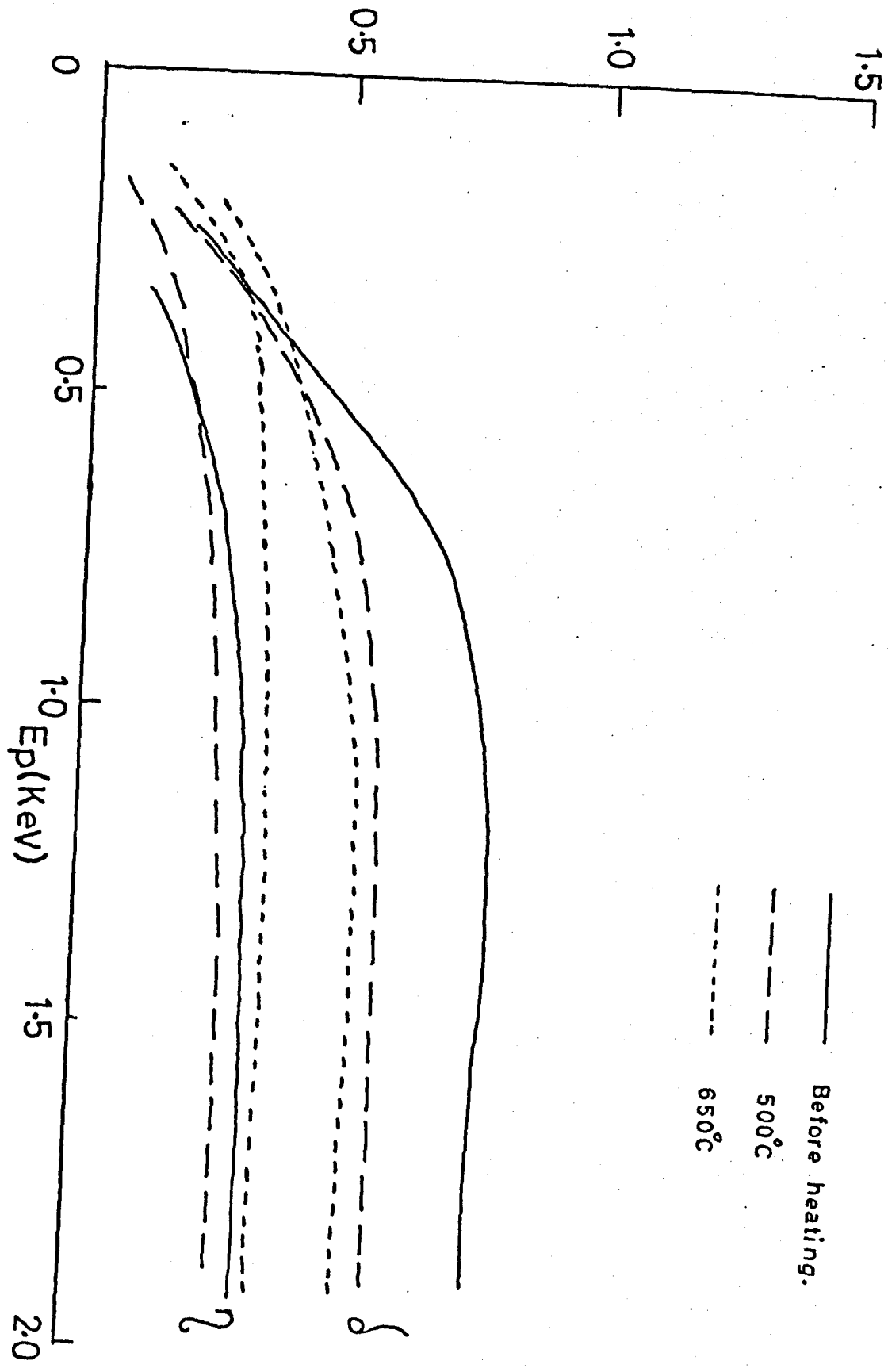

Figure 6.6 Yield curves for platinum black on a copper substrate

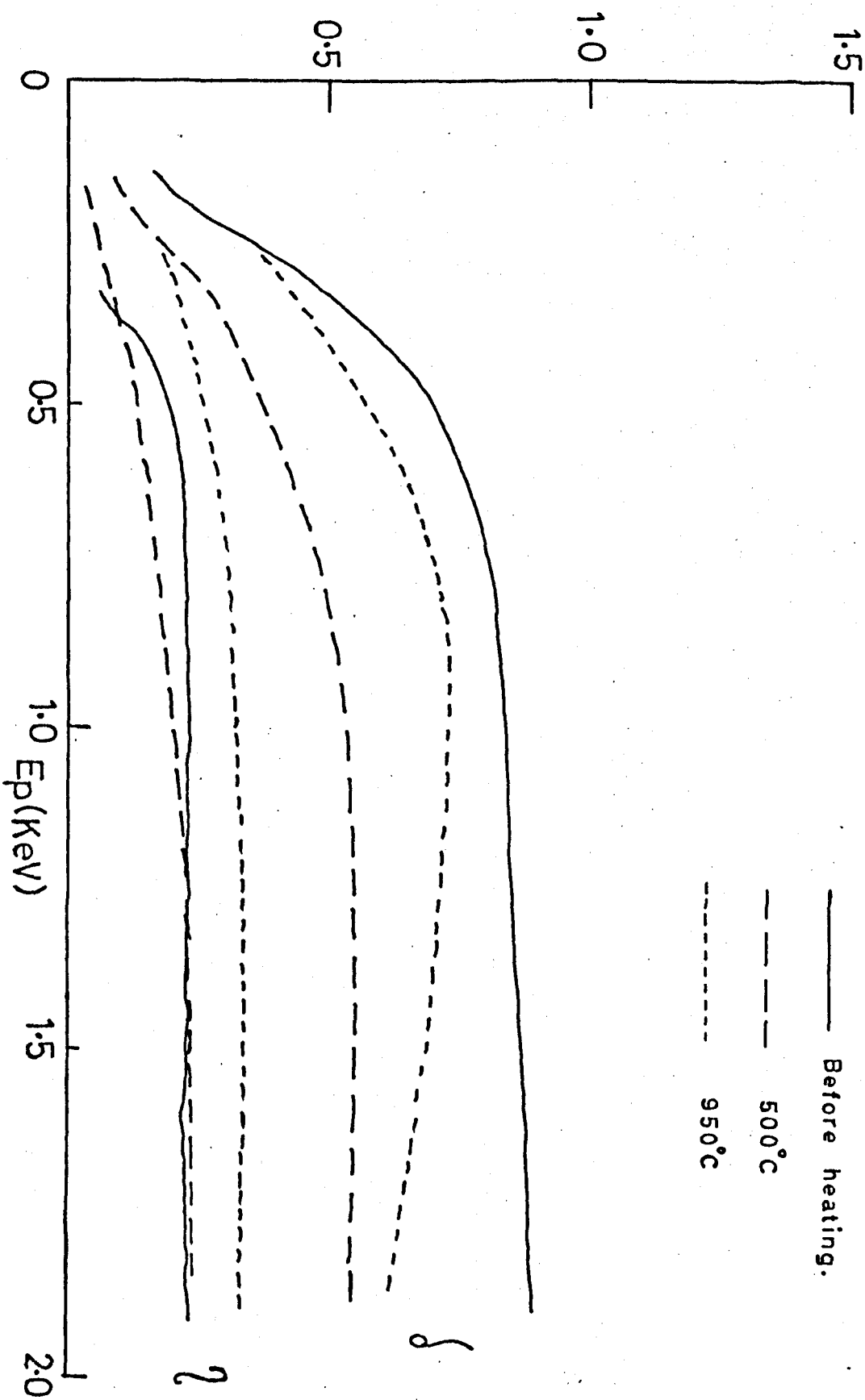

Figure 6.7 Yield curves for platinum black on a sintox substrate

6.2.1 Yield Curves

A comparison was made between the secondary electron emission properties of thin film platinum and platinum black, in order to see if such properties may be used to distinguish between the two surfaces. To this end, platinum (purity 5N) was evaporated in UHV, onto a polished tungsten substrate and yield curves were taken for this surface. Also, further secondary electron measurements were made on this surface which will be related later in this chapter.

Yield curves for the thin film of platinum are shown in Fig. 6.5. The curves have a normal shape (see Fig.1.1), with a $\delta_{max.}$ of 1.88 at an E_p of 550eV and an $\eta_{max.}$ of 0.36. These particular yield curves were taken in the three-grid UHV chamber where energy loss, slow peak and AES could be performed simultaneously.

In a subsidiary experiment, platinum black coatings were deposited on copper and sintox substrates, which were then transferred to the single-grid yield measurement apparatus. Similar experimental results to Figs. 6.1-6.4, were then taken to see if platinum black was capable of withstanding elevated temperatures without losing its low yield value. Figs. 6.6 and 6.7 show some of the curves obtained in this experiment. With no heating, the yield curves do not show a maximum, but level off at a δ value of about 0.85. Contrary to the case of copper black, the yield value of platinum black does not degrade with heat treatments, even up to 950°C. In the case of the copper substrate, the highest temperature reached was 650°C, since the 700°C heating cycle caused the copper substrate to alloy with its holder, and to melt.

It is therefore apparent that the secondary yield of platinum black will remain substantially below unity (0.6-0.7), even after heat treatments at typical brazing temperatures (800°C). Also the yield value remains comparatively independent of the primary electron energy which is useful for electron collection purposes.

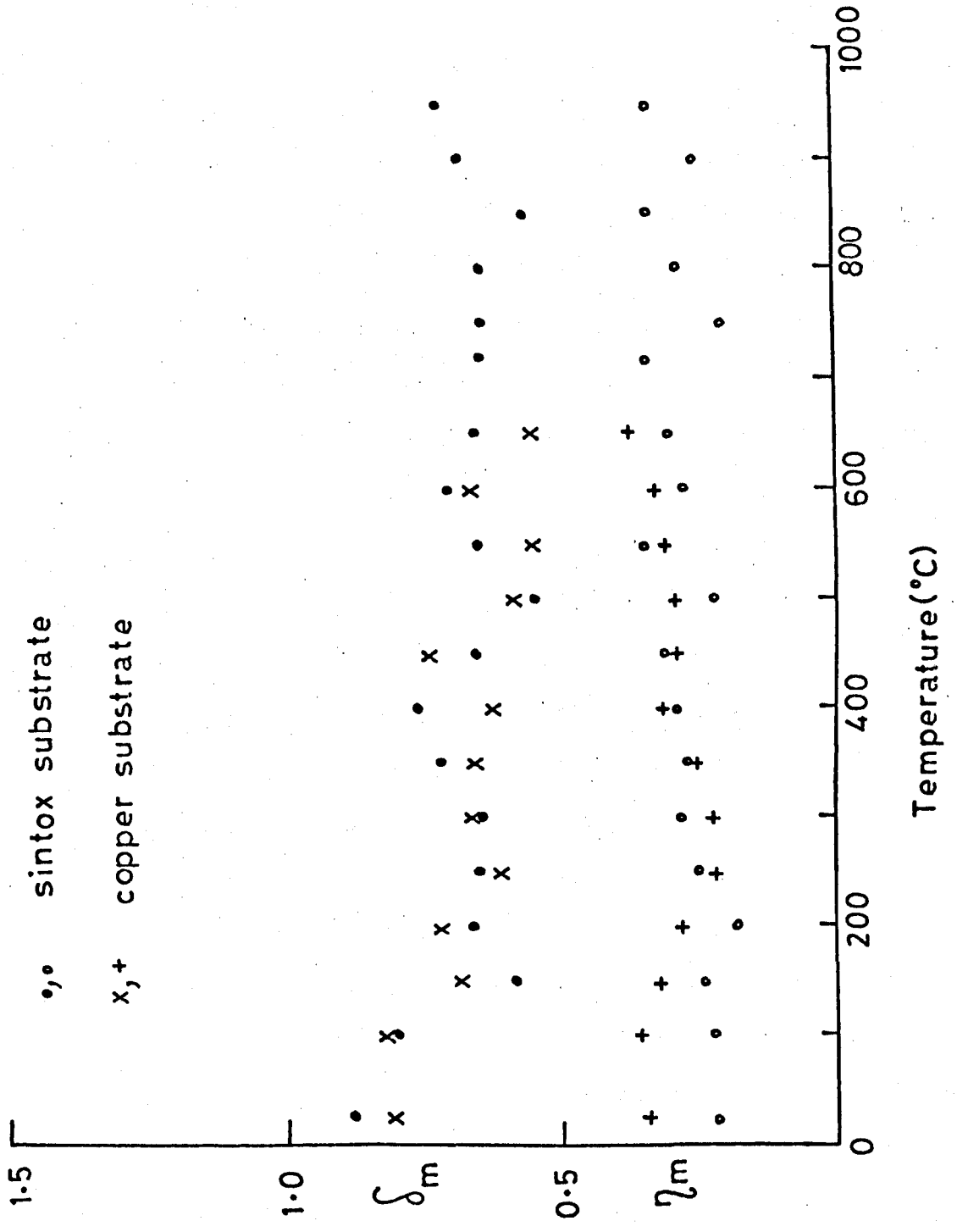

Figure 6.8 Max. yield/ temperature profile for platinum black on two substrates

Fig. 6.8 represents the total $\delta_{max.}$ data obtained in this subsidiary experiment, as a function of temperature. The yield maximum/temperature profile now shows none of the 'step-like' behaviour which was seen in Fig. 6.4. In fact, δ_m appears to improve slightly with heating. The scatter of points for each substrate, is presumably due to the effects of heating, but these effects could not be followed using AES in this particular apparatus. No colouration changes were observed in the platinum black coatings, again indicating the stability of this surface.

Although the yield of platinum black is about three times lower than that of its parent metal, it will be shown that the chemical nature of both surfaces is quite similar and we must therefore assume that the yield difference is due mainly to a surface topographic effect.

6.2.2 Auger Spectra

The secondary yield value of 'flat' surfaces is largely determined by the chemical make-up of the first few atomic layers of the surface. In this respect, AES makes a powerful contribution in characterising the surface composition, thereby giving much information on the surface processes affecting δ.

Two platinum surfaces were prepared for examination by AES including the one described previously i.e. thin film platinum on a polished tungsten substrate, and a second platinum black coated surface. This latter surface was prepared in the usual manner using a polished stainless steel substrate.

An Auger spectrum was taken from the platinum black surface after only a mild baking at 250°C, and is shown in Fig. 6.9. Tungsten (168eV), carbon (270eV) and oxygen (510eV) Auger peaks can be seen in the spectrum, with small platinum Auger peaks at 61 and 150eV. The Auger peaks from platinum black appeared to be somewhat attenuated when compared to those from thin film platinum. This attenuation was more pronounced

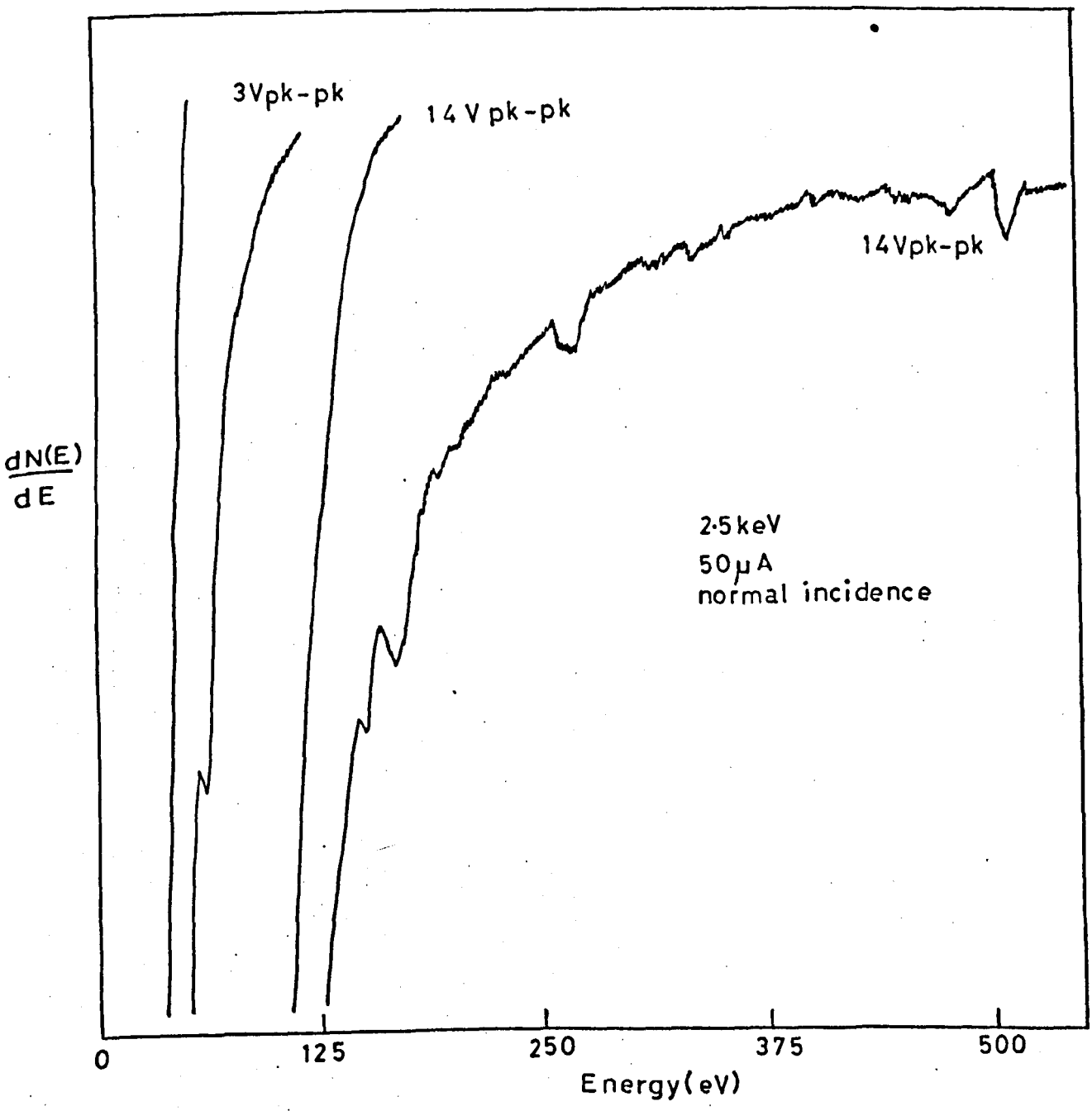

Figure 6.9 Auger spectrum of platinum black as prepared

at lower Auger electron energies, and was thought to be due to surface geometric factors giving the low values of δ and η.

This platinum black surface was then held at 750°C for one minute using electron bombardment heating and further Auger spectra were then taken. The resulting spectrum is shown in Fig. 6.10, in conjunction with the Auger spectrum obtained from the 'normal' thin platinum film. Auger peaks from the two surfaces appear to be quite similar apart from some intensity variations. The Auger peak values for the two surfaces have been listed in Table 6.1.

TABLE 6.1

Auger Electron Energies from Thin Film Platinum and Platinum Black (eV)

Thin Film Pt	12*	39.5	61.5	152	168	180	199	215	234	250	400
Pt Black			61	150	168		199	215	234		400

*taken from slow peak spectra (Fig. 6.15)

As a further check on the stability of a platinum black coating, secondary yield curves were obtained for this particular metal black before, and after flashing. Fig. 6.11 illustrates these curves. The full line corresponds to the Auger spectrum of Fig. 6.9 and the dashed line that of Fig. 6.10 (dashed spectrum). The figures indicate that the removal of contaminants such as W,C and O will lower the $\delta_{max.}$ value from about unity to 0.8. This $\delta_{max.}$ value of 0.8 was higher than had been observed previously (Fig. 6.8) and a likely explanation of this high value will be given later.

6.2.3 Electron Energy Loss Spectra

It has been shown by Thomas et. al.[149], that the electron energy losses of metal blacks can be widely different from those of their parent metal. Hence, an attempt was made to test this conclusion in the case of platinum black.

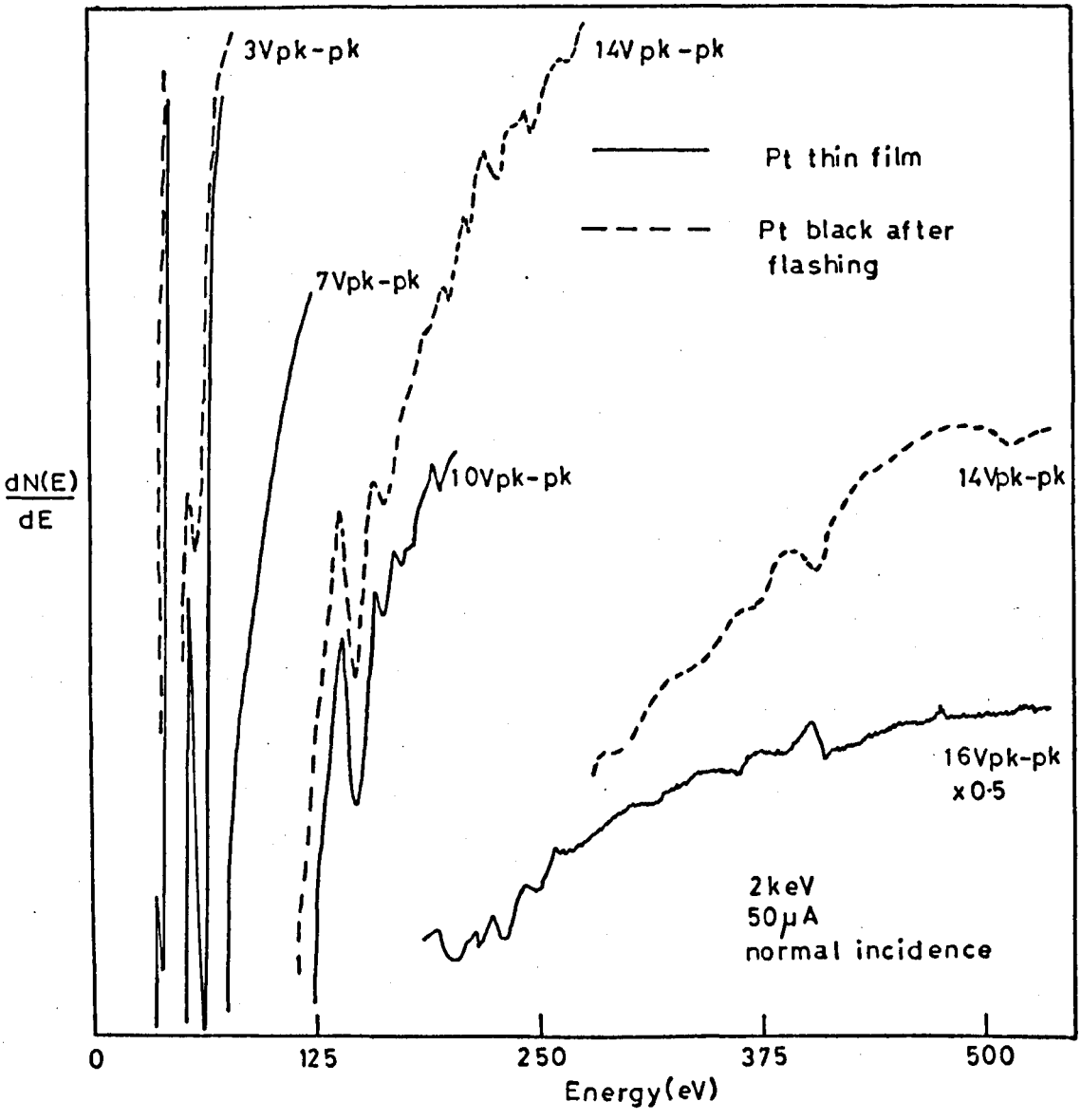

Figure 6.10 Auger spectra of Pt thin film and Pt black

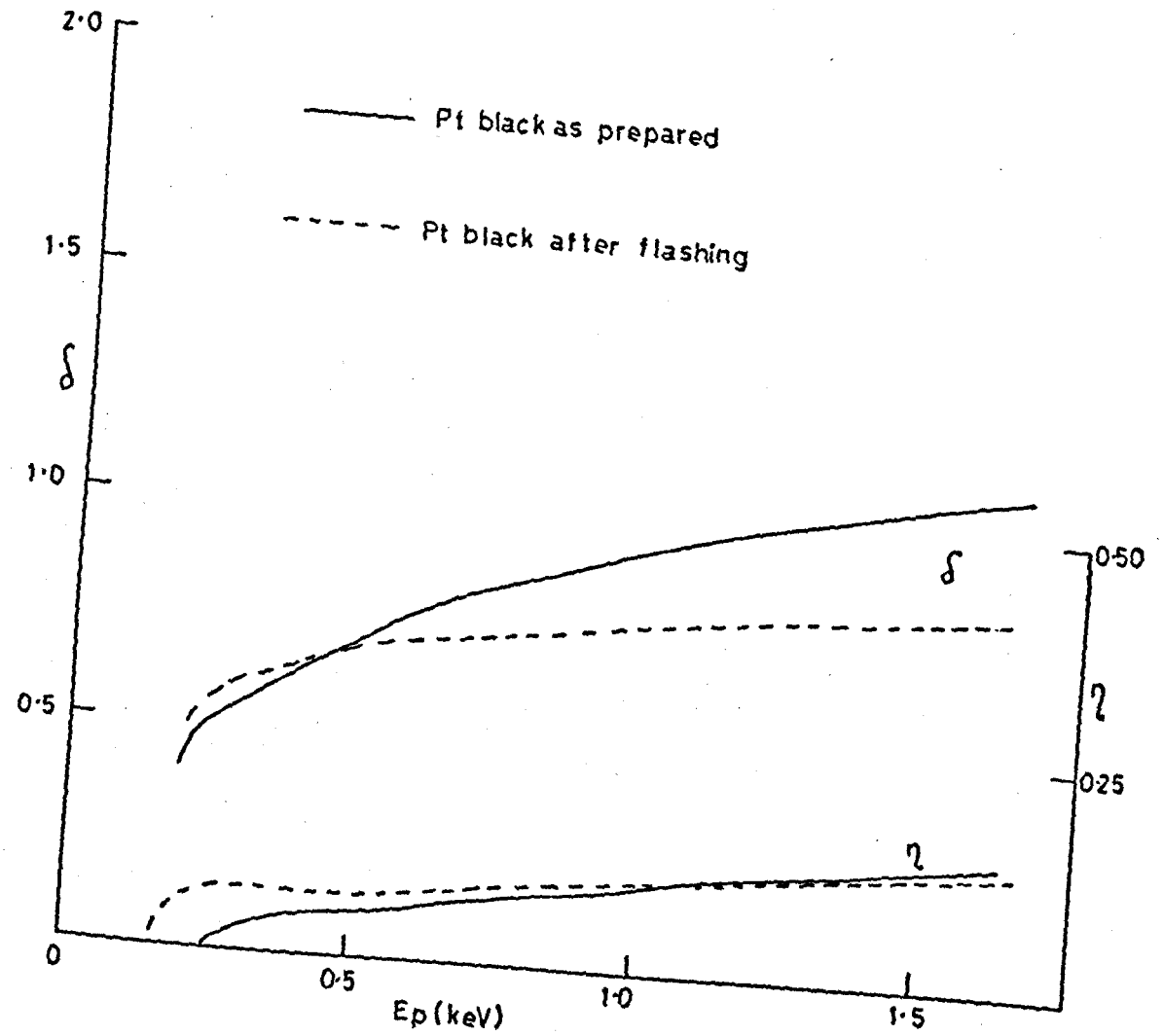

Figure 6.11 Yield curves for Pt black

Fig. 6.12 shows the manner in which the energy losses of thin film platinum change, as the incidence angle of the impinging electron beam varies. This type of plot should show up any surface dependent losses e.g. surface plasmon, as the incidence angle increases. However, no strong variations are seen to occur, apart from perhaps the 60° plot, when a peak appears at 6.0eV along with a strengthening of the 31eV loss.

The energy losses of both thin film platinum and platinum black are relatively weak as compared to the elastic peaks of Figs. 6.12 and 6.13 (2Vpk-pk plots). Fig. 6.13 corresponds to the Auger spectrum of Fig. 6.9 and it may be seen that the energy losses of platinum black are indeed similar to those of its parent metal. The loss at 14eV is resolved in the lower plot of Fig. 6.13 with the use of a low modulation voltage and higher gain.

The loss spectrum of platinum black did not change substantially after flashing and this is the one that is compared to that of thin film platinum in Fig. 6.14. There are differences in the peak intensities but apparent agreement in energy values. The intensity of the 43eV loss is greater in platinum black but the opposite is true for the 33eV loss. The reason for this behaviour is not understood at present. Electron energy loss values from both surfaces are compared in the following table.

TABLE 6.2

Comparison of the energy losses of platinum black and thin film platinum (in eV)

platinum black		14	25	33	45	55
thin film Pt	6.0	14	25	31	44	55

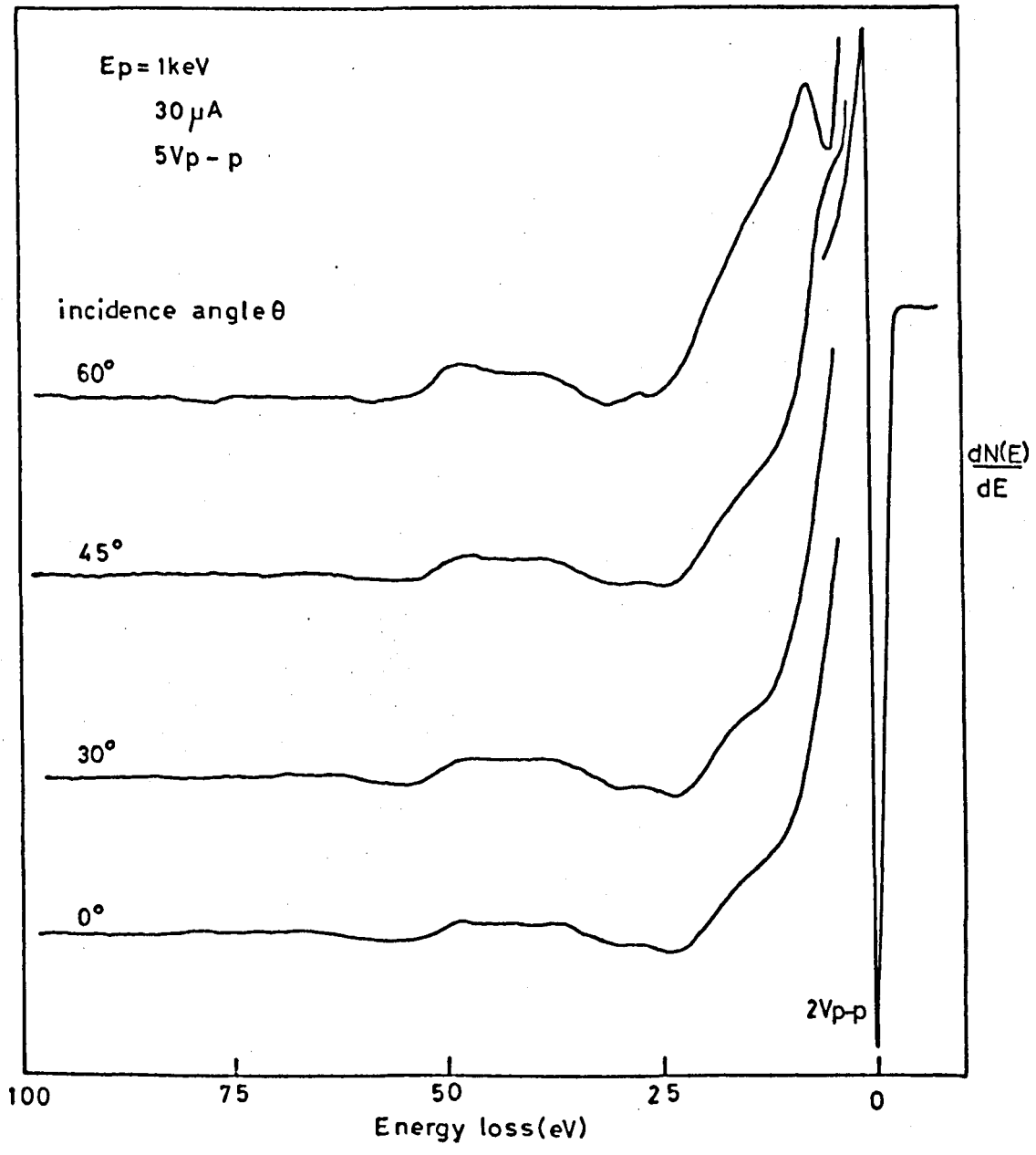

Figure 6.12 Energy losses of Pt thin film with θ variation

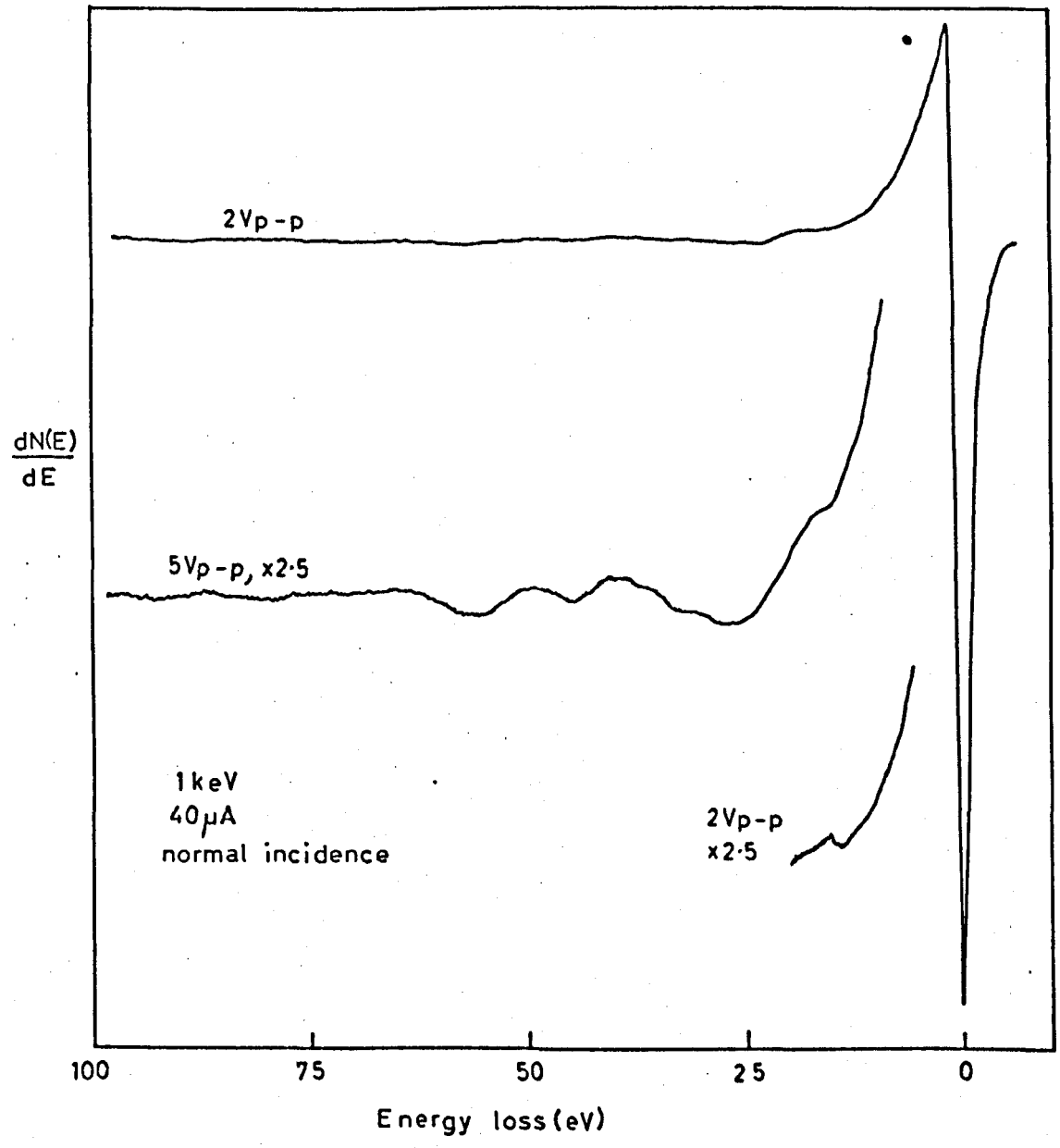

Figure 6.13 Energy losses of Pt black as prepared

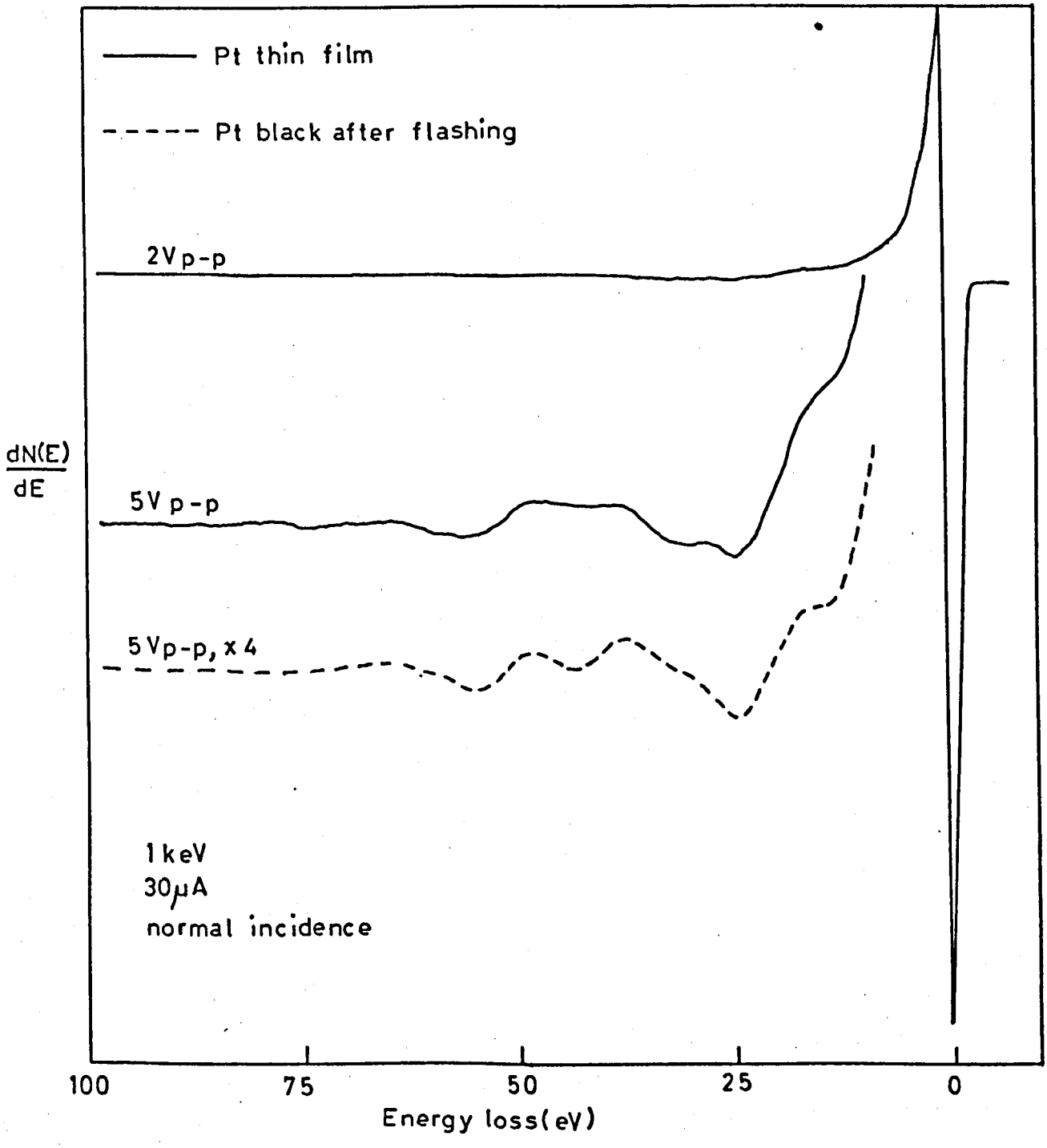

Figure 6.14 Comparison of the energy losses of Pt black and thin film Pt

6.2.4 Slow Secondary Electron Spectroscopy

The results of slow secondary electron spectroscopy of the two surfaces have been included so as to be able to compare spectra, rather than to explain the origin of these spectra. In fact, so far as is known, no published high-energy band structure for platinum exists, rendering the interpretation of the slow peak spectra extremely difficult.

The energy structure in the slow peaks of both surfaces is not strong but becomes stronger at lower primary energies, as seen in the lower plot of Fig. 6.15. Characteristic slow peak energy values will be taken from the minima of the dN(E)/dE plots. Fig. 6.15 shows the effect of primary electron energy variation on the slow peak, and it can be seen that although peaks at 11.5 and 8.5eV remain constant, other lower energy peaks exhibit energy shifts, which may well be due to changing background slopes. In fact, the peak at 1.5eV disappears altogether after the 500eV plot.

A direct comparison has been made in Fig. 6.16, between the slow peaks of thin film platinum and platinum black using a fixed angle of incidence (0°) and fixed primary energy (2keV). We can see that in the slow peak region, the spectra of the two surfaces closely resemble each other, apart from an obvious difference at 1.6eV. A comparison of the slow peak energy values from the two surfaces is given in Table 6.3.

TABLE 6.3

Slow peak energy values for platinum black and thin film platinum (in eV)

platinum black	1.5	3.4	5.4	6.1		11.2
Thin film Pt		3.2	4.5	6.0	8.5	11.5

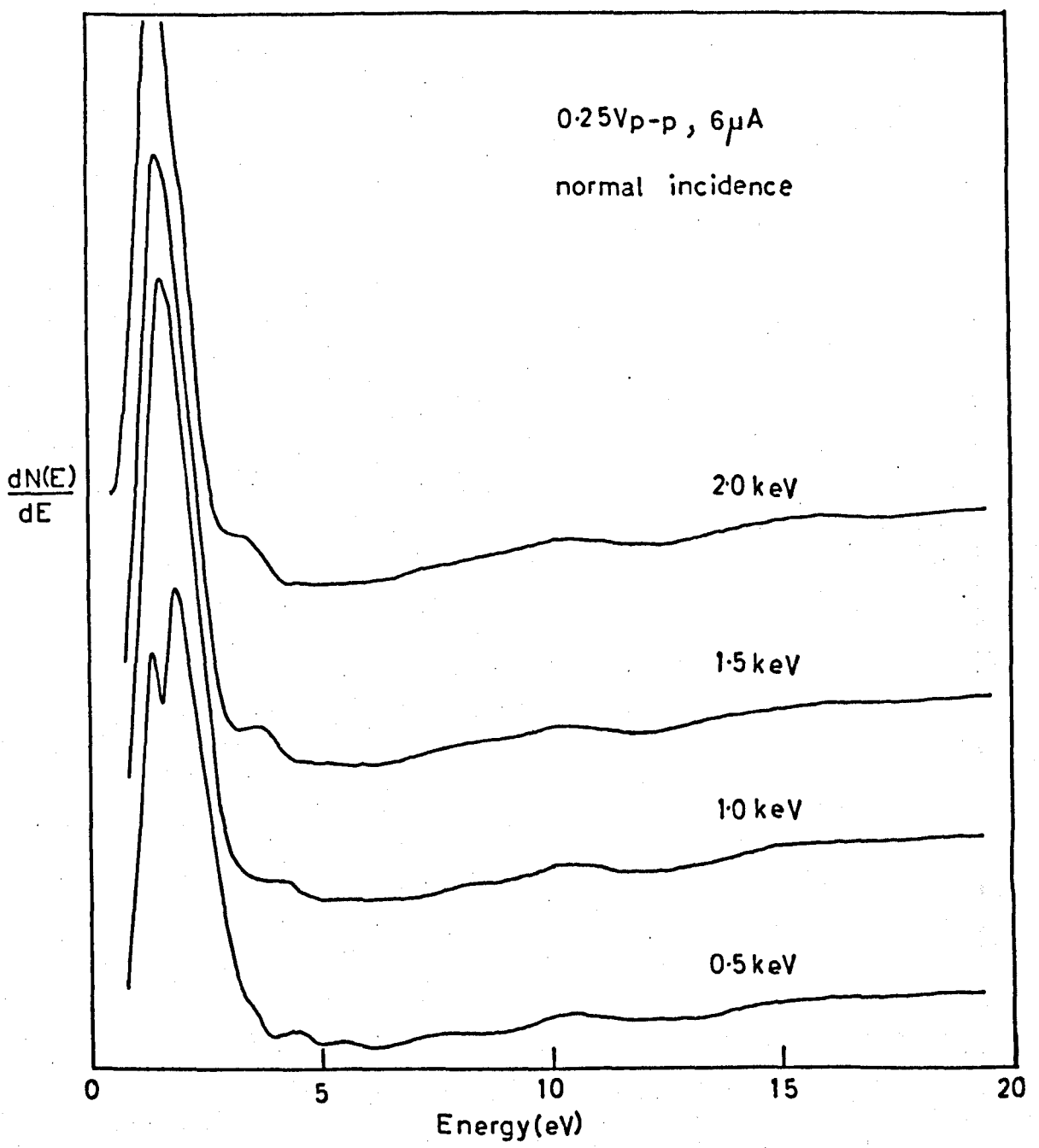

Figure 6.15 Effect of E_p variation on the slow peak of a platinum thin film

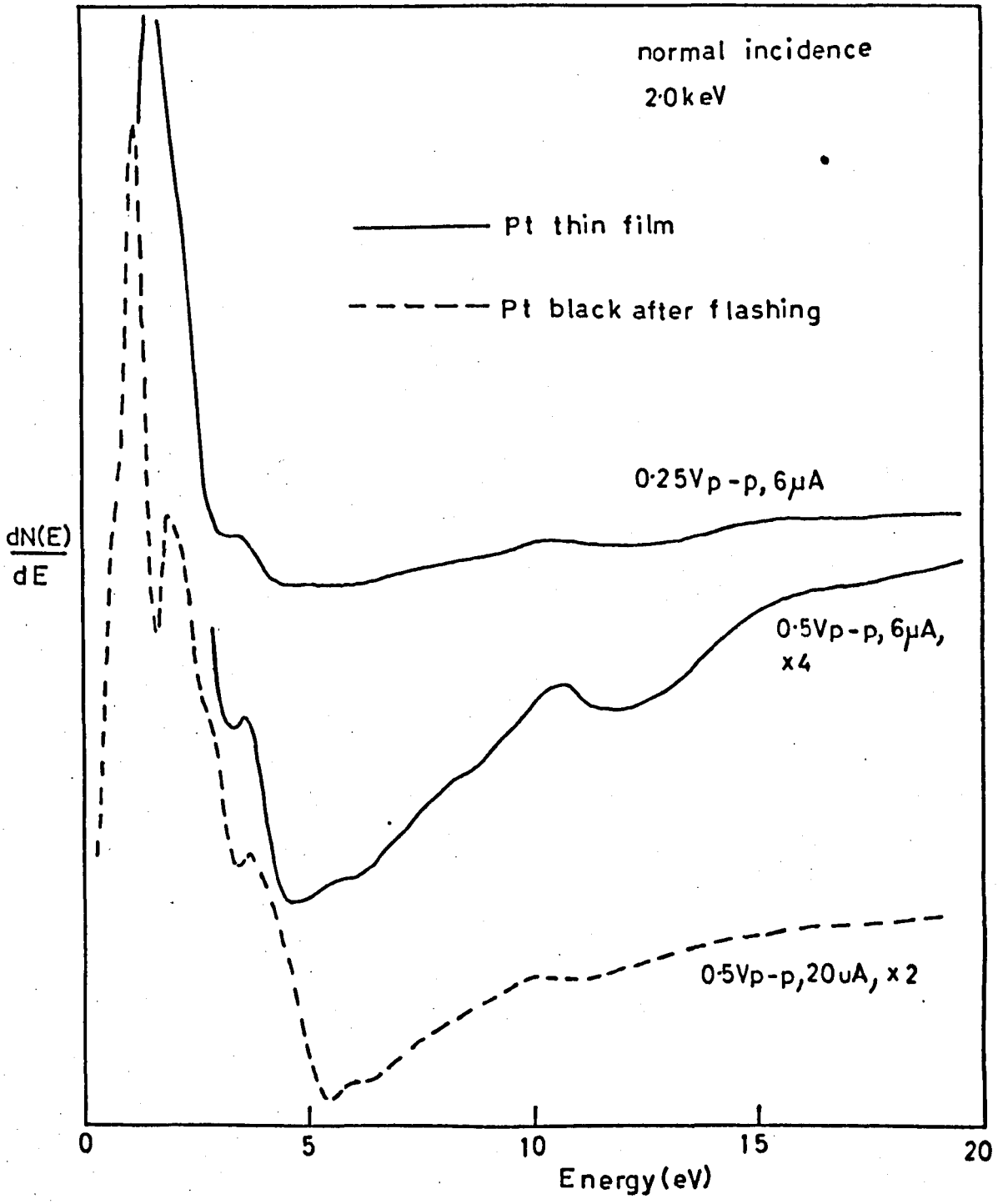

Figure 6.16 Comparison between slow peaks of Pt black and a platinum thin film

6.3 Discussion and Conclusions

It has been shown that a coating of copper black is a highly unstable surface at temperatures greater than 300°C. Thomas et. al.[149] used AES on a copper black surface but only obtained results for heatings up to 400°C. They found large amounts of carbon and only small Auger peaks due to copper. It seems reasonable therefore, that the yield transitions found for copper black, are more likely to be due to changes in surface topography rather than changes in surface composition. Heating may well cause copper black to increase its particle size i.e. to become less rough on a microscopic scale, until eventually, it becomes a comparatively smooth, clean copper surface. This is in effect a sintering process. The colouration changes noted earlier, tend to confirm this hypothesis because any finely divided surface will appear black, but as the particle size increases, so the surface reverts to its 'natural' colour and texture.

An explanation for the occurrence of two transition temperatures (350°C and 700°C) is not entirely obvious at present. If one considers that the sintering process effectively lowers the total surface energy (and area), it may be possible for a metastable sintered state to exist in the temperature range 350-700°C; the final sintered state being achieved when sufficient activation energy is available ($> 700°C$). Scanning electron micrographs of the coatings after various heat treatments, could well help to clarify the situation.

The chemical stability and high melting point of platinum, appears to prevent a platinum black coating from undergoing irreversible yield changes. It is this coating therefore, which is recommended for technological uses where a temperature-resistant coating is required. Also, the yield curve remains remarkably flat and low (0.55-0.70), up to an Ep of 2keV which makes it a useful surface as an electron collector i.e. its collection efficiency will not vary with the energy of the

TABLE 6.4

Comparison of observed Auger peaks from platinum (energies in eV)

Present work	Haas et. al.[47]	Palmberg et. al.[49]
12	12	
	24	
39.5		
	43	43
61.5	60*	64
		93
152	152	150
	160	158
168		168
	172	
180	180*	
		185
199	200*	199
		217
215		
	230*	
234		237
	245*	251
250		
		357
400		390

(no correction made for analyser work function)

*values read from spectra

incident electron. Losee and Burch[150] have independently agreed with my conclusions[151] regarding the yield and electron collection properties of platinum black. They prepared the coating chemically and took measurements of yield in a vacuum of only 10^{-6} torr pressure. Their main recommendation was the use of platinum black rather than gold black, for electron collection purposes.

Auger electron spectroscopy has revealed that the surface composition of the platinum black is quite similar to that of its parent metal. Table 6.4 compares the Auger peaks of platinum as observed in this work, to those found by other workers. The agreement is fair if one considers the lack of work function correction. However, the spectrum of Fig. 6.10 does show that the peak at 150eV is much stronger than its neighbouring peaks, which is not observed by the other workers of Table 6.4. It therefore seems likely that a strong contribution to this peak comes from sulphur in both spectra of Fig. 6.10. Apart from sulphur, it appears that flashing will remove the contaminants of W, C and O (Fig. 6.9) from a platinum black coated surface.

The sulphur was thought to have originated from the stainless steel substrate, since sulphur is known to strongly segregate on such a surface at elevated temperatures. Fig. 6.11 shows that whilst the yield of platinum black remains less than unity (0.8) after flashing, this value is somewhat higher than observed previously. The higher value is possibly due to the presence of sulphur on this surface.

The similarity of the energy loss spectra from different metal black coatings, as found by Thomas et. al.[149], cannot be endorsed in the case of platinum black. Table 6.5 has been drawn up to compare the energy losses observed for platinum by myself and other workers. Also, energy loss values for gold, platinum and copper blacks, have been added, for comparison purposes. One can see that in the case of platinum black, the losses give a better agreement with those of its parent metal than to

TABLE 6.5

Electron Energy Losses of Platinum and Some Metal Blacks (in eV)

Platinum			Metal Blacks		
Present Work	Powell[152]	Allen[153]	Pt Present work	Cu[149]	Au[149]
6.0	6.2	5.5			
14	14.3	13.2	14		
		18.6			
25	24.4	24.4	25	28.6	30
31		31.5	33		
		37.5			
44		42.0	45		
		50.1			
55		59	55	56	60
		71			
				108	108
				130	130
				187	187

those of other metal blacks (Cu and Au blacks). Since Thomas et. al.[149] found large carbon Auger electron peaks on both metal black surfaces, it seems likely that this common contaminant of carbon is the factor causing the similarity of loss spectra between two different metal blacks. Also, this contamination may well have led them to believe that the energy loss spectrum of the metal black is substantially different to that of its parent metal.

However, certain differences in the energy loss spectra of Pt and the Pt black surface are apparent in Fig. 6.14, and from Fig. 6.10 we know that the chemical make-up of both surfaces is similar. From these considerations, it appears that surface geometric factcrs may play some rôle as far as electron energy losses are concerned. Indeed, Zacharias et. al.[154] and Fujimoto et. al.[111] have shown that such factors can influence surface plasmon energies (lowering the energy). Unfortunately, neither of the two differences pointed out from Fig. 6.14 appear to be related to surface plasmon phenomena, so that the reason for such effects is still not clear.

The energy losses of platinum obtained in the present work are in reasonable agreement with those of other workers. The extra loss peaks at 18.6, 37.5 and 71eV, observed by Allen[153], were not observed by either myself or other workers listed by Allen. Despite this, Allen claims that the 18.6eV loss is a volume plasmon loss by assuming four electrons per atom available for oscillation. The 14eV loss would then be the surface plasmon loss. Since I observed a weak 14eV loss, but no loss at 18.6eV on a partially contaminated surface, his explanation would appear in doubt, since contamination will have a major effect on the surface plasmon loss, rather than the volume plasmon loss.

Fig. 6.12 does not help in resolving the problem, since no strong angular energy loss effects are seen. One could therefore conclude

that platinum does not show significant collective electron behaviour, and that most losses will be inter/intra-band transitions to levels above the Fermi level. A contribution to the 55eV loss may well come from the ionisation of O_3 energy level of platinum, at 51.7eV. A further consideration of this work is not desirable beyond this point, because the particular platinum surface under investigation was known to have sulphur contamination, which could well influence the observed energy loss spectrum.

In conclusion, we have seen that platinum black is a useful low secondary yield coating, compatible with the UHV environment, and capable of withstanding elevated temperatures (up to at least 950°C) whilst maintaining low secondary yield values. It is hoped that the stability of the platinum black coating will enable its use in a variety of technological areas, such as coatings for klystron windows, large valve anodes etc., and electron collection devices in general.

CHAPTER 7

ELECTRON ENERGY LOSS MEASUREMENTS FOR ANTIMONY

7.1 Introduction

It has been shown by Harris[155], that the element of antimony behaves in an anomalous fashion with regard to its plasma properties. This work by Harris has been checked and the electron energy losses of antimony were investigated in a more systematic manner, allowing a conclusive identification of the energy losses.

Antimony lies between arsenic and bismuth in Group V_B of the periodic classification. Its resistivity is 41μ ohm. cm. and it may be classed as a semi-metal. However, contrary to expectation, antimony shows a remarkable collective electron behaviour when exposed to an exciting electron beam, giving rise to relatively large plasma loss peaks below the elastic peak. A simple model will be suggested which could explain its behaviour.

The state of the antimony surface was verified using AES; oxygen being the only detected contaminant. Energy losses were measured using high gain to detect the weaker peaks, and angle of incidence and primary electron energy variation in order to observe corresponding changes in plasma behaviour.

The relatively strong plasma energy losses of antimony would suggest that a more extensive investigation of many semi-metal materials in the future, would be extremely useful in determining the extent of this phenomenon.

7.2 Energy Loss Measurements

Antimony thin films were prepared by the evaporation of antimony from tungsten wire baskets, onto a polished stainless steel substrate, in UHV. This method is quite efficient in producing a clean film, since antimony is not strongly reactive and also, it has a low melting point (630°C).

Auger electron spectra were taken before and after the energy loss measurements were made, in order to be sure that no contamination of the surface occurred whilst measurements were taken. Fig. 7.1 shows an Auger spectrum of antimony, taken after the energy loss measurements. The energy scale is expanded for easier viewing purposes. In an Auger scan from 0-600eV, oxygen was found to be the only contaminant, seen at 508eV in Fig. 7.1. The oxygen peak is small and it was thought that this would give a slight attenuation (and perhaps a shift) of the surface plasma energy losses.

However, the remainder of the spectrum in Fig. 7.1 is in good agreement with other workers. The splitting of the $M_{4,5}$ level in antimony, is illustrated by the doublet structure at 453 and 462eV. This splitting value of 9eV agrees well with the value of 9.4eV given in the energy level tables of Bearden and Burr[144]. Table 7.1 gives the observed Auger peaks, along with the values obtained by other workers. Agreement is quite good considering the lack of work function correction. The peak at 438eV is designated as a volume plasmon loss of the $M_5N_{4,5}N_{4,5}$ Auger electron. Such a loss must also occur for the $M_4N_{4,5}N_{4,5}$ Auger electron but this peak is probably obscured by the large background slope. Indeed, this loss peak may be the cause of the asymmetry of the $M_5N_{4,5}N_{4,5}$ Auger peak.

We have now characterised the antimony surface on which electron energy loss spectra are to be taken. Fig. 7.2 shows some energy losses of antimony taken under high gains at normal primary electron incidence. Using 2 or 3Vpk-pk modulation voltage, two peaks are seen at 11 and 15eV, with a broad loss at about 30eV. With 5Vpk-pk, this broad loss is seen as two peaks at 28 and 32eV, and also two further peaks appear at 47 and 52eV. With even larger modulation (8Vpk-pk), further weak losses can be seen at 59, 68, 80 and 91eV.

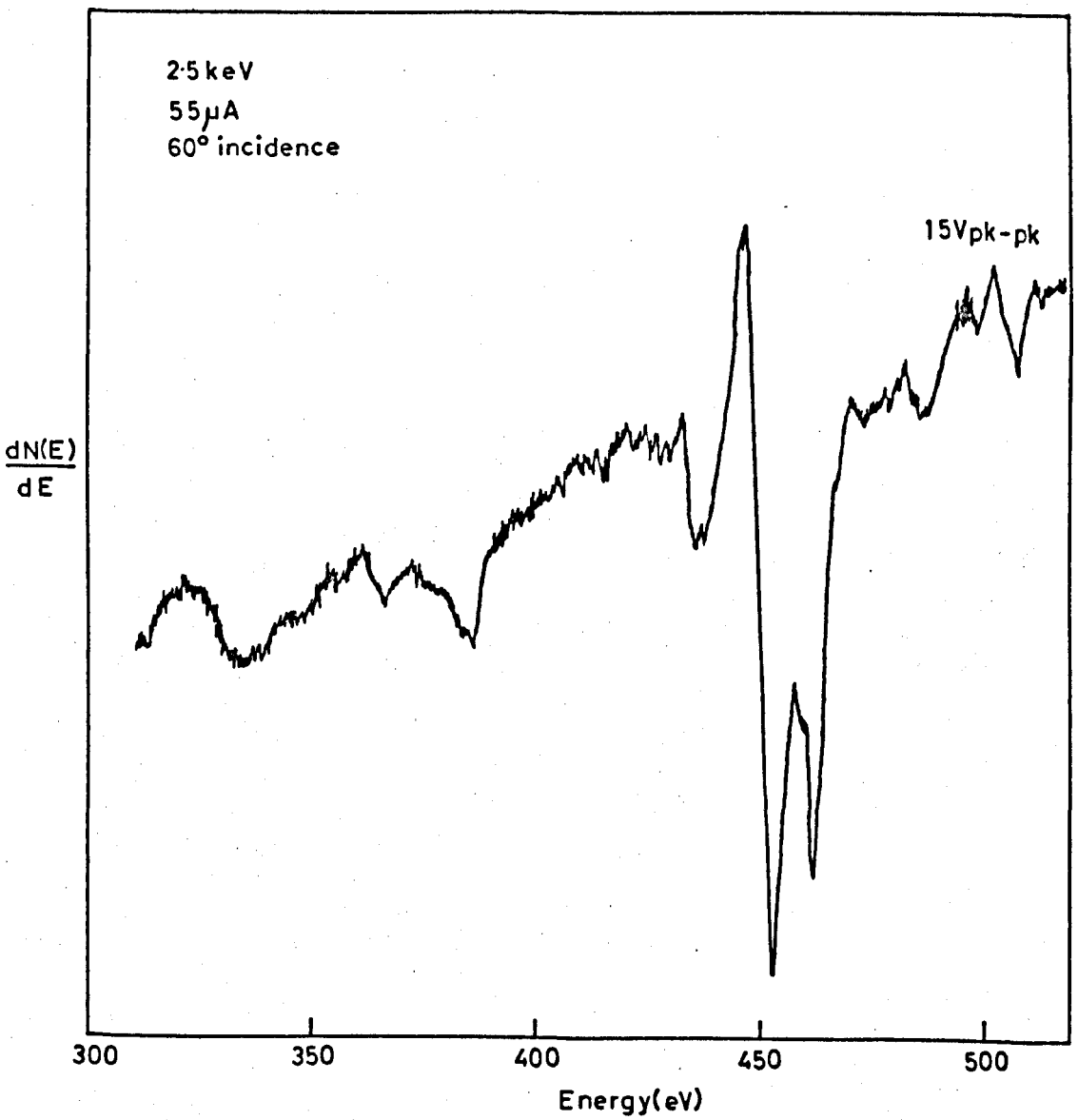

Figure 7.1 Auger spectrum of antimony

TABLE 7.1

Auger Electron Energies for Antimony (in eV)

Present work	Harris[155]	Palmberg et.al.[49]	Transition
		499	$M_4N_{4,5}O$
488	490	492	$M_5N_{4,5}O$
462	459.5	462	$M_4N_{4,5}N_{4,5}$
453	452.2	454	$M_5N_{4,5}N_{4,5}$
	450.5		
438	436	440	Plasmon loss of $M_5N_{4,5}N_{4,5}$
386	388	388	$M_{4,5}N_{2,3}N_{4,5}$
367	370		$M_{4,5}N_1O$
		342	
335	332	334	$M_{4,5}N_1N_{4,5}$

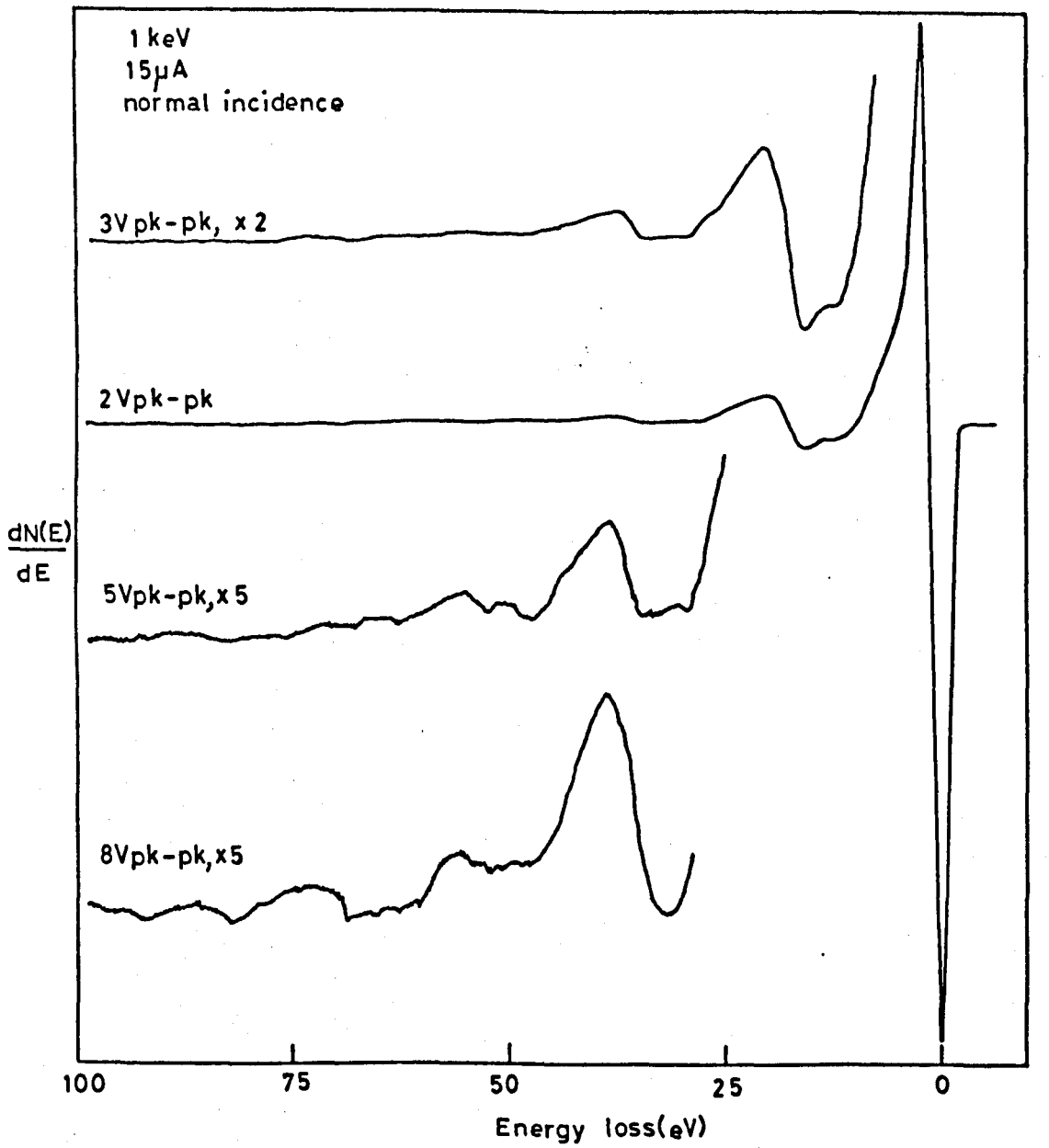

Figure 7.2 Energy losses of antimony (high gain)

If the intensities of the energy losses are compared to the intensity of the elastic peak, we see that the losses are relatively strong as compared to say those of platinum in the previous chapter. In fact, the intensity of the losses is comparable to those of the 'free-electron' metals, such as Be, Al and Mg.

If we now observe these energy losses as we vary the primary electron energy E_p and angle of incidence θ, we should be able to ascertain if these losses are due to plasma oscillation. As the angle of incidence approaches glancing, an incident electron will interact more strongly with the surface layers, and hence its probability of generating a surface plasmon and being elastically backscattered out of the surface (or vice versa) will be increased. Therefore as θ increases we may expect to see an increase in the signal strength of the surface plasmon loss, at the expense of the bulk plasmon loss. A similar interpretation may be used for the E_p variation case. As E_p falls, the incident electron has less penetrating power and tends to interact with the surface layer rather than the bulk, so again we may expect to see a relative increase in the surface plasmon loss.

We can see such effects on the plasma behaviour of antimony in Figs. 7.3 and 7.4. Fig. 7.3 shows the effect of a progressive increase in θ, on the energy losses. It is apparent that the loss at 11eV increases in size as θ increases, until at 45° it becomes larger than the 15eV peak. At 60° and 75°, the original peak at 15eV becomes a shoulder in the loss spectrum.

Fig. 7.4 shows the effect on the losses of a progressive change in E_p. Unfortunately as E_p falls so does the primary current, so that the amplifier gain was adjusted on the lower two plots to compensate this loss of sensitivity. However it is apparent that the 11eV energy loss

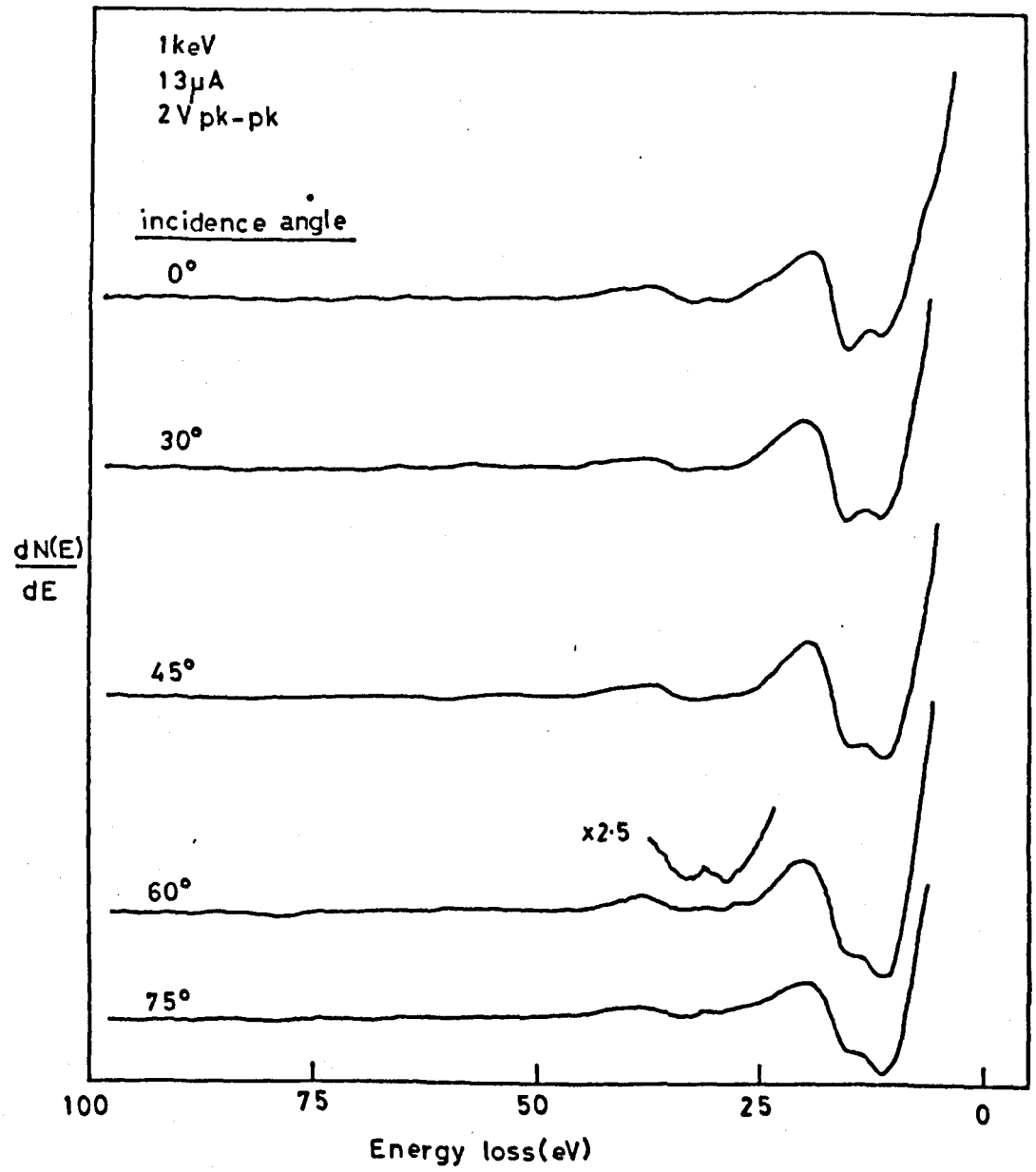

Figure 7.3 Energy losses of antimony with angle of incidence

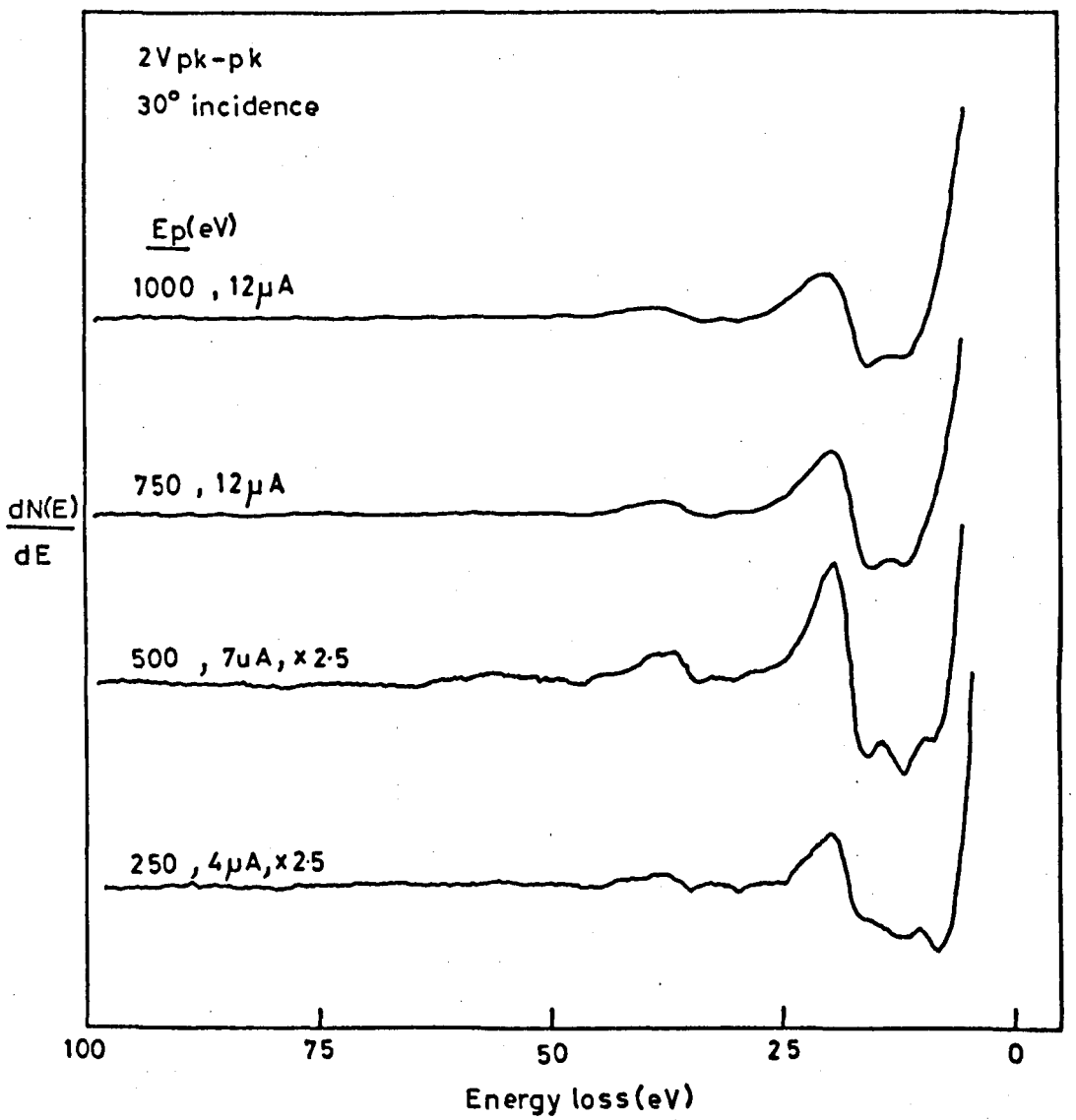

Figure 7.4 Energy losses of antimony with Ep

TABLE 7.2

Electron Energy Losses of Antimony

θ°	E_p(eV)	Losses (eV)	Figure
30	1,000	11,15,28,32	
30	750	11,15,28,32	7.4
30	500	7,11,15,28,32	
30	250	7,11,15, - 33	
0	1,000	11,15,28,32	
30	1,000	11,15,28,32	
45	1,000	11,15,28,32	7.3
60	1,000	11,15,28,32	
75	1,000	11,15, - 32	
0	1,000	11,15,28,32,47,52	7.2
		59,68,80,91	

TABLE 7.3

Assignments for the Energy Losses of Antimony (energies in eV)

Present Work	Sueoka[159]	Harris[155]	Powell[152]	Leder[156]	Assignment	Calc. Energy
7		6?		5.3	IB	
11		11.5	11.3		S	10.9
15	15.2	15.9	16	15.6	B	15.4
28		28	26.5	30.2	S+B	26.3
32		34	32.3		2B	30.8
					3S	32.7
		43				
47		49	48.8		3B	46.2
52					IB $(N_1\text{-}N_{2,3})$	53.6
59		63			4B	61.6
68					IB $(N_{2,3}\text{-}N_{4,5})$	67
80		81			5B	77
91					6B	92.4

S-surface plasmon, B-bulk plasmon, IB-interband transition

TABLE 7.4

Energy Levels of Antimony (Bearden and Burr[144])(eV)

$O_{2,3}$	O_1	$N_{4,5}$	$N_{2,3}$	N_1	M_5	M_4
2.1	6.7	31.4	98.4	152.0	527.5	536.9

increases in size relative to the 15eV loss, as E_p is lowered. On this occasion, a further peak was seen to develop at an E_p value of 500eV and below, becoming a major feature in the lower plot. Its energy value was 7eV.

All the observed energy losses for antimony have been collected and are displayed in Table 7.2.

7.3 Discussion and Conclusions

The presented results clearly show that antimony exhibits significant plasma behaviour. The energy losses at 11 and 15eV are thought to be due to surface and bulk plasmon losses respectively, due to their behaviour with θ and E_p variations. Assuming five free electrons per antimony atom, we can use equ. (4) (Chapter 1) to obtain a value of 15.4eV for the bulk plasmon energy. For a clean metal/vacuum interface, the surface plasmon energy would be 10.9eV. Hence, it is apparent that the assumption of free-electron behaviour for antimony, yields excellent agreement with the observed plasma loss values. The remainder of the energy losses can be interpreted in terms of combination and multiple plasmon losses apart from the losses at 52 and 68eV, which may be interband transitions.

Table 7.3 shows the assignments of the losses along with some observed values from other workers. The interband transition energies were calculated from the energy levels shown in Table 7.4. Multiple bulk plasmon losses may be seen down to the sixth order (6B) and only the single combination loss of bulk plus surface plasmon is seen at 28eV. The origin of the 7eV loss is a little obscure but two possibilities occur. An O_1-V interband transition is possible and also the surface plasmon energy may be shifted due to a dielectric overlayer (Equ. (5), chapter 1) partially covering the surface.

This strong plasma behaviour of antimony has prompted a consideration as to the possible reasons for its existence. The question may be put; why should a semi-metal like antimony exhibit this 'metallic' characteristic? If we look at the crystal structures of arsenic, antimony and bismuth in Group V_B, we see that the structure consists of double layers as shown in Fig. 7.5. Each atom has three close neighbours and three at a greater distance in the next layer. We may regard the double layers of antimony atoms, as constituting immense molecules in which the atoms are held together by simple co-valent linkages. The nature of the force which binds the double layers to one another was first thought to be of a van der Waals type, but the closest distance between atoms in adjacent chains is less than would be expected for normal van der Waals binding. In fact, von Hippel[158] has suggested that the bonding between adjacent chains probably involves some metallic character, owing to a resonance between molecular and ionic configurations. This conclusion may give us a clue as to the origins of the plasma behaviour in antimony.

Normally one considers an equilibrium number of charge carriers in a solid, many of which are produced by thermal activation. However, when a surface is bombarded by an energetic electron beam, a non-equilibrium situation occurs with a large charge carrier generation (i.e. the slow peak). It is therefore postulated, that in antimony, high electron densities are produced by the primary beam, in the 'metallic' region between the double layers of antimony atoms and subsequent plasma oscillation occurs in this region. Such primary beam effects must occur in materials like silicon, where the intrinsic carrier concentration is only 10^{10} cm^{-3} at room temperature, but nevertheless silicon shows strong plasma oscillation when activated by an electron beam. Charge carrier densities must be of the order of 10^{22} cm^{-3} in order to observe such strong plasma effects.

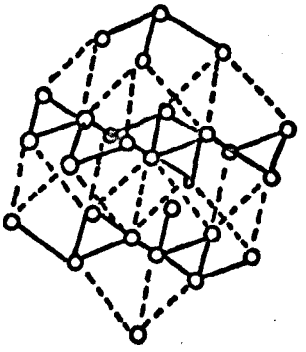

Figure 7.5 The crystal structure of antimony

(from Hume-Rothery[157])

We have seen that the characteristic energy loss spectrum of antimony is predominated by the effects of collective electron oscillation. Most of the observed energy losses have been interpreted in terms of combination and multiple plasmon losses, and good agreement was seen with calculated energy values. Also, a simple model has been suggested which qualitatively explains the relatively strong plasma effects.

We will now move on to Part 2 of the Results and Discussion of this thesis. Part 2 describes work on the slow peak spectroscopy of polycrystalline aluminium and magnesium, and perhaps represents the most fundamental work of this thesis. It is hoped that the results contained in the next two chapters will stimulate other workers to more fully investigate this sadly neglected area of secondary electron spectroscopy.

RESULTS AND DISCUSSION - PART TWO

Secondary Electron Emission Spectroscopy of Magnesium and Aluminium

CHAPTER 8

SECONDARY ELECTRON EMISSION SPECTROSCOPY OF MAGNESIUM

8.1 Introduction

Secondary electron emission spectroscopy of magnesium is complicated by the extreme reactivity of this surface with the UHV environment. All three energy regions of the secondary electron emission spectrum will be shown to be severely affected by surface oxidation.

The first part of this chapter will deal with the secondary emission properties of a clean magnesium surface, characterised by AES. Considerable fine structure has been observed in the low energy, 'true' secondary region (slow peak) and the detail and intensity of the structure is shown to be highly dependent on the modulating voltage applied to the retarding grids, even quite small voltages (about 1Vpk-pk) degrading the spectra considerably. The effects on this fine structure of variations in primary electron energy and angle of incidence, have also been investigated.

In addition, characteristic energy loss measurements were made with the same parameters (θ, Ep) in order to see if any correlation exists between the two types of characteristic phenomena. Losses due to interband transitions, surface and bulk plasmons and combination losses were easily identified from their variation with E_p and θ.

A tentative explanation of the slow peak structure is given in terms of transitions between critical points in the band structure of magnesium.

The second part of the chapter contains results concerning the effects of slow oxidation on this fine structure in the slow peak. In addition, the more well-known effects of oxidation on the energy loss and Auger spectrum of magnesium, have been included for completeness. A possible shifted surface plasmon loss and complimentary evidence for a feature in the slow peak of oxidised magnesium will be investigated.

Many changes occurred in the fine structure of the slow peak even before the first trace of oxygen was observed in the Auger spectrum, indicating that the technique may well be more sensitive to initial chemisorption changes than the corresponding Auger effect. Oxidation effects on the gross features of the slow peak are also presented and these are compared with recent published work.

The final section contains an analysis of the energy shifts of surface plasmons, as a dielectric overlayer thickness varies. The analysis shows that the accurate determination of such energy shifts will enable the evaluation of dielectric overlayer thicknesses, on surfaces of 'free-electron' materials. This calculation enabled a determination of the thickness of an MgO overlayer, when the Mg surface was fully oxidised.

8.2 Secondary Electron Emission Spectroscopy of Clean Magnesium

8.2.1 Auger Spectra

Clean magnesium thin film surfaces were prepared in the usual manner, by evaporation (or more correctly sublimation) of magnesium from tungsten wire baskets, onto a polished stainless steel substrate, in UHV. The magnesium was in the form of granules (purity 5N8), which were retained in the baskets with the use of fine tungsten mesh, placed across the mouthes of the baskets. Oxygen was allowed to build-up on the surface after each evaporation of magnesium and monitored by its Auger signal. Oxygen was found to be the only serious contaminant on such surfaces. After

many evaporations, the surface remained oxygen-free for several hours. The spectra in this first section were taken after this point had been reached.

A low energy Auger spectrum of a clean magnesium surface is shown in Fig. 8.1. This energy region encompasses the LVV Auger electron group. The large peak at 45eV has both a high and low energy satellite peak; the higher being about 35 times smaller than the main peak. These satellite peaks occur at 35.0 and 58.5eV. Under high resolution, the lower peak is seen to split to form an additional shoulder at about 30eV.

The KLL Auger electron group from magnesium is shown in Fig. 8.2. These peaks are relatively weak and some of the smaller ones are lost in the noise level. However, the observed peaks are seen at 1181, 1171, 1159, 1146, 1135, 1123 and 1098eV. The modulation voltage was limited to 10Vpk-pk in order to resolve these peaks with 10eV spacings.

8.2.2 Slow Secondary Electron Spectra

Extensive fine structure has been observed in this region of the secondary electron energy spectrum. The number of peaks detected is found to increase sharply as the applied modulation is reduced. Fig. 8.3 shows that a modulation amplitude of 2Vpk-pk yields two peaks (3.3eV and 6.2eV) with a shoulder at 10.2eV. This value of modulation is commonly used by many workers in the low energy region, but the remaining plots of Fig. 8.3 indicate that this value is too large for high resolution performance. As the modulation amplitude is reduced, considerable fine structure appears and a total number of 15 peaks have been observed.

Fig. 8.4 shows the effect of variation in primary electron energy on the slow peak at normal incidence. In this series of plots the instrumental sensitivity was kept constant by using a fixed primary current. It may be seen that the structure is enhanced as E_p is reduced and an anomalous variation of the amplitude of the 2eV doublet with E_p is apparent. Some peak amplitude variations will be caused by changes

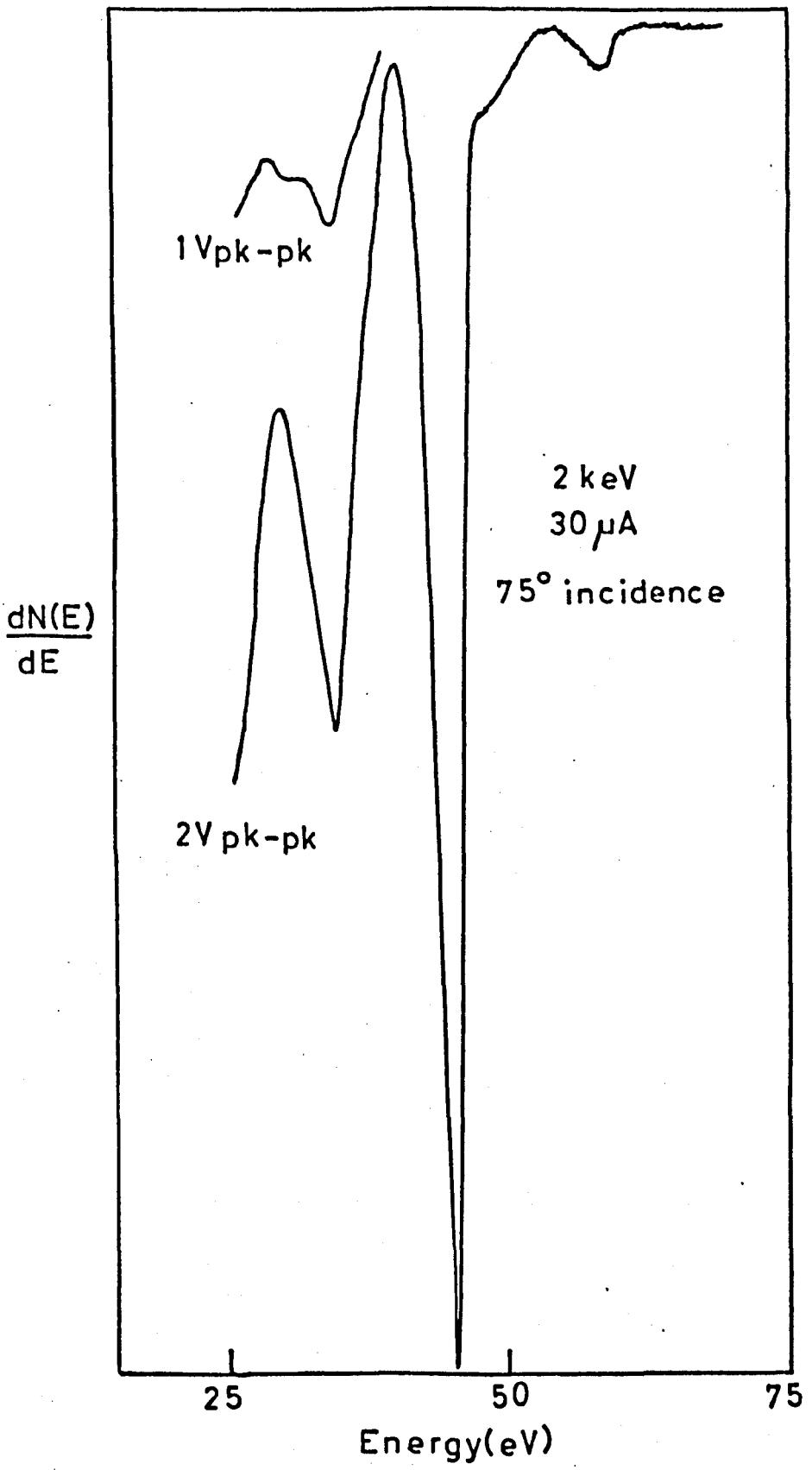

Figure 8.1 Low energy Auger spectrum of clean Mg

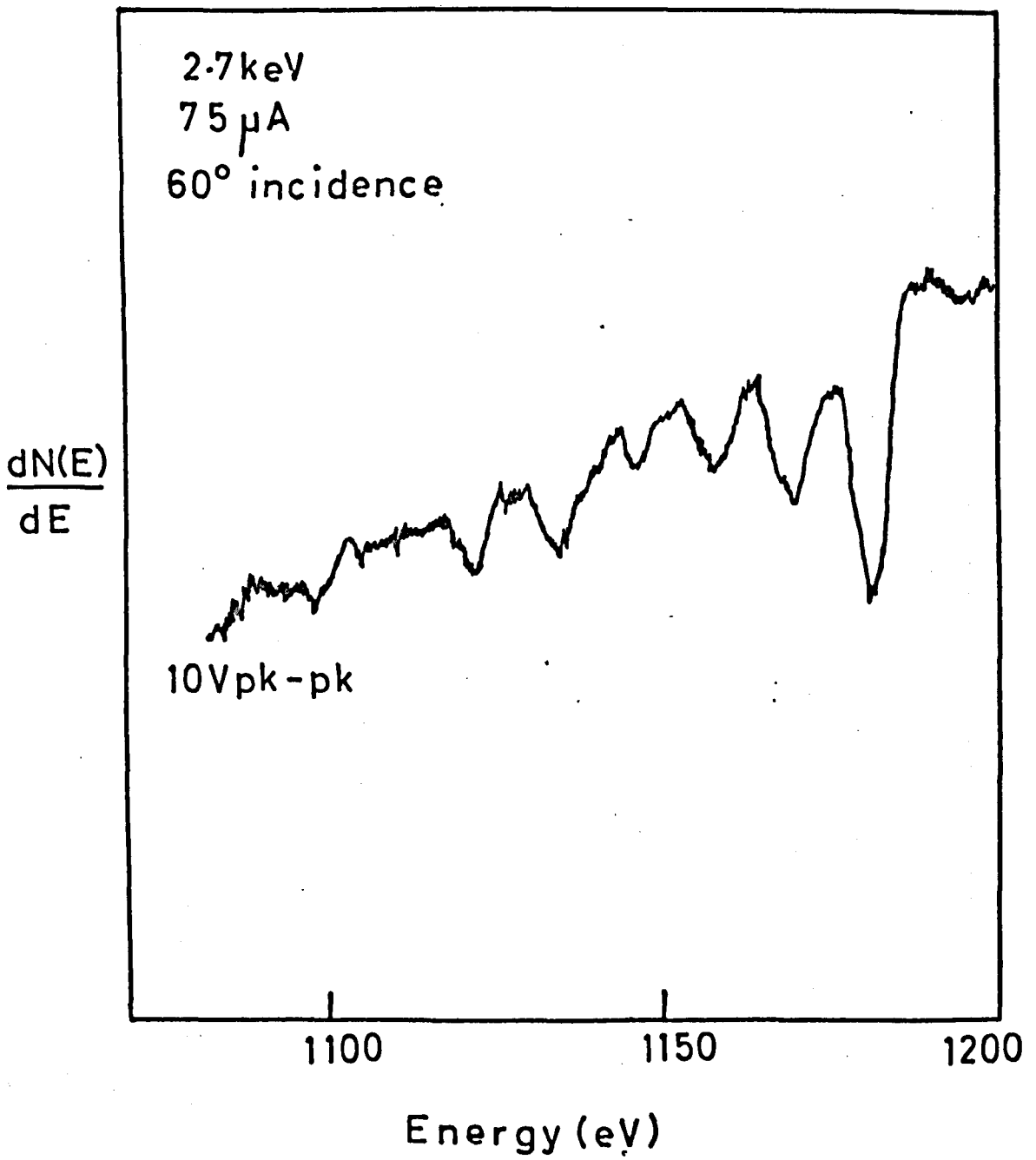

Figure 8.2 High energy Auger spectrum of Mg

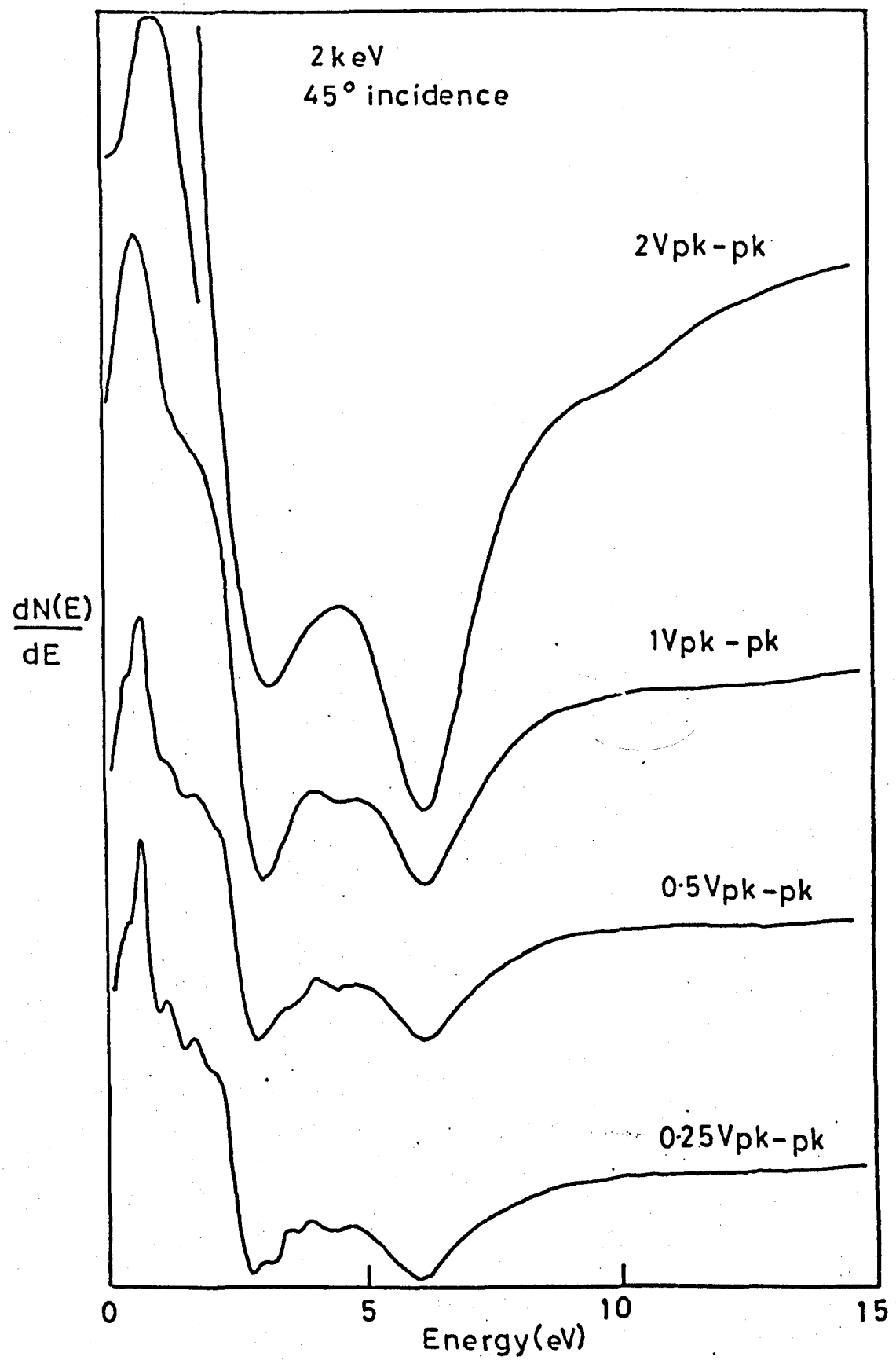

Figure 8.3 Slow peak from Mg surface with different applied modulation voltages

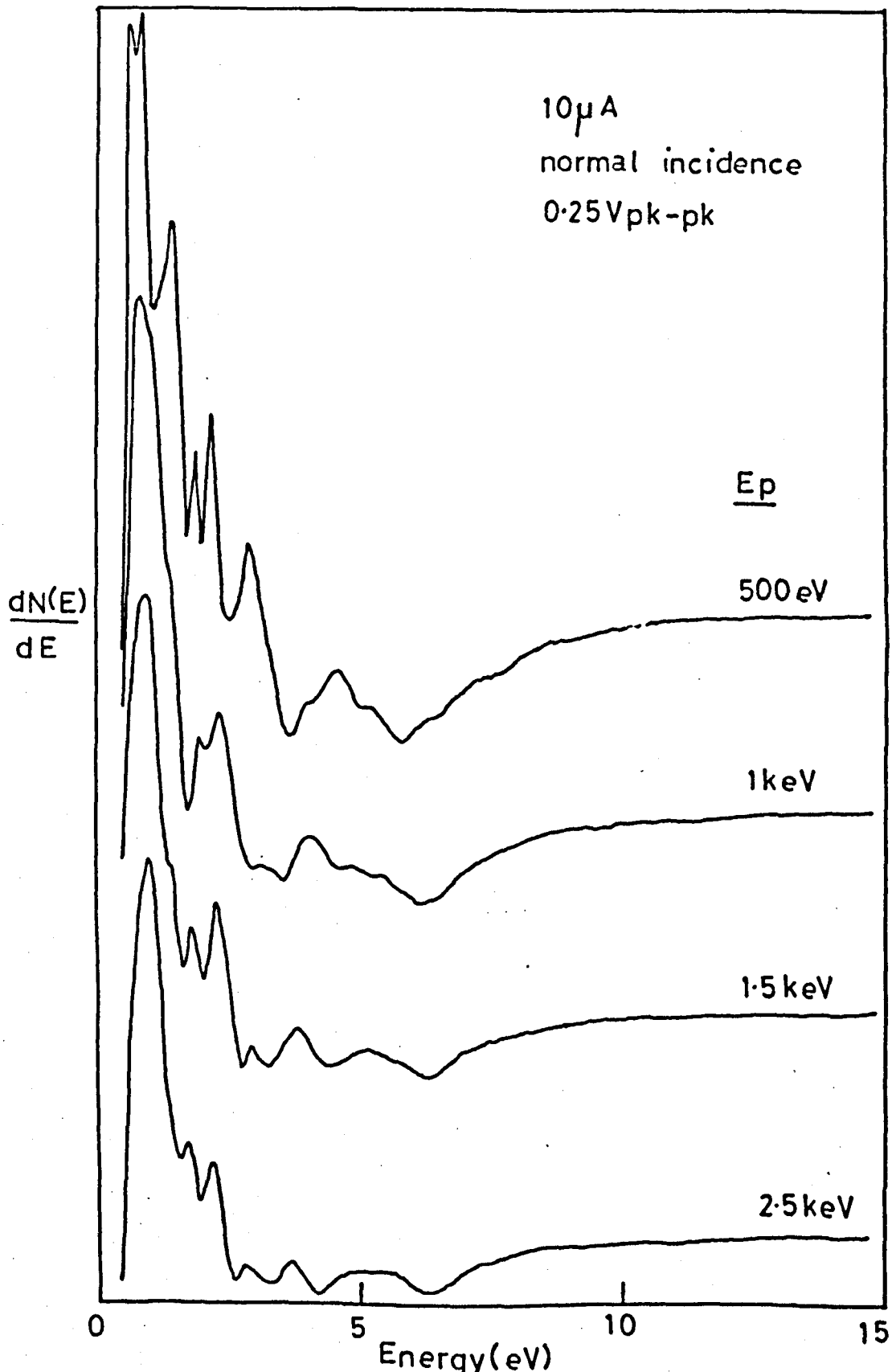

Figure 8.4 Slow peak of Mg surface with different primary electron energies

in the background slope as E_p varies. Normal incidence and a primary energy of 500eV were found to be the best conditions for the observation of the fine structure.

Figs. 8.5a and 8.5b show the effect of variation of incidence angle on the slow peak, using a fixed primary energy. Here of course, the size of the slow peak becomes smaller as θ tends to 0°, but in addition, the fine structure becomes clearer with smaller values of θ. One interesting feature is the reappearance of the 2eV doublet on the 65° plot. In Figs. 8.4, 8.5a and 8.5b, the strongest peaks appear at about 3eV and 6eV, in common with the gross features of the spectrum seen in the upper curve of Fig. 8.3

8.2.3 Electron Energy Loss Spectra

An attempt was made to observe a correlation between the characteristic energy losses of magnesium and the characteristic 'energy gains' observed in the slow peak. Modulation voltages as low as 0.25Vpk-pk were used to observe the elastic peak and the energy region immediately below it. Primary electron energies from 250eV to 1000eV were used with different angles of incidence but on no occasion was fine structure, comparable with that in the slow peak, observed in the loss region.

The top curve of Fig. 8.6 shows that by using a modulation of 5Vpk-pk, bulk plasmon losses down to the 7th order may be seen; the peaks occurring at intervals of 10.6eV from the elastic peak. The remaining curves in the figure show the effect of angle of incidence variation on the characteristic energy losses. As θ increases, the loss at 7.4eV grows with respect to the 10.6eV loss, indicating that the losses are due to surface and bulk plasmons respectively. At 75° incidence, the 7.4eV loss is predominant and multiple surface plasmon losses are seen down to the 4th order at 29eV. However, the loss at 10.6eV remains fairly constant with θ variation, indicating that this bulk plasmon peak may have an additional contribution from a 'surface sensitive' loss.

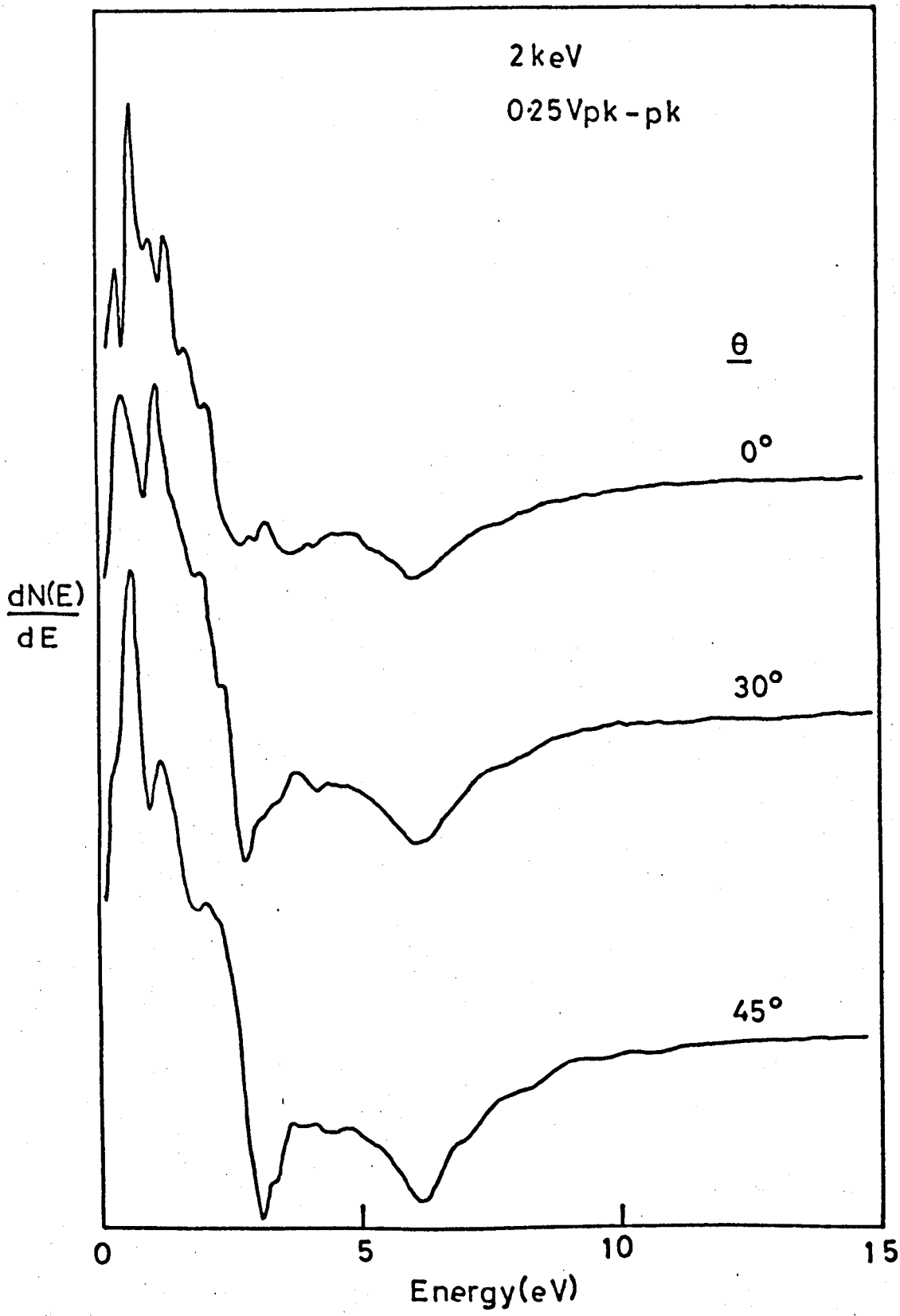

Figure 8.5a Slow peak from Mg surface with different angles of incidence θ

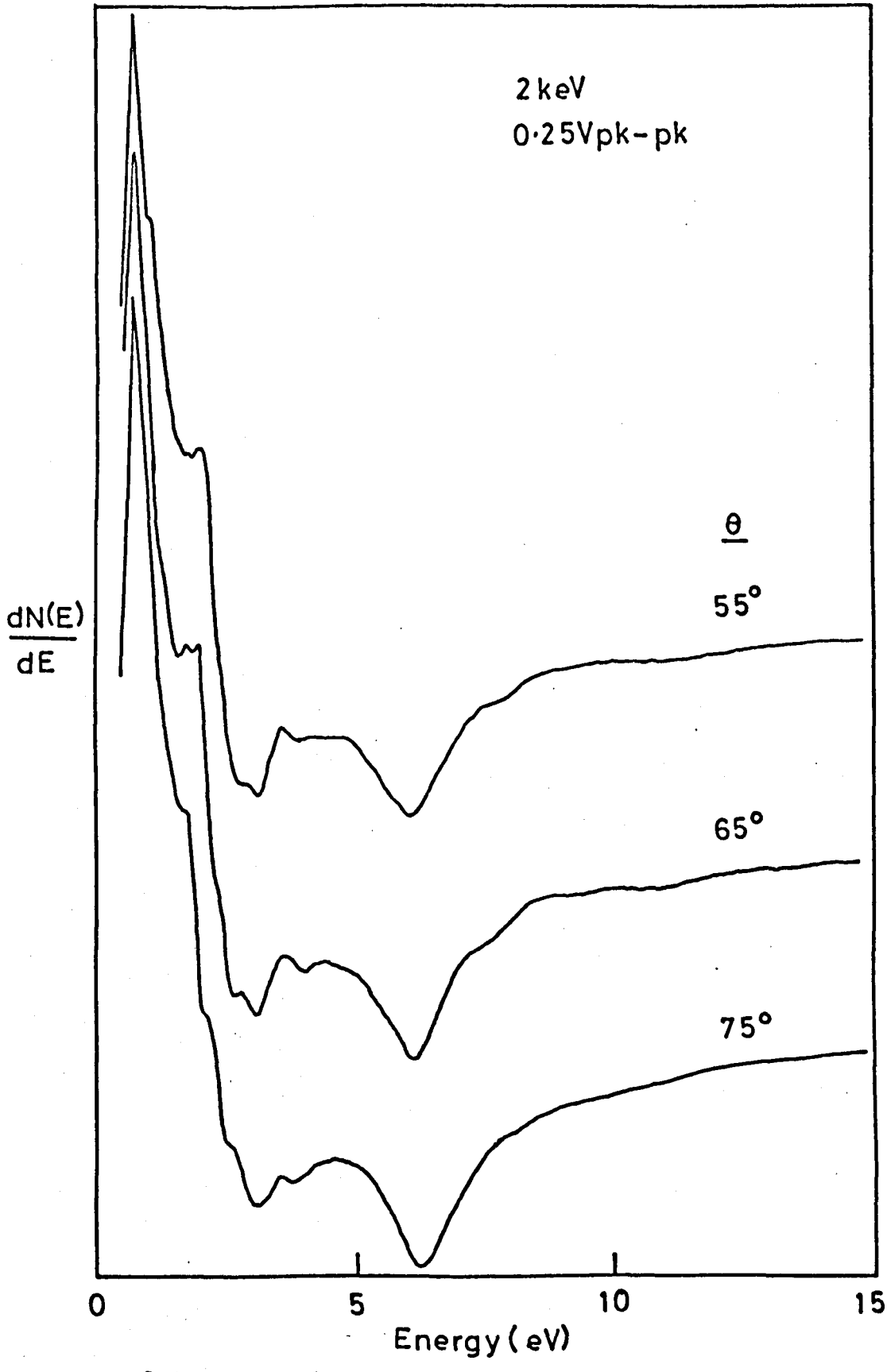

Figure 8.5b Slow peak from Mg surface with different angles of incidence θ

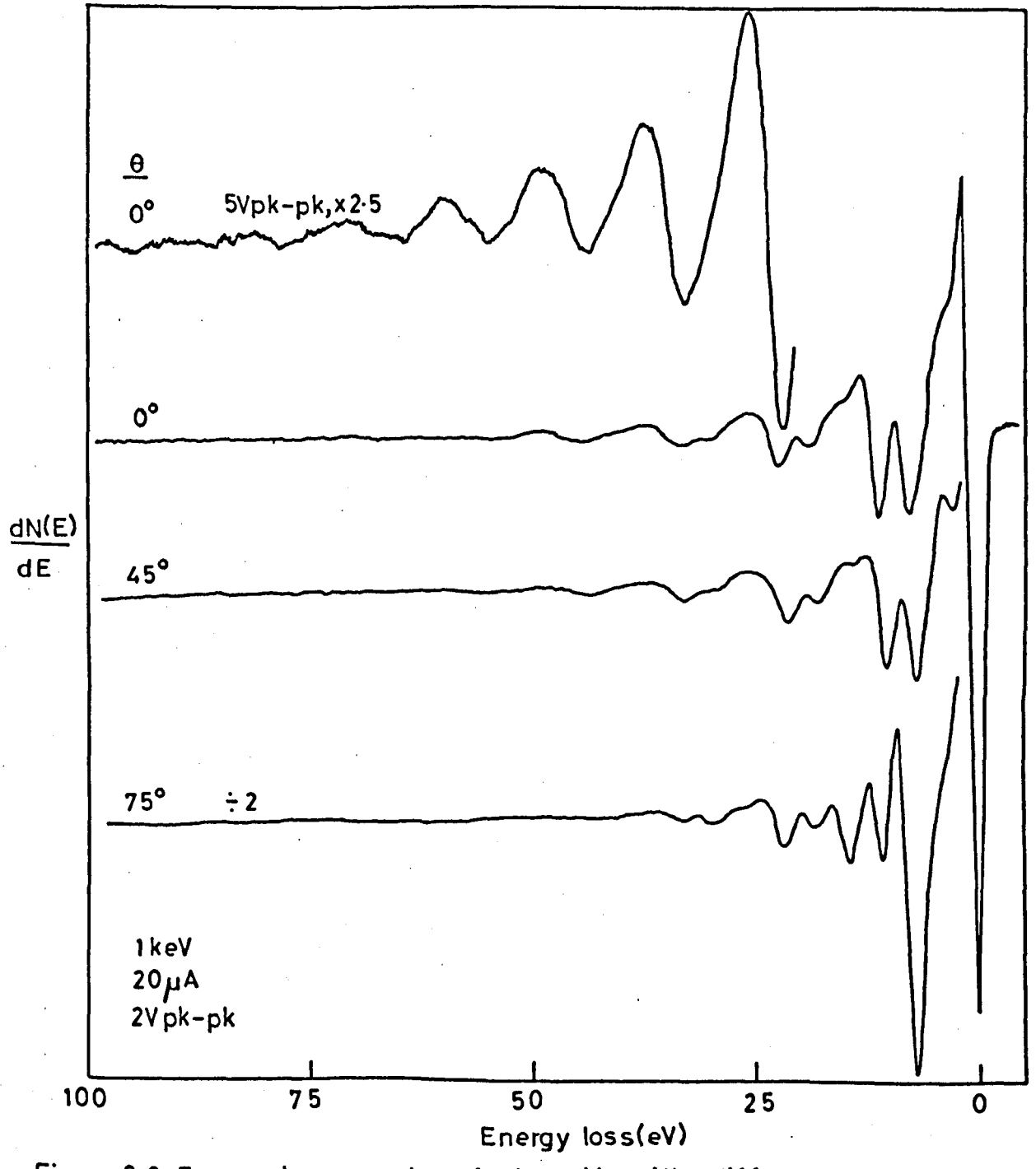

Figure 8.6 Energy loss spectra of clean Mg with different angles of incidence θ

TABLE 8.1

High and Low Energy Auger Electron Energies from Clean Magnesium (energies in eV)

Present work	Suleman & Pattinson[161]	Palmberg et. al.[49]	Jenkins Chung[85]
			26
30	31		
35.0	35	34	35
	37.5		38
45.0	45	45	45.6
58.5	58.5	58	59
		1085	
1098		1096	
		1106	
		1118	
1123		1129	
1135		1140	
1146		1153	
1159		1164	
1171		1175	
1181		1186	

Fig. 8.7 shows the effect of primary electron energy variation on the energy losses of magnesium. As the primary electron energy is reduced, the 7.4eV loss becomes stronger than the 10.6eV loss, again indicating the surface and bulk plasmon roles. The loss at 14.5eV intensifies as E_p rises, which indicates a contribution from a 'bulk sensitive' loss. The observed values of the energy losses, together with their assignments will be tabulated and discussed in the following sub-section.

8.2.4 Discussion

The discussion of the presented results will be split up into the three areas of work, namely AES, slow peak and energy loss spectroscopy of magnesium. The interelationships between the areas will be examined when found necessary.

Low energy AES of magnesium has been thoroughly investigated by a number of workers including Suleman and Pattinson[161], Salmeron et.al.[88], and Jenkins and Chung[85]. The high energy KLL Auger spectrum is less well documented and in fact so far as is known, only Palmberg et. al.[49] have published this spectrum. The energy values for the LVV and KLL Auger electrons found in this present work are presented in Table 8.1, along with values obtained from other workers. Most workers seem to agree on the low energy peak values apart from the weaker peaks of 26, 31 and 37eV. Suleman and Pattinson[161] have attributed the 26eV peak to an oxidation effect i.e. not characteristic of a clean magnesium surface. In the KLL energy region, Palmberg et. al.[49] have observed more energy structure than myself due to the use of the more sensitive cylindrical mirror analyser. However, the larger features have been resolved, but in my case the values appear to be consistently lower than his, by about 5eV. An explanation for this is not evident.

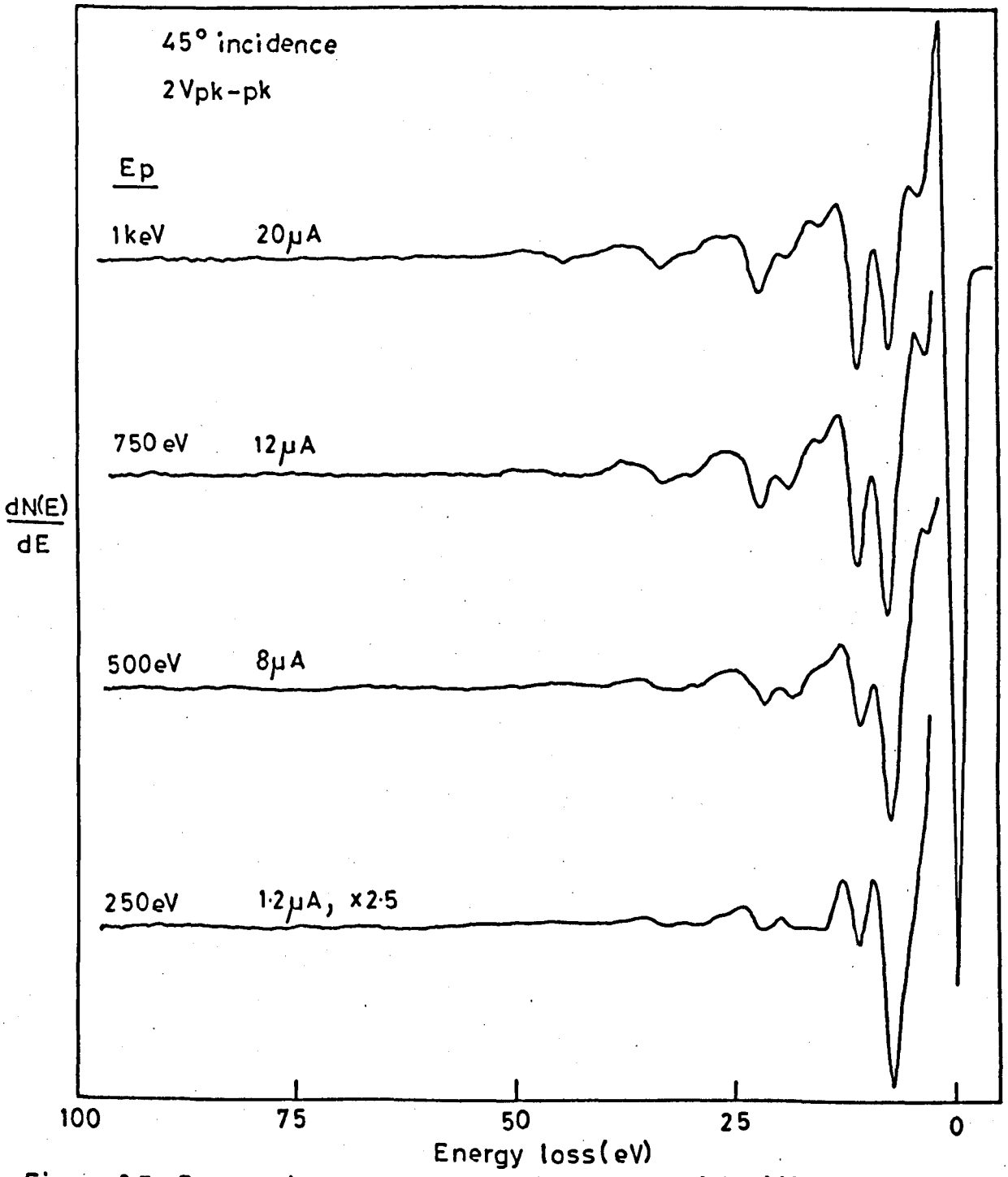

Figure 8.7 Energy loss spectra of clean Mg with different primary electron energies

TABLE 8.2

Magnesium Auger Peak Assignments

Transition	Calculated Energy (eV)	Observed Energy (eV)
$L_1L_{2,3}V$	33.5	30
PL	34.4	35.0
$L_{2,3}VV$	46.9	45.0
$(L_{2,3})_2VV$	59.0*	58.5
KL_1L_1	1093.4	1098
PL(?)	1127.4	1123
$KL_1L_{2,3}$	1138	1135
3PL	1149.2	1146
2PL	1159.8	1159
PL	1170.4	1171
$KL_{2,3}L_{2,3}$	1176	1181

PL - Bulk plasmon loss from experimental values of main transition

V - Fermi level

* from Salmeron et. al.[88]

The various assignments for the Auger peaks and calculated energy values are shown in Table 8.2. Assignments for the LVV energy region have been adequately discussed in the literature[85,87,88] and will not therefore be discussed here, except to confirm basic agreement with these other workers.

All three KLL Auger electron peaks were observed in the present work, if the assignments of Table 8.2 are correct. One puzzling feature of the largest peak ($KL_{2,3}L_{2,3}$ at 1181eV) is the occurrence of three relatively intense plasmon loss satellite peaks. Palmberg et. al.[49] have also observed these peaks as strong satellites. Obviously, these higher energy electrons will have a larger escape depth (20-30 Å) and will therefore have a greater chance of creating plasmons before escaping. Also, as pointed out in Chapter 2, plasmon creation may be enhanced by ionisation processes[119], which may be an additional reason for these strong losses.

With the aid of AES, we have characterised the surface on which the slow peak and energy loss measurements were made. Since there is good agreement between these AES results for magnesium and the results of other workers, it is now permissible to compare and criticize the other features of the secondary electron energy distribution, in relation to recently published results.

Fig. 8.3 has shown that when using 2Vpk-pk modulation, three peaks may be seen in the slow peak spectrum at 3.3, 6.2 and 10.2eV. These results compare favourably with those of Jenkins and Chung[85], who found peaks at 3.5, 7 and 11eV. However, their use of such high modulations (and perhaps a poorer instrumental resolution) did not enable their spectrum to show up the full structure of the slow peak.

An explanation of the origin of the fine structure observed in Figs. 8.3 - 8.5b, must obviously go further than that suggested by Jenkins and Chung. They concluded that two peaks originated from the plasmon gain mechanism (sub-section 2.3.1). Later, it will be shown

that the peak near 11eV is in fact characteristic of a partially oxidised surface, so that we need not consider this peak here. Jenkins and Chung did not realise this fact and so left open the question of exact peak origins. With the assumption of a work function correction of 4.5eV for the analysing grids, the original peak energies at 3.3 and 6.2eV become 7.8 and 10.7eV with respect to the magnesium Fermi level. These energy values are in close agreement with the surface and bulk plasmon energies (7.4 and 10.6eV respectively), and it seems possible that Fermi level electrons may therefore undergo this energy gain. Also from an electron population viewpoint, this process seems more likely than an energy gain in the slow peak electrons[85,96].

However, it is still not clear whether these gross features are produced by fine structure combinations, or are a completely distinct phenomenon. Evidence presented later on the oxidation effects, will tend not to support a plasmon gain hypothesis. The position at this time with regard to these gross features is therefore not fully settled.

Two mechanisms are offered at present to explain the origin of the slow peak fine structure. Firstly, electrons may be excited into energy states above the vacuum level and may leave the surface with an energy characteristic of their parent state (Willis et. al.[103]). Secondly, if a direct transition occurs between symmetry points in the Brillouin zones, this energy may be given to an electron causing it to be emitted from the surface (a $C_A C_B C_C$ Auger electron, where $C_{A,B,C}$ are the conduction band symmetry points involved). Unfortunately the data from Figs. 8.3 - 8.5b do not help to resolve the mechanism choice, since no systematic variation of peaks is seen. One major problem is the change of background slope, from one plot to another, which will alter peak strengths and positions. This problem is currently being tackled[162].

The 'direct emission' mechanism requires a knowledge of the high-energy band structure of magnesium, in order to test its predictions.

TABLE 8.3

Observed Slow Peak Energies and Calculated Symmetry Point Transitions for Mg (energies in eV)

Observed Peaks	Calculated Symmetry Point Transitions, brackets indicate symmetry line of transition
0.4*	0.3(M), 0.3(H), 0.55(K), 0.6(M)
0.8	0.8(M)
1.1*	1.1(M)
1.7*	1.6(L)
2.0*	
2.2	
2.5*	2.61(H)
3.0*	2.78(Γ), 2.89(H)
3.5	
4.0	
4.4	
5.1	5.05(M), 5.35(M), 5.66(M), 5.95(M)
6.2*	6.15(M), 6.76(M), 6.7(M)
7.6	8.1(Γ)
10.2	

* strong peaks

So far as is known, this information is not available in the literature so that the question remains open. Some correlation was found however, between the $C_AC_BC_C$ Auger mechanism and the observed energy values, if one makes the assumption that the transition energy is given to electrons close to the vacuum level. Table 8.3 lists the values of observed peaks along with the theoretical transition energies between symmetry points. The energies of the symmetry points were obtained from the energy band diagram of magnesium as calculated by Falicov[160]. The appropriate symmetry points and lines of the Brillouin zone are illustrated in Fig. 8.8.

The agreement in Table 8.3 is somewhat limited and the gaps in the table cannot be simply explained at present. It is possible that Tamm state (surface state) transitions may have an additional influence on the spectra. The strong peaks at 0.4, 3.0 and 6.2eV may be due to a high density of states at the H and M symmetry points (Fig. 8.8) owing to their position on the Brillouin zone. The large width of the peak at 6.2eV could be accounted for by the large spread in transition energies in this region (5.0eV - 6.8eV) along M symmetry lines.

The plasmon energies of magnesium are well-known[85,113] and other workers' results are in reasonable agreement with those presented in Table 8.4. The table combines both Figs. 8.6 and 8.7 and gives all the losses observed together with their identification.

Fig. 8.6 indicates that the loss at 7.4eV is highly surface sensitive and its identification as a surface plasmon loss agrees well with the theoretical value of 7.7eV, assuming two free electrons per Mg atom. Surface plasmon losses are visible down to the 4th multiple in the 75° plot, although the 3rd multiple loss coincides with the 2nd order bulk plasmon loss. The loss at 10.6eV remains fairly constant with θ variation indicating a possible contribution from a combination loss of the surface plasmon plus the 3.5eV loss.

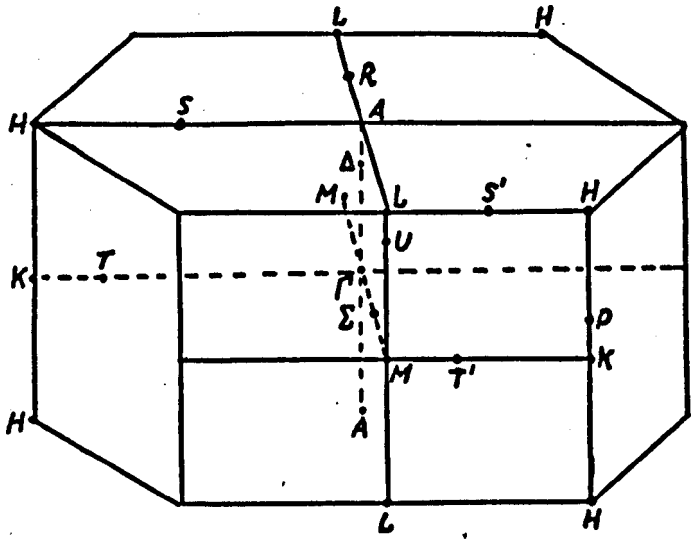

Figure 8.8 The Brillouin zone in the h.c.p. structure showing points and lines of symmetry (from Falicov[160])

TABLE 8.4

Observed Energy Losses for Mg (in eV) with Assignments

Observed Loss	Assignment
3.5	I
7.4	S
10.6	B and S+I
14.5	2S and B+I
18.5	S+B
21.6	2B and 3S
29.3	4S
32.3	3B
42.8	4B
54	5B and I
64	6B
76	7B

I - Ionisation or interband transition: B - bulk plasmon loss;

S - Surface plasmon loss

In Fig. 8.7, the increase in the size of the loss peak at 14.5eV as E_p rises shows a possible contribution to the peak, from a combination loss of bulk plasmon (10.6eV) plus the loss at 3.5eV. The fact that the loss at 18.5eV stays reasonably constant as E_p is varied is good evidence for the assignment of a combination loss of surface plus bulk plasmon.

From these results it appears that the fine structure observed in the slow peak of magnesium has no correlation with characteristic energy loss structure, although from a sensitivity viewpoint, such fine structure losses may well be difficult to observe.

8.3 Secondary Electron Emission Spectroscopy of a Slowly Oxidising Magnesium Surface

After the foregoing results had been taken, a further evaporation of magnesium was performed. This film was then allowed to oxidise slowly from the residual oxygen present in the UHV chamber. Whilst this slow oxidation occurred, secondary electron emission spectroscopy was performed intermittently on the surface, over a period of about four weeks until the surface became fully oxidised.

During this oxidation, only oxygen was found to be a major contaminant, but after the four week period was over, a small triplet of peaks was found near 100eV whose origin is unknown. This new magnesium film was thought to be less contaminated than the previous film (even though no contaminants were detected by AES) and evidence for this conclusion will be presented. In fact, this magnesium film was perhaps the twentieth film deposited, after about four weeks of evaporations without let-up to atmosphere.

8.3.1 Auger Spectra

Since changes were observed in the magnesium slow peak spectrum prior to the observation of the oxygen Auger peak, the elapsed time from film preparation will be quoted in the following figures, as well as the corresponding oxygen Auger peak scans. Initially, Auger spectra were taken using an E_p of 2keV and a primary current of 50μA so as to minimise electron beam effects during the first oxidation stages. Subsequently, an E_p of 2.7keV and a primary current of 80μA were used for the detection of oxygen (indicated by the approximate x2 factor in the following figures) The Auger spectra of oxygen were taken using a modulation voltage of 16Vpk-pk to maximise detection.

An attempt was made to obtain a rough estimate of the monolayer sensitivity to oxygen in our apparatus by applying the results of Vrakking and Meyer[58]. Our instrumental parameter values were used in

their equation for Auger current (Equ. (8), Chapter 2) and our electronic detection apparatus assumed to be similar to their detection equipment. With this latter assumption we were able to arrive at a figure of about 1% of a monolayer of oxygen for the limit of detection, using a normal incidence electron beam. This lower figure assumes that the oxygen lies purely at the surface, and is not distributed in the 'sensitive' volume detected by AES. The first oxygen Auger peak was resolved at 135 hours after film preparation, thus very approximately, this signal could be taken to represent 2% of an oxygen monolayer.

Figs. 8.9a-c show the effects of progressive oxidation on the low energy Auger peaks of magnesium. The initial effect is the rapid attenuation of the 45eV peak, coincident with the growth of the 35eV peak and the oxygen Auger peak. Also, a slight discontinuity develops at about 26eV. After 530 hours, the surface is fully oxidised, with the main peak at 45eV disappearing almost completely and the peak at 35eV becomes the largest peak in the spectrum (Fig. 8.9c). The original peak at 58.5eV is still seen as a shoulder at about 58eV. At this stage, a large triplet oxygen Auger peak was found at 508, 490 and 472eV.

8.3.2 Slow Secondary Electron Spectra

Slow peak spectra were taken using modulation voltages of 0.25, 1.0 and 2Vpk-pk, at normal incidence and with a primary electron energy of 500eV. A modulation voltage of 0.1Vpk-pk was used to check that no further fine structure was observable. In the actual experiments many more intermediate curves were in fact taken, but for the sake of clarity the slow peak spectra shown in the following figures are representative data only.

It is well known in the field of AES that surface contaminants (O, S, C etc.) have a predominant effect on the low energy Auger peaks. Hence, it was thought that fine structure in the slow peak may well be 'ultra' sensitive to the presence of surface contaminants. Several slow peak spectra were therefore taken during the first few hours after the

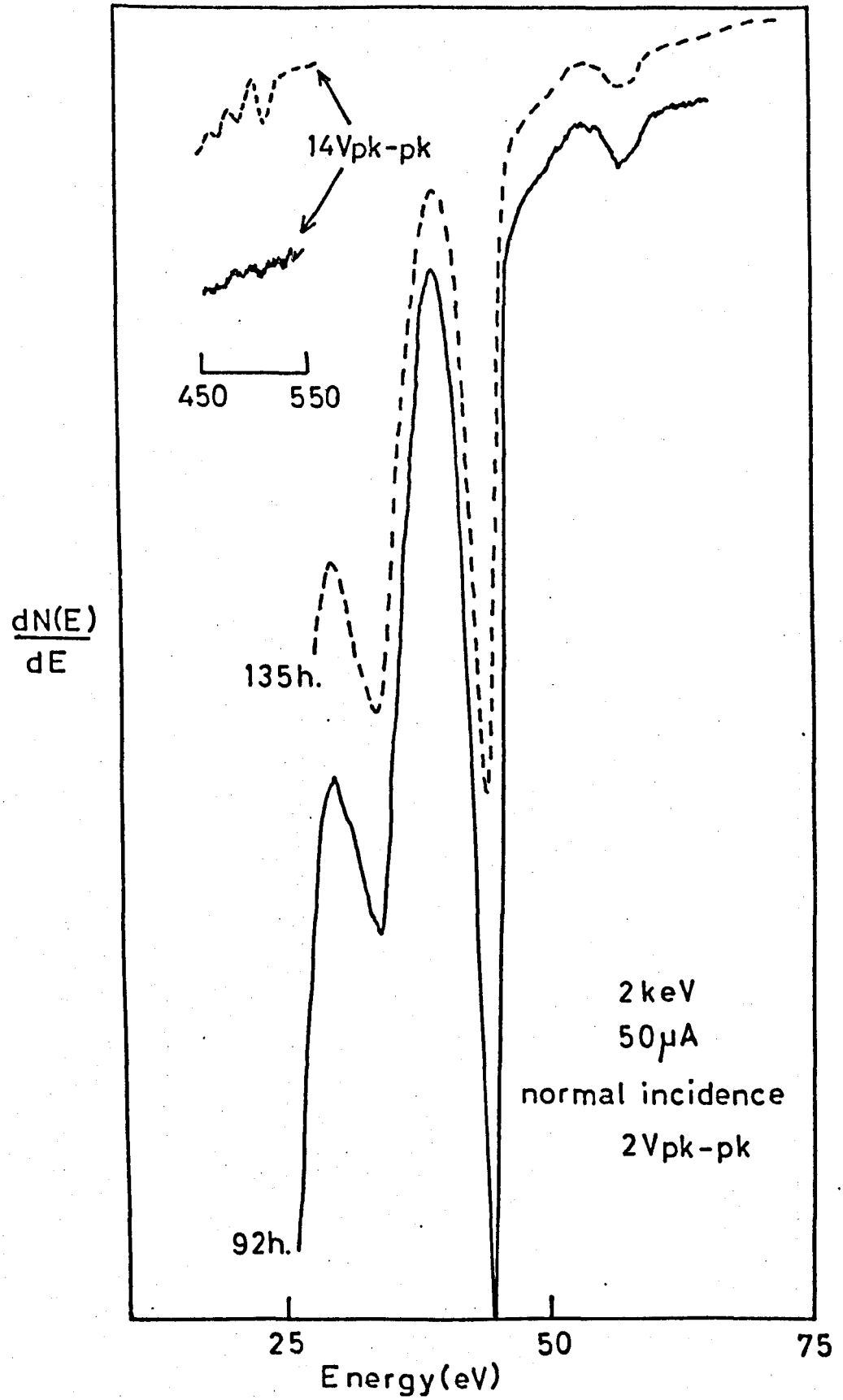

Figure 8.9a Successive oxidation effects on the Auger spectrum of Mg

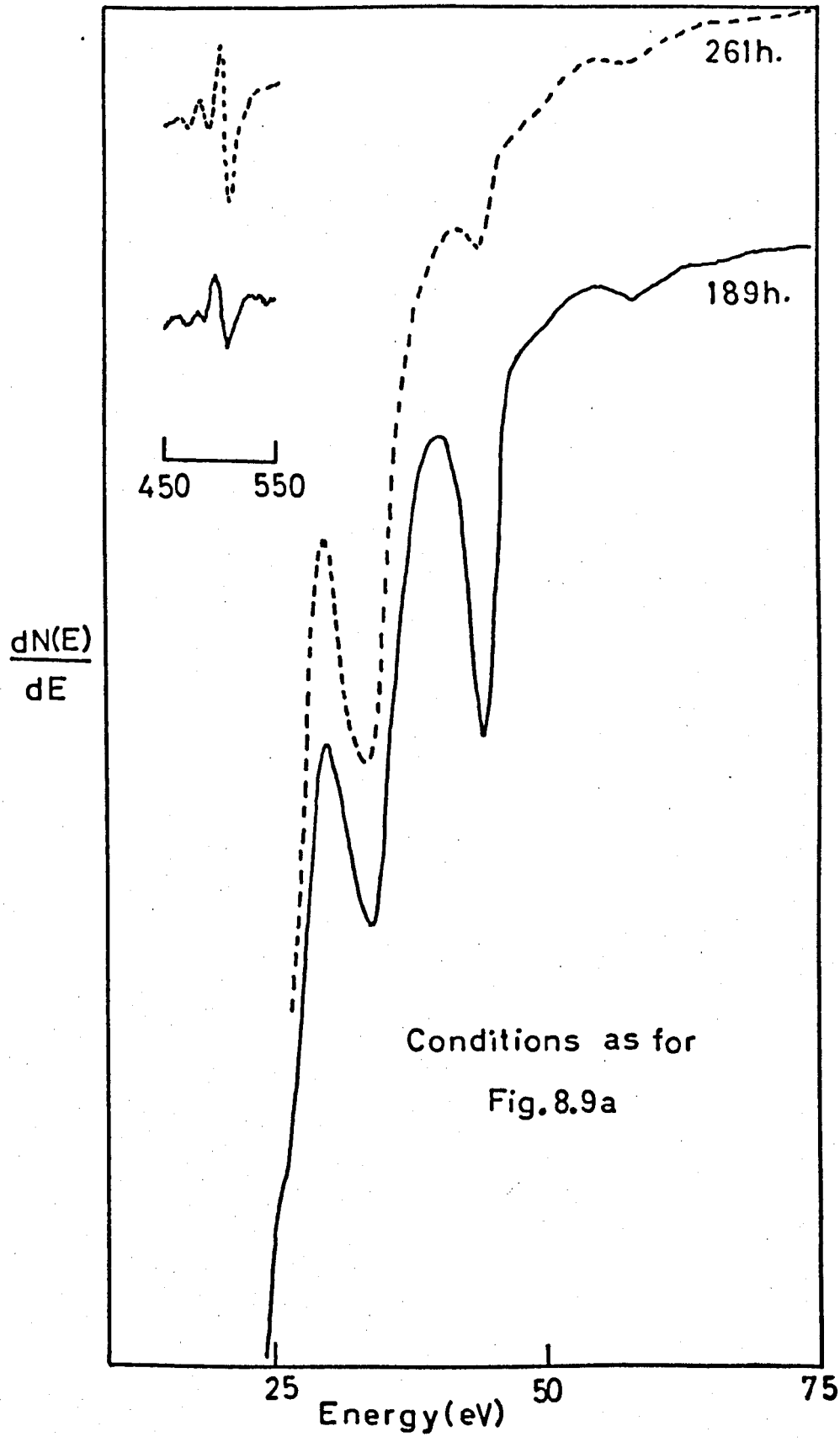

Figure 8.9b Successive oxidation effects on the Auger spectrum of Mg

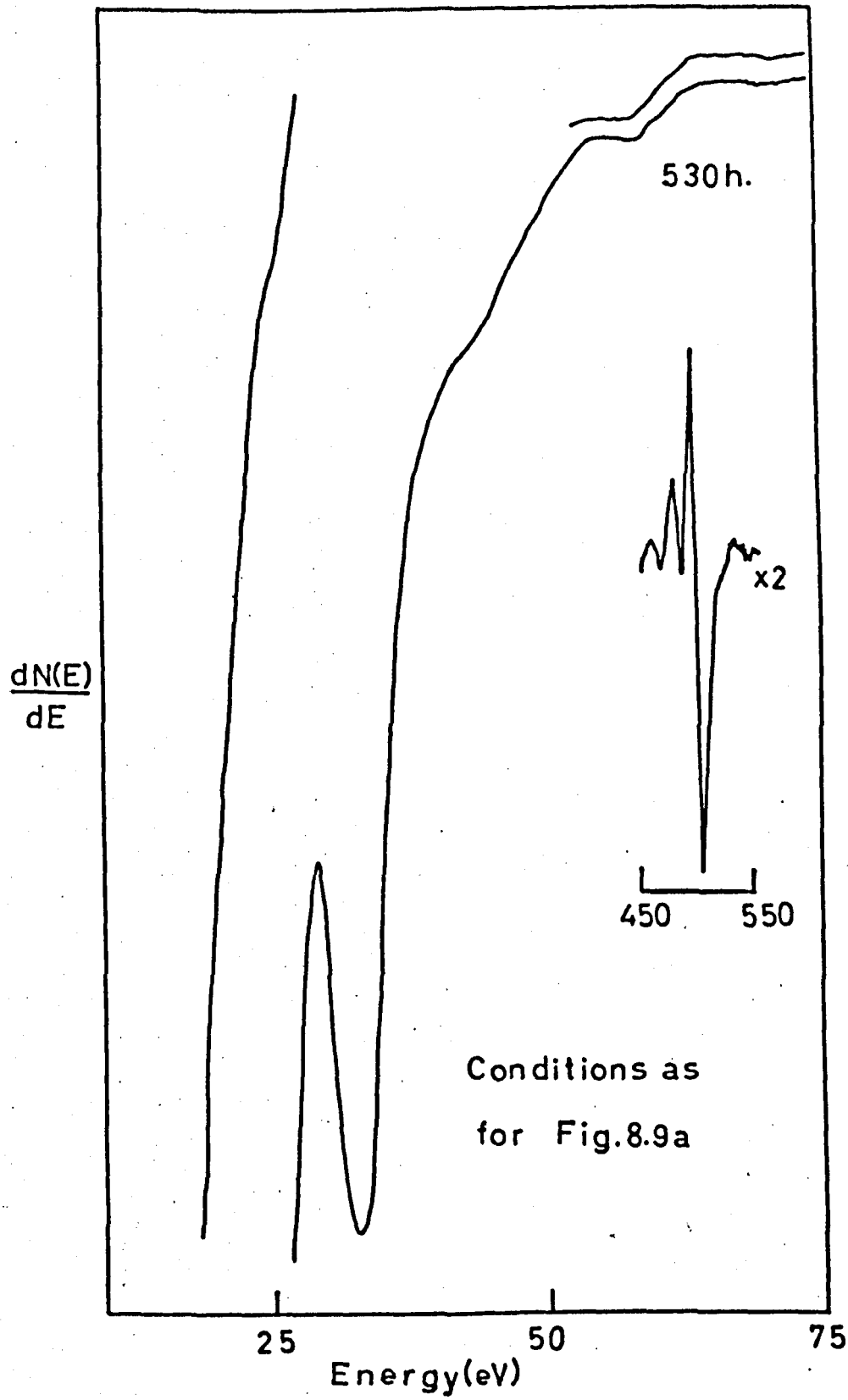

Figure 8.9c Auger spectrum of fully oxidised Mg surface

clean magnesium surface was produced and are shown in Fig. 8.10a. The time shown with each curve is the elapsed time from the production of the clean magnesium surface. During the first two hours, peaks at 1.4 and 1.7eV weaken whilst new peaks at 4.2, 4.8 and 5.8eV strengthen. Also, the total intensity increased as may be seen (note x $\frac{1}{2}$ scale factor). The oxygen levels corresponding to each spectrum are plotted on the right of the figure and show no detectable oxygen contamination above the noise level. As the elapsed time increases to 87 hours (Fig. 8.10b), the peaks at 0.9 and 1.6eV become stronger and many changes occur in the smaller peaks between 2.6 and 6.3eV. It is worth noting that the 87 hour curve of Fig. 8.10b shows a good resemblance to the corresponding curve of Fig. 8.4 (500eV plot), perhaps indicating slight contamination of this earlier magnesium film. One important emerging feature is the peak at 3.6eV, which has a strong influence on the gross features of the spectrum shown later.

Figs. 8.10c and 8.10d show the slow peak as the oxygen Auger signal progressively increases. The peak at 1eV is strengthening whilst peaks at 2.0 and 6.0eV are weakening. Also, a peak develops at 4.8eV, strengthens and shifts to 4.2eV. The large peak at 3.2eV, also strengthens and shifts to 2.6eV. Again, the general intensity of the slow peak has increased which is in accordance with the known larger secondary yield values for insulating surfaces such as MgO. At about 300 hours after the production of the clean magnesium surface, the slow peak spectrum becomes stabilised. The 470 hour plot shows a slight dip at 11eV which was better resolved with more gain (x 10) and is shown in Fig. 8.10d. This peak was more prominent in the gross feature spectra of Figs. 8.11a and 8.11b. However, at this point it should be mentioned that this peak width (about 2eV) is much greater than that of other peaks in the fine spectra. Hence it was thought that this new peak may well have a different origin to that of the other fine structure.

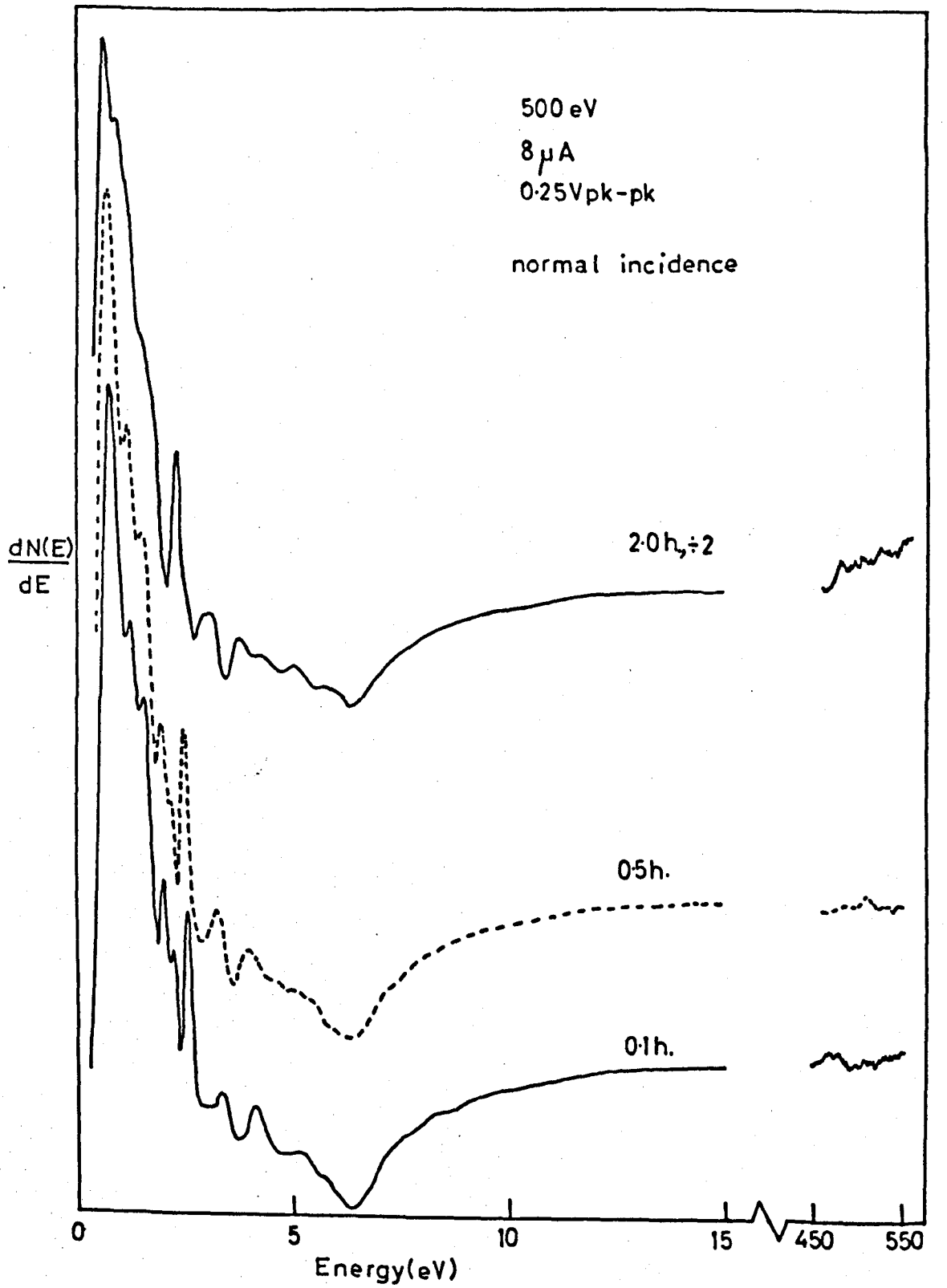

Figure 8.10a Successive oxidation effects on the slow peak fine structure of Mg

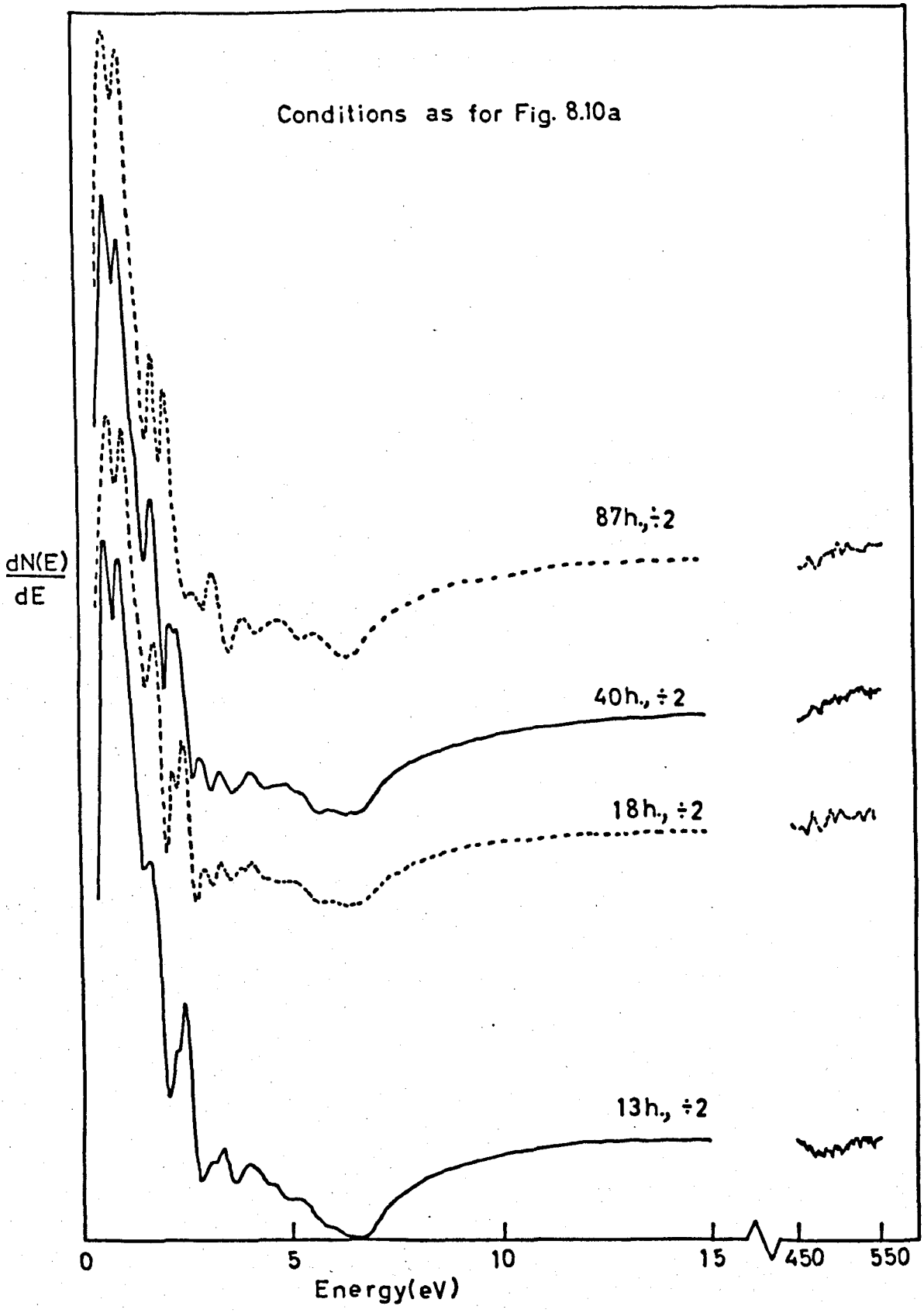

Figure 8.10b Successive oxidation effects on the slow peak fine structure of Mg

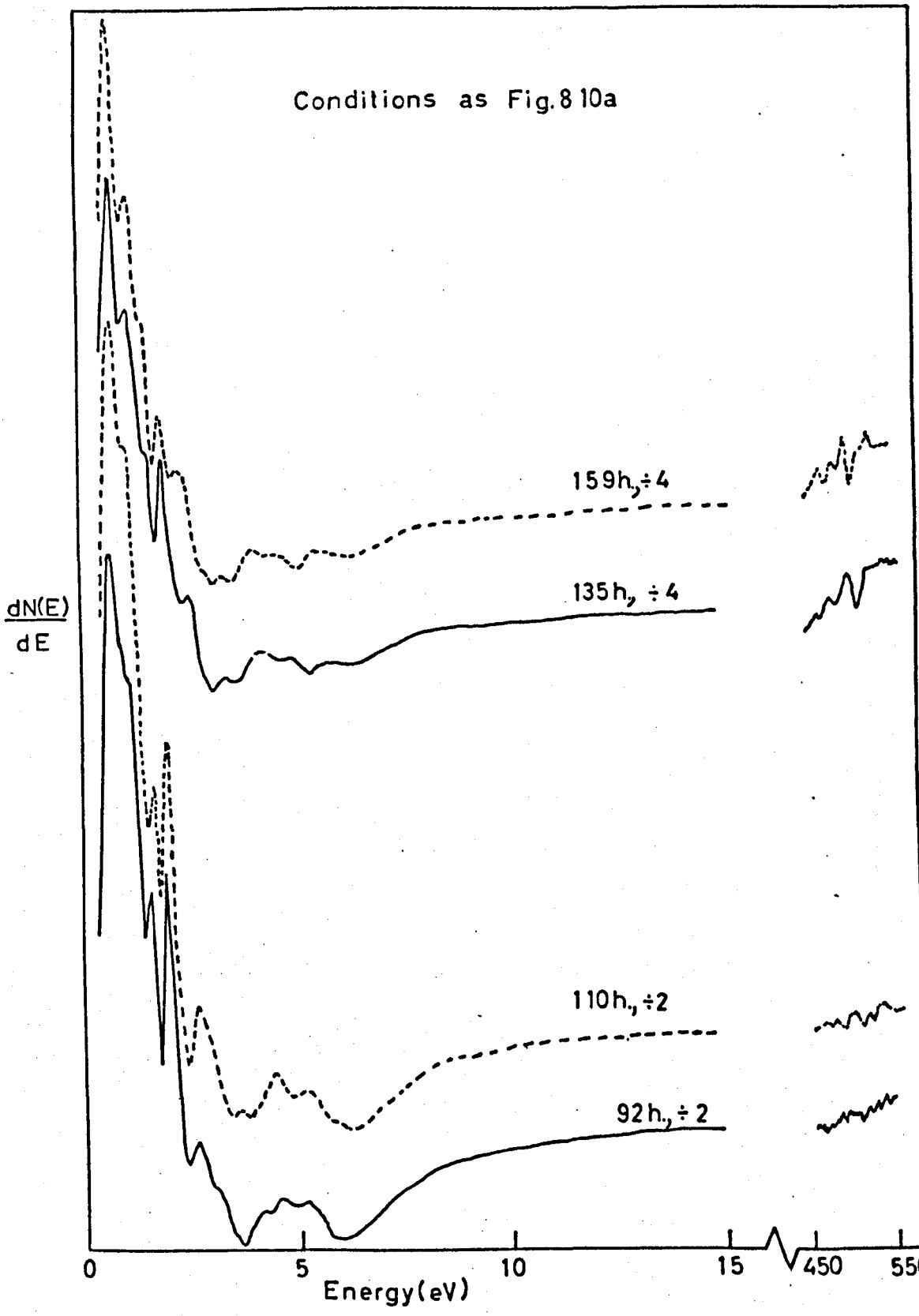

Figure 8.10c Successive oxidation effects on the slow peak fine structure of Mg

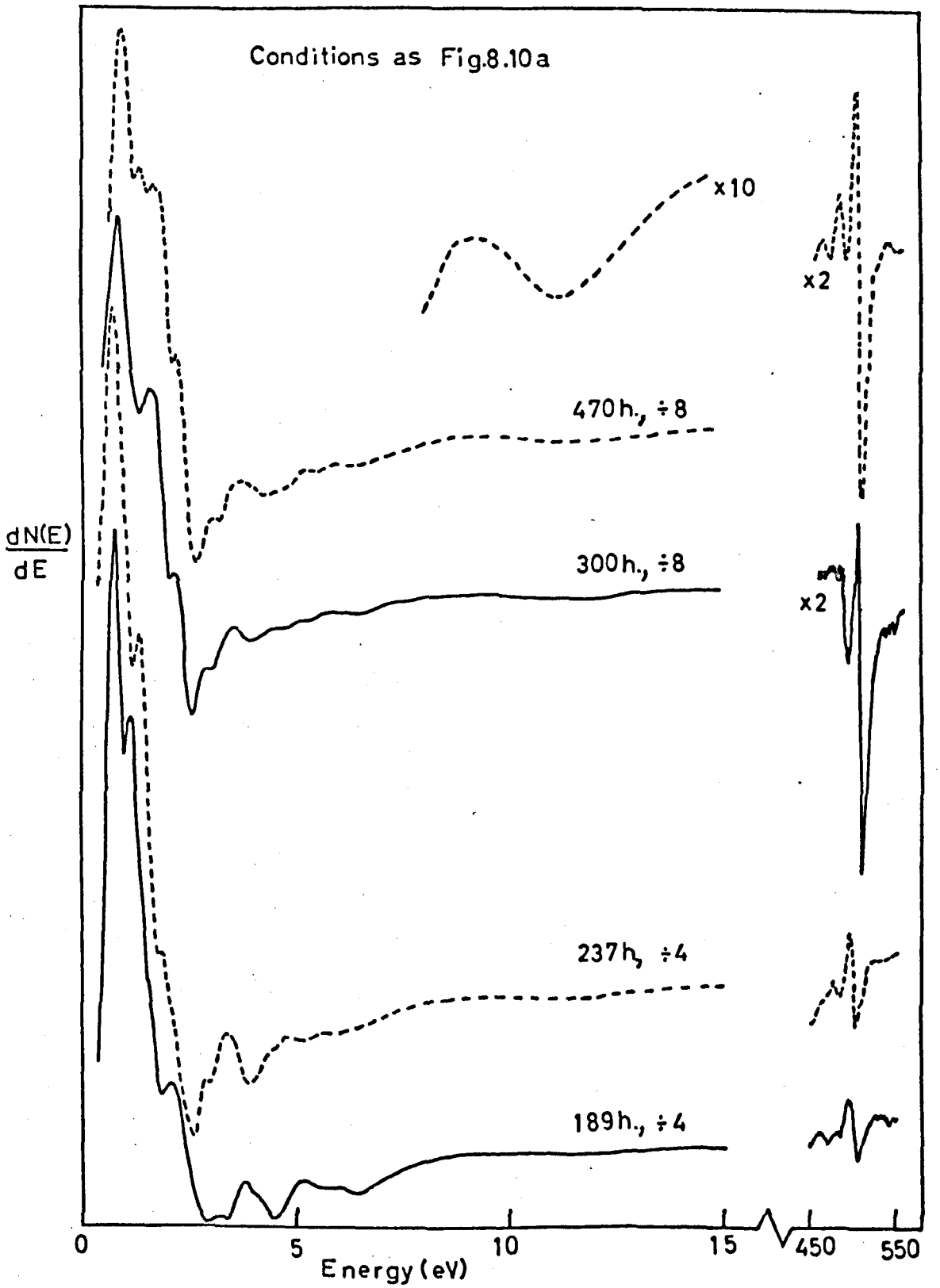

Figure 8.10d Successive oxidation effects on the slow peak fine structure of Mg

The gross features of the slow peak were usually observed using a modulation voltage of 2Vpk-pk. Figs. 8.11a and 8.11b show the changes in the gross features, accompanied by the corresponding oxygen levels at each time interval. On the clean surface as shown by the 4 hour curve (Fig. 8.11a), a peak is visible at 6.2eV with shoulders at 3.5 and 2.0eV. After a period of 92 hours, the peak at 3.5eV is larger and the shape of the spectrum closely resembles that of Fig. 8.3 (upper curve), apart from a missing shoulder at 11.0eV. The correspondence of these changes to those in the fine structure can be seen if reference is made to Figs. 8.10a-c. At 93 hours, the 3.5eV peak has again strengthened. During this one hour time interval, the surface was exposed to the electron beam continuously whilst other measurements were taken and it is thought that the beam caused the 3.5eV peak to strengthen. As more time elapsed there is a progressive change-over in intensity from the 6.3eV peak to the 3.5eV peak. In the 135 hour plot, oxygen is just becoming detectable and a discontinuity appears at about 11eV. The 470 hour plot shows the 3.6eV peak to shift to 2.6eV and the 4.2eV peak is seen to develop. The 6eV peak weakens considerably, whilst the discontinuity at 11.3eV strengthens and is resolved. The spectrum for the fully oxidised magnesium surface is in good agreement with that of Jenkins and Chung[85]. Table 8.5 lists the observed peaks for clean and fully oxidised magnesium.

TABLE 8.5

Observed Fine Structure in the Slow Peaks of Clean and Fully Oxidised Mg

Clean Mg (eV)	0.3	1.1	1.4	1.7	2.1	2.3	2.9	3.8	6.3
Oxidised Mg (eV)	0.4	1.3	1.6		2.6	3.3	4.2	6.3	11.3

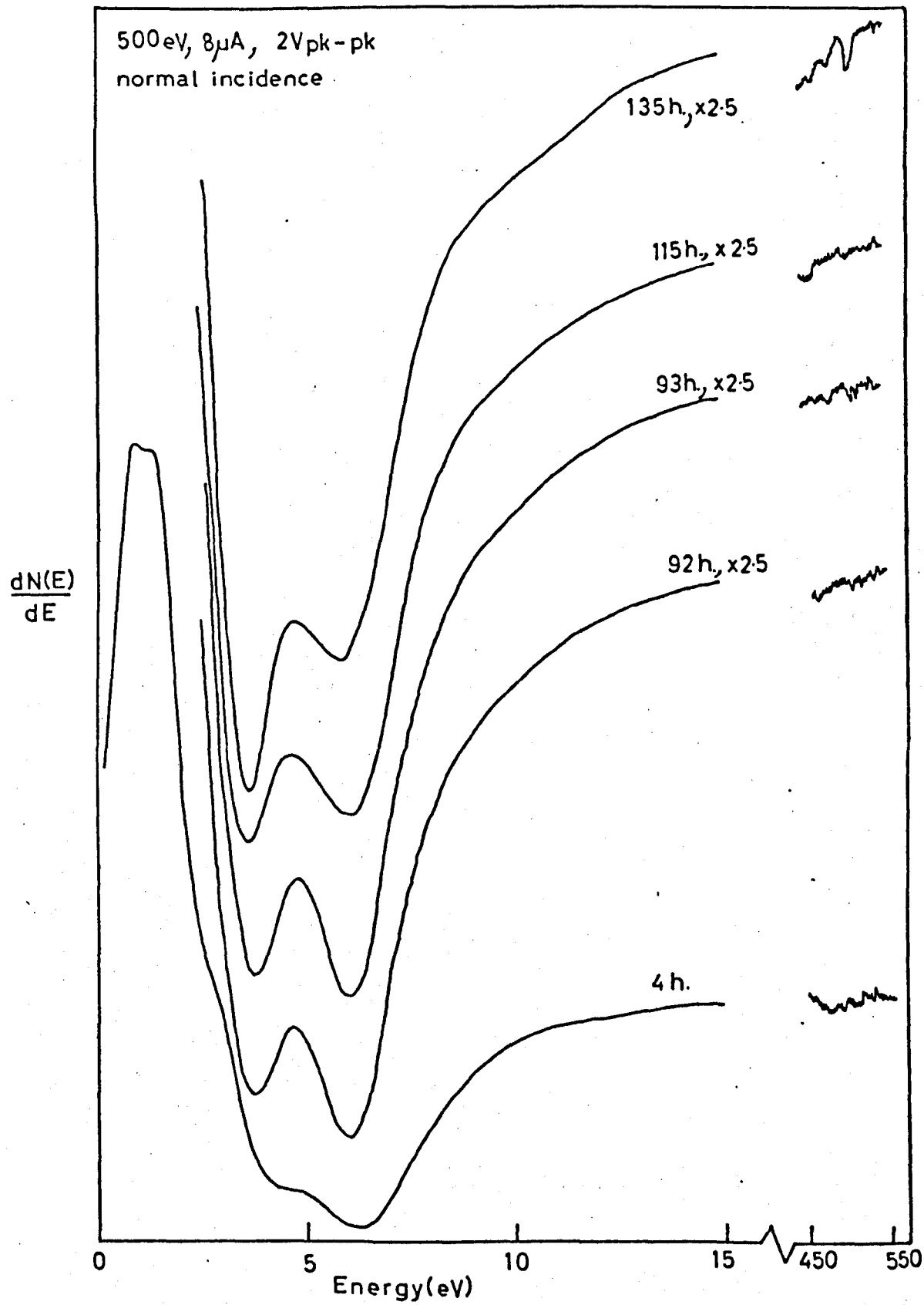

Figure 8.11a Successive oxidation effects on the slow peak gross structure of Mg

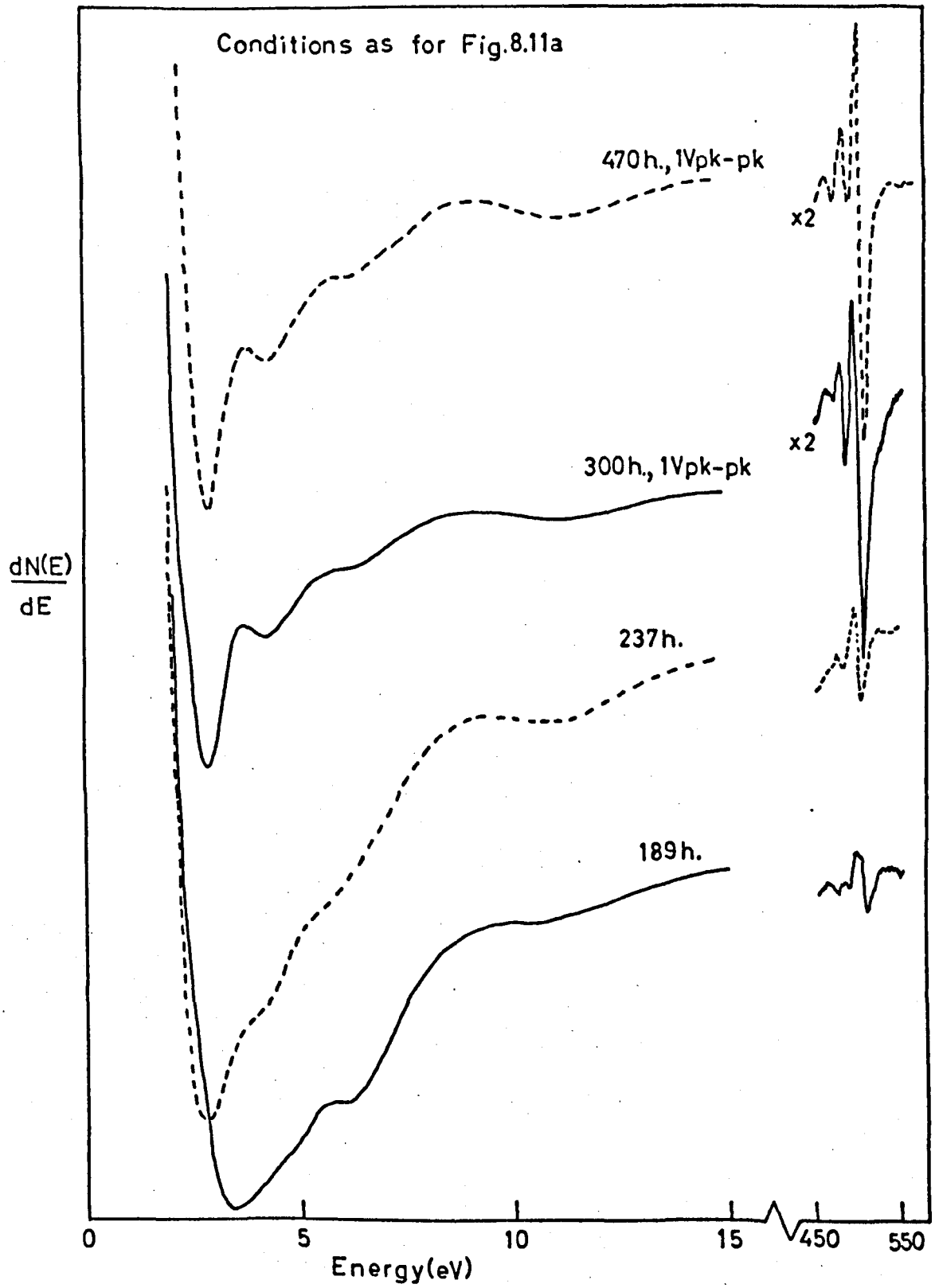

Figure 8.11b Successive oxidation effects on the slow peak gross structure of Mg

8.3.3 Electron Energy Loss Spectra

The energy losses of magnesium were also observed during this oxidation period. Fig. 8.12a shows the energy losses with various stages of oxidation. It can be seen that the surface plasmon loss in magnesium at 7.4eV, is strongly attenuated by the initial oxidation and eventually disappears after 237 hours. The bulk plasmon loss vanishes after 324 hours but there still remains a relatively weak loss at 22eV. The lowest plot of Fig. 8.12a shows this loss under larger gain, with accompanying losses at 17 and 58eV.

The energy losses of the fully oxidised magnesium surface are seen in Fig. 8.12b. With an E_p of 500eV, the observed losses were 17, 22 and 58eV. With the E_p of 1keV, losses at 6.0, 10.9, 22.6, 33 and 43eV were observed. The tentative identification of the 6.0eV loss is that of a shifted surface plasmon loss in magnesium, due to a dielectric overlayer of MgO.

8.3.4 Discussion

The effects of oxidation on the low energy Auger spectrum of magnesium have been considered by a number of authors[46,90,161] and the results of sub-section 8.3.1 appear to be largely consistent. The main peak at 35eV in the 'oxidised' spectrum is thought to be due to an $L_{2,3}VV$(MgO) transition involving the valence band levels of MgO. It may be pointed out that both Suleman and Pattinson[161] and myself have observed a weak peak at 58.5eV in the oxidised spectrum. If this peak were due to the 'plasmon gain' mechanism, its existence in the 'oxidised' spectrum would be difficult to explain. A further discussion is not necessary at this point, due to the availability of discussions in the literature[90,161].

Many changes were seen to occur in the fine structure of the slow peak of magnesium even before the first trace of oxygen was observed in the Auger spectrum, indicating that the method may well be more sensitive to initial chemisorption changes than the corresponding Auger effect. Oxidation effects on the gross features of the slow peak were also investigated and these will now be compared with recent published work.

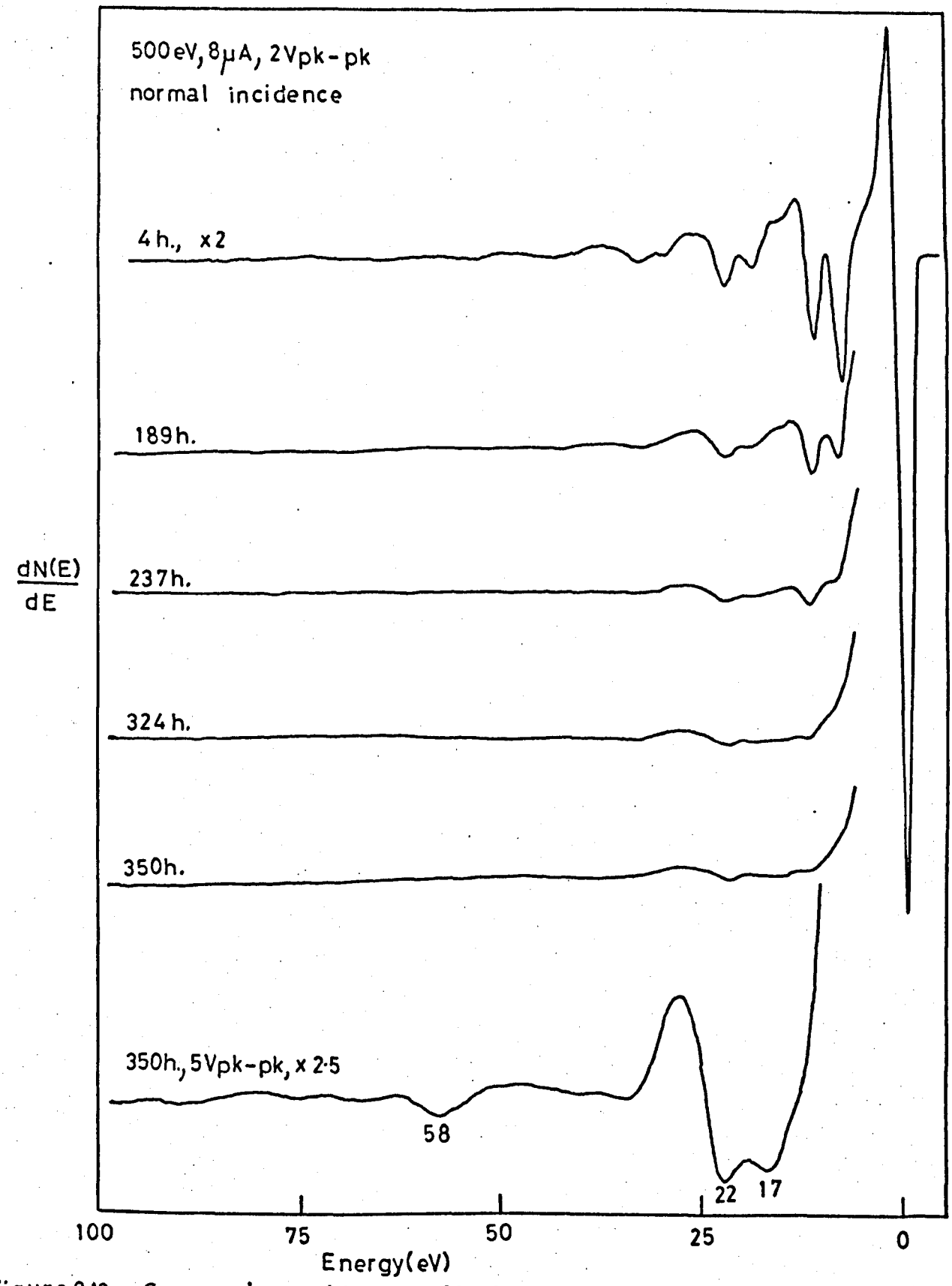

Figure 8.12a Successive oxidation effects on the energy losses of Mg

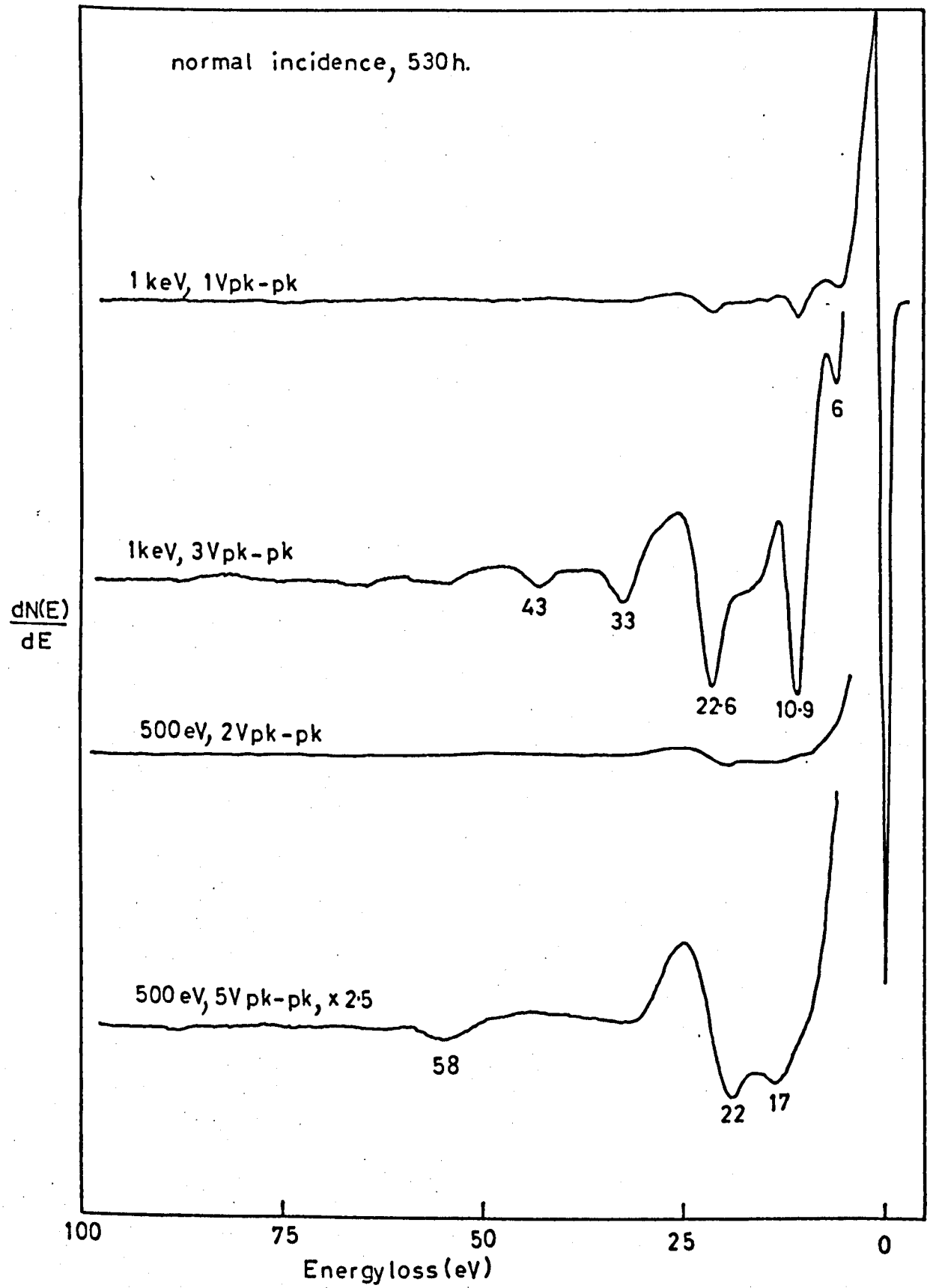

Figure 8.12b Energy loss spectra of a fully oxidised Mg surface

The gross features of the slow peak were found to vary more slowly than the fine structure, with oxygen build-up. It appears that a characteristic 'shape' in this energy region may give a sensitive method for determining the state of oxidation of a magnesium surface, and moreover shows that the spectra previously reported by Jenkins and Chung[85], and Wright and Pattinson[97] could well have originated from a partially oxidised magnesium surface although it would not have been evident from their Auger signal for oxygen.

Evidence for these proposals will now be discussed. The wide peak at 11.3eV (Fig. 8.10d and 8.11b), which developed as the oxygen level increased was thought to be an Auger peak (L_1VV) from oxygen. The valence band in MgO may be taken to be 4eV below the Fermi level (Fong, Saslow and Cohen[163]), and with an analyser work function correction of 4.5eV, we obtain a value of 11.2eV for the calculated energy of this "Auger" peak. The oxygen L_1 level was obtained from Bearden and Burr[144]. Agreement with the observed peak energy value is excellent. Further evidence for this assignment will be given in the discussion of characteristic energy losses.

If our assignment is correct, then previously reported 'clean' spectra (Jenkins and Chung[85], Wright and Pattinson[97]) were from partially oxidised magnesium surfaces, since the slow peak spectra showed shoulders at about 11eV. Moreover, previous 'clean' spectra showed equal intensities for the 3.6 and 6.3 eV peaks, whereas the gross structure after 4 hours (Fig. 8.11a) shows the two peaks to be asymmetric. Only later, as the surface became contaminated, did the two peaks become equal in intensity.

Attempts were made to correlate the fine structure observed in the oxidised magnesium spectrum with possible band structure mechanisms associated with their production. The band structure of MgO was taken from the work of Fong et. al.[163] Peak energies were corrected for the analyser work function and critical points taken from the band structure.

However, the corrected peak energies and critical points only showed agreement in energy range with poor quantitative agreement.

Direct transition energies between critical points were calculated and the discrete energies assumed to be given to electrons near the Fermi level or vacuum level. But in neither case could good agreement be found with the observed energies. It may well be that the assumption of a bulk band structure for a thin layer of MgO is an over-simplification, hence giving the poor agreement.

Although I can agree with Jenkins and Chung[85] on the gross features of the oxidised magnesium slow peak, their conclusion regarding the similarity of 'clean and oxidised' slow peaks cannot be endorsed, since we have seen many changes occurring in the slow peak before the final oxidised state. If the 3.6eV peak of the gross features is tentatively identified as a "surface plasmon gain", why should it grow upon oxidation with respect to the "bulk plasmon gain" at 6.3eV? Surely the opposite should be true for this situation. Hence, these findings do not appear to support this tentative identification.

Also Jenkins and Chung found a severe attenuation of the slow peak upon oxidation which is quite contrary to my findings. Perhaps a reason for this discrepancy may be found in their method of oxygen exposure, which consisted of an oxygen leak of 10^{-2}torr sec. at room temperature, followed by annealing. The slow peak shift to lower energies upon oxidation was observed by both Jenkins and Chung and myself. Unfortunately there is no other work in the literature at present with which further comparisons may be made, and so some of the questions just raised are difficult to answer at this time.

The tentative identification of the 6.0eV loss seen in Fig. 8.12b, is that of a shifted surface plasmon loss in magnesium, due to a dielectric overlayer of MgO. Using a dielectric constant of 3.0 for MgO in the equation derived by Stern and Ferrell[35] (equ.(5), Chapter 1),

the calculated value of the shifted surface plasmon loss is 5.3eV (assuming infinite dielectric thickness), which is in reasonable agreement with the observed value. The weak loss at 58eV in the oxidised magnesium loss spectrum, was thought to be an $L_{2,3}$ ionisation loss in magnesium ($L_{2,3}$ level - 56eV from Bearden and Burr[144], with ϕ_A correction), which is obscured in the clean magnesium loss spectrum, by the fifth order bulk plasmon loss. The weak loss at 17eV in MgO was more difficult to identify and was assumed to be an interband transition.

Energy losses in MgO have been studied by several authors including Roessler and Walker[164], Watanabe[165] and Jull[166], and in these cases a strong loss was seen at about 22eV. This loss was assumed to be a bulk plasma resonance in the valence band of MgO. The upper plots in Fig. 8.12b show that the bulk plasmon losses in magnesium are still visible on the MgO surface, using an E_p of ~1keV. The energy losses are 11, 23, 33 and 43eV and correspond to the multiple bulk plasmon losses in magnesium. However, the strongest loss at 22.6eV is too strong to be a pure second order bulk plasmon loss and must represent a combined loss. The value of this loss agrees well with the bulk plasmon loss for MgO, but the MgO overlayer must be thin (20-25 Å) in order to observe the bulk plasmon losses in magnesium. (Further evidence for this overlayer depth figure will be given in the next section). It was thought that a contribution to this loss must come from the L_1 ionisation loss in oxygen at 23.7eV (Bearden and Burr[144]). Additional evidence for this assignment comes from the loss spectra of oxidised Be and Al (Suleman and Pattinson[89]). In all three cases of the oxidised metals, the strongest loss occurs between 22 and 25eV which may be easily explained by the previous assignment.

Such vacancies produced in the L_1 shell of oxygen may cause the atom to undergo an L_1VV Auger transition. Hence, the wide strong peak observed at 11.3eV, which developed in the slow peak spectrum upon oxidation, could be a 'normal' Auger peak of oxygen. The appearance of the peak in previous spectra (Jenkins and Chung[85], Wright and Pattinson[97]) may well show that some oxygen contamination was present.

8.4 The Shifted Surface Plasmon Loss for Dielectric Overlayer Depth Determination

The surface mode of plasma oscillation depends on the surface conditions, because plasma oscillations are influenced by the surrounding charge distribution. Its frequencies are given by $w_s = w_p/\sqrt{2}$ (equ.(5), Chapter 1) for clean and plain surfaces, and $w_s = w_p / (1+\epsilon)^{\frac{1}{2}}$ for a surface covered with thick films having a dielectric constant ϵ.

However, when a semi-infinite metal is coated with a film of finite thickness, the dispersion relation of the surface plasmon frequency in the metal is:

$$\left[\frac{w_s}{w_p}\right]^2 = (\epsilon + \tanh kD) / (2\epsilon + (1+\epsilon^2) \tanh kD) \text{ - - - - - - - (16)}$$

where w_s and w_p are the frequencies of the surface and bulk plasmons respectively, D is the thickness of the film having a dielectric constant ϵ and k is the surface wave vector excited by the incident electron, corresponding to the surface plasma oscillation.

Murata and Ohtani[116] have used equ.(16) as a means of monitoring the progressive growth of oxide on a clean aluminium surface, by detecting the shifting surface plasmon energy. I have now extended this work to a magnesium surface and derived a suitable model for dealing with a normal incidence electron beam, where only backscattered electrons may produce surface electron oscillation. In addition, the expression for the surface plasmon wave vector in terms of the incident electron energy and surface plasmon energy, has been derived from first principles.

If we now examine Fig. 8.13, which describes the wave vectors of the incident electron (k_o), backscattered electron (k_h) and surface plasmon (k), we can apply conservation laws to derive an expression for k.

Conservation of momentum (parallel to surface)

$$\hbar k_o \cos\theta = \hbar k + \hbar k_h \cos\theta$$

$$\therefore k = \cos\theta\,(k_o - k_h) \text{ - - - - - - - - - - - - (17)}$$

Conservation of energy

$$\frac{(\hbar k_o)^2}{2m} = \hbar w_s + \frac{(\hbar k_h)^2}{2m}$$

where m is the electronic mass.

Re-arranging terms,

$$(k_o - k_h) = \frac{2m w_s}{\hbar(k_o + k_h)}$$

Substituting for $(k_o - k_h)$ in (17) we have:

$$k = \cos\theta \left[\frac{m w_s}{\hbar k_o}\right] \text{ - - - - - - - - - - (18)}$$

for $k_h \gg k$

Now $k_o = \frac{(2m E_p)^{\frac{1}{2}}}{\hbar}$ where E_p is the primary electron energy.

Substituting for k_o in (18) we have:

$$k = \cos\theta \left[\frac{m}{2 E_p}\right]^{\frac{1}{2}} \frac{Es}{\hbar} \text{ - - - - - - - - (19)}$$

We have eliminated w_s with the use of $E_s = \hbar w_s$ where E_s is the surface plasmon energy.

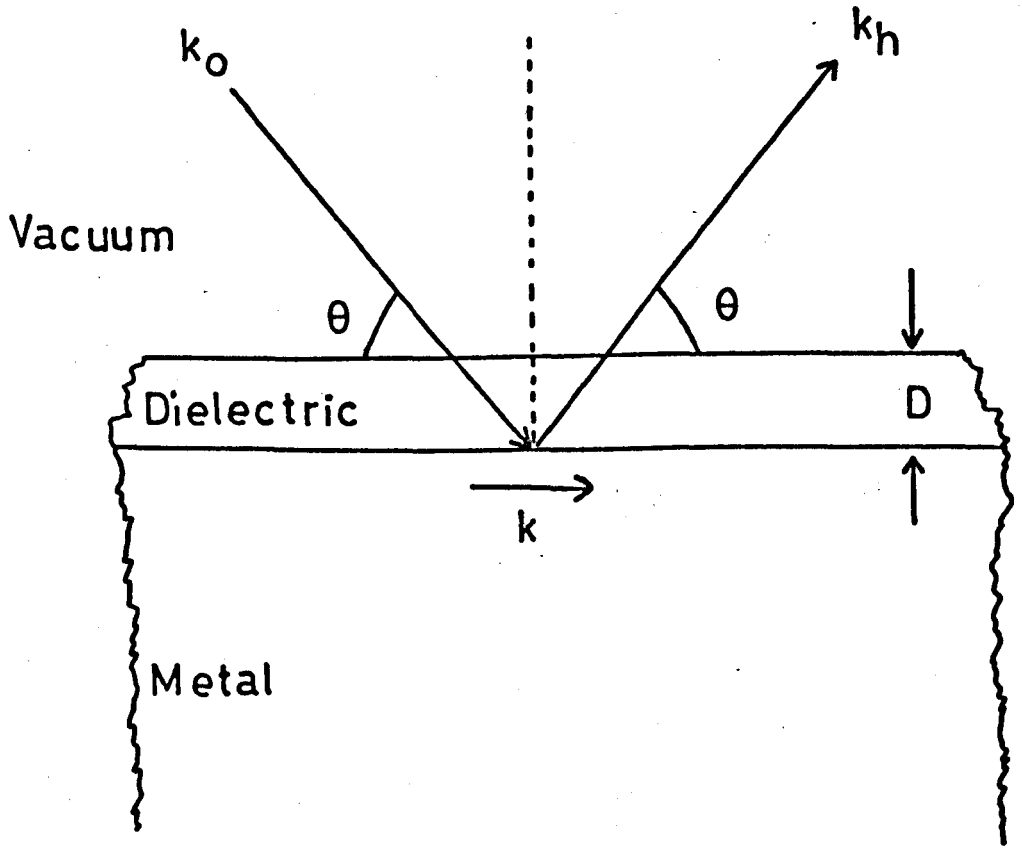

Figure 8.13 Wave vectors for electrons before and after scattering with excitation of the surface plasmon

For a normal incidence electron beam, cos θ = 0 and surface plasmons cannot be generated by the incident electron. Since plasmon losses are observed under these conditions, they must be generated by backscattered electrons. If we assume an angular distribution of backscattered electrons follows a sin θ relation (Burns[167]), where θ is defined in Fig. 8.13, we can calculate the mean angle ($\overline{\cos\theta}$) for surface plasmon production. We must also make the assumption that the efficiency of surface plasmon production is directly related to the surface velocity component of the exciting electron (cos θ function).

We can now arrive at an expression for the mean angle of surface plasmon production:

$$\overline{\cos\theta} = \frac{\int_0^{\pi/2} N(\theta).\ f(\theta).\ d\theta}{\int_0^{\pi/2} N(\theta).\ d\theta}$$

where N(θ) is the number of backscattered electrons at θ and f(θ) is the efficiency of surface plasmon production at θ.

$$\text{Hence,}\quad \overline{\cos\theta} = \frac{\int_0^{\pi/2} \sin\theta.\cos\theta\, d\theta}{\int_0^{\pi/2} \sin\theta\, d\theta} = 1/2$$

Hence, the expression for k, for a normal incidence exciting electron beam becomes:

$$k = \left[\frac{m}{2E_p}\right]^{\frac{1}{2}} \frac{E_s}{2\hbar} \qquad \text{- - - - - - - - - - - (20)}$$

If we now re-arrange equ. (16) to obtain D, we have as our final equation:

$$D = \frac{1.}{2k} \ln\left[\frac{\epsilon - 1 - (E_s/E_p)^2\ (2\epsilon - \epsilon^2 - 1)}{-\epsilon - 1 + (E_s/E_p)^2\ (\epsilon^2 + 2\epsilon + 1)}\right] \text{- - - - - - (21)}$$

where k is interpreted from equ. (20), for the normal incidence beam.

A computer programme was written in BASIC to allow the calculation D and k as a function of the shifted surface plasmon energy E_s, the results of which are plotted in Fig. 8.14. The shape of the thickness curve bears a strong resemblance to the theoretical equivalent curves of Murata and Ohtani[116].

We are now in a position to estimate the depth of the MgO overlayer, produced in the previous experimental work. The shifted surface plasmon loss was found at 6.0eV which corresponds to an overlayer thickness of 24.5Å of MgO, as read from Fig. 8.14. In addition, we could see the bulk plasmon losses in magnesium using a 1keV primary beam, so the overlayer thickness must be comparable to the escape depth of a 1keV electron, which is about 20 Å (Fig. 1.5). Hence, the two methods give reasonably consistent results.

Because of the success of this method, a more general computer programme has now been written in BASIC, allowing the input of any selection of chosen parameters in equs. (20) and (21).

8.5 Conclusions

We have seen that the slow peak energy structure of magnesium has considerable complexity and an exact interpretation of all the observed fine structure is not available to date. However, the present results indicate that slow peak spectra may well prove valuable in verifying a clean surface of polycrystalline magnesium. In addition, the spectra should have great value in assessing the validity of band structure calculations.

The final section of this chapter has shown that the accurate determination of surface plasmon energy shifts enables the evaluation of a dielectric overlayer thickness, on surfaces of 'free-electron' materials such as magnesium.

We will now move on to look at the results of a similar experiment performed on aluminium. The literature on this element is more abundant but even so, most authors have failed to observe the large amount of energy structure present in the slow peak of clean aluminium, when viewed under high resolution.

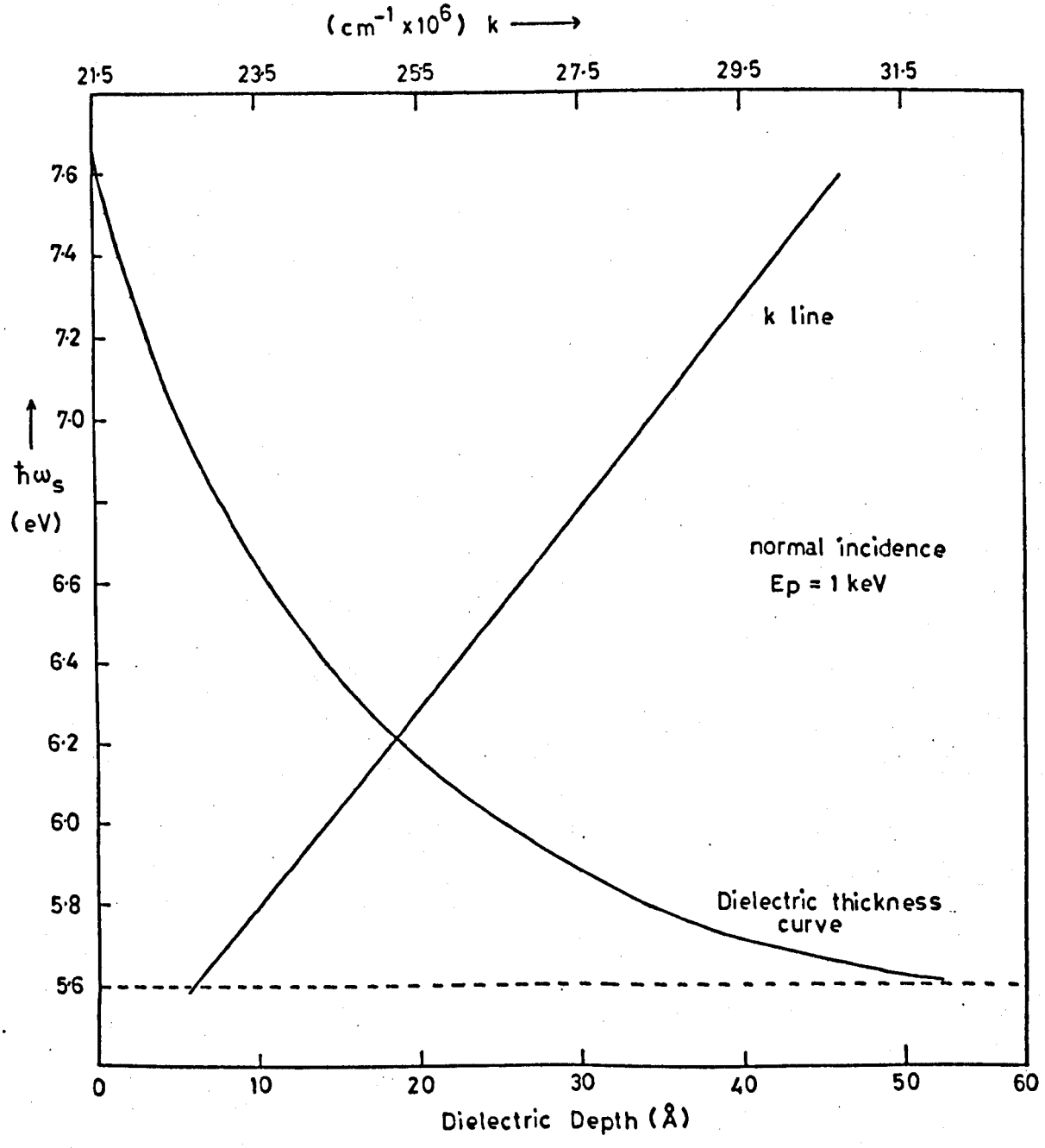

Figure 8.14 Surface plasmon energy v/s MgO depth, with corresponding k line

CHAPTER 9

SECONDARY ELECTRON EMISSION SPECTROSCOPY OF ALUMINIUM

9.1 Introduction

Several publications have recently appeared in the literature concerned with slow secondary electron energy spectra originating from an aluminium surface. The interpretation generally offered for the spectra is in terms of plasmon effects based on the two or three peaks that have been observed. These workers also showed that traces of contaminants on the aluminium surfaces indicated by AES, had a predominant effect on these low energy electron spectra.

Hence, a rigorous experiment was performed to try to obtain the maximum observable slow peak energy structure. This proved to be successful and extensive fine structure was observed which will be discussed in the later sections of this chapter.

As in the case of magnesium, the detail and intensity of the fine structure was found to be highly dependent on the applied modulating voltage. The variables of primary electron incidence angle and energy, again appear to influence both the number and intensity of the peaks.

An interpretation of the fine structure is discussed, in terms of direct electron emission from critical points in the high-energy band structure of aluminium. The critical point energies were obtained from a recent calculation by Hoffstein and Boudreaux[168].

Some problems were encountered with regard to the reproducibility of fine energy structure. This problem was found to be more serious in the case of aluminium than in the previous case of magnesium. Usually the fine structure was found to intensify as more aluminium evaporations were performed, but sometimes strong fine structure was not observable, even after many evaporations. It was thought that the substrate might

cause such an effect and so this possibility was investigated by the evaporation of aluminium onto several different substrates. Unfortunately, the situation is not yet fully clarified and it may well be, that the additional analytical tool of LEED will be required, to establish the reasons for the reproducibility difficulties.

9.2 Auger and Electron Energy Loss Spectra

The clean polycrystalline surface of aluminium was prepared by evaporation of 5N purity aluminium, from three previously out-gassed tungsten wire baskets, onto various substrates in UHV. AES showed oxygen to be the only serious contaminant on the first few evaporated surfaces, but thereafter, the aluminium surface would remain oxygen-free for several hours.

The low energy Auger spectrum of aluminium was found to be independent of the substrate on which the aluminium had been deposited. In the case of the Pt black substrate, the Auger spectrum was somewhat attenuated due to the low value of yield for this surface. A typical spectrum is seen in Fig. 9.1, illustrating the high and low energy satellite peak structure. The large peak at 67eV is the well-known $L_{2,3}VV$ Auger transition in aluminium, and the other peaks occur at 41, 51, 81 and 104eV.

The strong energy losses of aluminium are well-known and the effects of θ and E_p variations on the losses can be seen in Figs. 9.2, 9.3 and 9.4. All the observed energy losses can be explained in terms of surface and bulk plasmon losses, multiple and combination losses. A very strong surface plasmon loss at 10.6eV can be seen in Fig. 9.2 at 60° incidence and also multiple surface plasmon losses. Multiple bulk plasmon losses may be seen up to the sixth order at approximately 15.5eV intervals, and the surface plasmon loss is seen to grow relative to the bulk plasmon loss as θ is increased.

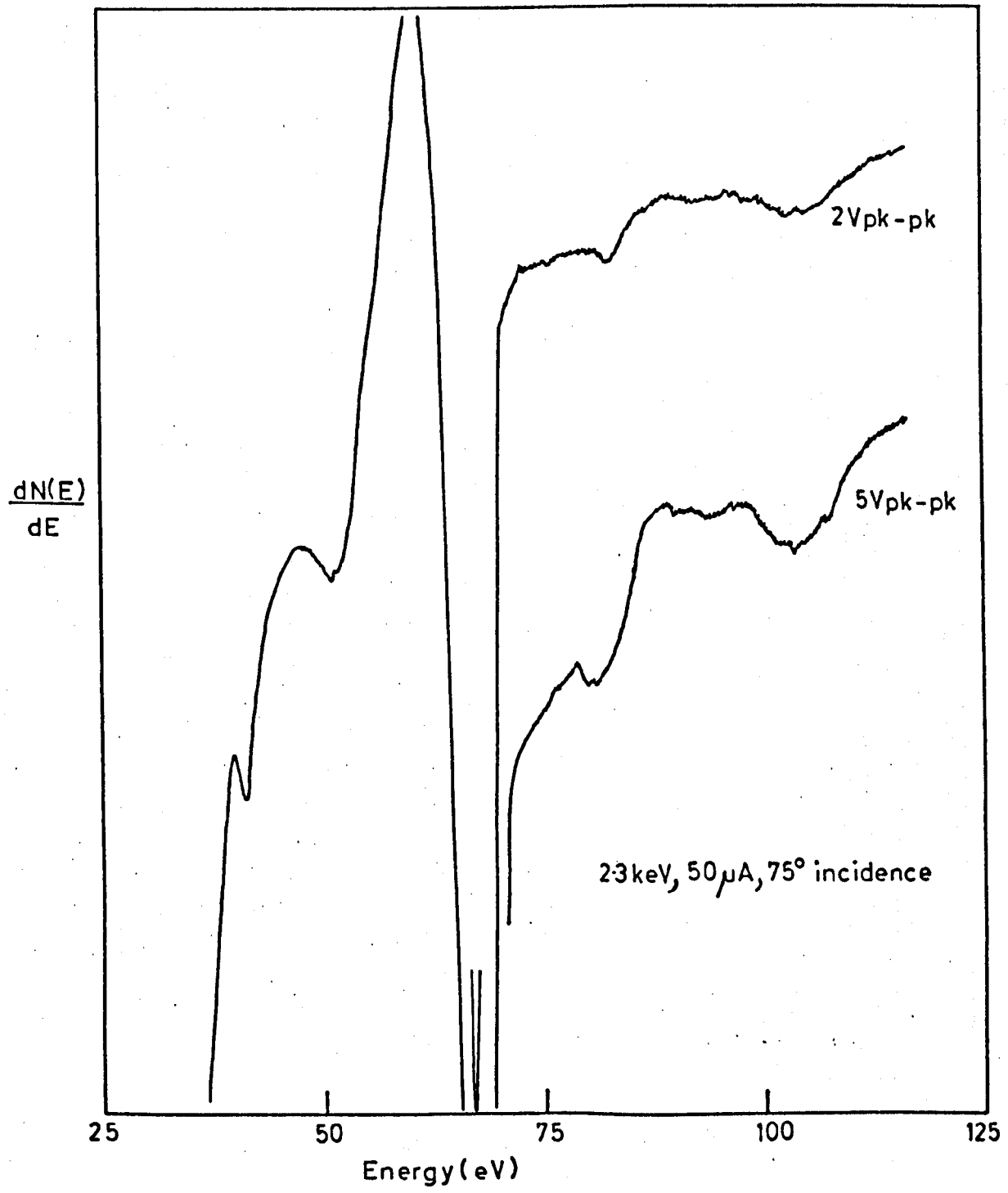

Figure 9.1 Low energy Auger spectrum of Al showing satellite peak structure

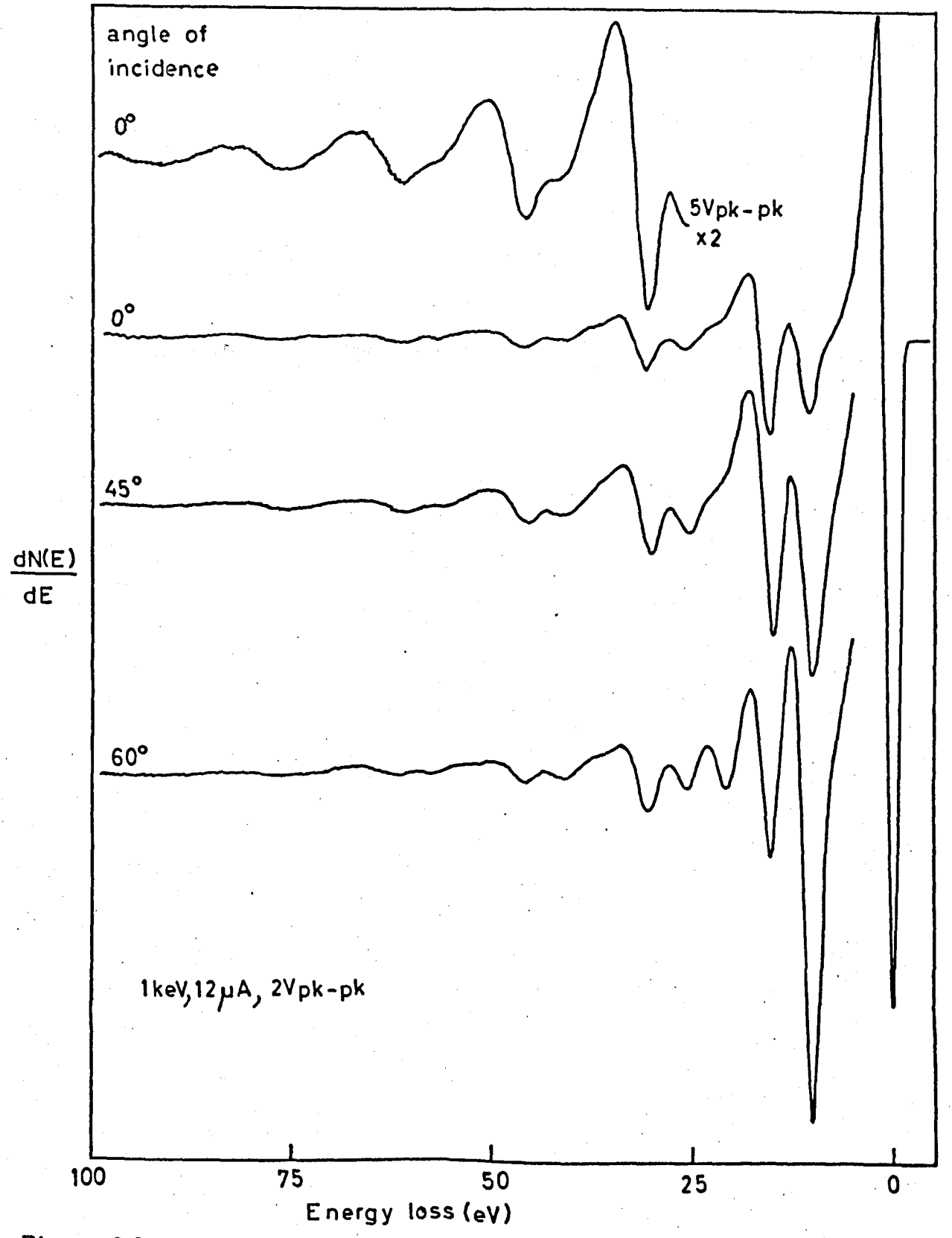

Figure 9.2 Energy loss spectra of clean Al with different angles of incidence

In the case of aluminium deposited on a Pt black substrate, these angular effects were not observed. Fig. 9.3 illustrates this situation. At normal incidence, the surface and bulk plasmon losses have roughly equal intensities, whereas in the corresponding curve of Fig. 9.2, the bulk plasmon loss is the stronger.

In Fig. 9.4, the energy loss at 10.6eV is seen to increase relative to the 15.5eV loss as E_p is reduced, illustrating the surface sensitivity of the 10.6eV loss. Modulation voltages as low as 0.25Vpk-pk revealed no extra structure in the energy loss region (as in the case of magnesium), so again there appears to be no correlation between the 'energy gains' of the slow peak and the energy losses of the elastic peak.

9.3 Slow Secondary Electron Spectra

Aluminium was evaporated onto a number of different substrate surfaces and slow peak spectra were taken. One such spectrum is shown in Fig. 9.5, plotted using both the N(E) and N'(E) modes. The conditions for both plots are identical, apart from the ordinate scale. We can see the large enhancement of energy structure with the use of the N'(E) mode over that of N(E). In the N(E) mode, two discontinuities occur in the slow peak at about 5 and 10eV. These appear as minima in the N'(E) curve at about 6 and 11eV, and in addition, further structure has become visible between 0 and 6eV.

The strongest structure was seen after aluminium was evaporated on a clean MgO surface (in fact, the fully oxidised Mg surface of Chapter 8, after exposure to air). Figs. 9.6, 9.7 and 9.8 refer to energy structure observed using this particular substrate. Fig. 9.6 shows that the use of 2Vpk-pk modulation (as used by many workers) does not enable the full structure of the slow peak to be observed. The high angle of incidence was used so that a direct comparison could be made with the results of other workers. With 2Vpk-pk, two peaks are seen at about 6 and 11eV and a slight shoulder at about 4eV. As the applied modulation is reduced, considerable fine structure appears between 0 and 6eV.

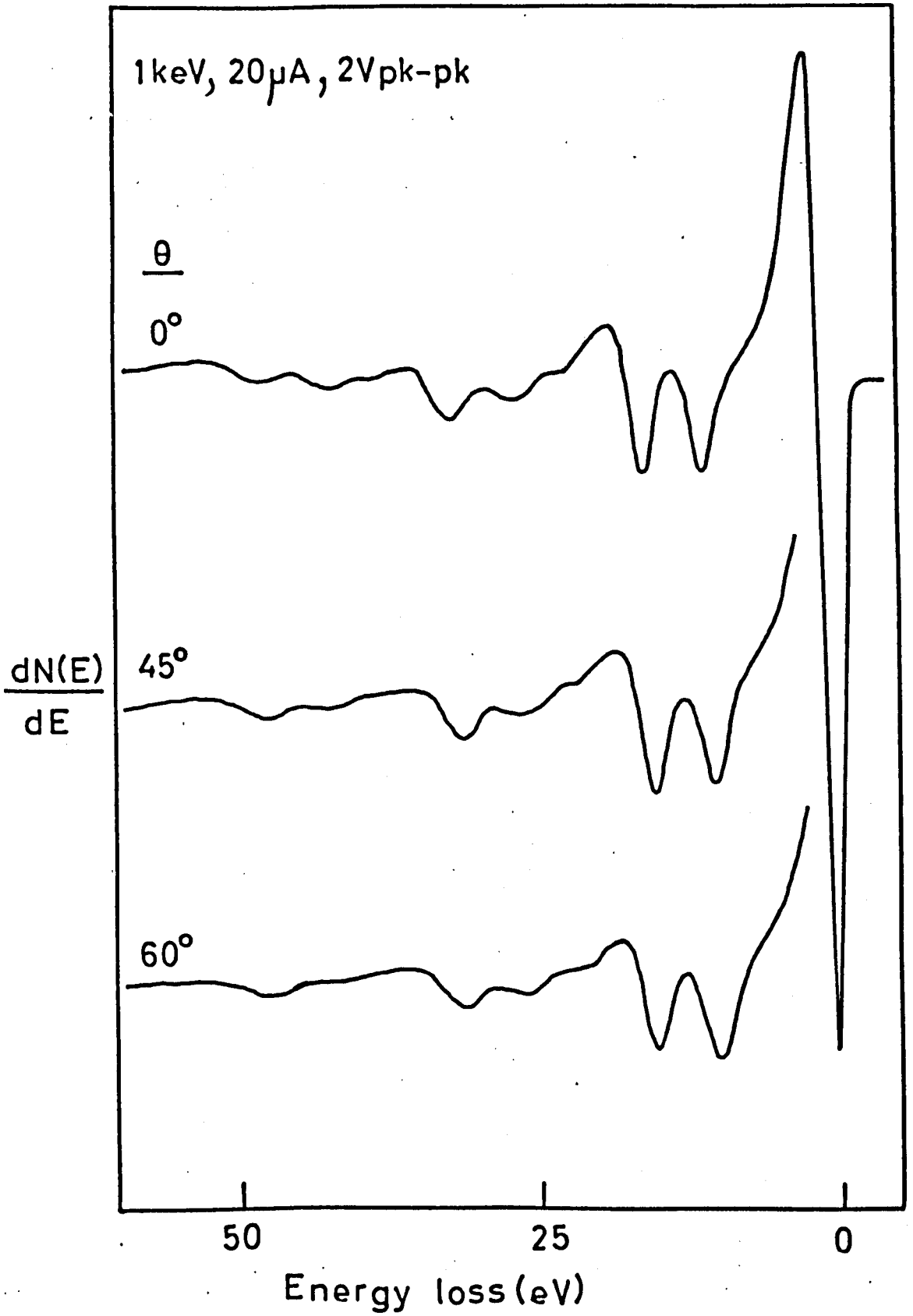

Figure 9.3 Energy loss spectra of clean Al deposited on a Pt black substrate

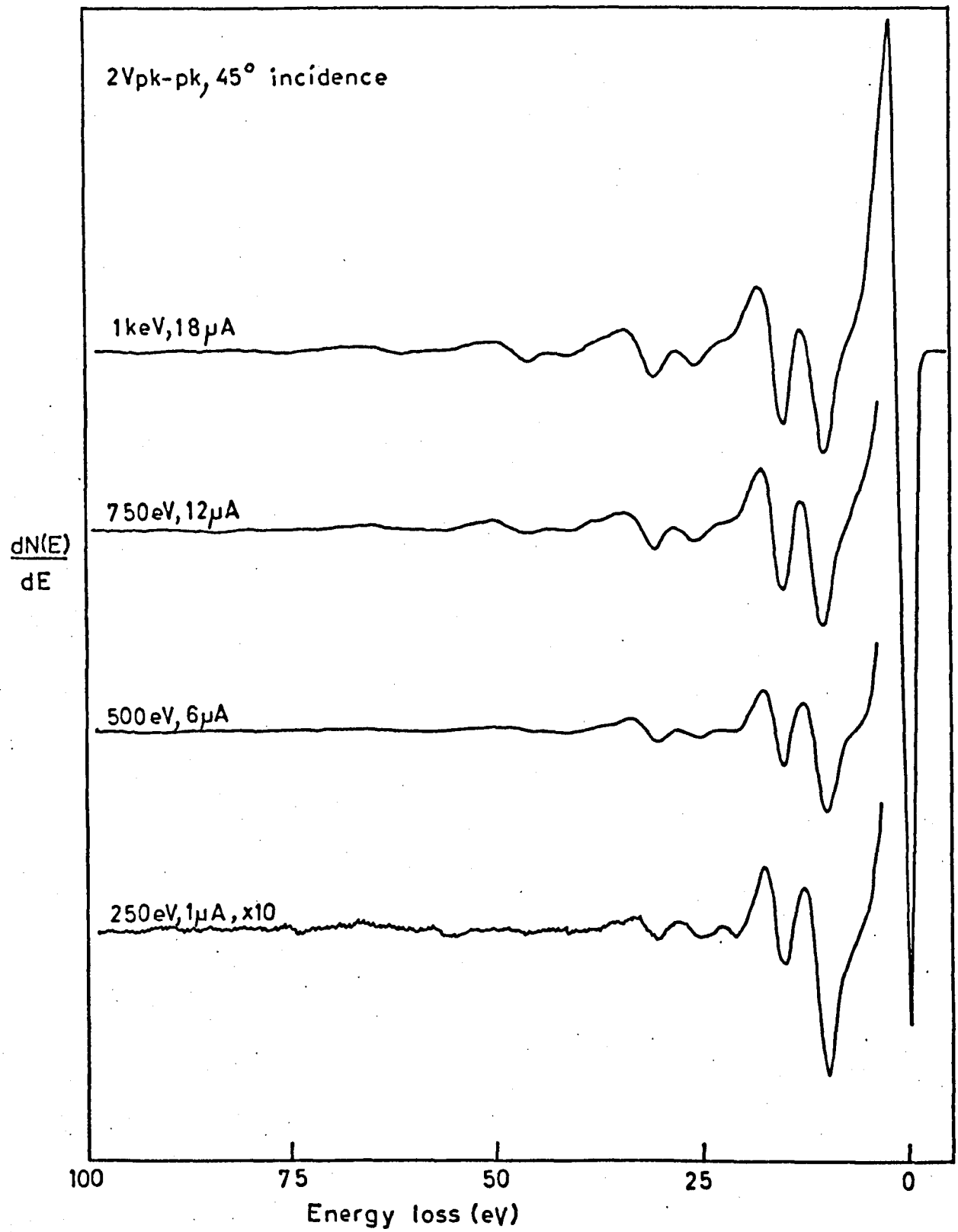

Figure 9.4 Energy loss spectra of clean Al with different primary electron energies

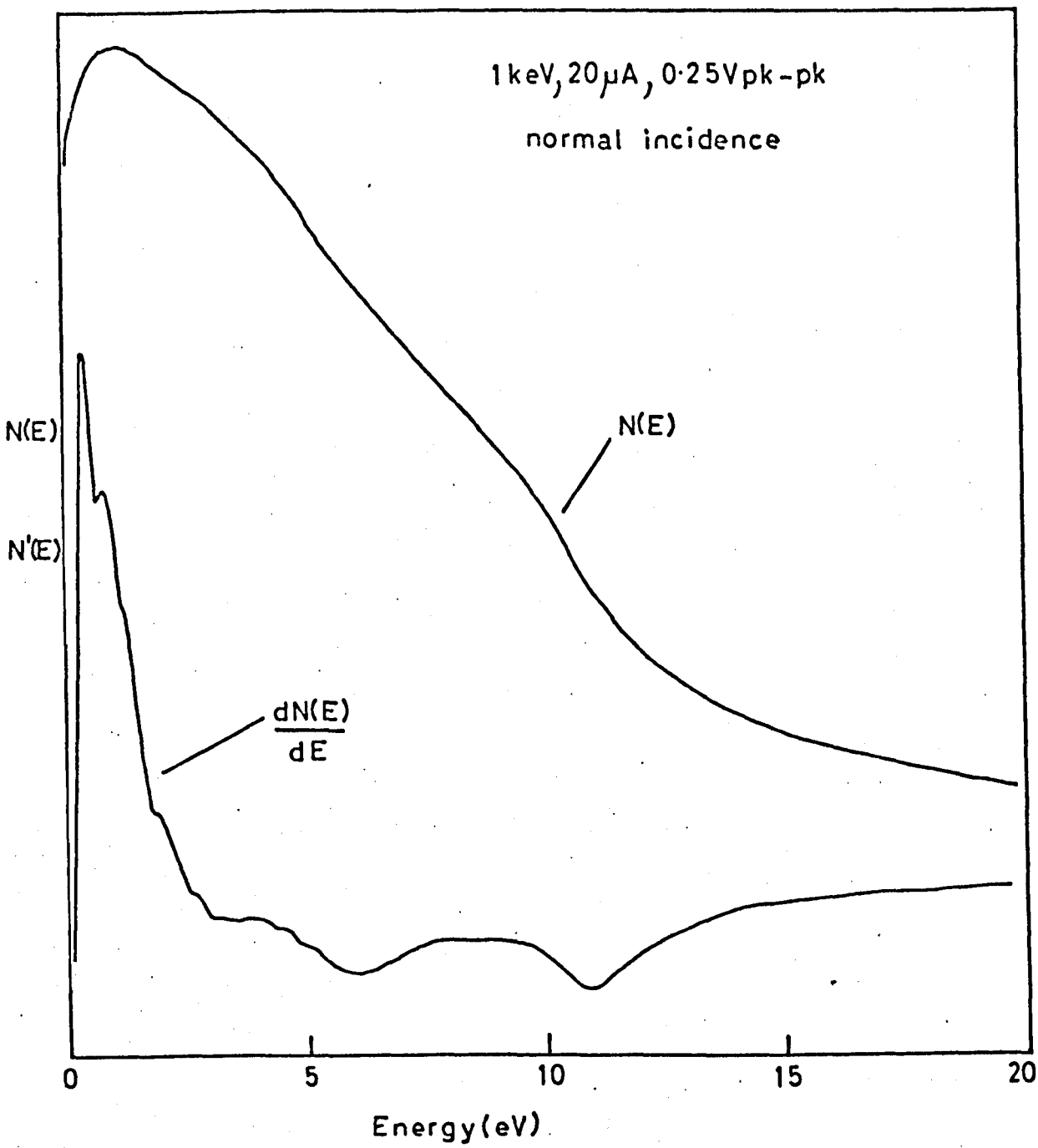

Figure 9.5 Slow peak of Al deposited on a Pt black substrate

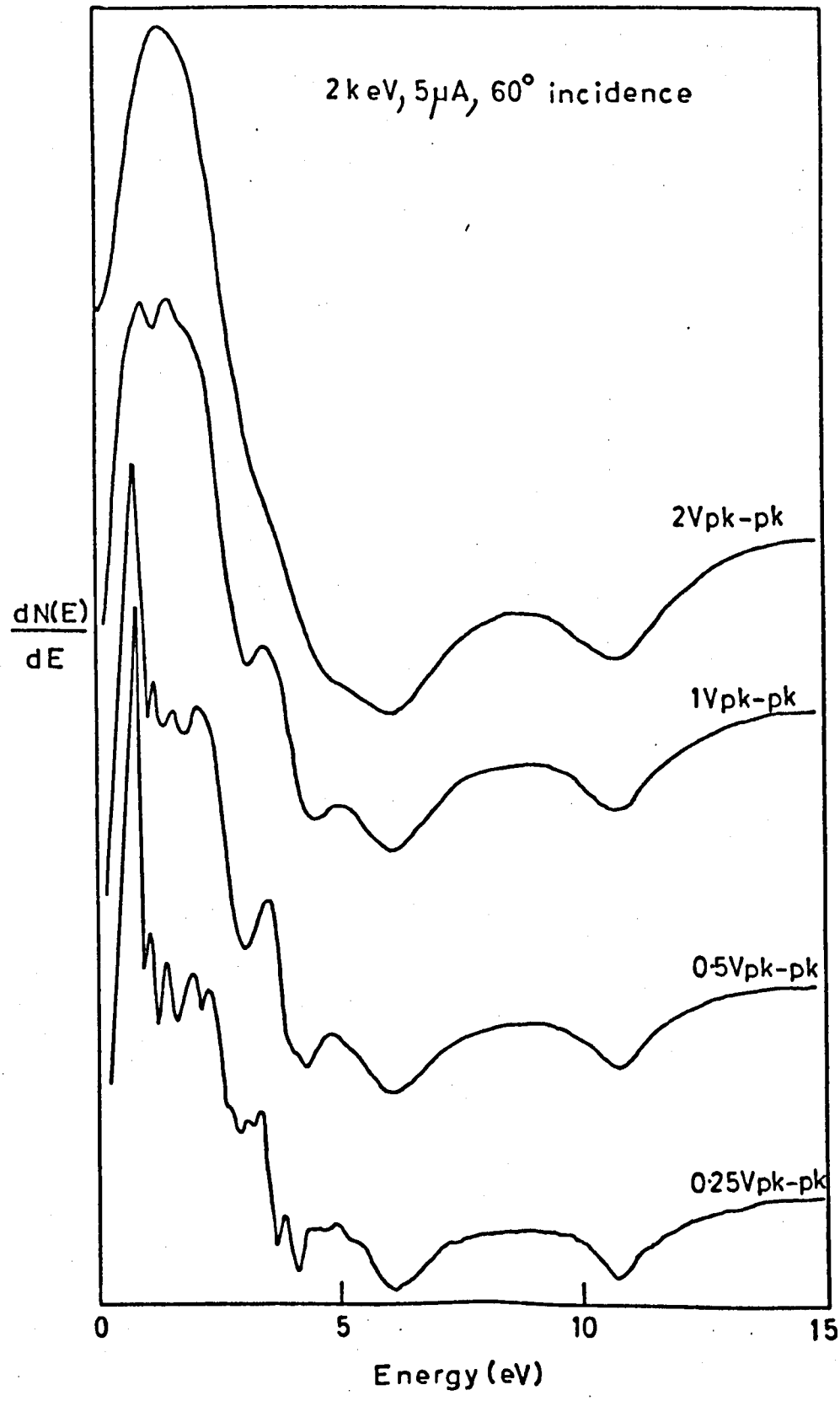

Figure 9.6 Slow peak of Al with different applied modulation voltages

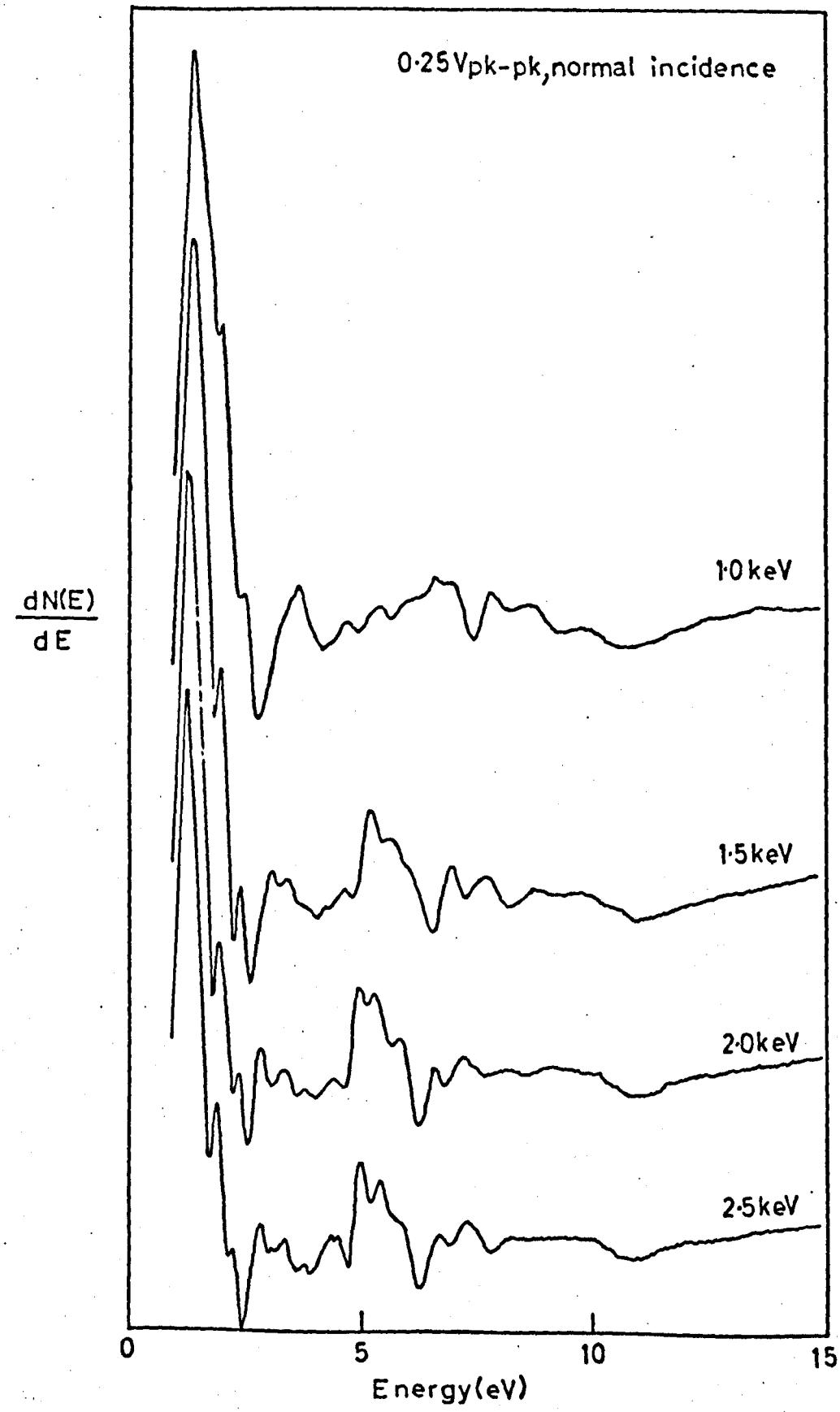

Figure 9.7 Slow peak of Al with different primary electron energies

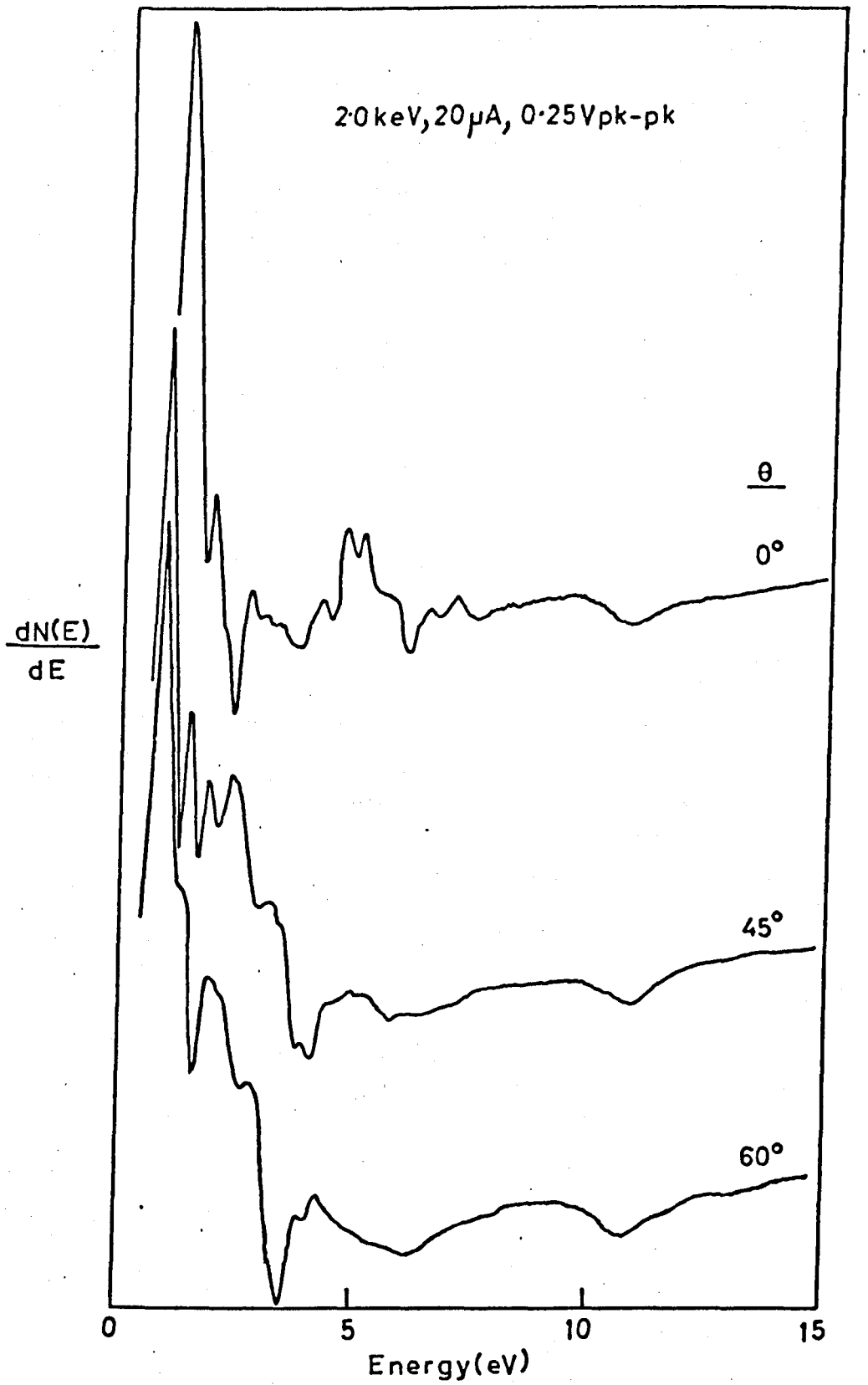

Figure 9.8 Slow peak of Al with different angles of incidence θ

The effect of E_p variation on the slow peak is seen in Fig. 9.7. Many features of the spectrum are reproducible as E_p changes, but a shift to higher energies is apparent as E_p falls. The reason for this shift is not at all certain, although the changing background slope as E_p varies could exert an influence. Contrary to the case of magnesium, most structure is visible at the higher values of E_p. The spectra of Fig. 9.7 were obtained over a period of about 30 minutes.

Fig. 9.8 shows the effect of incidence angle variation on the slow peak spectra. At the higher angles of incidence, the structure is less pronounced, which is in accordance with the case of magnesium. However, the reproducibility from plot to plot is restricted to peaks at about 6 and 11eV. The plots of Figs. 9.7 and 9.8 were taken on the same aluminium surface, with a time lapse of about one hour between the figures. If we compare the upper plot of Fig. 9.8 with the 2keV plot of Fig. 9.7, we should have identical spectra. It is immediately evident that the relevant curve of Fig. 9.8 has become slightly 'smeared out' during the time of surface analysis; the weaker peaks becoming shoulders in Fig. 9.8. Possible reasons for the 'fleeting nature' of this structure will be discussed in the next section.

The spectra shown in Fig. 9.6 were taken on an earlier clean surface of aluminium, with a further two aluminium evaporations between Fig. 9.6, and Figs. 9.7 and 9.8. If we now refer to the lowest plot of Fig. 9.6 and the 45° and 60° plots of Fig. 9.8, we can see an agreement with the larger features of the spectra, but again a 'smearing out' of the finer energy structure of Fig. 9.6. This indicates the first aspect of our reproducibility problem.

The second aspect of the problem relates to the reproducibility of the slow peak spectra of aluminium deposited on different substrates. Aluminium was evaporated several times onto a number of different substrates, most of which have been incorporated in Fig. 9.9. The substrate surfaces

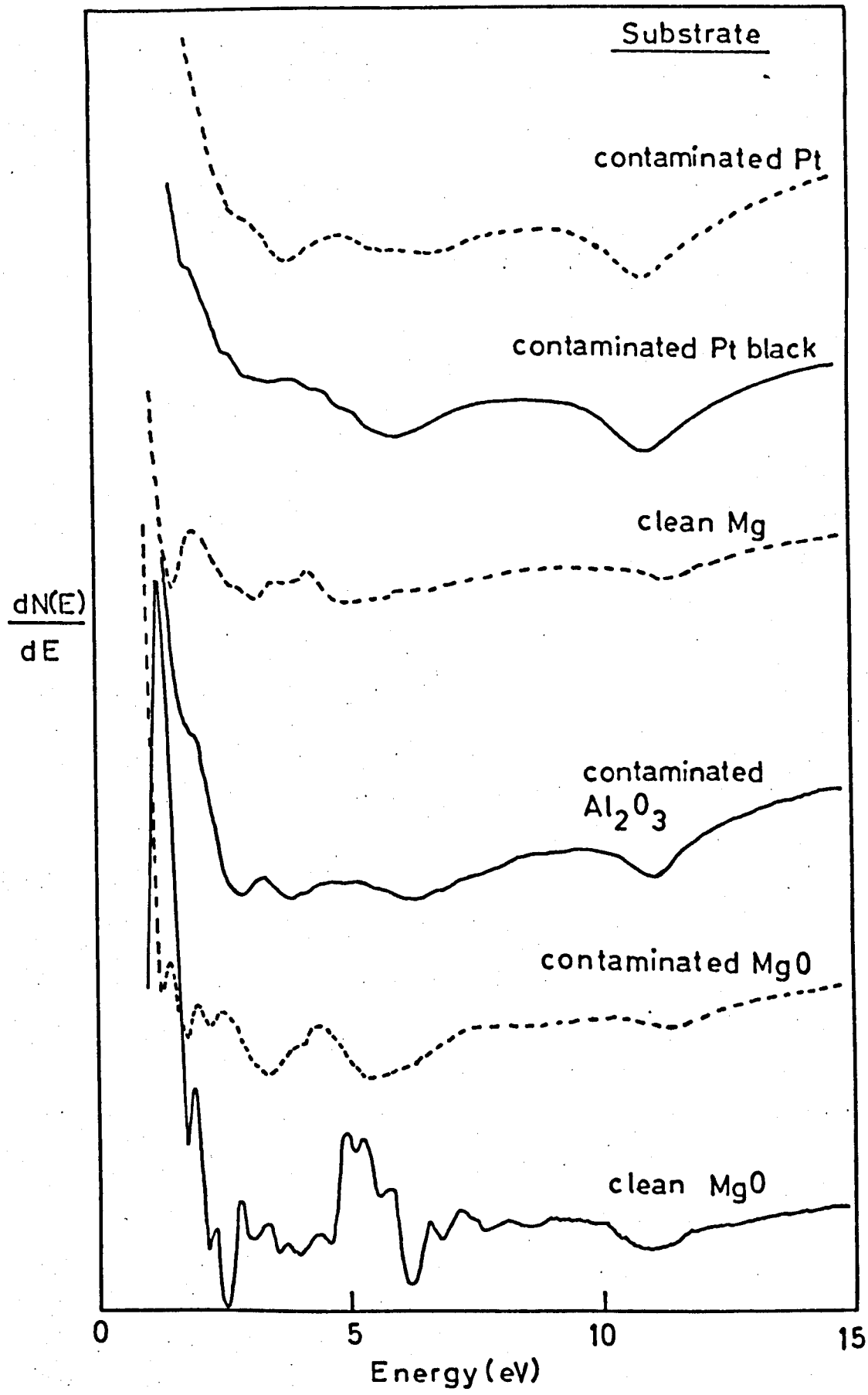

Figure 9.9 Slow peak of Al deposited on various substrates

of Pt and Pt black were prepared by evaporation of Pt in a commercial coating unit and were then transferred to the UHV chamber. The remaining surfaces were prepared by evaporations of Mg and Al respectively, in the UHV chamber, followed by exposure to air if required, to produce the corresponding MgO and Al_2O_3 surfaces. The spectra of Fig. 9.9 were taken with similar experimental conditions (apart from E_p differences), and the aluminium surfaces were clean as determined by AES. We can immediately see the strong fine structure which was observed using the clean MgO substrate. Using a similar substrate, but with some carbon contamination (contaminated MgO), the structure has weakened but is still stronger than the remaining spectra. The contaminants present on the other substrates were C on Al_2O_3, S and C on Pt black and K,S, C and O on Pt. The only consistently reproducible peaks from substrate to substrate appear to be those at 6 and 11eV.

9.4 Discussion

The AES and energy losses of aluminium have been adequately discussed in the literature and will therefore not be discussed in detail here.

The low energy Auger spectrum of aluminium shown in Fig. 9.1, is in basic agreement with the findings of other workers[42,89,91]. The weak peak at 104eV, detected by Harris[155] and Suleman[169], is verified in Fig. 9.1. Table 9.1 lists the observed Auger electron energy values for aluminium together with their assignments.

TABLE 9.1

Observed low energy Auger peaks for aluminium and assignments

Present Work (eV)	41	51	67	81	104
Assignment	$L_1L_{2,3}V$	PL	$L_{2,3}VV$	$(L_{2,3})_2VV$	L_1VV

PL - Auger electron suffering a bulk plasmon loss

The energy losses of aluminium are also well-known[42,91,114] and the observed energy losses are in agreement with other workers' results. Table 9.2 lists the observed energy losses together with their identification. All the energy losses can be rationalised in terms of multiple and combination plasmon losses, as in the case of magnesium.

The anomalous behaviour of the energy losses of aluminium deposited on a Pt black substrate (Fig. 9.3), can be explained as follows. An aluminium coating on the microscopically rough Pt black surface (Chapter 6), should approximately follow the contours of that surface. To prevent 'shadowing' effects, the Pt black surface was rotated through 180° with respect to the incident aluminium beam, during aluminium evaporations. Many non-normal surfaces will therefore be presented to the analysing electron beam, when it is at normal incidence with respect to the macroscopic target. This will cause a larger proportion of

TABLE 9.2

Energy Losses for Clean Aluminium

Observed Energy Loss (eV)	Assignment
10.6	S
15.5	B
20.0	2S
26.1	S+B
30.8	3S and 2B
42	2B + S
46	4S and 3B
57	2S + 2B and 3B +1S
62	4B
77	5B
92	6B

S - Surface plasmon loss, B - Bulk plasmon loss

TABLE 9.3

Observed Slow Peak Energies for Aluminium (eV)

(values taken from minima in N'(E) or maxima in N(E) as indicated)

Present results	von Koch[96]	Powell & Woodruff[91]	Henrich[41]	Jenkins & Chung[42]	Pattinson & Harris[100]	Guennou, Dufour & Bonnelle[170]
N'(E)	N(E)	N'(E)	N'(E)	N'(E)	N'(E)	N(E)
1.8					1.2	
2.2	absolute			2.0		
2.5	energy scale					
3.0	not				2.8	
3.5	determined					
4.0					4.0	
4.6						
5.1						
5.6		5.7	5.5	5.5	5.7	
6.2						
6.8					6.8	
7.2						
8.2						8.0
9.4		10.3	10.5	10	10.3	10.5
10.8						
	15.2				11.5	

surface plasmons to be generated as seen by the upper curve of Fig. 9.3. The remaining curves of the figure indicate that the incident electron has 'no knowledge' of its angle to the macroscopic target's surface. It appears therefore that the proportion of normal to non-normal microscopic surfaces remains fairly constant as the macroscopic angle changes. This type of situation might exist for a surface covered by tiny spheres say.

We will now turn to the less well understood area of the slow peak spectroscopy of aluminium. We have seen the importance of analysing this energy region using both the N'(E) mode and small values of modulating voltage. Table 9.3 collects and compares our present slow peak results with those of other workers. The values listed under 'present results' were obtained from the strong fine structure seen in Fig. 9.7 (2.0keV plot).

Only Pattinson and Harris[100] and myself[99] used evaporated films of aluminium; the other authors using polycrystalline and single crystal bulk samples, in conjunction with argon ion sputtering and annealing techniques. Many of the authors' results were taken using at least 1Vpk-pk modulation voltage thus giving poor resolution. Henrich[41] used +1.35V on the inner grid to remove space charge effects, and we have already seen the unfortunate consequence of such biassing, on the energy resolution of retarding potential analysers (sub-section 3.2.5

However, most authors including myself appear to agree that the strongest peaks in the slow peak spectrum occur at about 5.5 and 10eV. Furthermore, Fig. 9.9 shows that these two peaks are consistently reproducible from substrate to substrate. The plasmon gain hypothesis predicts peaks at 6 and 11eV if Fermi electrons are involved, which agrees fairly well with the observed energy values. Henrich[41] explains these two peaks in terms of the closing of plasma loss channels for hot electrons (sub-section 2.3.1). Guennou, Dufour and Bonnelle[170] consider two

TABLE 9.4

Correlation Test for Observed Slow Peak Energies and Symmetry Point Energies

Observed Peak Energy (eV)	Critical Point Energy (eV)	Critical Point
6.3	6.0	X_3
6.7	6.7	L_1
7.0	7.0	X'_5
7.5		
8.0		
8.5		
9.1		
9.6		
10.1	9.9	X_1
10.7		
11.3		
11.7	12.0	L_2
12.7	12.7	L_4
	13.4	Γ'_{25}
13.9		
	14.3	L_3
15.3	15.2	Γ_{15}
-	19.0	Γ'_2

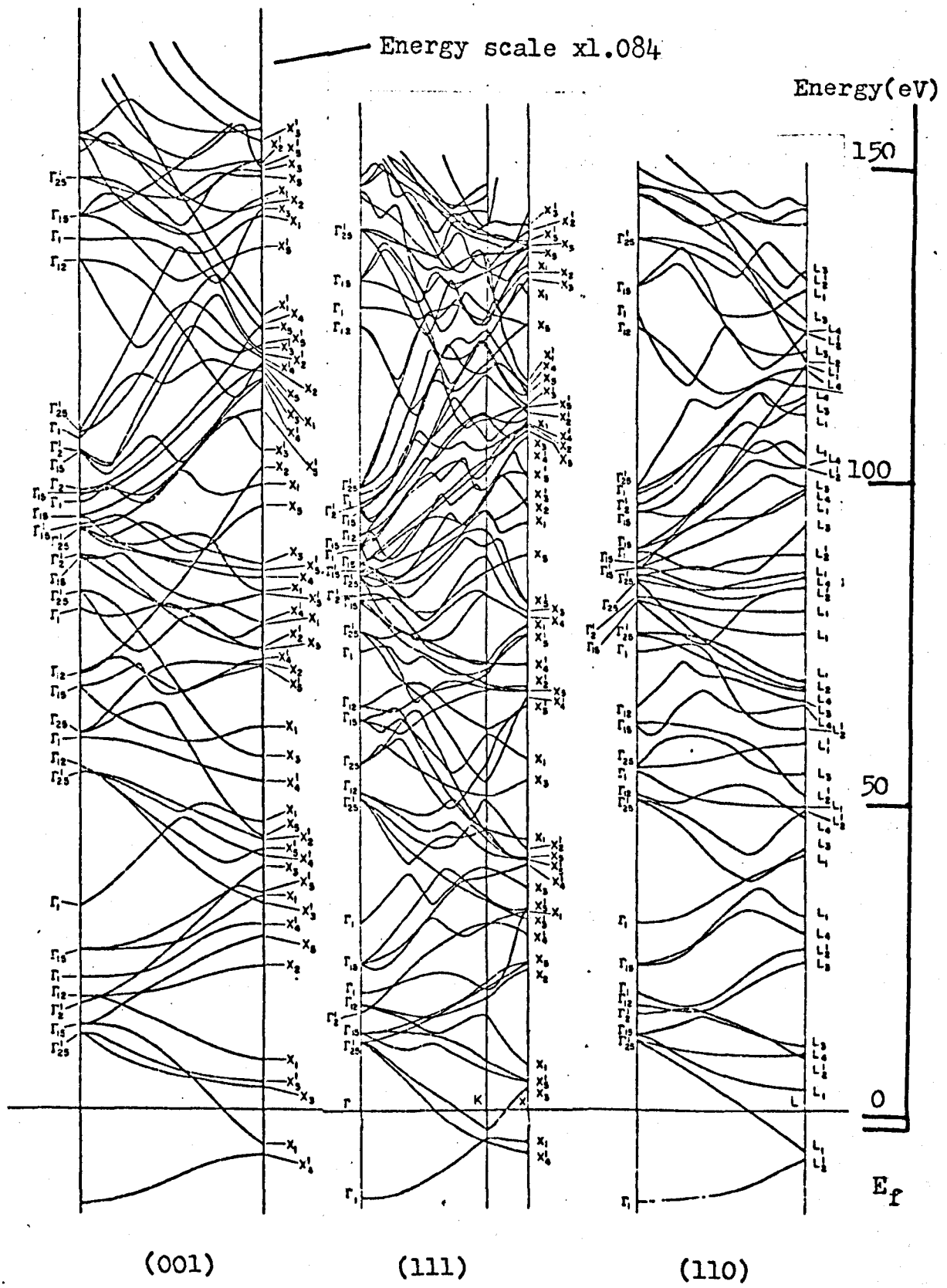

Figure 9.10 High-Energy Band Structure of Aluminium

(from Hoffstein and Boudreaux[168])

high-energy density of states maxima above the vacuum level and situated at the appropriate energies. Electrons would then be promoted to these levels by electron-electron interactions.

Up to the present, no interpretations are capable of explaining a possible number of 15 peaks in this energy region. Although Henrich[41] dismissed the effects of band structure when using polycrystalline samples and collecting the electrons emitted at all angles, Willis et. al.[105] have shown that this is not justified at least in the case of germanium. It is therefore possible that such high-energy band structure effects may be present.

In a polycrystalline sample (such as an evaporated thin film), we may expect that most of the possible crystal orientations will be presented to the incident electron beam, and hence the effects of the 'total' band structure should be observed. Excited electrons within the slow peak will tend to populate band minima at critical points due to relaxation processes. These electrons will 'bunch' at the critical point energies and may leave the surface with an energy $E_{cp} - \phi_s$, where E_{cp} is the critical point energy with respect to the Fermi level and ϕ_s is the work function for the surface. A recent high-energy band structure calculation by Hoffstein and Boudreaux[168], has enabled a correlation test to be performed. They used a pseudopotential method and obtained results for the Δ, Λ and Σ symmetry directions of the fcc lattice. The critical points were taken from their complete band structure diagrams, illustrated in Fig. 9.10. Unfortunately, the energy values had to be read directly from the diagrams so some possible reading errors may be present. The correlation test is presented in Table 9.4 and a work function correction is made, so that the energies are referred to the Fermi level of aluminium.

The critical points taken, incorporate the three symmetry directions: (001), (111) and (110). The agreement is somewhat limited and two gaps appear in the table between 7.5 and 9.6eV and between 10.7 and 11.7eV. It is possible that these gaps may be filled when more critical points are calculated for other symmetry directions.

There still remains the rather puzzling question of reproducibility. We have seen that the strong slow peak fine structure of aluminium, observed using the clean MgO substrate, appears to 'smear out' with the passage of time and/or electron beam exposure. In addition, such strong fine structure is not observed as a general rule when using other substrates. It may well be that surface structural effects could give rise to such observations e.g. a surface of microcrystalline structure will present many crystal orientations to the electron beam, whereas larger grains will present fewer symmetry directions. Aluminium was therefore evaporated onto a number of substrates including Pt black which is known to have a microscopically rough surface. Fig. 9.9 shows that simple surface roughness does not appear to give results of a substantially different nature to those from other surfaces. The exact explanation for the stronger fine structure in the cases of the MgO substrates is as yet elusive, although it may be possible to shed some light on the issue, by the use of LEED in conjunction with a high resolution retarding potential analyser.

9.5 Conclusions

The slow secondary electron spectrum of polycrystalline aluminium has been shown to be considerably more complex than previously published work has indicated. In addition, a new interpretation has been offered for the observed energy structure in terms of the high-energy band structure of aluminium, although the effects of plasmon-type structure are not ruled out. Reproducibility problems from surface to surface have been encountered and their origin is as yet not fully understood, although it it hoped that additional analytical techniques will help to over-come these difficulties.

CHAPTER 10

CONCLUSIONS AND SUGGESTIONS FOR FUTURE STUDIES

The technique of AES has undergone a rapid expansion since its inception in 1968. We have seen that the technique has grown from a pure surface research tool into a method of significant technological importance. Many researchers are now using AES in conjunction with other surface techniques such as LEED, work function, electron energy loss measurements etc., in order to monitor the presence of relevant surface chemical species.

Some theoretical aspects of AES are not well understood, including the calculation of Auger electron transition probabilities and Auger electron energies. However much progress has been made using semi-empirical approaches.

We have seen the extreme surface sensitivity of AES to surface species and in particular, the case of Cs on Au, where about 1-2% of a Cs monolayer is capable of being detected. A calibration curve for this system has been obtained and it was shown that an approximate linear relation was followed between the Auger signal of Cs and its fractional coverage, at submonolayer thicknesses.

The combined AES-SEM instrument appears to be of great technological importance when the surface spatial resolution of chemical species is required, e.g. microcircuit analysis. The preliminary results of Chapter 3 indicate the possibility of a simple conversion of an existing Auger electron spectrometer, to the combined AES-SEM instrument. Further improvements to both the detection electronics and electron beam spot sizes, should considerably improve the spatial resolution of the instrument.

The new retarding grid assembly, mentioned in Chapter 3, should hopefully give far less trouble in use, especially with regard to the energy resolution after grid re-assembly. Also it is hoped that the improved grid perfection will give an increase in resolution. A further improvement to the existing apparatus will be the construction of a $4\frac{1}{2}$" pumping tube on the chamber, which is connected to 6" liquid nitrogen-cooled diffusion pump, utilizing polyphenyl ether as the working fluid. This should considerable increase the pumping speed of the experimental chamber, enabling pressures to be kept low ($< 10^{-10}$ torr), especially during the evaporation of materials for the production of clean surfaces.

The strong surface reactivity of zirconium was investigated in Chapter 5, with a special emphasis on the technological implications of this work. An Auger spectrum of zirconium was presented which appears to originate from a cleaner surface than others published in the literature. However, some contamination was present and perhaps further work would enable the complete cleaning of a zirconium surface, to obtain its characteristic Auger spectrum.

Some thermal degradation problems of metal black surfaces have been discussed and a new temperature-resistant metal black coating (Pt black) has been thoroughly investigated, with the technique of secondary electron spectroscopy. Some work remains to be done here with regard to the reasons for the degradation of a copper black surface.

The energy losses of antimony have been systematically investigated, and a strong plasma-like behaviour was observed. A simple model for this behaviour was proposed which qualitatively explains the anomalous energy losses.

A major section of the work of the thesis concerns the elements of magnesium and aluminium, which have been rigorously analysed with the techniques of AES, electron energy loss and slow peak spectroscopy. Considerable fine energy structure has been observed in the slow peak regime of both aluminium and magnesium, and in the case of magnesium, this fine structure was observed as the surface slowly oxidised. The fine structure appeared to be more sensitive to initial chemisorption changes than the corresponding Auger effects. The observation of electron energy losses as the surface slowly oxidised, enabled further evidence to be obtained for a possible oxygen L_1VV Auger peak and also enabled an approximate figure for the MgO overlayer thickness to be calculated.

The retarding potential analyser appears to be one of the best electron spectrometers available for the analysis of very slow secondary electrons. However, the complex electron energy structure which has been observed in the low energy region will require considerably more theoretical and experimental investigation before its full potential is appreciated. To this end, additional analytical techniques are being developed and constructed, including UPS and XPS, which will shed more light on the energy levels and bands of the solid which may be participating in the electron stimulated electron emission processes. Also, LEED would be a useful tool when investigating the possible effects of surface structure on slow secondary electrons, but unfortunately, most LEED systems in current use do not have the required energy resolution.

REFERENCES

1. Lander, J., Phys. Ref., 91, 1382 (1953)
2. Reuter, W., Surf. Sci., 25, 80 (1971)
3. Müller, E.W., Modern Diffraction and Imaging Techniques in Materials Science, ed. S. Armelinckx et. al. (Amsterdam: North Holland) pp. 701-34 (1970)
4. Socha, A.J., Surf. Sci., 25, 147 (1971)
5. Siegbahn, K. et. al., Atomic, Molecular and Solid State Structure Studied by Means of Electron Spectroscopy, ESCA (Uppsala: Almqvist and Wiksell) (1967)
6. Smith, D.P., Surf. Sci., 25, 171 (1971)
7. Estrup, P.J. and McRae, E.G., Surf. Sci., 25, 1 (1971)
8. Prutton, M., Metall. Rev., 5, 57 (1971)
9. Weber, R.E. and Peria, W.T., J. Appl. Phys., 38, 4355 (1967)
10. Bruining, H., Physics and Applications of Secondary Electron Emission, McGraw-Hill, New York (1954)
11. Hachenberg, O. and Brauer, W., Advances in Electronics and Electron Physics (ed. Marton, L.) Vol. 11, Academic Press, New York (1959)
12. Willis, R.F. and Skinner, D.K., Sol. State Comm., 13, 685 (1973)
13. Harris, L.A., J. Appl. Phys., 39, 1419 (1968)
14. Auger, P., J. Phys. Radium, 6, 205 (1925)
15. Harris, L.A., J. Appl. Phys., 39, 1428 (1968)
16. Palmberg, P.W., Bohn, G.K. and Tracy, J.C., Appl. Phys. Lett., 15, 254 (1969)
17. Chang, C.C., Surf. Sci., 25, 53 (1971)
18. Gallon, T.E. and Matthew, J.A.D., Rev. Phys. Technol., (GB), 3, 31 (1972)
19. Gjostein, N.A. and Chavka, N.G., J. Test and Eval. J. TEVA 1, 183 (1973)
20. Weber, R.E., Research Development, Oct. (22-28), (1972)
21. Quinto, D.T. and Robertson, W.D., Surf. Sci., 27, 645 (1971)

22. Bishop, H.E. and Rivière, J.C., J. Appl. Phys., 40, 1740 (1969)

23. Neave, J.H., Foxon, C.T. and Joyce, B.A., Surf. Sci., 29, 411 (1972)

24. Burhop, E.H.S., 'The Auger effect and other raditionless transitions', (University Press, Cambridge), (1952)

25. Chung, M.F. and Jenkins, L.H., Surf. Sci., 22, 479 (1970)

26. Tarng, M.L. and Wehner, G.K., J. Appl. Phys., 44, 1534 (1973)

27. Eastman, Physical Electronics Conf., Albuquerque, (1972)

28. Ridgeway, J.W.T. and Haneman, D., Surf. Sci., 26, 683 (1971)

29. Ridgeway, J.W.T. and Haneman, D., Surf. Sci., 24, 451 (1971)

30. Palmberg, P.W. and Rhodin, T.N., J. Appl. Phys., 39, 2425 (1968)

31. Jacobi, K., Surf. Sci., 26, 54 (1971) In German

32. Musket, R.G. and Bauer, W., Appl. Phys. Lett., 20, 455 (1972)

33. Pines, D. and Bohm, D., Phys. Rev., 92, 609 (1953)
Pines, D., Phys. Rev., 92, 626 (1953)

34. Ritchie, R.H., Phys. Rev., 106, 874 (1957)

35. Stern, E.A. and Ferrell, R.A., Phys. Rev., 120, 130 (1960)

36. Gerlach, R.L., J. Vac. Sci. Tech., 8, 599 (1971)

37. Wolff, P.A., Phys. Rev., 95, 56 (1954)

38. Streitwolf, H.W., Ann. Physik, 3, 183 (1959)

39. Seah, M.P., Surf. Sci., 17, 132 (1969)

40. Gornyi, N.B., Sov. Phys. S.S., 8, 1535 (1966)

41. Henrich, V.E., Phys. Rev. B 7, 3512 (1973)

42. Jenkins, L.H. and Chung, M.F., Surf. Sci., 28, 409 (1971)

43. Willis, R.F., Feuerbacher, B. and Fitton, B., Phys. Rev. B 4, 2441 (1971)

44. Painter, G.S. and Ellis, D.E., Phys. Rev. B 1, 4747 (1970)

45. Harrower, G.A., Phys. Rev., 102, 304 (1956)

46. Zinke, O.H., Phys. Rev., 106, 1163 (1957)

47. Haas, T.W., Grant, J.T. and Dooley, G.J., Phys. Rev. B 1, 1449 (1970)

48. Aksela, S., Pessa, M. and Karras, M., Z. Physik 237, 381 (1970)

49. Palmberg, P.W., Riach, G.E., Weber, R.E. and MacDonald, N.C., 'Handbook of Auger Electron Spectroscopy', pub. Physical Electronics Industries Inc. (1972)

50. Palmberg, P.W., J. Vac. Sci. Tech., 9, 160 (1971)

51. Dooley 111, G.J., J. Vac. Sci. Tech., 9, 145 (1972)

52. Ellis, W.P., J. Vac. Sci. Tech., 9, 1027 (1972)

53. Macdonald, N.C., App. Phys. Lett., 16, 76 (1970)

54. Waldrop, J.R. and Marcus, H.L., JTEVA 1, 194 (1973)

55. Arthur, J.R., J. Vac. Sci. Tech., 10, 136 (1973)

56. Dooley 111, G.J. and Haas, T.W., J. Metals, 17, Nov. (1970)

57. Bonzel, H.P., Surf. Sci., 27, 387 (1971)

58. Vrakking, J.J. and Meyer, F., Surf. Sci., 33, 271 (1972)

59. King, R.J., Vacuum, 22, 493 (1972)

60. Weber, R.E. and Johnson, A.L., J. Appl. Phys., 40, 314 (1969)

61. Thomas, S. and Haas, T.W., J. Vac. Sci. Tech., 9, 840 (1972)

62. Thomas, S. and Haas, T.W., J. Vac. Sci. Tech., 10, 218 (1973)

63. Florio, J.V. and Robertson, W.D., Surf. Sci., 18, 398 (1969)

64. Perdereau, M., Surf. Sci., 24, 239 (1971)

65. Pollard, J.H., Surf. Sci., 20, 269 (1970)

66. Levenson, L.L., Davis, L.E., Bryson 111, C.E., Melles, J.J. and Kou, W.H., J. Vac. Sci. Tech., 9, 608 (1972)

67. Musket, R.G. and Ferrante, J., J. Vac. Sci. Tech., 7, 14 (1970)

68. Bouwman, R., Toneman, L.H. and Holscher, A.A., Vacuum, 23, 163 (1972)

69. Seah, M.P., Surf. Sci., 40, 595 (1973)

70. Shell, C.A. and Rivière, J.C., Surf. Sci., 40, 149 (1973)

71. Houston, J.E., Surf. Sci., 38, 283 (1973)

72. Grant, J.T., Haas, T.W. and Houston, J.E., Phys. Lett, 45A, 309 (1973)

73. Grant, J.T., Haas, T.W. and Houston, J.E., Surf. Sci., 42, 1 (1974)

74. Baker, J.M. and McNatt, J.L., J. Vac. Sci. Tech., 9, 792 (1972)

75. Ekelund, S. and Leygraf, C., Surf. Sci., 40, 179 (1973)

76. Allen, G.C. and Wild, R.K., Chem. Phys. Lett., 15, 279 (1972)

77. Färber, W. and Braun, P., Surf. Sci., 41, 195 (1974)

78. Szalkowski, F.J. and Somorjai, G.A., J. Chem. Phys., 56, 6097 (1972)

79. Farrell, H.H., Surf. Sci., 34, 465 (1973)

80. Grant, J.T. and Haas, T.W., Surf. Sci., 24, 332 (1971)

81. Watts, C.M.K., J. Phys. F: Metal Phys., 2, 574 (1972)

82. Jenkins, L.H. and Chung, M.F., Surf. Sci., 26, 151 (1971)

83. Hansson, W.F. and Arakawa, E.T., Z. Physik, 251, 271 (1972)

84. Chung, M.F. and Jenkins, L.H., Surf. Sci., 26, 649 (1971)

85. Jenkins, L.H. and Chung. M.F., Surf. Sci., 33, 159 (1972)

86. Rowe, J.E. and Christman, S.B., Sol. State Comm., 13, 315 (1973)

87. Löfgren, H. and Wallden, L., Sol. State Comm., 12, 19 (1973)

88. Salmeron, M., Baro, A.M. and Rojo, J.M., Surf. Sci., 41, 11 (1974)

89. Suleman, M. and Pattinson, E.B., J. Phys. F: Metal Phys., 1, L21 and L24 (1971)

90. Dufour, G., Guennou, H. and Bonnelle, C., Surf. Sci., 32, 731 (1972)

91. Powell, B.D. and Woodruff, D.P., Surf. Sci., 33, 437 (1972)

92. Schilling, J. and Raether, H., J. Phys. C: Sol. State Phys., 6, L 358 (1973)

93. Zehner, D.M., Clausing, R.E., McGuire, G.E. and Jenkins, L.H., Sol. State Comm., 13, 681 (1973)

94. Jenkins, L.H., Zehner, D.M. and Chung, M.F., Surf. Sci., 38, 327 (1973)

95. Thomas, S., Sol. State Comm., 13, 1593 (1973)

96. von Koch, C., Phys. Rev. Lett., 25, 792 (1970)

97. Wright, B. and Pattinson, E.B., J. Phys. F: Metal Phys., 3, 1237 (1973)

98. Wright, B. and Pattinson, E.B., J. Phys. F: Metal Phys., 4, 176 (1974)

99. Wright, B. and Pattinson, E.B., J. Phys. F: Metal Phys., In press.

100. Harris, P.R. and Pattinson, E.B., J. Electron Spect., 1,500 (1973)

101. Gornyi, N.B., Sov. Phys. JETP, 3, 175 (1956)

102. Scheibner, E.J. and Tharp, L.N., Surf. Sci., 8, 247 (1967)

103. Willis, R.F., Feuerbacher, B. and Fitton, B., Phys. Lett., 34A, 231 (1971)

104. Willis, R.F. and Fitton, B., J. Vac. Sci. Tech., 9, 651 (1972)

105. Willis, R.F., Laude, L.D. and Fitton, B., Phys. Rev. Lett., 29, 220 (1972)

106. Koshikawa, T. and Shimizu, R., Phys. Lett., 44A, 112 (1973)

107. Ellis, W.P., Surf. Sci., 41, 125 (1974)

108. Raether, H., Springer Tracts in Modern Physics, Vol. 38 (Springer-Verlag, Berlin) (1965)

109. Ritchie, R.H., Surf. Sci., 34, 1 (1973)

110. Fujimoto, F. and Komaki, K., J. Phys. Soc. Jap., 25, 1679 (1968)

111. Fujimoto, F., Komaki, K. and Ishida, K., J. Phys. Soc. Jap., 23, 1186 (1967)

112. Ashley, J.C. and Ritchie, R.H., Phys. Stat. Sol., 38, 425 (1970)

113. Powell, C.J. and Swan, J.B., Phys. Rev., 116, 81 (1959)

114. Powell, C.J. and Swan, J.B., Phys. Rev., 115, 869 (1959)

115. Powell, C.J. and Swan, J.B., Phys. Rev., 118, 640 (1960)

116. Murata, Y. and Ohtani, S., J. Vac. Sci. Tech., 9, 789 (1972)

117. Bishop, H.E. and Rivière, J.C., App. Phys. Lett., 16, 21 (1970)

118. Fiermans, L. and Vennik, J., Surf. Sci., 38, 257 (1973)

119. Salmeron, M., Baro, A.M. and Rojo, J.M., Sol. State Comm., 13, 1869 (1973)

120. Palmberg, P.W., J. Appl. Phys., 38, 2137 (1967)

121. Palmberg, P.W., Appl. Phys. Lett., 13, 183 (1968)

122. Taylor, N.J., Rev. Sci. Inst., 40, 792 (1969)

123. Blauth, E., Z. Physik, 147, 228 (1957)

124. Roy, D. and Carrette, J.D., Can. J. Phys., 49, 2138 (1971)

125. Gerlach, R.L., J. Vac. Sci. Tech., 10, 122 (1973)

126. Zashkvara, V.V., Korsunskii, M.I. and Kosmachev, O.S., Sov. Phys. Tech. Phys., 11. No. 1 (1966)

127. Bas, E.B. and Bänninger, U., Surf. Sci., 41, 1 (1974)

128. Ashwell, G.W.B., Todd, C.J. and Heckingbottom, R., J. Phys. E: Sci. Inst., 6, 435 (1973)

129. Morabito, J.M., Thin Sol. Films, 19, 21 (1973)

130. Thomas, S. and Pattinson, E.B., J. Phys. D., 3, 349 (1970)

131. Palmberg, P.W., Johnson, de W.C. and Boll, H.J., Rev. Sci. Inst., 35, 244 (1964)

132. Cross, J.A., J. Phys. D: Appl. Phys., 6, 622 (1973)

133. Koshikawa, T. and Shimizu, R., J. Phys. D: Appl. Phys., 6, 1369 (1973)

134. Weber, R.E. and Cordes, L.F., Rev. Sci. Inst. (USA), 37, 112 (1966)

135. Stewart, W.R.C., Private communication (1974)

136. Tracy, J.C., J. Chem. Phys., 56, 2736 (1972)

137. Christensen, N.E. and Seraphin, B.O., Phys. Rev. B4, 3321 (1971)

138. Joyner, R.W. and Roberts, M.W., J. Chem. S. Fl. 1242 (1973)

139. Macrae, A.U., Muller, K., Lander, J.J. and Morrison, J., Surf. Sci., 15, 483 (1969)

140. Desplat, J.L., Sol. State Comm., 13, 689 (1973)

141. Hartley, B.M., Phys. Lett., 24A, 396 (1967)

142. Todd, C.J., Conf. AES: Materials applications and quantification, N.P.L., Teddington Oct. 1973

143. Fehrs, D.L., Lee, T.J., Hopkins, B.J. and Stickney, R.E., Surf. Sci., 21, 197 (1970)

144. Bearden, J.A. and Burr, A.F., Rev. Mod. Phys., 39, 125 (1967)

145. Siegbahn, K. et. al., ESCA, North Holland, New York (1967)

146. Harris, P.R. and Pattinson, E.B., Vacuum 22, 405 (1972)

147. Holliday, J.E., Soft X-ray band spectra, Academic Press, New York (1967)

148. Thomas, S. and Pattinson, E.B., J. Phys. D: Appl. Phys., 3, 1469 (1970)

149. Thomas, S., Suleman, M. and Pattinson, E.B., J. Phys. D: Appl. Phys., 3, L77 (1970)

150. Losee, J.R. and Burch, D.S., Rev. Sci. Inst., 43, 146 (1972)

151. Wright, B. and Pattinson, E.B., J. Phys. D: Appl. Phys., In press

152. Powell, C.J., Proc. Phys. Soc., 76, 593 (1960)

153. Allen, R.M.,Ph.D. thesis, University of Keele, (1969)

154. Zacharias, P. and Kreibig, U., Z.Physik,231, 128 (1970)

155. Harris, P.R., Ph.D. thesis, University of Keele, (1973)

156. Leder, L.B., Phys. Rev., 103, 1721 (1956)

157. Hume-Rothery, H., Atomic theory for students of metallurgy, Inst. of Metals Monograph and Report Series No. 3 (1962)

158. von Hippel, A.R., J. Chem. Phys., 16, 372 (1948)

159. Sueoka, O., J. Phys. Soc. Jap., 20, 2203 (1965)

160. Falicov, L.M., Phil. Trans. R. Soc., A255, 55 (1962)

161. Suleman, M. and Pattinson, E.B., Surf. Sci., 35, 75 (1973)

162. Stewart, W.R.C., Private communication, (1974)

163. Fong, C.Y., Saslow, W. and Cohen, M.L., Phys. Rev., 168, 992 (1968)

164. Roessler, D.M. and Walker, W.C., Phys. Rev., 159, 733 (1967)

165. Watanabe, H., Phys. Rev., 95, 1684 (1954)

166. Jull, G.W., Proc. Phys. Soc., B69, 1237 (1956)

167. Burns, J., Phys. Rev., 119, 102 (1960)

168. Hoffstein, V. and Boudreaux, D.S., Phys. Rev. B2, 3013 (1970)

169. Suleman, M., Ph.D. thesis, University of Keele, (1971)

170. Guennou, H., Dufour, G. and Bonnelle, C., Surf. Sci., 41, 547 (1974)